

© 2008

Ming-Tsung Ho

ALL RIGHTS RESERVED

*IN SITU* TRANSMISSION INFRARED SPECTROSCOPY OF HIGH- $\kappa$   
OXIDE ATOMIC LAYER DEPOSITION ONTO SILICON SURFACES

By

Ming-Tsung Ho

A Dissertation submitted to the  
Graduate School-New Brunswick  
Rutgers, The State University of New Jersey  
in partial fulfillment of the requirements

for the degree of

Doctor of Philosophy

Graduate Program in Physics

written under the direction of

Yves J. Chabal

and approved by

---

---

---

---

---

New Brunswick, New Jersey

January 2008

## ABSTRACT OF THE DISSERTATION

### *In situ* Transmission Infrared Spectroscopy of High- $\kappa$ Oxide Atomic Layer Deposition onto Silicon Surfaces

by Ming-Tsung Ho

Dissertation Director:  
Yves J. Chabal

Ultra-thin aluminum oxide ( $\text{Al}_2\text{O}_3$ ) and hafnium oxide ( $\text{HfO}_2$ ) layers have been grown by atomic layer deposition (ALD) using tri-methyl-aluminum (TMA) and tetrakis-ethyl-methyl-amino-hafnium (TEMAH) respectively with heavy water ( $\text{D}_2\text{O}$ ) as the oxidizing agent. Several different silicon surfaces were used as substrates such as hydrogen terminated silicon (H/Si), SC2 (or RCA 2) cleaned native silicon oxide ( $\text{SiO}_2/\text{Si}$ ), and silicon (oxy)nitride. *In-situ* transmission Fourier transform infrared spectroscopy (FTIR) has been adopted for the study of the growth mechanisms during ALD of these films.

The vibrational spectra of gas phase TEMAH and its reaction byproducts with oxidants have also been investigated. Density functional theory (DFT) normal mode calculations show a good agreement with the experimental data when it is combined with linear wave-number scaling method and Fermi resonance mechanism. Ether ( $-\text{C}-\text{O}-\text{C}-$ ) and tertiary alkylamine ( $\text{N}(\text{R}_1\text{R}_2\text{R}_3)$ ) compounds are the two most dominant products of TEMAH reacting with oxygen gas and water. When ozone is used as the oxidant, gas phase  $\text{CH}_2\text{O}$ ,  $\text{CH}_3\text{NO}_2$ ,  $\text{CH}_3-\text{N}=\text{C}=\text{O}$  and other compounds containing  $-(\text{C}=\text{O})-$  and  $-\text{C}-\text{O}-\text{C}-$  (or  $-\text{O}-\text{C}-$ ) segments are observed.

With substrate temperatures less than  $400^\circ\text{C}$  and  $300^\circ\text{C}$  for TMA and TEMAH

respectively, Al oxide and Hf oxide ALD can be appropriately performed on silicon surfaces. Thin silicon (oxy)nitride thermally grown in ammonia on silicon substrate can significantly reduce silicon oxide interlayer formation during ALD and post-deposition annealing. The crystallization temperature of amorphous ALD grown  $\text{HfO}_2$  on nitridized silicon is  $600^\circ\text{C}$ , which is  $100^\circ\text{C}$  higher than on the other silicon surfaces.

When  $\text{HfO}_2$  is grown on H/Si(111) at  $100^\circ\text{C}$  deposition temperature, minimum 5 – 10 ALD cycles are required for the full surface coverage. The steric effect can be seen by the evolution of the H-Si stretching mode at  $2083\text{ cm}^{-1}$ . The observed red shift of H-Si stretching to  $\sim 2060\text{ cm}^{-1}$  can be caused by Si-H...Hf interactions or by the dielectric screening effect of as-grown high- $\kappa$  moiety. A summary of local bonding models with vibrational mode assignments of the adsorbed TMA and TEMAH on silicon surfaces is presented based on the analysis of the substructure of silicate interfacial band at  $900 - 1100\text{ cm}^{-1}$ .

*To my family-*

*Pin-Hsiu, Tzu-Yu and Tzu-Tzai*

## ACKNOWLEDGEMENT

I would like to give my special gratitude to Dr. Chien-Lan Hsueh, who has been a devoted coworker, a close friend and an enthusiastic mentor in my accompany to support and help me through the fantastic journey, a dramatic switch of research field from more than trillion-electron-volts (TeV) energy scale physics to less than one electron-volts energy scale surface chemistry. My work won't be able to start without Dr. Hsu-Chang Lu and Dr. Martin Frank, who served as excellent senior mentors to help and guide me this way far. Without the help and delicate work by physics department machine shop fellows, including Mr. Ernie Erskine, Mr. Eric Paduch, Mr. Schneider William and Mr. Arvid Knutsen, there won't be an end to my degree completion. Finally, I'd like to thank Professor Watts and Professor Langreth for their precious comments and suggestions to improve this thesis and Dr. Jihee Kwon for her great assistance in thesis writing. Thank you all for haveing made the part of my life in New Jersey and the nice memory of Rutgers. Thank you.

# TABLE OF CONTENTS

|   |           |
|---|-----------|
| <b>TITLE PAGE .....</b>   | <b>i</b>  |
| <b>ABSTRACT .....</b>   | <b>ii</b> |
| <b>ACKNOWLEDGEMENT .....</b>  | <b>v</b>  |
| <b>TABLE OF CONTENTS.....</b>   | <b>vi</b> |
| <b>LIST OF TABLES .....</b>   | <b>ix</b> |
| <b>LIST OF FIGURES .....</b>  | <b>x</b>  |
| <b>CHAPTER 0 INTRODUCTION .....</b>   | <b>1</b>  |
| <b>Conclusion.....</b>  | <b>9</b>  |
| <b>References .....</b>   | <b>11</b> |
| <b>CHAPTER 1 EXPERIMENT SETUPS, SUBSTRATE<br/>PREPARATION AND IR ABSORPTION DATA ANALYSIS<br/>.....</b> | <b>13</b> |
| <b>1.1 <i>In Situ</i> Transmission IR Setups and Silicon Surface Preparation</b>                        | <b>13</b> |
| <b>1.2 Transmission IR Data Analysis: .....</b>   | <b>18</b> |
| <b>1.3 Substrate Temperature in Atmospheric Pressure Purged Reactor<br/>.....</b>                       | <b>22</b> |
| <b>References .....</b>   | <b>23</b> |

## CHAPTER 2 TMA/D<sub>2</sub>O ALUMINUM OXIDE ALD ON THERMAL AMMONIA NITRIDIZED SILICON SURFACES.....25

### 2.1 Nitridized Silicon Surfaces Grown by Ammonia Exposure on H/Si .....25

- A. *Nitridation of H/Si(111) by 4 % Ammonia/N<sub>2</sub> at Atmospheric Pressure..... 26*
- B. *Nitridation of H/Si(100) by 4 % Ammonia/N<sub>2</sub> at Atmospheric Pressure..... 30*
- C. *Silicon Nitride Saturation Growth ..... 36*

### 2.2 D<sub>2</sub>O Exposure on Thermal Ammonia Nitridized Silicon Surface.40

### 2.3 TMA/D<sub>2</sub>O Aluminum Oxide ALD on Thermal Ammonia Nitridized Silicon Surfaces .....48

- A. *TMA/D<sub>2</sub>O ALD on Annealed Nitridized Silicon Surface..... 54*
- B. *TMA/D<sub>2</sub>O ALD on Thicker Silicon Nitride ..... 57*

### Conclusion: .....61

### References .....62

## CHAPTER 3 INFRARED ABSORPTION STUDY OF TEMAH.....67

### 3.1 TEMAH Gas Phase IR Spectrum.....67

### 3.2 TEMAH Gas Phase Reaction Products .....76

- A. *TEMAH Vapor Reaction with O<sub>2</sub>..... 78*
- B. *TEMAH Vapor Reaction with D<sub>2</sub>O or H<sub>2</sub>O ..... 80*
- C. *TEMAH Vapor Reaction with Ozone/ O<sub>2</sub> ..... 83*

### 3.3 TEMAH Reaction on Silicon Surfaces/ Accumulative TEMAH Exposure on Silicon Surfaces at Different Temperatures.....86

- A. *TEMAH Exposure on H/Si(100) Surface..... 88*
- B. *TEMAH Exposure on SC2 Wet Chemistry Silicon Oxide Surface..... 95*
- C. *TEMAH Exposure on 605° C Ammonia Nitridized Silicon Surface ..... 98*

### Conclusion..... 100



|  |            |
|--|------------|
| References .....   | 101        |
| <b>CHAPTER 4 TEMA<sub>H</sub>/ D<sub>2</sub>O HAFNIUM OXIDE ALD ON SILICON SURFACES.....</b>   | <b>105</b> |
| <b>4.1 ALD of Hafnium Oxide on H/Si(111).....</b>  | <b>105</b> |
| <i>A. Transmission IR Spectrum Overview.....</i>   | <i>105</i> |
| <i>B. Initial Nucleation Stage.....</i>  | <i>114</i> |
| <i>C. Surface Organic Complex .....</i>  | <i>117</i> |
| <i>D. Post Deposition Annealing .....</i>  | <i>122</i> |
| <b>4.2 Hafnium Oxide grown by ALD with TEMA<sub>H</sub> / D<sub>2</sub>O on H/Si(100)<br/>    .....</b>  | <b>126</b> |
| <i>A. IR Spectrum Overview .....</i>   | <i>126</i> |
| <i>B. Post Deposition Annealing .....</i>  | <i>128</i> |
| <b>4.3 H-Si Stretching Mode Red-shift.....</b>   | <b>130</b> |
| <b>4.4 TEMA<sub>H</sub>/D<sub>2</sub>O Hafnium Oxide ALD on SC<sub>2</sub> Oxidized and Thermal<br/>    Ammonia Nitridized Silicon Surfaces .....</b>    | <b>139</b> |
| <i>A. Hafnium Oxide ALD on SC<sub>2</sub> Oxidized Silicon Surface.....</i>  | <i>140</i> |
| <i>B. Hafnium Oxide ALD on Thermal Ammonia Nitridized Silicon Surface.....</i>   | <i>142</i> |
| <b>4.5 Post Deposition Annealing of ALD Grown Hafnium Oxide on SC<sub>2</sub><br/>    Oxidized and Thermal Ammonia Nitridized Silicon Surfaces .....</b> | <b>145</b> |
| <i>A. Post Deposition Annealing of ALD Hafnium Oxide on SC<sub>2</sub> Oxidized Silicon<br/>        Surface.....</i>                                     | <i>146</i> |
| <i>B. Post Deposition Annealing of ALD Hafnium Oxide on Nitridized Silicon<br/>        Surface.....</i>  | <i>149</i> |
| <b>4.6 Interfacial Bands of Single TMA and TEMA<sub>H</sub> Exposed Silicon<br/>    Surfaces .....</b>   | <b>152</b> |
| <b>Conclusion.....</b>   | <b>159</b> |
| <b>References .....</b>  | <b>161</b> |
| <b>CURRICULUM VITA.....</b>  | <b>165</b> |

## LIST OF TABLES

|  |     |
|--|-----|
| Table 1-1 Purge type reactor thermocouple temperature readings and<br>correspondent optical pyrometer temperature readings .....                             | 23  |
| Table 3-1 Comparison of major observed TEMAH, EtMeNH and scaled<br>DFT calculated peak modes.....  | 73  |
| Table 4-1 Principal Relevant Bond Stretching Frequencies[25-27] for<br>TEMAH/D <sub>2</sub> O Hafnium Oxide Growth.....                                      | 118 |
| Table 4-2 Correlation Table of Surface Carbonate Compound[19].....   | 121 |
| Table 4-3 Stretching Vibration Frequencies of NO <sub>3</sub> <sup>-</sup> and NO <sub>2</sub> <sup>-</sup> in Inorganic<br>Coordination Compounds[19] ..... | 122 |

# LIST OF FIGURES

|   |    |
|---|----|
| Fig. 0-1 Ball-and-stick models of TEMAH and TMA molecules .....   | 4  |
| Fig. 1-1 Schematic drawing of <i>in situ</i> transmission IR ALD reactor .....  | 14 |
| Fig. 1-2 Transmission IR absorbance spectrum at 70° incident angle of H/Si(100) at 60.1°C and reduced spectrometer purge referenced to the single beam spectrum (taken 1 hour ahead) of the same H/Si(100) at 60 °C.....  | 20 |
| Fig. 2-1 Transmission IR absorption spectra of ammonia exposure (40 ml/min diluted by ~1000 ml/min N <sub>2</sub> for 2 minutes) on H/Si(111) which is heated to calibrated 380 °C, 439 °C, 496 °C, 605 °C and 715°C temperatures. ....   | 27 |
| Fig. 2-2 Transmission step difference IR absorption spectra of ammonia exposure (40 ml/min diluted by ~1000 ml/min N <sub>2</sub> for 2 minutes in purged chamber) on H/Si(111) heated to calibrated 439 °C, 496 °C, 605 °C and 715°C temperatures. ....  | 29 |
| Fig. 2-3 Transmission IR absorption spectra referenced to starting H/Si(100) of 15-second 319 °C flash of starting surface, ammonia exposure (40 ml/min diluted by ~1000 ml/min N <sub>2</sub> for 2 minutes in purged chamber) on H/Si(100) heated to calibrated 319 °C, 380 °C, 439 °C, 496 °C, 605 °C and 715°C temperatures, then followed by 2 minutes of 400ml/min N <sub>2</sub> carrying D <sub>2</sub> O vapor exposure (diluted by 400 ml/min N <sub>2</sub> ) from a bubbler (~26°C). .... | 30 |
| Fig. 2-4 Transmission step difference IR absorption spectra of 15-second 319 °C flash of starting surface, ammonia exposure (40 ml/min diluted by ~1000 ml/min N <sub>2</sub> for 2minutes in purge style chamber) on H/Si(100) heated to calibrated 319 °C, 380 °C, 439 °C, 496 °C, 605 °C and 715°C temperatures, then followed by 2 minutes of 400ml/min N <sub>2</sub> carrying D <sub>2</sub> O vapor exposure (diluted by 400 ml/min N <sub>2</sub> ) from a bubbler (~26°C). ....              | 31 |

Fig. 2-5 Transmission IR spectra of different incident angles of  $\text{NH}_3$  exposure on H/Si(100). The nitridation is carried out in vacuum chamber (different from those of Fig. 1-4). Before the three H/Si(100) samples are respectively raised to  $500^\circ\text{C}$  for 2 minutes,  $600^\circ\text{C}$  for 30 seconds and  $700^\circ\text{C}$  for 30 seconds, each is pre-heated to  $200^\circ\text{C}$ ,  $300^\circ\text{C}$  and  $400^\circ\text{C}$  (1minute for each stage) in ammonia ambient (40 sccm  $\text{NH}_3$  diluted by 1000sccm  $\text{N}_2$  with the partial closed throttle valve resulting in an extrapolated total pressure~20-30 Torr) to reduce oxygen incorporation..... 35

Fig. 2-6 Transmission step difference IR spectra (left panel) and spectra referenced to starting H/Si(100) (right panel) of the accumulated  $\text{NH}_3$  exposures (30 seconds, 30 seconds, 1minute and 5 minutes 40 s.c.c.m.  $\text{NH}_3$  diluted by 1000s.c.c.m.  $\text{N}_2$  with the partial closed throttle valve for an extrapolated total pressure~20-30 Torr. ) to H/Si(100) at  $700^\circ\text{C}$ . Before the very first 30 seconds ammonia exposure to  $700^\circ\text{C}$  H/Si(100), the H/Si(100) is pre-heated to  $200^\circ\text{C}$ ,  $300^\circ\text{C}$  and  $400^\circ\text{C}$  (1minute for each stage) in ammonia ambient (40 s.c.c.m.  $\text{NH}_3$  diluted by 1000 s.c.c.m.  $\text{N}_2$  with the partial closed throttle valve for an extrapolated total pressure~20-30 Torr in vacuum chamber) to reduce oxygen incorporation. The inset in the right panel shows the plot of  $833\text{cm}^{-1}$  peak area over ammonia exposure time in seconds..... 37

Fig. 2-7 Plot of the integrated  $45^\circ$  incident angle IR (Si-N) mode~  $840\text{-}900\text{cm}^{-1}$  absorbance peak areas of the accumulated silicon nitride grown at increasing temperatures ammonia exposure on H/Si(100) (Fig. 2-1) and on H/Si(111) (Fig. 2-3) over the substrate temperatures. The MEIS calibrated average silicon nitride thicknesses are denoted in angstroms..... 39

Fig. 2-8 The transmission IR spectra referenced to starting H/Si(100) surface(the first and second panel from right), step difference spectra (the third panel from right), spectra referenced to the as-grown nitride surface (the fourth panel from right) of  $605^\circ\text{C}$  grown (40 ml/min ammonia flow diluted by ~1000 ml/min  $\text{N}_2$  for 2 minutes) silicon nitride film (assessed 3~4 Å thick by IR integrated area)

exposed to 1 minute 400ml/min N<sub>2</sub> carrying D<sub>2</sub>O vapor exposure diluted by 400 ml/min N<sub>2</sub> at 189, 319, 380, 439, 496, 605 and 715°C. The IR spectra of H/Si(100) exposed to the same D<sub>2</sub>O vapor exposure at 319, 380, 439, 496 and 605°C substrate temperatures in the most left panel for comparison. .... 41

Fig. 2-9 The IR integrated area of 500°C (~30s ammonia exposure time) grown silicon nitride moiety shows estimated thickness of 1.5~2 Å which is impossible to fully cover substrate surface. Spectra referenced to starting H/Si(100) surface on right panel and nitridized surface on left panel show obvious Si-O/ silicon oxide species~ 900-1200cm<sup>-1</sup> starts to grow with D<sub>2</sub>O exposure at 300°C. The Step difference spectra of the middle panel show the silicon nitride species mode~830-900cm<sup>-1</sup> consumed at 200°C D<sub>2</sub>O exposure and obvious silicon oxide TO-LO mode splitting at 500°C D<sub>2</sub>O exposure. .... 43

Fig. 2-10 The IR integrated area of 600°C (~30s ammonia exposure time) grown silicon nitride moiety shows estimated thickness of 3~4 Å which might barely cover substrate surface. The shapes of grown Si-O/ silicon oxide moiety in spectra are similar to those of 500°C grown silicon nitride, while the loss of silicon nitride mode~830-900cm<sup>-1</sup> is not obvious. .... 44

Fig. 2-11 The IR integrated area of 700°C grown (~30s ammonia exposure time) silicon nitride moiety shows estimated thickness of ~5 Å which might have fully covered substrate surface. The bottom nitride film spectrum taken at 70° incident angle in light green verifies 1150cm<sup>-1</sup> peak the silicon nitride LO mode. The structure of grown Si-O/ silicon oxide moiety modes is similar to that grown on other thermal ammonia nitridized silicon surfaces grown at 500 °C and 600°C. .... 45

Fig. 2-12 The IR integrated area of 700°C grown saturated silicon nitride by extra long ammonia exposure time~7 minutes shows estimated thickness of 11~12 Å which surely cover substrate surface with a layer of stoichiometric silicon nitride. Again the structure of grown Si-O/ silicon oxide moiety modes is

- similar to that grown on nitridized surface with shorter (~30 seconds ) ammonia exposure..... 46
- Fig. 2-13 Left plot: the integrated IR absorbance peak areas of silicon oxide moiety~1000cm<sup>-1</sup> grown by thermal D<sub>2</sub>O exposure on 500°C (light blue triangle), 600°C (pink triangle), 700°C (olive triangle) ammonia nitridized silicon surfaces and 700°C saturated silicon nitride (blue triangle) versus annealing temperatures. The dashed line indicating the absorbance peak area of SC2 wet chemistry silicon oxide TO mode (~1030cm<sup>-1</sup>). Right-top view graph: penetration growth of silicon-oxygen moiety; right-lower view graph: thick enough silicon nitride film sustaining oxidation. .... 47
- Fig. 2-14 Transmission IR absorption spectra referenced to the starting SC2 oxidized silicon surface and at incident angle 70° of sequential operations: 1, 5, 30 seconds 100 sccm N<sub>2</sub> carrying TMA exposure to 60°C silicon oxide surface followed by 30 seconds same flow exposure on substrate at 200, 300, 400 and 500°C in vacuum chamber..... 49
- Fig. 2-15 Transmission IR absorption step difference spectra at incident angle 70° of sequential operations: 1, 5, 30 seconds 100 sccm N<sub>2</sub> carrying TMA exposure to 60°C silicon oxide surface followed by 30 seconds same flow exposure on substrate at 200, 300, 400 and 500°C in vacuum chamber..... 50
- Fig. 2-16 Transmission IR absorption spectra of 30-second 100 sccm N<sub>2</sub> carrying TMA exposure to 60°C H/Si(100) at 70° incident angle, thermal ammonia nitridized silicon surface (2-minute ammonia pretreated at 610°C) at 70° incident angle and SC2 oxidized silicon surface at 20° and 70° incident angles. The bottom nitridized silicon surface referenced to H/Si(100) at 70° incident angle in red and local spectrum section of SC2 wet chemistry pre-treated H/Si(100) referenced to H/Si(100) at 70° incident angle in yellow-green are for comparison..... 52

|  |    |
|--|----|
| Fig. 2-17 The in-situ IR spectra referenced to H/Si(100) of 380°C aluminum oxide ALD on 605°C annealed 496°C ammonia treated H/Si(100) surface are taken at incident angle of 45° .....  | 54 |
| Fig. 2-18 The in-situ IR step difference spectra of 380°C aluminum oxide ALD on 605°C annealed 496°C ammonia treated H/Si(100) surface are taken at incident angle of 45° .....  | 55 |
| Fig. 2-19 The in-situ IR spectra referenced to H/Si(100) of 380°C aluminum oxide ALD on 605°C ammonia treated H/Si(100) surface are taken at incident angle of 45° .....   | 58 |
| Fig. 2-20 The colored in-situ IR spectra referenced to 605°C ammonia treated surface of 380°C aluminum oxide ALD on 622°C ammonia treated H/Si(100) surface are taken at incident angle of 45°. The bottom 622cNSi spectrum in black is referenced to H/Si(100). .....   | 59 |
| Fig. 2-21 Sections of base-lined and Gaussian curve fitted transmission IR spectra referenced to nitridized silicon surface in 800-1250cm <sup>-1</sup> of 1 cycle and 4 cycles 380°C TMA/D <sub>2</sub> O ALD on 495°C (left panel) and 605°C (right panel) ammonia treated H/Si(100). .....  | 60 |
| Fig. 2-22 Al oxide mode (~950cm <sup>-1</sup> ) absorbance peak area of 380°C TMA/D <sub>2</sub> O ALD grown on H/Si(100) (Si-H; black solid square), SC2 oxidized silicon surface (SiO <sub>2</sub> ; red open circle) and 605°C-4% ammonia grown silicon nitride film (Si <sub>x</sub> N <sub>y</sub> ; blue solid triangle) plot over ALD cycle numbers. ....   | 60 |
| Fig. 3-1 (a) $\nu_{Observed} / \nu_{Calculated}$ scaling fitting plots and fitting lines. (solid squares and triangles in red are minor peaks not included for linear fitting) (b) Top in black is the observed TEMA <sup>h</sup> FTIR absorption spectrum, the middle in brown is the WLS scaled DFT/PBE/modified TZVP calculation peak profile, and the bottom is the WLS scaled DFT/ B3LYP/LANL2DZ(5D,7F) calculation peak profile. DFT calculation peak profiles are made by superposing all 144 4cm <sup>-1</sup> -wide Gaussian shape functions parametrized by the DFT calculated intensities |    |

and WLS scaled frequencies. All the major peak frequencies are denoted therein. .... 75

Fig. 3-2 Local  $\nu(\text{C-H})$  and  $\delta(\text{C-H})$  details of the observed TEMAH FTIR absorption spectrum (top in black) and the WLS scaled DFT/PBE/modified TZVP calculation peak profile (bottom in brown) The overtone of TEMAH  $1420\text{cm}^{-1}$  C-H bending mode couples with the DFT-suggested  $2799\text{cm}^{-1}$  C-H stretching mode through Fermi resonance mechanism to eliminate the extraordinary strong DFT-suggested band and enhance the absorption bands around  $2875\text{cm}^{-1}$  (and possibly  $2649\text{cm}^{-1}$ ). .... 76

Fig. 3-3 Example of processing technique of absorbance spectrum subtraction: The subtraction result HOD absorbance spectrum (d) is obtained by subtracting the reactant,  $\text{H}_2\text{O}$  (b) and  $\text{D}_2\text{O}$  (c), absorbance spectra from the absorbance spectrum of  $\text{D}_2\text{O}+\text{H}_2\text{O}$  mixture (a). .... 78

Fig. 3-4 Comparison of the processed mixture spectra referenced to empty reactor made by suitable spectrum subtractions and the relevant subtraction coefficients: (a) enhanced atmospheric pressure TEMAH in  $\text{O}_2$  ambient at  $\mu_{\text{TEMAH}}=1.1785$ , (b) atmospheric pressure TEMAH+ $\text{D}_2\text{O}$  mixture at  $\mu_{\text{D}_2\text{O}}=0.5898$ ,  $\mu_{\text{HDO}}=0.4596$  and  $\mu_{\text{TEMAH}}=0$  (c) low pressure ( $\sim 8.5$  Torr) TEMAH+ $\text{D}_2\text{O}$  mixture at  $\mu_{\text{D}_2\text{O}}=0.8580$ ,  $\mu_{\text{HDO}}=0$  and  $\mu_{\text{TEMAH}}=0$  and (d) high pressure ( $\sim 16\text{-}25\text{Torr}$ ) TEMAH+ $\text{H}_2\text{O}$  mixture at  $\mu_{\text{H}_2\text{O}}=0.6221$  and  $\mu_{\text{TEMAH}}=0$ . .... 83

Fig. 3-5 Ozone (top) absorbance spectrum and its three primary fundamental vibrations  $\sim 680, 720\text{cm}^{-1}$  doublet ( $\nu_2$ ),  $1038, 1055\text{cm}^{-1}$  doublet ( $\nu_1$ ) and  $1743\text{cm}^{-1}$  ( $\nu_3$ ) and overtones  $\sim 2100, 2123\text{cm}^{-1}$  ( $\nu_2$  or  $2\nu_1$ )  $3055\text{cm}^{-1}$  ( $3\nu_1$ ) as the cited assignment by Sutherland-Penney in Ref.30 ;  $2800\text{cm}^{-1}$  and  $1165\text{ } 1131\text{cm}^{-1}$  doublet are too weak to be manifested in current plot scale. The processed TEMAH+ozone/ $\text{O}_2$  ( $\sim 8.5$  Torr) IR absorption spectrum made by subtraction coefficients,  $\mu_{\text{ozone}}=0.9904$ ,  $\mu_{\text{CO}_2}=1.2062$ ,  $\mu_{\text{H}_2\text{O}}=0.2941$  and  $\mu_{\text{TEMAH}}=0$ , (middle) shows the existence of  $\text{CH}_2\text{O}$ ,  $\text{CH}_3\text{NO}_2$ ,  $\text{CH}_3\text{-N=C=O}$  and other  $\text{-(C=O)-}$  and  $\text{-}$



C-O- features  $\sim 1710\text{cm}^{-1}$  and  $1250\text{-}1000\text{cm}^{-1}$  respectively in gas phase reaction products. (the dips around  $710$ ,  $1043$  and  $2110\text{ cm}^{-1}$  are due to imperfection of ozone spectrum subtraction and  $2060\text{cm}^{-1}$  indicated in parenthesis is  $\nu_s(\text{CH}_3)$  frequency for  $\text{CH}_3\text{NO}_2$  and  $\text{CH}_3\text{-N=C=O}$  ) The high pressure ( $\sim 16\text{-}25\text{Torr}$ ) TEMAH+ $\text{H}_2\text{O}$  spectrum is shown in bottom for contrast. .... 86

Fig. 3-6 The colored spectra at  $20^\circ$  incident angle referenced to initial surface of the accumulatively dosing TEMAH (10 seconds 50 s.c.c.m. carrying  $\text{N}_2$ ) to H/Si(100) in vacuum chamber with 100 s.c.c.m.  $\text{N}_2$  flow at different temperatures of the first  $60^\circ\text{C}$ , the second  $60^\circ\text{C}$ ,  $100^\circ\text{C}$ ,  $150^\circ\text{C}$ ,  $200^\circ\text{C}$ ,  $250^\circ\text{C}$ ,  $300^\circ\text{C}$ ,  $350^\circ\text{C}$  and  $400^\circ\text{C}$ , then 2 minutes of annealing at  $500^\circ\text{C}$  and  $700^\circ\text{C}$ . .... 88

Fig. 3-7 Selected colored step difference spectra at  $20^\circ$  incident angle of the accumulatively dosing TEMAH (10 seconds 50 s.c.c.m. carrying  $\text{N}_2$ ) to H/Si(100) in vacuum chamber with 100 s.c.c.m.  $\text{N}_2$  flow at stepped temperatures from  $60^\circ\text{C}$ - $300^\circ\text{C}$ . .... 89

Fig. 3-8 The colored spectra at  $70^\circ$  incident angle referenced to initial surface of the accumulatively dosing TEMAH (10 seconds 50 s.c.c.m. carrying  $\text{N}_2$ ) to H/Si(100) in vacuum chamber with 100 s.c.c.m.  $\text{N}_2$  flow at different temperatures of the first  $60^\circ\text{C}$ , the second  $60^\circ\text{C}$ ,  $100^\circ\text{C}$ ,  $150^\circ\text{C}$ ,  $200^\circ\text{C}$ ,  $250^\circ\text{C}$ ,  $300^\circ\text{C}$ ,  $350^\circ\text{C}$ ,  $400^\circ\text{C}$ , then 2 minutes of annealing at  $500^\circ\text{C}$  and  $700^\circ\text{C}$ ..... 92

Fig. 3-9 Colored selected step difference spectra in of the accumulatively dosing TEMAH (10 seconds 50 s.c.c.m. carrying  $\text{N}_2$ ) to H/Si(100) in vacuum chamber with 100 s.c.c.m.  $\text{N}_2$  flow at lower temperatures of the first  $60^\circ\text{C}$ , the second  $60^\circ\text{C}$ ,  $100^\circ\text{C}$ ,  $150^\circ\text{C}$ ,  $200^\circ\text{C}$ ,  $250^\circ\text{C}$  and  $300^\circ\text{C}$  at  $70^\circ$  incident angle. .... 93

Fig. 3-10 The colored spectra at  $45^\circ$  incident angle referenced to the initial surface of the accumulatively dosing TEMAH (40 s.c.c.m.  $\text{N}_2$  carrying) for 20 minutes to  $\text{SC2}$  oxidized silicon surface in atmospheric pressure purge style chamber with

200 s.c.c.m. and 440 s.c.c.m. N<sub>2</sub> flow purge in KBr window and chamber through precursor delivery lines during TEMAH dosing and extra 600 s.c.c.m. N<sub>2</sub> flow purge in KBr window after dosing and IR spectrum taking at different calibrated temperatures (thermocouple temperatures in parenthesis) of 67°C, 123°C, 190°C, 255°C, 319°C, 380°C, 496°C, then 255°C again, and final 1 minute D<sub>2</sub>O exposure (400 s.c.c.m. N<sub>2</sub> carrying) at 156°C..... 95

Fig. 3-11 The colored step difference spectra at 45° incident angle of the accumulatively dosing TEMAH (40 s.c.c.m. N<sub>2</sub> carrying) for 20 minutes to SC2 oxidized silicon surface in atmospheric pressure purge style chamber with 200 s.c.c.m. and 440 s.c.c.m. N<sub>2</sub> flow purge in KBr window and chamber through precursor delivery lines during TEMAH dosing and extra 600 s.c.c.m. N<sub>2</sub> flow purge in KBr window after dosing and IR spectrum taking at different calibrated temperatures (thermocouple temperatures in parenthesis) of 67°C, 123°C, 190°C, 255°C, 319°C, 380°C, 496°C, then 255°C, and final 1 minute D<sub>2</sub>O exposure (400 s.c.c.m. N<sub>2</sub> carrying) at 156°C. Those peaks at 877, 980, 1213, 2788, 2858, 2875, 2938 and 2969 denoted by dashed lines in the top panel are due to TEMAH vapor residual in chamber and the spectrum in black in the bottom panel is the TEMAH gas phase spectrum for contrast. .... 96

Fig. 3-12 The colored spectra at 45° incident angle referenced to the initial surface of the accumulatively dosing TEMAH (40 s.c.c.m. N<sub>2</sub> carrying) for 20 minutes to ammonia pretreated 605°C H/Si(100) surface in atmospheric pressure purge style chamber with 200 s.c.c.m. and 440 s.c.c.m. N<sub>2</sub> flow purge in KBr window and chamber through precursor delivery lines during TEMAH dosing and extra 600 s.c.c.m. N<sub>2</sub> flow purge in KBr window after dosing and IR spectrum taking at different calibrated temperatures (thermocouple temperatures in parenthesis) of 67°C, 123°C, 190°C, 255°C, 319°C, 380°C, 496°C and final 1 minute D<sub>2</sub>O exposure (400 s.c.c.m. N<sub>2</sub> carrying) at 156°C. Those peaks at 877, 980, 1213, 2788, 2858, 2875, 2938 and 2969 denoted by dashed lines in the top panel are due to TEMAH vapor residual in chamber. 98

Fig. 3-13 The colored step difference spectra at 45° incident angle of the accumulatively dosing TEMAH (40 s.c.c.m. N<sub>2</sub> carrying) for 20 minutes to ammonia pretreated 605°C H/Si(100) surface in atmospheric pressure purge style chamber with 200 s.c.c.m. and 440 s.c.c.m. N<sub>2</sub> flow purge in KBr window and chamber through precursor delivery lines during TEMAH dosing and extra 600 s.c.c.m. N<sub>2</sub> flow purge in KBr window after dosing and IR spectrum taking at different calibrated temperatures (thermocouple temperatures in parenthesis) of 67°C, 123°C, 190°C, 255°C, 319°C, 380°C, 496°C and final 1 minute D<sub>2</sub>O exposure (400 s.c.c.m. N<sub>2</sub> carrying) at 156°C. Those peaks at 877, 980, 1213, 2788, 2858, 2875, 2938 and 2969 denoted by dashed lines in the top panel are due to TEMAH vapor residual in chamber..... 99

Fig. 4-1 Transmission IR absorption spectra of TEMAH/D<sub>2</sub>O hafnium oxide ALD on H/Si(111) up to 40 cycles referenced to the starting H/Si(111) surface..... 106

Fig. 4-2 Comparison of the half-cycle exposure transmission IR spectra of TEMAH/D<sub>2</sub>O hafnium oxide ALD growth and the TEMAH gas phase spectrum in the frequency range 700-1900 cm<sup>-1</sup> and 2550-3050 cm<sup>-1</sup>..... 108

Fig. 4-3 Step difference transmission IR absorption spectra of TEMAH/D<sub>2</sub>O hafnium oxide ALD on H/Si(111) in the frequency range of 650-3050 cm<sup>-1</sup>. ..... 109

Fig. 4-4 IR half-cycle step difference absorption spectra of TEMAH/D<sub>2</sub>O hafnium oxide ALD on H/Si(111) in the frequency range of 1850-2300 cm<sup>-1</sup> relevant to H-Si stretching mode..... 111

Fig. 4-5 (a) (Top) Transmission IR absorption spectra of H-terminated Si(111) after the specific number of TEMAH and water exposures in the H-Si stretch region. All spectra are referenced to an oxidized surface. Inset plot shows the sharp mode integrated absorbance area varying with ALD cycle numbers. (b) (Bottom) Surface hydrogen coverage after TEMAH and water exposures. The ratio is calculated from the integration of the Si-H stretch mode intensity after a specific number ALD cycles. The hafnium oxide thickness measured with

|  |     |
|--|-----|
| RBS increases linearly with the number of ALD cycles with a slightly smaller growth rate in the first three cycles. ....   | 112 |
| Fig. 4-6 Full-cycle transmission IR absorption spectra referenced to fully H-terminated Si of TEMAH/D <sub>2</sub> O hafnium oxide ALD on H/Si(111) in the frequency range of 400-1300 cm <sup>-1</sup> relevant to the interface and grown film phonon mode showing the development of peaks at ~510, 680 cm <sup>-1</sup> , 1000 cm <sup>-1</sup> during the ALD process (the anti-peak at 627 cm <sup>-1</sup> indicating the loss of surface hydrogen). The inset shows the absorbance integrated area of the 1000cm <sup>-1</sup> band, exhibiting saturation at ~0.021 cm <sup>-1</sup> after about 5–10 cycles of hafnium oxide deposition..... | 115 |
| Fig. 4-7 Step difference transmission IR absorption spectra of TEMAH/D <sub>2</sub> O hafnium oxide ALD on H/Si(111) in the frequency range of 800-1100 cm <sup>-1</sup> . ....  | 116 |
| Fig. 4-8 Step difference transmission IR absorption spectra of TEMAH/D <sub>2</sub> O hafnium oxide ALD on H/Si(111) in the frequency range of 800-1850cm <sup>-1</sup> for surface organic complex species identification.....  | 121 |
| Fig. 4-9 The overall view of annealing spectra taken overnight referenced to H/Si(111) starting surface show baseline structure with a very broad lump in 3500-2500cm <sup>-1</sup> decreasing with spectrometer operation time. The grown OD, CH <sub>x</sub> and modes in 1600-1100 cm <sup>-1</sup> during ALD are either partially removed or decreasing with the annealing temperatures, while silicon oxide and strong modes ~900-500 cm <sup>-1</sup> appear during annealing. ....   | 123 |
| Fig. 4-10 Transmission IR spectra of 20 cycle TEMAH/D <sub>2</sub> O ALD grown hafnium oxide on H/Si(111) annealed up to 300, 400, 500, 600 and 700°C. (The spectra in the third panel from left are reference to the silicon oxide surface, and the spectra in the other panels are referenced to the initial H/Si(111) ) .....   | 124 |
| Fig. 4-11 Transmission spectra of 40 cycle TEMAH/D <sub>2</sub> O grown ALD hafnium oxide referenced to H/Si(111) and 700°C annealed spectra referenced to H/Si(111) and as-deposited 40 cycle grown film at incident angles of 20° and 70°. ....  | 125 |

|   |     |
|---|-----|
| Fig. 4-12 Full cycle transmission spectra of 100°C grown TEMAH/D <sub>2</sub> O hafnium oxide ALD on H/Si(100) referenced to the starting surface.....  | 126 |
| Fig. 4-13 Selected absorbance spectra of TEMAH/D <sub>2</sub> O exposures on H/Si(100) referenced to 100°C annealed Ge(100) surface. ....   | 127 |
| Fig. 4-14 Transmission absorbance spectra of 100°C grown 20 cycle TEMAH/D <sub>2</sub> O ALD hafnium oxide on H/Si(100) surface annealed to 300°C, 400°C, 500°C and some temperature higher than 500°C but lower than 600°C. ....   | 128 |
| Fig. 4-15 Step difference absorbance spectra of 100°C grown 20 cycle TEMAH/D <sub>2</sub> O ALD hafnium oxide on H/Si(100) surface annealed to 300°C, 400°C, 500°C and some temperature higher than 500°C but lower than 600°C.....   | 129 |
| Fig. 4-16 Transmission spectra referenced to starting H/Si(100) of TEMAH, TMA and ammonia exposure respectively on 100°C, 60 °C and 430 °C H/Si(100). ....  | 130 |
| Fig. 4-17 Top: schematic drawing of TEMAH molecule reacting with surface silicon dihydride. Bottom: the linear fitting plot of the dependence of H-Si stretching mode frequency on crystalline silicon surface to the stability-ratio electronegativity sum of its nearest bonding neighbor atoms. .... | 132 |
| Fig. 4-18 Top: schematic drawing of hafnium oxide-silicon interface of hafnium oxide ALD on H/Si. Bottom: schematic drawing for simple dipole oscillator model. ....  | 134 |
| Fig. 4-19 Transmission IR absorption spectra of the H-Si stretching mode of 10 full cycle of TEMAH/D <sub>2</sub> O ALD growth on H/S(100)(top) and H/Si(111)(bottom). ...  | 138 |
| Fig. 4-20 Half-cycle transmission IR spectra of TEMAH/D <sub>2</sub> O hafnium oxide ALD exposures on SC2 treated H/Si(100) surface.....  | 140 |
| Fig. 4-21 Step difference spectra of TEMAH/D <sub>2</sub> O hafnium oxide ALD exposures on SC2 wet chemistry pre-treated H/Si(100). ....  | 141 |

- Fig. 4-22 Bottom black spectrum is the prepared ammonia treated 600°C H/Si(100) surface referenced to H/Si(100), the other colored are transmission IR spectra of TEMAH/D<sub>2</sub>O hafnium oxide ALD for the first four half cycles and the 20th full cycle referenced to the ammonia nitridized surface (the starting surface for ALD exposures)..... 143
- Fig. 4-23 Bottom black spectrum is the prepared ammonia treated 600°C H/Si(100) surface referenced to H/Si(100), the other colored are step difference spectra of TEMAH/D<sub>2</sub>O hafnium oxide ALD for the first four half cycles and the 20th full cycle. .... 143
- Fig. 4-24 Transmission IR absorbance spectra, referenced to the as-deposited hafnium oxide surface, of 100°C grown 20 cycle TEMAH/D<sub>2</sub>O ALD hafnium oxide on SC2 wet chemistry pre-treated H/Si(100) surface annealed to 300°C, 400°C, 500°C, 600°C and 700°C . .... 147
- Fig. 4-25 Absorbance spectra, referenced to starting surface before ALD, of 100°C grown 20 cycle TEMAH/D<sub>2</sub>O ALD hafnium oxide on SC2 wet chemistry pre-treated H/Si(100) surface annealed to 300°C, 400°C, 500°C, 600°C and 700°C ..... 147
- Fig. 4-26 Step differential absorbance spectra of 100°C grown 20 cycle TEMAH/D<sub>2</sub>O ALD hafnium oxide on SC2 wet chemistry pre-treated H/Si(100) surface annealed to 300°C, 400°C, 500°C, 600°C and 700°C ..... 148
- Fig. 4-27 The post-annealing absorbance spectra referenced to as-deposited 20-cycle 100°C TEMAH/D<sub>2</sub>O grown ALD hafnium oxide on ammonia treated 600°C H/Si(100); the spectrum (bottom in left panel) denoted “600c NSi” in black is the ammonia treated 600°C H/Si(100) referenced to H/Si(100)..... 150
- Fig. 4-28 Transmission IR spectra of 300oC-700oC post-deposition annealing of 20-cycle 100oC TEMAH/D<sub>2</sub>O grown ALD Hf oxide on ammonia treated 600oC H/Si(100) referenced to the ammonia treated H/Si(100) surface ..... 150

- Fig. 4-29 Step difference IR spectra of 300°C-700°C post-deposition annealing of 20-cycle 100°C TEMAH/D<sub>2</sub>O grown ALD hafnium oxide on ammonia treated 600°C H/Si(100); the spectrum (bottom in left panel) denoted “600c NSi” in black is the ammonia treated 600°C H/Si(100) referenced to H/Si(100) referenced to the ammonia treated H/Si(100) surface. .... 151
- Fig. 4-30 Transmission IR spectrum sectors for 700°C annealed 20-cycle TEMAH/D<sub>2</sub>O ALD hafnium oxide grown at 100°C on H/Si(111), SC2 oxidized silicon surface and ammonia treated 600°C H/Si(100). All spectra are referenced to as-deposited 20-cycle ALD hafnium oxide surface. .... 152
- Fig. 4-31 70° incident angle transmission spectra referenced to starting H/Si surfaces of 10s TEMAH pulse exposure on 100°C H/Si(100) (the 1<sup>st</sup> from top) and H/Si(111) (the 3<sup>rd</sup> from top), and 30s TMA pulse exposure on 70°C H/Si(100) (the 2<sup>nd</sup> from top). The spectrum segment of SC2 wet chemistry silicon oxide TO/LO modes in different scale at bottom. .... 153
- Fig. 4-32 Transmission IR spectra referenced to the starting surface of the 1<sup>st</sup> TEMAH in SC2 wet chemistry pre-treated H/Si(100), H/Si(100), H/Si(111) and ammonia treated 600°C H/Si(100). .... 154
- Fig. 4-33 70° incident angle transmission spectra of 30s TMA pulse exposure on 2-minute ammonia pretreated 610°C H/Si(100) at 60°C referenced to nitridized surface (the first from top), 2-minute ammonia pretreated 610°C H/Si(100) referenced to starting H/Si surfaces (the third from top), 10s TEMAH pulse exposure on 30s ammonia pretreated 600°C H/Si(100) at 100°C referenced to nitridized surface (the second from top), and 30s ammonia pretreated 600°C H/Si(100) referenced to starting H/Si(100)(the bottom). .... 156
- Fig. 4-34 Transmission spectra referenced to starting H/Si surfaces of (top two) 30s TMA pulse exposure on 60°C SC2 oxidized silicon surface at 20° and 70° incident angles, (the 3<sup>rd</sup> from top) 10s TEMAH pulse exposure on 100°C SC2 oxidized

|  |     |
|--|-----|
| silicon surface at 70° incident angle, and SC2 wet chemistry silicon oxide TO/LO modes in different scale at bottom. ....                            | 157 |
| Fig. 4-35 Schematic local bonding models for TEMAH and TMA exposure on silicon surfaces and the associated major observed peak frequencies. ....     | 159 |
| Fig. 4-36 Areal hafnium atom counts converted into bulk hafnium oxide thickness on different silicon surfaces as functions of ALD cycle numbers..... | 160 |



## CHAPTER 0

# INTRODUCTION

Since the invention of the transistor and the following successful development of silicon based semiconductor applications, we have been greatly influenced by this technology and directed into an information oriented trend. As a result, there is an increasing requirement for even more compact and powerful devices to help manage the growing information flow.

Present silicon-based semiconductor integrated devices consist of many metal oxide semiconductor field effect transistors (MOSFET). Each MOSFET contains a drain electrode, a source electrode and a gate stack with a thin silicon oxide electrical insulation layer. By applying voltage to the gate electrode, a conduction channel can be induced under the gate stack to let charge carriers pass between source and drain electrodes. The thin silicon oxide electrical insulation layer exists to eliminate the leakage current from gate electrode to the induced conduction channel. In order to increase silicon-based semiconductor device performance, there is a trend to increase the number transistors per unit area in chips and reduce the transistor physical size. This trend was predicted first by Gordon E. Moore in 1965. He said, "...the number of [transistors](#) that can be inexpensively placed on an [integrated circuit](#) is increasing exponentially, doubling approximately every two years..." (Moore's law).

With further reduction in scale, however, the gate silicon oxide layer becomes too thin to sustain good electrical insulation property, and the tunneling current through thin silicon oxide insulation layer becomes too high for the proper transistor function. Based on the present technology and scaling trend, the projected characteristic length scales of

equivalent silicon oxide layer thickness and gate length will come down to sub-nanometer and 22nm by the end of year 2008.[Process Integration, Devices, and Structures of 2005 ITRS roadmap and 2006 update <http://www.itrs.net/>]

Under the constraints of compatibility to the existent silicon based complementary metal oxide semiconductor (CMOS) process and higher demand for performances including higher transistor switching speed and higher area density of transistor unit, the replacement of silicon oxide by new high dielectric constant (high- $\kappa$ ) material is a potential solution for the silicon based semiconductor industry to keep up the pace. A high- $\kappa$  insulation layer not only increases the effective capacitance in gate stack and thus the maximum saturation current through the induced conducting channel, but also shortens the switch time and potentially reduces the switch transient power dissipation for logic transistor applications. With the same equivalent effective gate capacitance, it can have a thicker gate insulation layer, thus reducing gate leakage current tunneling.

There have been a great number of searches for appropriate high- $\kappa$  materials and the related growth and process methods compatible to the existent industry production process. Large category of binary high- $\kappa$  compounds such as metal oxides and nitrides was preliminarily sorted out according to their thermodynamic properties. Thermodynamically unstable high- $\kappa$  oxides in contact with silicon have been excluded because they form low- $\kappa$  silicide, silicon oxide ( $\kappa \sim 4$ ) or silicate interlayer, thus reducing gate capacitance. On the other hand, promising high- $\kappa$  materials are subject to the interlayer formation, mostly in the form of silicon oxide during film growth and post-deposition annealing which is carried out for conducting channel activation. The search for the appropriate thin film growth method to avoid undesired interlayer reaction and

give reliable and controllable growth yield is one of the most important concerns toward the successful high- $\kappa$  substitute.[1-8]

The process of silicon oxidation for the gate stack which produces almost perfect interfaces with a very low defect density gives a solid ground for successful engineering control of the interface and thus of the electricity properties of silicon based devices. With further scaling, device performance becomes even more dependent on interfaces than ever. By controlling temperature and exposure, conventional chemical vapor deposition (CVD) can easily grow films more than thousands of atomic layers per second in one exposure, but it has no good control over the conformity of subnanometer-thick film deposition. Meanwhile, physical vapor deposition (PVD) usually produces more roughness and defects at interfaces due to the high kinetic momentum of the chemical compound for deposition (precursor) and is limited to low product throughput and high vacuum requirement.

Atomic layer deposition (ALD) has been developed as a variation of the CVD method. Films are grown layer by layer using ALD through the surface reaction of alternating doses of precursors which contain elements of film composition. It has been used to deposit high- $\kappa$  and other materials for the surface/interface oriented technology.[9-15] In principle, it would give more uniformity and conformality, and better control over both atomic level thickness and the interface formation. The practical surface reactions, surface states after precursor exposures and the interface formation are subject to the chemical properties of precursors, kinetic conditions and reactivity/functionality of initial substrates. Therefore understanding the relevant interface formation and surface reaction mechanism is significant to establish the solid

ground for a successful engineering.

*In situ* transmission FTIR is a powerful non-destructive technique for characterizing the surface adsorbed species, growing films and interfaces. Rutherford Back Scattering (RBS) is used as the complementary surface analysis to quantify the areal density of heavy atoms such as aluminum (Al) and hafnium (Hf). Their relevant IR-active vibration modes for the relevant molecules fall in the mid-IR range.

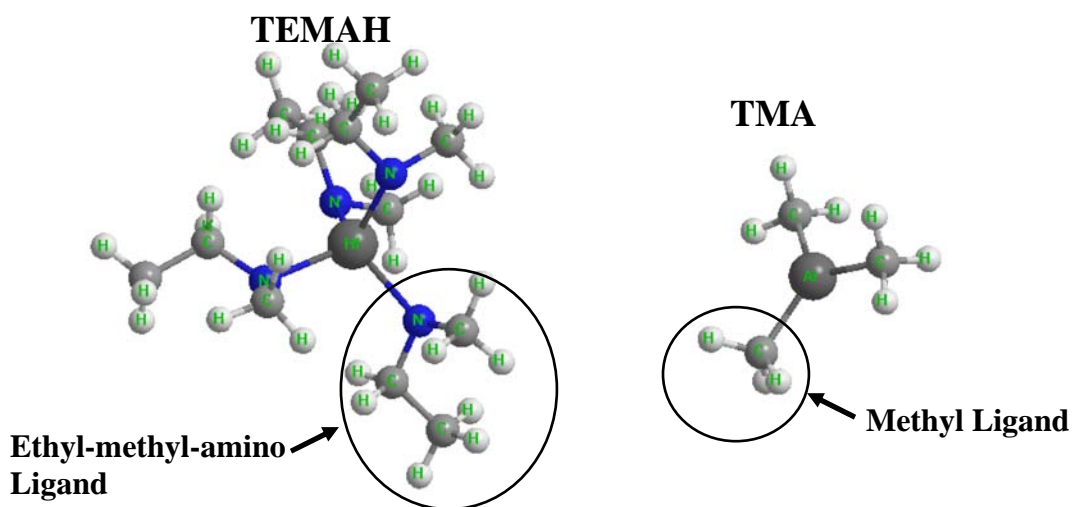


Fig. 0-1 Ball-and-stick models of TEMAH and TMA molecules

Tri-methyl-aluminum (TMA;  $\text{Al}(\text{CH}_3)_3$ ) and tetrakis-ethyl-methyl-amino-hafnium (TEMAH;  $\text{Hf}(\text{N}(\text{CH}_3)(\text{C}_2\text{H}_5))_4$ ) are used as the metallic organic precursors with deuterium-oxide ( $\text{D}_2\text{O}$ , isotopic molecule of  $\text{H}_2\text{O}$ ) to grow ALD Al oxide ( $\kappa \sim 12$ ) and Hf oxide ( $\kappa > 20$ ) on silicon surfaces. We demonstrate that ALD using TMA/ $\text{D}_2\text{O}$  or TEMAH/ $\text{D}_2\text{O}$ , though a few initial cycles do not fully cover the starting silicon surfaces, still produces a fractional mono-layer of amorphous Al oxide or Hf oxide on silicon surfaces after each full ALD cycle. The relevant surface reactions are not limited to the

ligand substitution reactions. The surface functional groups dramatically affect the nucleation condition in initial ALD stage. Also the IR absorption frequencies presented in this thesis provide much information to characterize the resultant surface state after ALD exposures. They help outline the practical ALD reaction mechanisms and relevant film/interface formation, though the relevant electrical characterization issues are out of their reach.

Chapter summary of this thesis is as follows:

Chapter 1 contains the experimental sections including the descriptions of the *in situ* transmission FTIR setups used for all the IR absorption spectra in this thesis, typical ALD growth conditions, sample preparation and some details of FTIR data processing and data analysis techniques.

Chapter 2 is focusing on the ALD Al oxide growth on silicon surfaces using TMA/D<sub>2</sub>O, especially on the ammonia pretreated silicon surface (NSi). Ultra-thin, non-uniform and atomically inhomogeneous silicon nitride (Si<sub>x</sub>N<sub>y</sub>,  $\kappa \sim 8$ ) grown on the heated hydrogen terminated silicon surface (H/Si) exposed to ammonia, was used as a buffer layer to minimize the interfacial silicon oxide formation during ALD. IR spectra of accumulative TMA exposure to the RCA-2 or standard clean-2 (RCA-2 or SC2) [16] oxidized silicon surface (also see the preparation details in Section 1.1) , (SC2-OSi) at different substrate temperatures indicate 400°C is the upper bound temperature for ALD processes. IR spectra and band assignments of TMA reacting with H/Si, SC2-OSi and thermal ammonia nitridized silicon surfaces are briefly discussed therein and will be reviewed at the end of Chapter 4.

ALD grown Al oxides on H/Si, SC2-OSi and NSi are compared, which shows the reactivity in the order of SC2-OSi>NSi>H/Si.

Chapter 3 shows the study of TEMAH molecular IR spectrum and its gas phase reaction products with oxidants such as D<sub>2</sub>O (H<sub>2</sub>O), O<sub>2</sub> and ozone (O<sub>3</sub>). Two sets of linear wavenumber scaled (LWS) normal mode profiles based on the *ab initio* density functional theory calculation of two different basis and functional choices are compared to the observed IR absorption spectrum of TEMAH. Calculated results and the observed spectrum are in very good agreement. The major discrepancy of frequency shift from the C-H stretching mode  $\sim 2799\text{ cm}^{-1}$  associated with methyl-amino segment is accounted through the C-H bending( $\sim 1420\text{ cm}^{-1}$ ) overtone coupling known as Fermi Resonance mechanism. Molecular O<sub>2</sub> is much less reactive to TEMAH than D<sub>2</sub>O (H<sub>2</sub>O) and O<sub>3</sub>. Transmission IR spectra show ether-like (-C-O-C-) and tertiary alkylamine-like (N(R<sub>1</sub>R<sub>2</sub>R<sub>3</sub>)) compounds are the major products of O<sub>2</sub>, D<sub>2</sub>O and H<sub>2</sub>O reacting with TEMAH. Gaseous CH<sub>2</sub>O, CH<sub>3</sub>NO<sub>2</sub>, CH<sub>3</sub>-N=C=O and other compounds containing -(C=O)- and -C-O-C- (or -O-C-) segments dominate the products of TEMAH/ O<sub>3</sub> gas phase reaction. A similar accumulative TEMAH exposure test on H/Si, SC2-OSi and NSi surfaces at different substrate temperature indicates 300°C upper limit for TEMAH ALD application is not sensitive to the functional group on silicon surfaces. During TEMAH exposure, substrate temperature higher than 300°C will result in CVD-like carbon-nitride alloy growth.

Chapter 4 covers the IR studies of TEMAH/D<sub>2</sub>O ALD on H/Si, SC2-OSi, NSi, and extensive discussion of a local chemical model of TEMAH and TMA adsorption. Transmission FTIR spectra manifest partial alkylamino and hydroxyl (OD) ligand substitution in half-cycle exposure. The vibrational modes around 1100-1800cm<sup>-1</sup> indicate the existence of surface organic groups such as Hf-N(-O)(-O-Hf), (Hf-O-)<sub>2</sub>NO and Hf-O-(CO<sub>2</sub>), possibly due to cross-reaction among adsorbed surface species or ligand decomposition. Significant portion of surface hydrogen survives up to 30 full ALD cycles. The growth of amorphous Hf oxide is evidenced by broad bands at ~ 690 cm<sup>-1</sup>(LO) and 510 cm<sup>-1</sup> (TO), and the interface mode associated with Hf-O-Si is also seen at ~ 1000cm<sup>-1</sup>. Silicon oxide interlayer formation is not observed during Hf oxide ALD on hydrogen terminated Si(111) surface (H/Si(111)) at 100°C. We can characterize the nucleation and film growth mechanisms by quantifying the H-Si stretching mode ( $\nu$ (H-Si)) and interfacial mode peak areas and combining *ex situ* RBS measurements, Surface hydride survives even up to 30 ALD cycles because the adsorption is not limited to defect sites. The growth is through island expansions susceptible to steric hindrance, which explains the observation of hydro-carbon and deuterium hydroxyl(OD) groups in films. Lower Hf atom areal density on H/Si(111) than on OSi and NSi in initial stages is due to the different reactivity of the starting surfaces. The possible mechanisms for the observed  $\nu$ (H-Si) red-shift during TEMAH exposure are discussed in length. In brief, it can be either interactions with nearby metal atom Si-H....Hf (Si-H....Al) or the dielectric screening effect by as-grown high- $\kappa$  moiety. Ligand substitutions and the

reactions of surface functional groups with TEMAH are qualitatively presented by relevant mode intensity losses in the IR spectra of Hf oxide ALD on SC2-OSi and NSi as well. The evolution of as-grown films and interfaces during post-deposition annealing, a necessary process for field effective transistor channel activation, is also investigated by IR spectra. Post-deposition annealing induces silicon oxide interlayer formation at 400°C and gives rise to monoclinic crystallization modes at  $\sim 787$ ,  $656\text{ cm}^{-1}$  (LO) and  $510\text{ cm}^{-1}$  (TO) at 500°C for H/Si and SC2-OSi and 600°C for NSi. The cross comparison of IR absorption modes associated with the interface of TEMAH or TMA exposed silicon surfaces is elaborated in length, and the detailed band assignment is summarized in **Fig. 4-39** of this chapter.

To sum up, the initial ALD growth nucleation process depends on both the reactivity of the precursors and the starting surface. The steric hindrance apparently affects the interface and film formation. (Metal-organic precursor TEMAH is more reactive than TMA, wet chemistry silicon oxide or ammonia pretreated silicon surface are more reactive than H/Si, and hydroxyl groups and organic groups can be found in as-deposited ALD oxide film.) Even though the surface functional group sites in starting surfaces are not fully consumed by precursor molecules, ALD grown oxide moiety can nonetheless spread over the substrate and make full surface coverage by sufficient numbers of ALD cycles. Thus the as-deposited oxide films are not in well-ordered and packed structures, and voids and impurities are expected in grown films. Interfacial silicon oxide formation during ALD can be avoided by reducing the deposition temperature or by introducing thermal nitride buffer layer, which also increases the crystallization temperature of Hf



oxide film. Low density amorphous ALD grown high- $\kappa$  oxides can be identified by broad LO/TO phonon modes in contrast to sharper modes of their crystalline phase in IR absorption spectra. In ALD of high- $\kappa$  oxide on H/Si, close local packing of the existent surface hydride and as-deposited high- $\kappa$  moiety intensifies their interaction, inducing dielectric screening effect which modulates the local field. It can effectively change the resonance frequency, thus causing the anomalous red-shift of the surface H-Si stretching mode in IR spectrum.

## Conclusion

ALD is a process that relies on the complete coverage of the surface by the precursor molecules and the complete removal of their ligands. Since the most interesting metal precursors involve relatively large molecules (i.e. with bulky ligands), a key issue during ALD is the accessibility of the precursor to the surface. If a portion of the existing surface reactive sites remains unreacted, there is the potential for the surface to exhibit a fractional mono-layer coverage (imperfect coverage) on starting surfaces and for residual impurities to be trapped in the films. If the amorphous films grown during ALD (i.e. prior post-deposition annealing) contain residual impurities, they may not be suitable for integrated device engineering. Post deposition annealing may improve the situation; however it may not eliminate all impurities that affect electrical properties of the films.

The growth characteristics are also important. The low nucleation seeding in initial growth stage, which implies a strong island growth pattern, will give a higher roughness of the thinnest film of full substrate coverage. Equivalently, that increases the scaling reduction limit of high- $\kappa$  oxide thickness, and thus decreases the maximum effective gate

capacitance of the high- $\kappa$  oxide. Furthermore, for the industry, lower nucleation seeding coverage of ALD definitely implies higher cost in product.

In this thesis, we have shown how IR absorption spectroscopy is critical to provide the necessary interfacial information during the ALD process to determine what the issues are. We have shown that the level of residual impurities can be reduced by post deposition annealing or even by raising growth temperature to kinetically increase the reactivity of surface groups. However, at the same time the interfacial barriers against substrate oxidation, such as the thermal ammonia nitridized layer, thin wet chemistry silicon oxide or the residual silicon hydrides in interface, will break down, and that results in the silicon oxide interlayer formation. We have investigated various surface pretreatments that can both maximize the initial nucleation seeding coverage and stabilize the newly formed interface of high- $\kappa$  material and silicon substrate up to post deposition annealing temperature. Our findings show that the chance for that to have the clear-cut interface of silicon and working ALD high- $\kappa$  oxides is very slim under the existing semiconductor production process.

Our work suggests that, because of the inevitable silicon oxide interlayer formation, electrical characterization of the post deposition annealed ALD high- $\kappa$  oxides should be done to get the idea of the trace interfacial silicon oxide tolerance as a compromise for short term goal. It also suggests that thin layers of hafnium silicide ( $\text{HfSi}_x$ ) or hafnium nitride ( $\text{HfN}_x$ ) may be good candidates to suppress interfacial  $\text{SiO}_2$  formation by reducing the diffusion of oxygen to the interface during post deposition annealing and eventually form a final hafnium silicate ( $\text{HfSi}_x\text{O}_y$ ) or hafnium silicate nitride ( $\text{HfSi}_x\text{O}_y\text{N}_z$ ) gate stack.

## References

1. Wilk, G.D., R.M. Wallace, and J.M. Anthony, *High-kappa gate dielectrics: Current status and materials properties considerations*. Journal of Applied Physics, 2001. **89**(10): p. 5243-5275.
2. Hubbard, K.J. and D.G. Schlom, *Thermodynamic stability of binary oxides in contact with silicon*. Journal of Materials Research, 1996. **11**(11): p. 2757-2776.
3. Wallace, R.M. and G. Wilk, *High-kappa gate dielectric materials*. Mrs Bulletin, 2002. **27**(3): p. 192-197..
4. Schlom, D.G. and J.H. Haeni, *A thermodynamic approach to selecting alternative gate dielectrics*. Mrs Bulletin, 2002. **27**(3): p. 198-204.
5. Wallace, R.M. and G. Wilk, *High-kappa gate dielectric materials*. Mrs Bulletin, 2002. **27**(3): p. 192-197.
6. Wallace, R.M. and G.D. Wilk, *High-kappa dielectric materials for microelectronics*. Critical Reviews in Solid State and Materials Sciences, 2003. **28**(4): p. 231-285.
7. Wilk, G.D., R.M. Wallace, and J.M. Anthony, *Hafnium and zirconium silicates for advanced gate dielectrics*. Journal of Applied Physics, 2000. **87**(1): p. 484-492.
8. Wilk, G.D., R.M. Wallace, and J.M. Anthony, *High-kappa gate dielectrics: Current status and materials properties considerations*. Journal of Applied Physics, 2001. **89**(10): p. 5243-5275.
9. Hausmann, D.M. and R.G. Gordon, *Surface morphology and crystallinity control in the atomic layer deposition (ALD) of hafnium and zirconium oxide thin films*. Journal of Crystal Growth, 2003. **249**(1-2): p. 251-261.
10. Jones, A. C., H. C. Aspinall, P. R. Chalker, R. J. Potter, K. Kukli, A. Rahtu, M. Ritala, and M. Leskela, *Some recent developments in the MOCVD and ALD of high-kappa dielectric oxides*. Journal of Materials Chemistry, 2004. **14**(21): p. 3101-3112.
11. Kukli, K., M. Ritala, J. Lu, A. Harsta, and M. Leskela, *Properties of HfO<sub>2</sub> thin films grown by ALD from hafnium tetrakis(ethylmethanamide) and water*. Journal of the Electrochemical Society, 2004. **151**(8): p. F189-F193.
12. Kukli, K., M. Ritala, T. Sajavaara, J. Keinonen, and M. Leskela, *Atomic layer deposition of hafnium dioxide films from hafnium tetrakis(ethylmethanamide) and water*. Advanced Materials, 2002. **14**(17): p. A199-+.
13. Kukli, K., M. Ritala, T. Sajavaara, J. Keinonen, and M. Leskela, *Atomic layer deposition of hafnium dioxide films from hafnium tetrakis(ethylmethanamide) and water*. Chemical Vapor Deposition, 2002. **8**(5): p. 199-204.
14. Leskela, M. and M. Ritala, *Atomic layer deposition (ALD): from precursors to thin film structures*. Thin Solid Films, 2002. **409**(1): p. 138-146.
15. Leskela, M. and M. Ritala, *Atomic layer deposition chemistry: Recent developments and future challenges*. Angewandte Chemie-International Edition, 2003. **42**(45): p. 5548-5554.
16. Kern, W., *Handbook of semiconductor wafer cleaning technology science, technology, and applications*. Materials science and process technology series.

Electronic materials and process technology. 1993, Park Ridge, N.J., U.S.A.:  
Noyes Publications.

# CHAPTER 1

## EXPERIMENT SETUPS, SUBSTRATE PREPARATION AND IR ABSORPTION DATA ANALYSIS

All the IR absorption spectra shown in this thesis are taken with two *in situ* transmission IR absorption setups. One has an atmospheric pressure purge style reactor sitting in the spectrometer compartment of existing commercial IR spectrometers. The other has a vacuum chamber outside the spectrometer compartment and uses external mirrors to direct the beam from the spectrometer, through the chamber and to an external IR detector.

### 1.1 *In Situ* Transmission IR Setups and Silicon Surface Preparation

Both setups have similar home-made sample holder rotor containing tantalum clamps for sample heating and a small tantalum clip spot-welded with K-type thermocouple to monitor the sample temperature. The atmospheric-pressure reactor has a pair of shutters and uses nitrogen purge flow to pressurize the space in-between the shutter and the KBr window to protect each KBr window from contamination during precursor dosing. The other vacuum reaction chamber uses air-tight viton-sealed gate valves and nitrogen purge flow to protect the KBr windows. Aluminum (Al) oxide ALD using trimethylaluminum (TMA) and deuterium oxide ( $D_2O$ ) precursors is mainly carried out in the purged reactor, while hafnium (Hf) oxide ALD using tetrakis-ethyl-methyl-amino hafnium (TEMAH) and  $D_2O$  and TEMAH gas phase reaction experiments is carried out in the vacuum reaction chamber. (See **Fig. 1-1**)

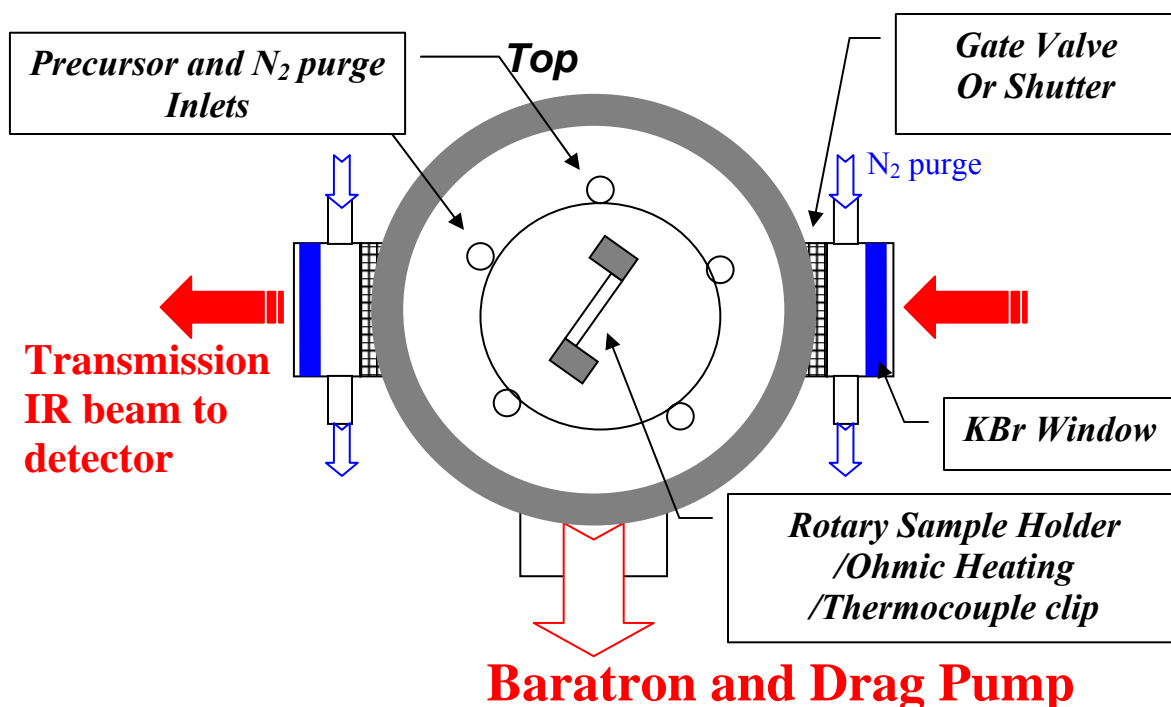


Fig. 1-1 Schematic drawing of *in situ* transmission IR ALD reactor

For Al oxide ALD, both TMA and D<sub>2</sub>O vapors are produced by letting carrier nitrogen gas flow through bubblers. Each bubbler has a bypass valve connection loaded with condensed phase TMA or D<sub>2</sub>O at room temperature and is connected by 1/4" stainless steel tubing lines to the reaction cell. The typical delivery or purge nitrogen flow is 100 standard cubic centimeters per minutes (s.c.c.m.) monitored and controlled manually by a flow meter. To avoid the possible reaction of the oxygen-sensitive precursor taking place during delivery, ultra-low oxygen concentration nitrogen gas (U-lo-Oxy N<sub>2</sub>) is used for both the delivery and purge flow. The U-lo-Oxy N<sub>2</sub> in use is produced by a commercial CenTorr N<sub>2</sub> purifier with a home-made heating copper wool oxygen prefilter (~250°C) connected to a liquid nitrogen supply tank for evaporating nitrogen gas. The typical oxygen element concentration in U-lo-Oxy N<sub>2</sub> is less than 10<sup>-5</sup>

parts per million and monitored by a flow-type oxygen sensor installed in the Centorr purifier. By opening the bubbler inlet and outlet valves and closing bypass valve, U-lo-Oxy N<sub>2</sub> is directed into the condensed phase precursor to produce gaseous bubbles containing precursor vapors, and thus the precursor vapor can be delivered to the reaction cell for practical ALD film growth. Before the substrate is heated up to the growth temperature for subsequent precursor exposure, the KBr window shutters are closed and the shutter-window space is purged with extra U-lo-Oxy N<sub>2</sub> to avoid KBr window contamination. After each exposure, the reaction cell is purged by 400 ml/min U-lo-Oxy N<sub>2</sub> flow for sufficient long time to evacuate the precursor residual and gaseous reaction products and the substrate temperature is lowered down to the spectrum taking temperature before the window shutters are opened for transmission IR acquisition. In this thesis, the typical transmission IR incident angle and substrate temperature for IR acquisition in the atmospheric-pressure purged reactor are 45° and 50°C, unless specified.

For Hf oxide ALD and gas phase reaction experiments, condensed TEMAH is loaded in a stainless steel bubbler heated to 80°C~83°C within a furnace under the main chamber to produce a high enough concentration of TEMAH vapor (TEMAH has less than 0.1 Torr. vapor pressure at room temperature.) The TEMAH and U-lo-Oxy N<sub>2</sub> mixture is delivered to the ALD reactor through 1/4" stainless steel/ VCR fitting connection tubing line heated in the furnace. The mixture dose is controlled both by time-programmed MKS mass flow controller and *Swagelok* pneumatic valves. Room temperature (~25°C) deuterium oxide (D<sub>2</sub>O) vapor is the oxygen source for Hf oxide growth, and is used without U-lo-Oxy N<sub>2</sub> flow. The ALD reactor is composed of a 6" flange chamber with two 2.75" flange KBr window view ports for transmission of the IR

beam. Each KBr window is protected from contamination during exposures by a U-lo-Oxy N<sub>2</sub>-purged viton O-ring gate valve. The ALD reactor is pumped by an Alcatel 1250c corrosive duty drag-diaphragm dry pump unit from a side 2.75" flange. The reactor pressure is monitored by a MKS baratron (range 10<sup>-3</sup>~10 Torr.), and the monitored vacuum base pressure is less than 10<sup>-3</sup> Torr. The TEMAH gas phase reaction experiments are carried out by mixing 50 s.c.c.m. U-lo-Oxy N<sub>2</sub> carried TEMAH flow with room temperature evaporated D<sub>2</sub>O(H<sub>2</sub>O), 50 s.c.c.m. O<sub>2</sub> or 50 s.c.c.m. ozone/O<sub>2</sub> flows in separate experiments. Contrary to Hf oxide ALD, KBr windows gate valves are opened though purged at total U-lo-Oxy N<sub>2</sub> flow of 400 s.c.c.m. to reduce contamination in KBr windows during exposure. Instead of 1000 scan/4 cm<sup>-1</sup> resolution for typical ALD experiments, 200 scan/4 cm<sup>-1</sup> resolution FTIR data acquisition parameter is used in TEMAH gas phase reaction experiments. Different from the atmospheric pressure purge style setup for Al oxide ALD, the vacuum style setup for Hf oxide ALD uses an external detector for IR data acquisition. The infrared beam extracted from a port of Nicolet Nexus 670 commercial FTIR spectrometer is first reflected and focused on the center of loaded substrate by an external parabola mirror, then the transmitting beam is reflected and focused again onto an external liquid nitrogen cooled MgCdTd-B detector by an external ellipsoidal mirror.

In all ALD experiments, silicon substrates (0.5"x 1.7") are cut from 4" double side polished and low-doped (~10 ohm-cm) silicon wafers. Hydrogen-terminated silicon (100) surfaces (H/Si(100)) are prepared by 15~20% hydrofluoric (HF) acid solution etching after a 10-minute SC1 clean (cooked in the chemical mixture of de-ionized (DI) water:H<sub>2</sub>O<sub>2</sub>:NH<sub>4</sub>OH=4:1:1 at 80°C) and a DI water rinse, followed by a 10-minute SC2



clean (cooked in the chemical mixture of DI water:H<sub>2</sub>O<sub>2</sub>:HCl=4:1:1 at 80°C) and a DI water rinse . Hydrogen terminated silicon (111) surfaces (H/Si(111)) are prepared by adding an additional etching step for 2.5~3 minutes in 49% ammonium fluoride. The hydrophilic SC2 oxidized silicon surface (SC2-OSi) is prepared by treating H/Si(100) with the SC2 procedure followed by a DI water rinse and normal nitrogen gas drying. The prepared wet chemistry silicon oxide of average 5Å thickness is not uniform and may contain various hydroxyl, hydrogenic, void and even dangling bond defects. [1-7] Silicon (oxy-)nitride surfaces are prepared by heating H/Si gradually up to temperature higher than 380°C in ammonia ambient, and the study of thermal ammonia nitridation will be detailed in Chapter 2.

Once prepared, the silicon sample is quickly loaded on a rotating sample holder of ALD reactor purged by U-lo-Oxy N<sub>2</sub>. After the ALD reactor is pumped down to its base pressure, the silicon substrate is resistively heated by passing current through it. During each precursor exposure, the substrate temperature for ALD is maintained by a Eurotherm PDI temperature controller. After each ALD exposure, the system is purged for 5 minutes by 300-100s.c.c.m. U-lo-Oxy N<sub>2</sub> gas interrupted by a couple evacuation cycles. During post-growth annealing, 100 s.c.c.m.. U-lo-Oxy N<sub>2</sub> flow is applied to the reactor. After each precursor exposure and purge/evacuation cycle, the KBr window gate valves are opened for transmission infrared absorption measurements. Usually the substrate temperature during measurements in the vacuum style reactor is maintained at 60°C.

The base pressures of both ALD reactors (vacuum and atmospheric-purge reactors) are higher than in typical ultra-high vacuum systems ( $\sim 10^{-10}$  Torr.). There is consequently

the possibility of substrate contamination from chamber-wall desorption or leakage. A simple analysis is presented below to estimate the inner wall desorption contamination based on the molecule mean free path lengths at different pressure levels. The mean free path length ( $\lambda$ ) for molecule is related to gas pressure ( $P$ ) by  $\lambda = \frac{1}{n\sigma} \sim \frac{kT}{\pi d^2 P}$ ; where  $n$  for molecular number density,  $\sigma$  for molecular cross section,  $T$  for gas temperature, Boltzmann constant  $k \sim 1.38 \times 10^{-23}$  joules/kelvin, and  $d$  for molecule diameter. In the atmospheric-pressure purged cell, the gas molecule mean free path length at 760 Torr. and 40~70°C is about  $5.7 \times 10^{-6}$  cm; while in the vacuum reactor at typical ambient pressures of  $10^{-3}$  Torr and temperatures of 40~70°C, the mean free path length of gas molecule is about 4.7 cm (by assuming molecule diameter  $\sim 5 \text{ \AA}$ ). That implies that inner wall contamination in the vacuum reactor may desorb and directly reach the silicon sample surface, while wall contamination in the purged cell mostly reaches the substrate by diffusion, limiting the surface contamination. As a result, wall contamination in the reactor purged at atmospheric pressure is less severe than in the vacuum reactor. This observation explains why a purer nitride film is formed when an atmospheric-pressure  $\text{NH}_3$  flow is used, than when nitridation is performed in the vacuum reactor. In the latter case, oxynitride is typically observed (with a phonon at  $\sim 960 \text{ cm}^{-1}$ ) due to the background levels of  $\text{H}_2\text{O}$  in the vacuum reactor. Similarly, hafnium silicate (with a mode at  $\sim 1000 \text{ cm}^{-1}$ ) is typically observed for  $\text{HfO}_2$  grown with TEMAH on H/Si in the vacuum reactor. However, the atmospheric purged system suffers from low evacuation efficiency, giving rise to other problems.

## 1.2 Transmission IR Data Analysis:

IR absorbance is used for IR absorption presentation in this thesis. Absorbance ( $A$ ) is defined by  $A = -\log\left(\frac{S(\nu)}{S_0(\nu)}\right)$ , where  $S(\nu)$  and  $S_0(\nu)$  are respectively the intensity of the IR beam recorded after transmission through the sample (substrate+surface) and the reference (usually substrate+clean surface). The frequency, shape and intensity of an absorbance band in the spectrum are related to the bonding structure and concentration of the IR active species on the sample surface (relative to the reference surface).

When analyzing the IR absorption spectra taken with our *in situ* setups, one has to pay cautions to some artifacts, which are not associated with the changes on the substrate surface. The typical absorbance peak height in one pass transmission IR absorption spectrum for sub-monolayer crystalline silicon surface adsorbed species is only  $10^{-3} \sim 10^{-5}$ . That is so weak as to be easily overlooked or concealed by artifacts. To avoid mistaking the artifacts as the real changes in substrate surface, one has to identify as many artifacts as possible for correct IR spectrum interpretation. These IR absorption spectrum artifacts with our setups can be produced by the systematic errors in IR optical bench or the general ambient variations, and they can be categorized as follows:

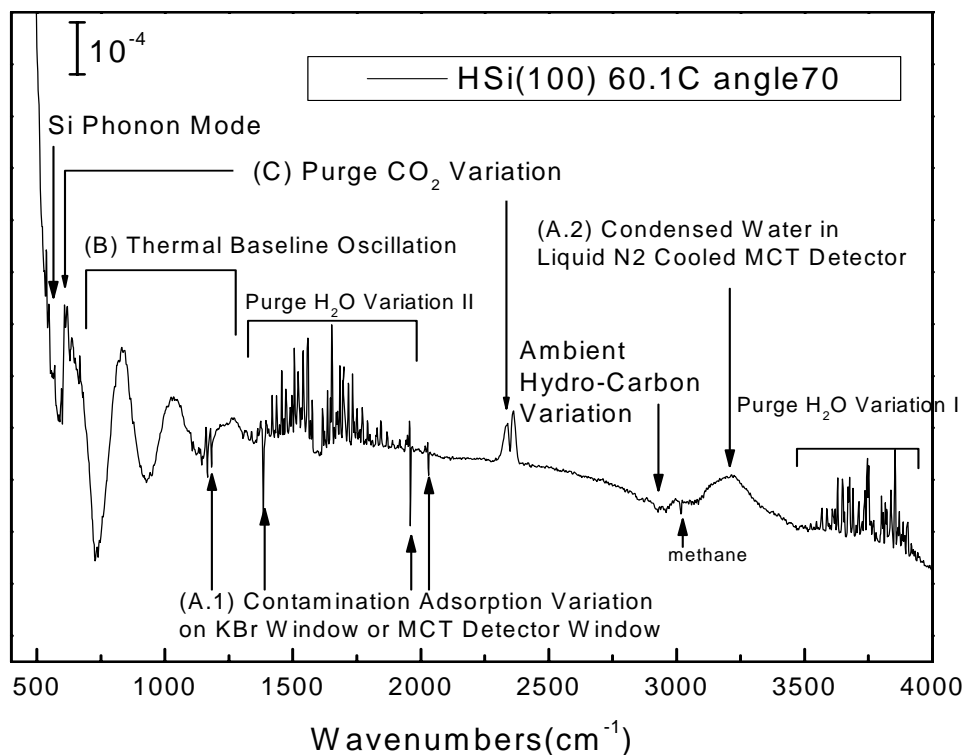


Fig. 1-2 Transmission IR absorbance spectrum at 70° incident angle of H/Si(100) at 60.1°C and reduced spectrometer purge referenced to the single beam spectrum (taken 1 hour ahead) of the same H/Si(100) at 60°C.

**A. Mercury Cadmium Telluride (MCT) detector and KBr window contamination artifacts:**

(i) Single beam spectra of the vacuum chamber system using the external MCTB detector show several unexpected extraordinarily narrow sharp dips (absorption) at 2029, 1960, 1385, 1258 and 1167 $\text{cm}^{-1}$ . The existence of these modes doesn't disappear with the removal of loaded substrate, and thus they are not related with any change on the substrate in the ALD reactor. Besides, they can not be found with the other internal built-in MCT detector inside the spectrometer, and that excludes the possibility of spectrometer KBr beam splitter degradation. The

MCTA detector used in atmospheric pressure purge style system has very weak artifacts  $\sim 2143$ ,  $2030$  and  $1960\text{cm}^{-1}$ .

(ii) MCT detector needs liquid nitrogen cooling to work properly. However the liquid nitrogen cooling often causes water vapor condensation in the detector window or on the semiconductor sensor, and gives rise to an obvious artifact broad peak of condensed water at  $\sim 3230\text{cm}^{-1}$  with  $\sim 3355\text{cm}^{-1}$  shoulder.

**B.** IR beam optical path variation due to temperature variation in substrate or KBr window. In **Fig. 1-2**, the strong oscillation in frequency range  $600\text{-}1500\text{cm}^{-1}$  peaked at  $837$ ,  $1037$ ,  $1265$ , and  $1470\text{ cm}^{-1}$  is mainly due to the  $0.1^\circ\text{C}$  increase in silicon substrate temperature. The higher substrate temperature difference between the subject and the reference is, the stronger the oscillation intensity is. The bigger the incident angle is, the higher the oscillation intensity is. (The oscillation intensity of  $70^\circ$  incident angle is almost the double of that of  $45^\circ$  incident angle.) However, the featured frequencies don't change very much with the substrate material, incident angles and substrate thickness. (For example, H/Si(111) has oscillation peaks at  $837$ ,  $1027$ ,  $1257$ ,  $1497\text{cm}^{-1}$  and native oxide passivated germanium substrate has oscillation peaks at  $838$ ,  $1036$ ,  $1256$ ,  $1473\text{cm}^{-1}$ .) Besides the temperature variation in KBr window caused by chamber baking or KBr window purge flow change also gives rise to the oscillation in absorbance spectrum, though the intensity is much lower than that caused by substrate temperature variation.

**C.** Water vapor, hydrocarbon species and  $\text{CO}_2$  features due to spectrometer and mirror box purge variation.

**D.** Silicon bulk multi-phonon modes at below listed frequencies ( $\text{cm}^{-1}$ ) will appear in absorbance spectrum, if there is substrate temperature increase in the referenced single beam spectrum.

|         |         |                 |         |     |              |      |
|---------|---------|-----------------|---------|-----|--------------|------|
| 602-609 | 732-708 | 829 (anti-peak) | 808~795 | 859 | 947 (weaker) | 1100 |
|---------|---------|-----------------|---------|-----|--------------|------|

**E.** Curved baseline over large frequency scale ( $4000\text{-}400\text{cm}^{-1}$ ) may occur in absorbance spectra. That is mainly attributed to the instability of IR optical bench, either the IR source (globar) temperature variation with time or MCTB detector cooling temperature variation with time.

### 1.3 Substrate Temperature in Atmospheric Pressure Purged Reactor

As described in **Section 1.1**, in both types of in situ setups substrate temperature is monitored by thermocouple with a tantalum clip on substrate. However in the atmospheric pressure purged reactor, due to the strong convection cooling effect by the purging flow, the thermocouple gives temperature readings that are significantly lower than the actual substrate temperatures. The comparison of the thermocouple temperature readings and corresponding pyrometer temperatures by an infrared optical pyrometer is tabled as following:

**Table 1-1 Purge type reactor thermocouple temperature readings and correspondent optical pyrometer temperature readings**

| Thermocouple Temperature(°C) | Optical Pyrometer(°C) | Thermocouple Temperature(°C) | Optical Pyrometer(°C) |
|------------------------------|-----------------------|------------------------------|-----------------------|
| 100                          | 123                   | 400                          | 496                   |
| 200                          | 255                   | 450                          | 551                   |
| 250                          | 319                   | 500                          | 605                   |
| 300                          | 380                   | 600                          | 715                   |
| 350                          | 439                   | 700                          | 826                   |

The substrate temperatures of atmospheric pressure reactor used in following chapters are the pyrometer calibrated temperatures, which are close to actual substrate temperatures. And those temperatures noted in parenthesis next to the substrate temperatures are thermo-couple reading temperatures.

## References

1. Aoyama, T., T. Yamazaki, and T. Ito, *Nonuniformities in Chemical Oxides on Silicon Surfaces Formed during Wet Chemical Cleaning*. Journal of The Electrochemical Society, 1996. **143**(7): p. 2280-2285.
2. Grundner, M., *High-resolution electron energy-loss spectroscopy measurements on hydrophilic silicon (100) wafers: Temperature and aging effects*. Journal of Vacuum Science & Technology A: Vacuum, Surfaces, and Films, 1987. **5**(4): p. 2011-2015.
3. Gurevich, A. B., M. K. Weldon, Y. J. Chabal, R. L. Opila, and J. Sapjeta, *Thermal evolution of impurities in wet chemical silicon oxides*. Applied Physics Letters, 1999. **74**(9): p. 1257-1259.
4. Ohwaki, T., M. Takeda, and Y. Takai, *Characterization of silicon native oxide formed in SC-1, H<sub>2</sub>O<sub>2</sub> and wet ozone processes*. Japanese Journal of Applied Physics Part 1-Regular Papers Short Notes & Review Papers, 1997. **36**(9A): p. 5507-5513.
5. Sugita, Y. and S. Watanabe, *In situ infrared spectroscopy on the wet chemical oxidation of hydrogen-terminated Si surfaces*. Japanese Journal of Applied

- Physics Part 1-Regular Papers Short Notes & Review Papers, 1998. **37**(6A): p. 3272-3277.
6. Sugita, Y., S. Watanabe, and N. Awaji, *X-ray reflectometry and infrared analysis of native oxides on Si (100) formed by chemical treatment*. Japanese Journal of Applied Physics Part 1-Regular Papers Short Notes & Review Papers, 1996. **35**(10): p. 5437-5443.
  7. Yamashita, Y., K. Namba, Y. Nakato, Y. Nishioka, and H. Kobayashi, *Spectroscopic observation of interface states of ultrathin silicon oxide*. Journal of Applied Physics, 1996. **79**(9): p. 7051-7057.



## CHAPTER 2

# TMA/D<sub>2</sub>O ALUMINUM OXIDE ALD ON THERMAL AMMONIA NITRIDIZED SILICON SURFACES

ALD of Al<sub>2</sub>O<sub>3</sub> using TMA/D<sub>2</sub>O directly on hydrogen terminated Si surfaces at 300°C forms interfacial silicon oxide [1], thus reducing the effective gate capacitance. This formation of interfacial silicon oxide on the oxygen free surface (H/Si) is due to the oxygen from D<sub>2</sub>O exposure thermodynamically combining with silicon. One of the attempts to minimize the interfacial layer formation is to grow Al oxide on H/Si at moderate temperature  $\sim 80^\circ\text{C}$  by physisorption followed by annealing at  $\sim 300^\circ\text{C}$ . [2] Another way is to grow a thin buffer layer to prevent oxygen from reacting with underlying silicon and forming interlayer silicon oxide. Thermally grown silicon nitride ( $\kappa \sim 6$ ) in ammonia is used as the ultra-thin buffer layer in this study.

In this chapter, thermal nitridation of Si in ammonia and ALD of Al oxide on this ultra thin ( $< 1\text{nm}$ ) silicon nitride surface studied by *in-situ* FTIR are presented.

## 2.1 Nitridized Silicon Surfaces Grown by Ammonia Exposure on H/Si

Many studies on silicon nitride films grown by various deposition techniques have been reported in the literatures [3, 4] [5] [6] [7-9]. Among them, the ultra-thin and asymptotically self-saturated grown thermal silicon nitride layers by ammonia have received great attention from the MOS semiconductor community for its oxidation barrier property in high-k dielectric applications [5]. Kinetic studies of thermal nitridation on clean silicon by ammonia have been performed using various analytical techniques [10-

12], but no IR absorption study on thermal nitridation on H/Si by ammonia has been done.

Nitridation of H/Si can be carried out either in the atmospheric pressure purged reactor or in a vacuum chamber. By annealing the substrate in ammonia ambient for 2 minutes (using ~ 40 ml/min ammonia flow diluted by extra 1 liter/min pure N<sub>2</sub> gas for the atmospheric pressure reactor or 100 s.c.c.m. ammonia flow with 7.1% partially opened throttle valve at calibrated 20~30 Torr pressure in the vacuum chamber), we have grown silicon nitride films and used transmission IR spectroscopy to characterize the changes in H/Si as a function of sample temperature.

#### **A. Nitridation of H/Si(111) by 4 % Ammonia/N<sub>2</sub> at Atmospheric Pressure**

After a H/Si(111) sample is loaded in the atmospheric pressure purged reactor, it is flashed up to 319°C (250°C TC) for 25 seconds in pure nitrogen ambient. The IR spectra show that H/Si(111) remains stable. There are no observed changes in the  $\nu(\text{H-Si}) \sim 2083 \text{ cm}^{-1}$  band up to 350°C. When H/Si(111) is heated up to a few different temperatures in temperature range 380-715°C in ammonia ambient, there are changes due to reaction with ammonia gas as detailed below.

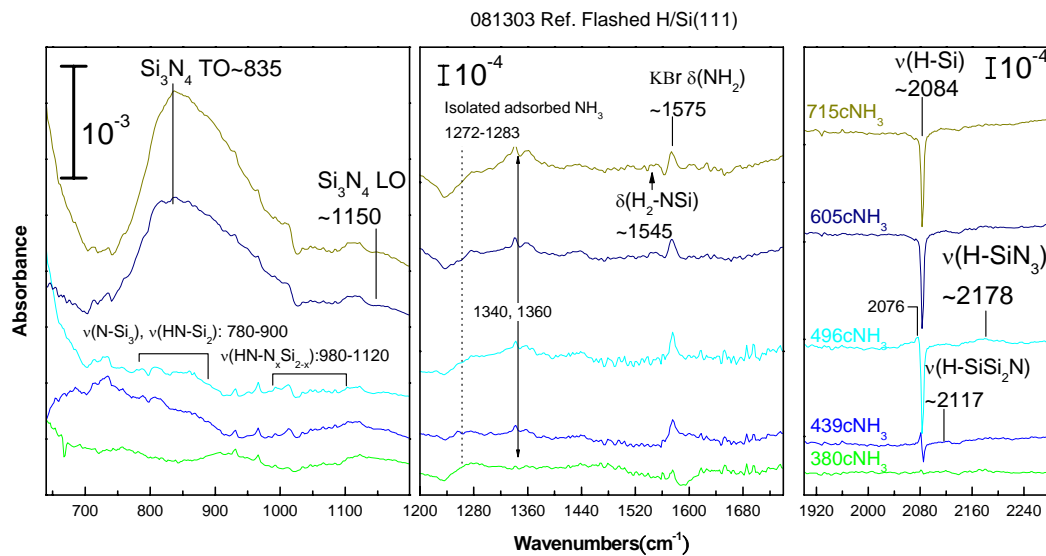


Fig. 2-1 Transmission IR absorption spectra of ammonia exposure (40 ml/min diluted by ~1000 ml/min  $N_2$  for 2 minutes) on H/Si(111) which is heated to calibrated 380 °C, 439 °C, 496 °C, 605 °C and 715°C temperatures.

The green 380 °C  $NH_3$  spectrum in the right panel of **Fig. 2-1** shows that H/Si(111) is stable up to 380 °C under  $NH_3$  exposure, which is consistent with the reported value of 370 °C [13]. The major loss of surface hydrogen silicon stretching mode ~ 2084  $cm^{-1}$  shown in the light blue 439 °C  $NH_3$  spectrum in the right panel of **Fig. 2-1** indicates that the primary surface hydride is removed. Significant growth of silicon nitride, indicated by the appearance of a band at 835  $cm^{-1}$  mode and the removal of most surface hydrogen, is not observed until 605 °C  $NH_3$  exposure (dark blue spectrum in the left panel of **Fig. 1**). The growth of red-shifted surface silicon hydride stretching mode  $\nu(H-Si) \sim 2076 \text{ cm}^{-1}$  peak of the light blue 496 °C  $NH_3$  spectrum in the right panel of **Fig. 2-1** is caused by the interaction of the left-over surface silicon mono-hydride with as-grown silicon nitride moiety, while the blue-shifted  $\nu(H-SiN_3) \sim 2178 \text{ cm}^{-1}$  is due to nitrogen insertion into surface Si-Si backbonds. The average thickness of as-grown silicon nitride can be assessed by calibrating the integrated silicon nitride IR absorption peak area to the

Medium Energy Ion Scattering (MEIS) measurement. It indicates that a nitride film with an average thickness of 7 Å is grown after the last NH<sub>3</sub> exposure at 715°C.

Before the exposure temperature is raised to 605°C to give significant silicon nitride growth, the spectra of lower temperature exposure (<605°C) in the left panel of **Fig. 2-1** do not show reliable features to construct a model for the initial nitridation of the surface. Interferences in the low frequency region of the spectrum observed after lower temperature ammonia exposures (<605°C) in left panel are mainly due to KBr window and changes in silicon phonon absorption occurring during slight temperature variations between the reference spectrum and subsequent spectra, and ammonia adsorption on KBr window.

The 1575cm<sup>-1</sup> δ(NH<sub>2</sub>) mode noted in middle panel might be attributed to ammonia decomposition adsorption on the KBr windows, while a very weak mode~1545cm<sup>-1</sup> can be attributed to the surface δ(NH<sub>2</sub>) on the substrate. Reported studies [13] [14] [15] of ammonia nitridation on silicon surfaces indicate H<sub>2</sub>N-Si dominates in the initial adsorption stage at room temperature, while HN(-Si)<sub>2</sub> can only be produced at higher exposures or annealing temperatures. H-N(-Si)<sub>2</sub> groups have bending mode~1140-1180cm<sup>-1</sup> overlapping with the high frequency edge of the extended Si nitride and Si oxynitride phonon modes[16] and stretching modes~3330-3360cm<sup>-1</sup> [8] [9, 17] [18] overlapping with the water absorption band due to water condensed on the detector. Also our present transmission geometry of 45° (non-grazing) incident angle is not optimized for detecting surface species with modes perpendicular to the surface. All these make the identification of surface H-N(-Si)<sub>2</sub> groups, if any, very difficult with the present transmission geometry.

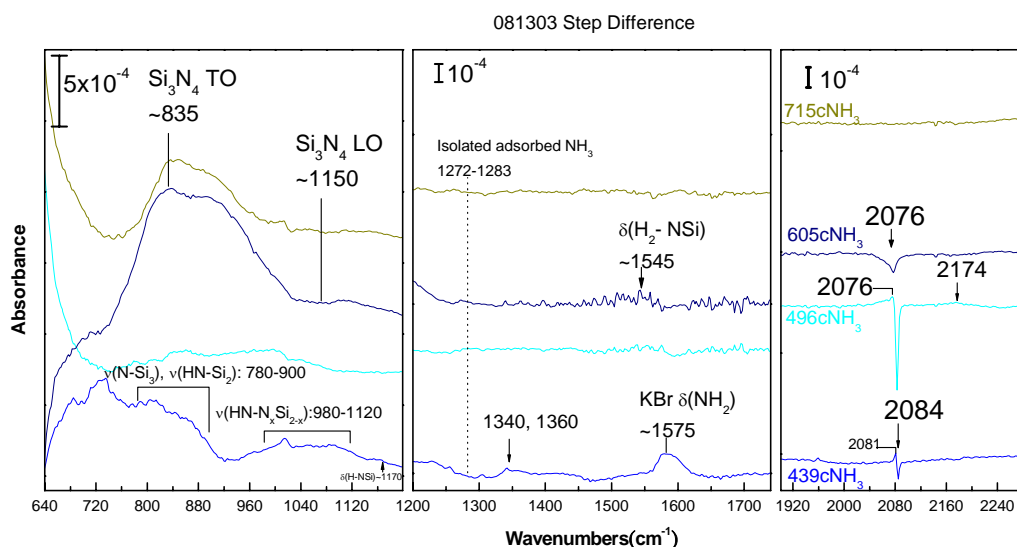


Fig. 2-2 Transmission step difference IR absorption spectra of ammonia exposure (40 ml/min diluted by ~1000 ml/min N<sub>2</sub> for 2 minutes in purged chamber) on H/Si(111) heated to calibrated 439 °C, 496 °C, 605 °C and 715 °C temperatures.

**Fig. 2-2** shows the transmission IR absorption spectra where each spectrum is referenced to the previous one. Surface hydrogen is completely removed with NH<sub>3</sub> exposure at 605 °C, and silicon nitride moiety growth is observed at 496 °C. Silicon nitride grows dramatically at 605 °C, and further but less growth is observed at higher temperature 715 °C. In a separate experiment it is found that the 1575 cm<sup>-1</sup> δ(NH<sub>2</sub>) mode at 439 °C does not change with ammonia or D<sub>2</sub>O exposure. Therefore it is attributed to the decomposed ammonia adsorption on the KBr window. In contrast to the reported high growth of silicon nitride on clean silicon surface through ammonia dissociation at temperature as low as 80 K, in case of the H/Si(111) surface, the IR absorption spectra unambiguously show that nitrogen insertion takes place at 439 °C (350 °C T/C) and silicon nitride grows after major removal of surface hydrogen.

## B. Nitridation of H/Si(100) by 4 % Ammonia/N<sub>2</sub> at Atmospheric Pressure

Microscopically rough H/Si(100) has more complicated H-Si bonding structure and more defect sites, and thus would be more reactive to adsorbents than H/Si(111). Similar experiments of H/Si(100) exposure to ammonia are carried out. **Fig. 2-3** and **Fig. 2-4** show the related IR absorption spectra.

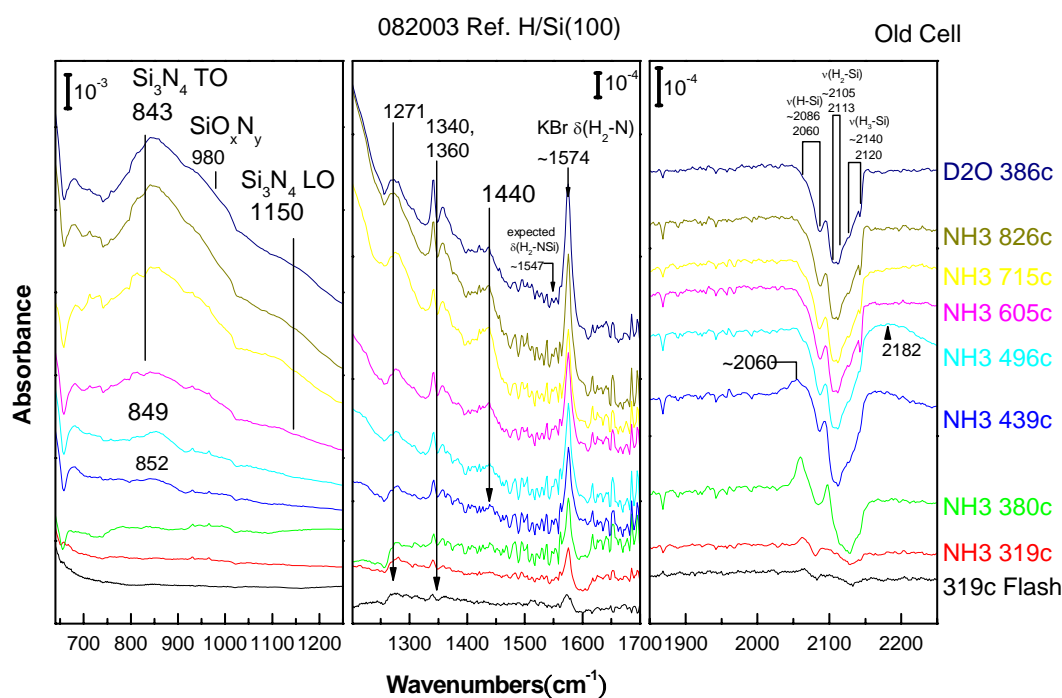


Fig. 2-3 Transmission IR absorption spectra referenced to starting H/Si(100) of 15-second 319 °C flash of starting surface, ammonia exposure (40 ml/min diluted by ~1000 ml/min N<sub>2</sub> for 2 minutes in purged chamber) on H/Si(100) heated to calibrated 319 °C, 380 °C, 439 °C, 496 °C, 605 °C and 715 °C temperatures, then followed by 2 minutes of 400ml/min N<sub>2</sub> carrying D<sub>2</sub>O vapor exposure (diluted by 400 ml/min N<sub>2</sub>) from a bubbler (~26 °C).

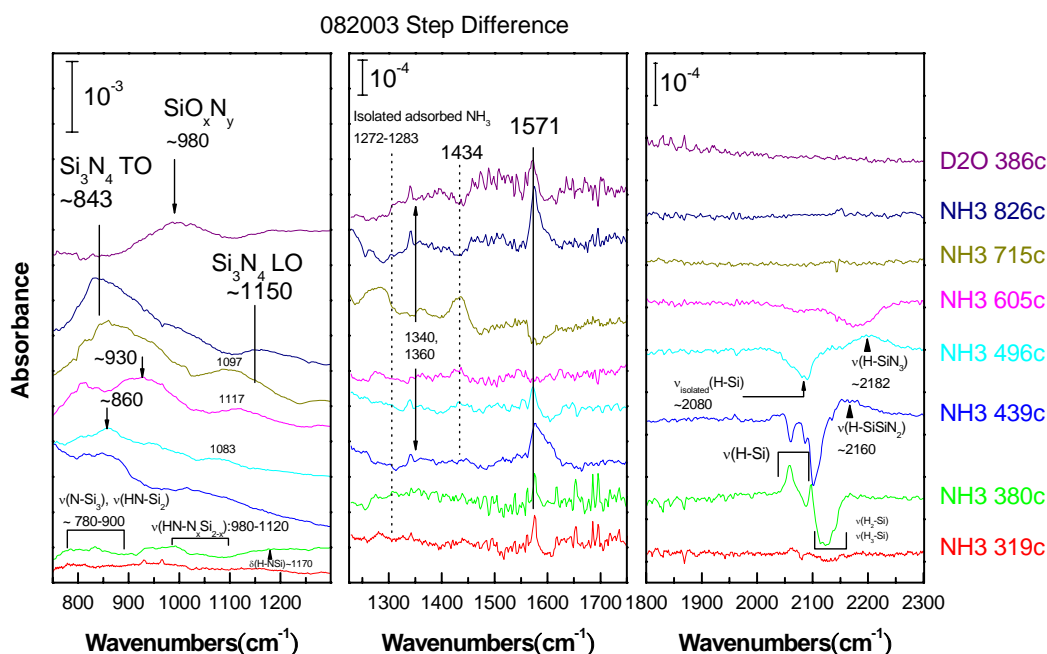


Fig. 2-4 Transmission step difference IR absorption spectra of 15-second 319 °C flash of starting surface, ammonia exposure (40 ml/min diluted by ~1000 ml/min N<sub>2</sub> for 2 minutes in purge style chamber) on H/Si(100) heated to calibrated 319 °C, 380 °C, 439 °C, 496 °C, 605 °C and 715°C temperatures, then followed by 2 minutes of 400ml/min N<sub>2</sub> carrying D<sub>2</sub>O vapor exposure (diluted by 400 ml/min N<sub>2</sub>) from a bubbler (~26°C).

According to the integrated area of  $\nu(\text{H-Si})$ , less than 5% of surface hydrogen are lost during 319°C annealing for 25 seconds. In the following annealing at 319~439°C in NH<sub>3</sub> ambient, Si-N moiety growth is observed at ~852 cm<sup>-1</sup> as well as loss of the most Si tri- and di- hydride ( $\nu(\text{H}_3\text{-Si})$ ~2120-2140cm<sup>-1</sup> and  $\nu(\text{H}_2\text{-Si})$  ~2105-2113cm<sup>-1</sup>). Mono-hydride stretching mode ( $\nu(\text{H-Si})$ ~ 2080cm<sup>-1</sup>) is partly shifted toward the lower frequency ~ 2060 cm<sup>-1</sup> at 319°C and then higher frequency ~ 2177 - 2182 cm<sup>-1</sup> at ~ 439°C due to more nitrogen insertion to the silicon backbonds. The  $\nu(\text{H-SiN}_x)$  modes at ~ 2177 - 2182 cm<sup>-1</sup> disappear at higher temperature (496~605°C) in NH<sub>3</sub> ambient and meantime a significant increase of silicon nitride modes is observed at this stage. The  $\delta(\text{NH}_2)$  at 1574 cm<sup>-1</sup>, as described at the previous section, is due to the KBr window contamination by

ammonia.

**Figure 2-4** shows transmission IR absorption spectra where each spectrum is referenced to the previous one. There is a significant loss of tri- and di- hydride ( $\text{H}_3\text{-Si}$  and  $\text{H}_2\text{-Si}$ ) and a red-shift of mono-hydride ( $\text{H-Si}$ ) mode toward  $\sim 2060\text{ cm}^{-1}$  caused by surface morphology change by the ammonia reaction at  $380^\circ\text{C}$ . More desorption of surface di- and mono-hydride is observed at  $439^\circ\text{C}$  accompanied by initial nitrogen insertion into substrate. The inhomogeneous non-stoichiometric nitrogen insertion into Si atoms is evidenced by a blue-shift of the  $\text{H-Si}$  stretch mode toward  $2160\text{ cm}^{-1}$  and  $\text{N-Si}$  band at  $\sim 860\text{ cm}^{-1}$ .

The  $\sim 2060\text{ cm}^{-1}$  red-shifted  $\text{H-Si}$  stretching mode at  $380^\circ\text{C}$  is also observed with a metallic organic precursor exposure on  $\text{H/Si}$  at  $60$  and  $100^\circ\text{C}$ . Theoretical calculations by Fattal et al. [19] and Widjaja et al. [20, 21] show ammonia favors the dissociative adsorption of  $\text{NH}_2 + \text{H}$  bonded to the silicon dimer of clean  $\text{Si}(100)(2\times 1)$ , where is unexpectedly red-shifted toward  $\sim 2078\text{-}2055\text{ cm}^{-1}$  according to Queeney et al. [22] The *ab initio* quantum mechanical density functional theory calculation therein indicates that the  $\text{NH}_2 + \text{H}$  bonding on surface silicon dimer and bonded pair interaction are responsible for the red-shift of  $\nu(\text{H-Si})$  mode. It also shows that the opposite orientated  $\text{NH}_2 + \text{H}$  bonded silicon dimer pair configuration gives the biggest frequency shift. This may imply ammonia exposures on  $\text{H/Si}(100)$  at  $380^\circ\text{C}$  and on  $\text{H/Si}(111)$  at higher temperature give rise to the similar  $\text{NH}_2 + \text{H}$  bonded silicon dimer pair configuration before the extensive nitrogen insertion takes place. All these reported studies suggest the  $\text{H-Si}$  stretching frequency red-shifts of ammonia exposure on  $\text{H/Si}$  ( $\text{H/Si}(100)$  at  $380^\circ\text{C}$  and  $\text{H/Si}(111)$  at  $496^\circ\text{C}$ ) can be caused by the similar interaction of  $(\text{NH}_x)\text{-Si}$  and  $\text{H-Si}$  on the substrate.



The other reported H-Si stretching frequency red-shifts ( $\sim 2065\text{cm}^{-1}$ ) were ever observed in such systems as H/Si(111)-(1x1) silicon wafer bonding [23] [24], hydrogen implanted silicon [25] and hydrogen chemi-sorption on vicinal Si(100)(2x1) [26]. They are caused by the Si-H...H-Si interaction among the closely packed silicon hydride groups. However, this is unlikely one of the mechanisms to account the red-shifted H-Si stretching mode due to two reasons. First, the substrate temperatures of  $380^\circ\text{C}$  for H/Si(100) and  $496^\circ\text{C}$  for H/Si(111) are not high enough to mobilize silicon atoms and make a dramatic silicon surface topographical to form “surface recess” for closely packed hydride groups.; those temperatures are only high enough to change the hydride phase on crystalline silicon surface.[27] The second, as estimated by the integrated IR absorption peak area, the surface hydride coverages for the ammonia exposures on H/Si(100) at  $380^\circ\text{C}$  and on H/Si(111) at  $496^\circ\text{C}$  are respectively 65% and 50%, and the red-shifted hydrides are only less than 1/5 in number of those left-over surface hydrides. If the red-shift were caused by a thermodynamically induced extensive surface topographical change, the IR absorption intensity of the red-shifted H-Si stretching should be higher. Contrarily, the smaller number of the mono-hydrides on hydride domain boundary, where the  $(\text{Si-NH}_x)\dots(\text{H-Si})$  interaction takes place,, is consistent with the weak red-shifted stretching intensity. Therefore the adsorbed amine groups interacting with mono-hydrides is more likely the account for the mono-hydride stretching red-shift.

A similar red-shift of H-Si stretching mode is also observed in H/Si exposed to TMA (Section 2.3) or TMAH (Chaper 3 and 4). The significant difference in Pauling electronegativities of relevant atoms such as N(3.04), O(3.44), Al(1.3) and Hf(1.61) may imply a possible common account for the “coincidence”. The common account, if any,

needs to be insensitive to the individual chemistry of the involved precursors. Later in Chapter 4, another model based on a caved H-Si oscillator is proposed to account the red-shift.

At higher temperature extensive nitrogen insertion and surface hydrogen removal take place more actively. At 496°C the H-Si stretch mode shifts to a higher frequency  $\sim 2177\text{-}2182\text{ cm}^{-1}$  due to more nitrogen insertion to the silicon substrate. Si-N moiety growth is evidenced by the mode at  $\sim 860\text{ cm}^{-1}$ . At 605°C surface hydrogen is completely removed and the 930 and 1117  $\text{cm}^{-1}$  modes appear, implying a stoichiometric silicon nitride development.

The surface hydrogen stability in ammonia ambient at different temperatures and the shifts of the H-Si stretching mode reveal that the surface defect site and reactivity of di- and tri-hydride are crucial in amine group adsorption on H/Si(100) in the initial stage. It also shows that the nitrogen insertion into the silicon substrate won't take place without thermal activation at temperature higher than 380°C.

Several experimental factors makes it difficult to identify dominant surface species after hydrogen desorption in this experiment; high water variation during measurements, low sensitivity due to low object concentration, and non-grazing incident angle (45°). A separate experiments of ammonia nitridation with grazing incident angle (70°) shows  $\delta(\text{H}_2\text{-NSi})$  at 1545  $\text{cm}^{-1}$ .

In order to have a better understanding of the resultant surface state after ammonia nitridation, the comparison of transmission IR spectra of thermal ammonia nitridized silicon surfaces at different incident angles is conducted and shown in **Fig. 2-5**:

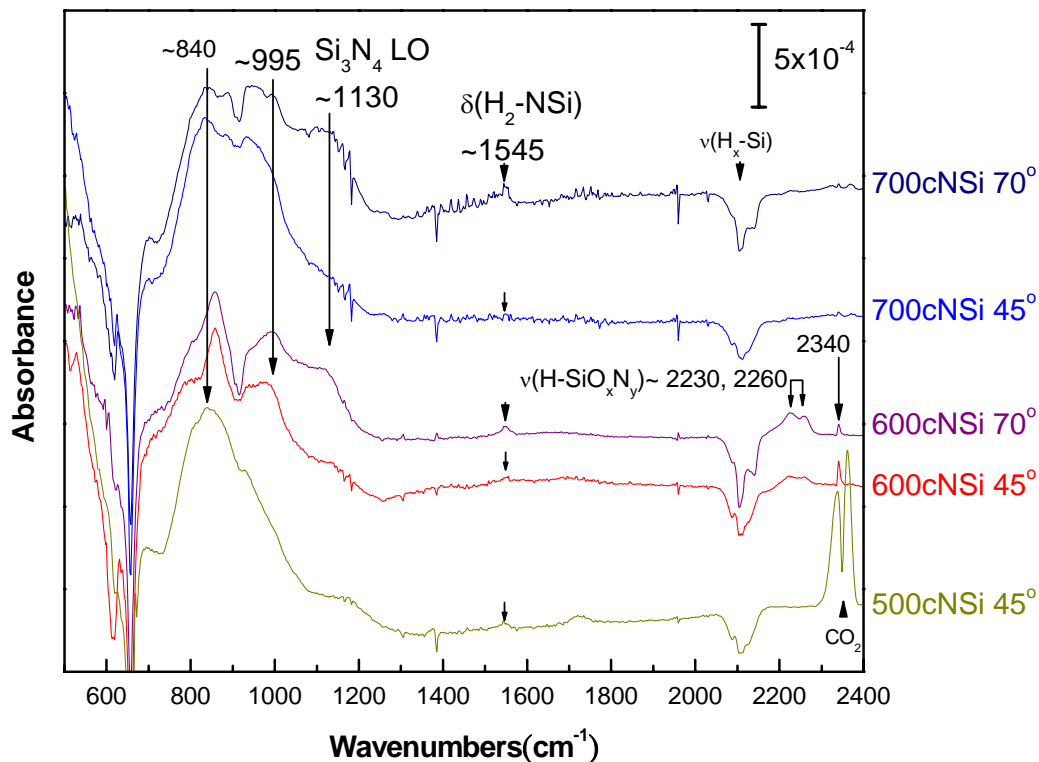


Fig. 2-5 Transmission IR spectra of different incident angles of  $\text{NH}_3$  exposure on  $\text{H}/\text{Si}(100)$ . The nitridation is carried out in vacuum chamber (different from those of Fig. 1-4). Before the three  $\text{H}/\text{Si}(100)$  samples are respectively raised to  $500^\circ\text{C}$  for 2 minutes,  $600^\circ\text{C}$  for 30 seconds and  $700^\circ\text{C}$  for 30 seconds, each is pre-heated to  $200^\circ\text{C}$ ,  $300^\circ\text{C}$  and  $400^\circ\text{C}$  (1 minute for each stage) in ammonia ambient (40 sccm  $\text{NH}_3$  diluted by 1000 sccm  $\text{N}_2$  with the partial closed throttle valve resulting in an extrapolated total pressure  $\sim 20\text{-}30$  Torr) to reduce oxygen incorporation.

Transmission IR spectra of  $\text{H}/\text{Si}(100)$  exposed to  $\text{NH}_3$  at  $500^\circ\text{C}$ ,  $600^\circ\text{C}$  and  $700^\circ\text{C}$  show the silicon nitride TO ( $840\text{ cm}^{-1}$ ), LO ( $1130\text{ cm}^{-1}$ ), silicon oxynitride ( $995\text{ cm}^{-1}$ ), N-H bending  $\delta(\text{H-N})$  ( $1177\text{ cm}^{-1}$ ), and  $\delta(\text{H}_2\text{-NSi})$  ( $1545\text{ cm}^{-1}$ ).  $2230$  and  $2260\text{ cm}^{-1}$  modes in  $600\text{cNSi}$  spectrum are different from  $\nu(\text{H-SiO}_x)$  of oxidized  $\text{H}/\text{Si}$  surfaces around  $2200$  and  $2270\text{ cm}^{-1}$  and are assigned as  $\nu(\text{H-SiO}_x\text{N}_y)$ . The intensity of the mode at  $2340\text{ cm}^{-1}$  ( $600^\circ\text{C}$ ) is stronger at  $45^\circ$  than at  $70^\circ$  and sometimes increases during IR measurements. But otherwise its intensity is invariant with annealing and water exposure. It might be attributed to either  $-\text{NH}_x^+$  ( $x=1,2$ ) or  $-\text{C}\equiv\text{N}$  [28] adsorbed on the window or substrate. If

so, it suggests that those surface species are produced and adsorbed on the KBr window or survive in the cell ambient at 600°C. Since the H/Si(100) surface is pre-heated and cooled down in ammonia ambient in order to reduce possible oxygen contamination, the exact formation temperature of surface amine species ( $H_xN-Si$ ) is not known. The 1-minute 500°C ammonia exposure spectrum at 45° incident angle has higher peak integrated area of silicon nitride mode than the 30-second 600°C ammonia exposure spectrum at 45° incident angle and doesn't have the residual  $H-SiO_xN_y$ . These suggest 30 seconds of ammonia exposure time is not long enough for the saturated silicon nitride growth on H/Si(100), and the oxygen incorporation still takes place under such a growth condition. The existence of NH species is not clear due to the overlapping with phonon modes. Other experiments carried out with a higher ammonia flow (~100sccm) or higher concentration during thermal nitridation show the suppression of oxynitride growth and NH group mode at  $1170\text{ cm}^{-1}$  which changes with temperature. This is consistent with the reported X-ray photo-electron emission study [15, 29] of clean silicon surface exposed to ammonia.

### C. Silicon Nitride Saturation Growth

H/Si(100) is heated to 700°C in ammonia ambient for different length of time, and the integrated area of corresponding silicon nitride phonon mode is used to investigate the nitridation saturation (see **Fig, 2-6**).

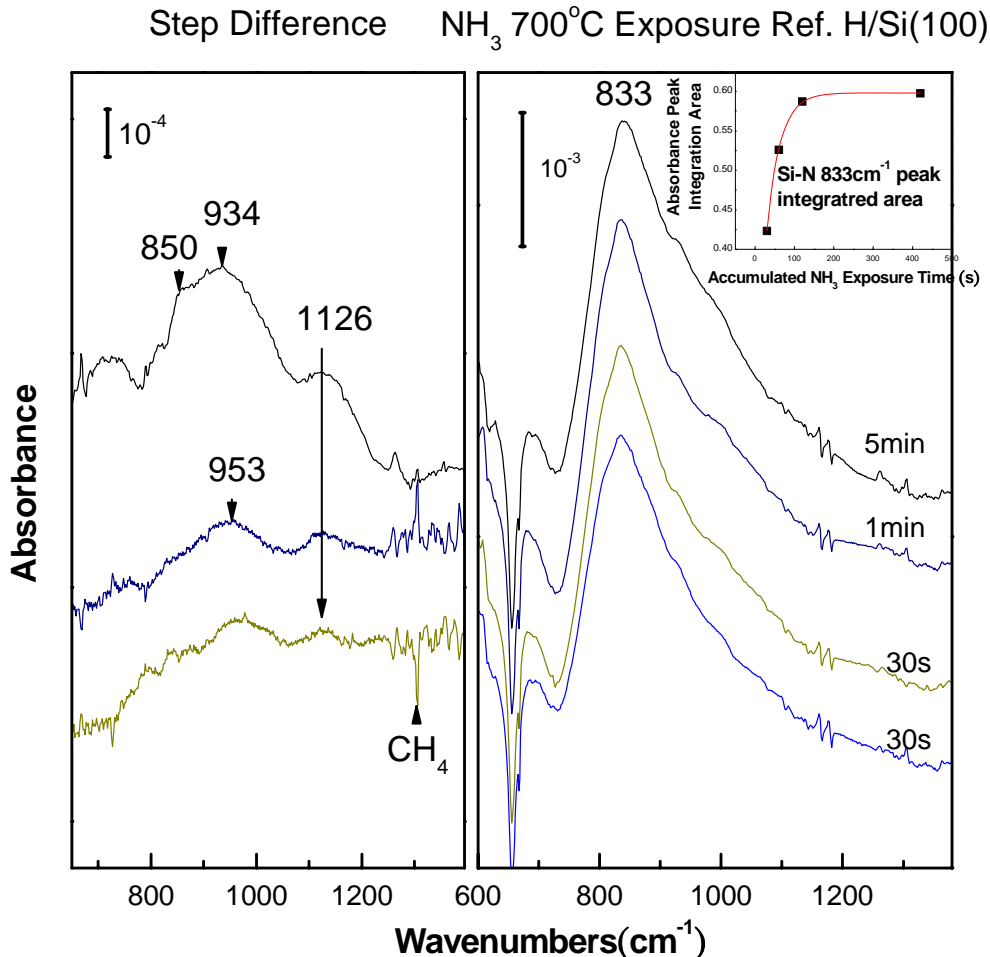


Fig. 2-6 Transmission step difference IR spectra (left panel) and spectra referenced to starting H/Si(100) (right panel) of the accumulated  $\text{NH}_3$  exposures (30 seconds, 30 seconds, 1minute and 5 minutes 40 s.c.c.m.  $\text{NH}_3$  diluted by 1000s.c.c.m.  $\text{N}_2$  with the partial closed throttle valve for an extrapolated total pressure~20-30 Torr. ) to H/Si(100) at 700°C. Before the very first 30 seconds ammonia exposure to 700°C H/Si(100), the H/Si(100) is pre-heated to 200°C, 300°C and 400°C (1minute for each stage) in ammonia ambient (40 s.c.c.m.  $\text{NH}_3$  diluted by 1000 s.c.c.m.  $\text{N}_2$  with the partial closed throttle valve for an extrapolated total pressure~20-30 Torr in vacuum chamber) to reduce oxygen incorporation. The inset in the right panel shows the plot of 833 $\text{cm}^{-1}$  peak area over ammonia exposure time in seconds.

The spectra and the inset plot of **Fig. 2-6** show that the growth rate of silicon nitride is much higher at the initial stage and asymptotically saturates around 200 seconds exposure time. This observation is also confirmed by other analysis techniques. According to the integrated area of silicon nitride phonon mode at 883  $\text{cm}^{-1}$  calibrated by medium-energy ion scattering (MEIS), the saturated silicon nitride film thickness grown

at 700°C is 7.8~10.6Å. Stoichiometric silicon nitride  $\text{Si}_3\text{N}_4$  forms a diffusion barrier against nitrous reactant reacting with underlying transitional substoichiometric silicon nitrides  $\text{Si}_x\text{N}_y$  and silicon. The modes at 850, 943 and  $1126\text{cm}^{-1}$  in “Step Difference” spectra are mainly related to the stoichiometric silicon nitride, though their broad feature may imply existence of silicon oxynitride produced by oxygen sources outgassed from the reactor wall. The saturation behavior suggests the reactant diffusion into the substrate as a dominant growth mechanism in contrast to the surface reactivity at the initial stage.

The difference in thermal nitridation of H/Si(111) and H/Si(100) can be explained in terms of their initial surface reactivity and diffusion barrier of the intermediate silicon nitride morphology during ammonia exposure which has more effect at higher temperature.

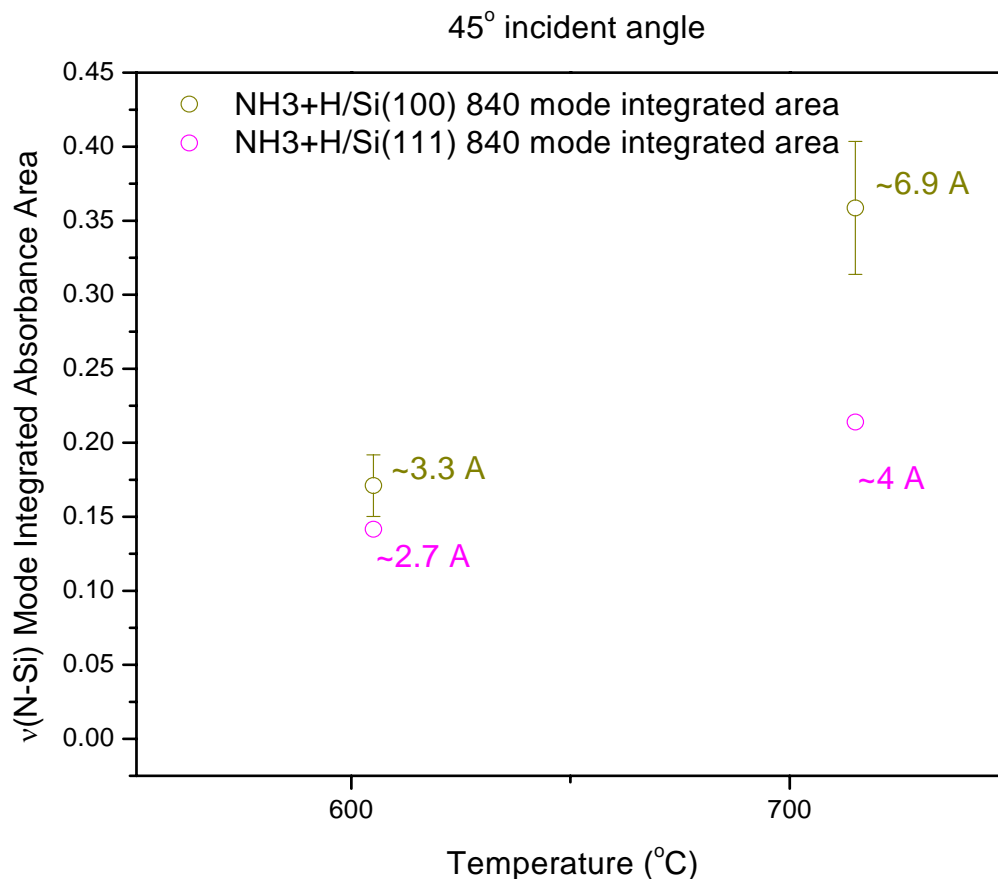
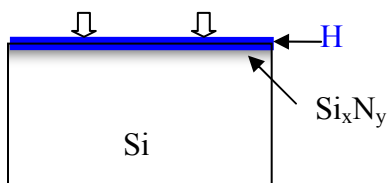


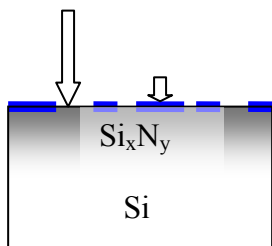
Fig. 2-7 Plot of the integrated 45° incident angle IR  $\nu(\text{Si-N})$  mode  $\sim 840\text{-}900\text{cm}^{-1}$  absorbance peak areas of the accumulated silicon nitride grown at increasing temperatures ammonia exposure on H/Si(100) (Fig. 2-1) and on H/Si(111) (Fig. 2-3) over the substrate temperatures. The MEIS calibrated average silicon nitride thicknesses are denoted in angstroms.

In **Fig. 2-7** the integrated area of  $\nu(\text{Si-N})$  mode at  $840\text{-}900\text{ cm}^{-1}$  shows more silicon nitride growth with higher growth rate on H/Si(100) than on H/Si(111). It agrees with the assumption that the morphology of growing silicon nitride would affect the diffusion of nitrogen reactants to the underlying transitional layer for further stoichiometric silicon nitride development. It also suggests that ultra-thin silicon nitride on H/Si(111) may give a thinner but higher diffusion barrier [30] [31, 32] against nitrogen agent reaching the underlay silicon than that on H/Si(100).

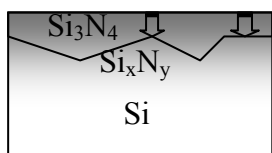
The silicon nitride film growth mechanism can be summarized by below view graphs:



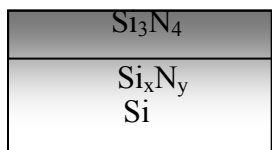
Before surface major hydrogen desorption very little nitrogen insertion takes place in substrate  $\sim 439^\circ\text{C}$



With major surface hydrogen removal more reactive surface site exposed to ammonia and more sub-stoichiometric silicon nitride formed in substrate  $\sim 496^\circ\text{C}$



Stoichiometric silicon nitride starts to form and reactant diffusion becomes the dominant mechanism for silicon nitride growth



Eventually the grown stoichiometric silicon nitride thickness gets close to the saturation thickness of the growth temperature and no significant amount of stoichiometric silicon nitride can be grown unless the growth temperature is raised higher.

## 2.2 D<sub>2</sub>O Exposure on Thermal Ammonia Nitridized Silicon Surface

In order to investigate how thermally grown silicon nitride in ammonia ambient can prevent the oxidation of underlying silicon, and how the silicon nitride film itself is



oxidized, we expose the films to D<sub>2</sub>O at different temperatures.

3-4 Å thick silicon nitride grown on H/Si(100) at 605°C would form a continuous coverage on silicon substrate with a typical Si-N bond length  $\sim 1.7\text{\AA}$ , assuming the grown film is homogeneous. Silicon nitride film grown at 496°C has too small projected average thickness of 1.2 Å for full coverage. [33] 3-4 Å thick silicon nitride film is used for the following experiments.

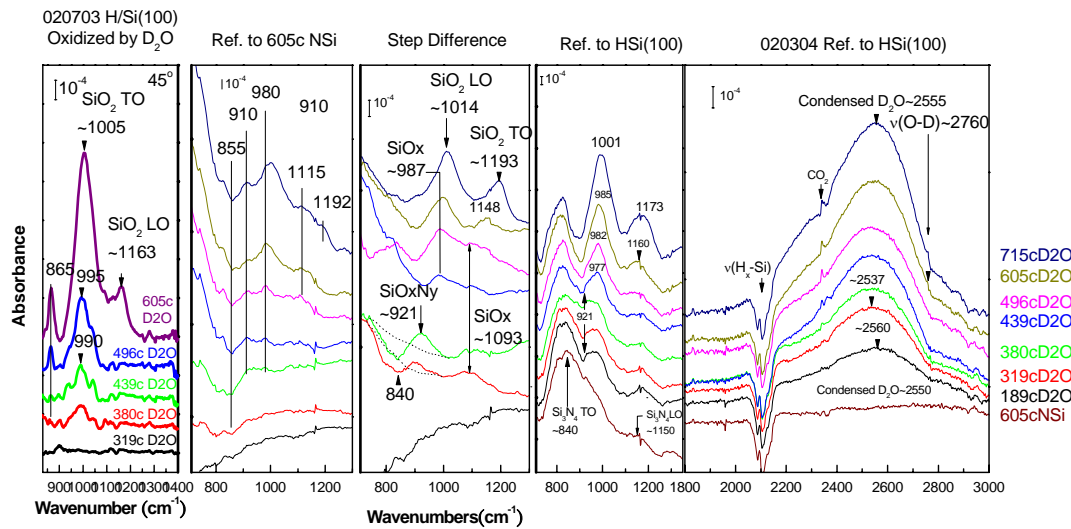


Fig. 2-8 The transmission IR spectra referenced to starting H/Si(100) surface (the first and second panel from right), step difference spectra (the third panel from right), spectra referenced to the as-grown nitride surface (the fourth panel from right) of 605°C grown (40 ml/min ammonia flow diluted by  $\sim 1000$  ml/min N<sub>2</sub> for 2 minutes) silicon nitride film (assessed 3-4 Å thick by IR integrated area) exposed to 1 minute 400ml/min N<sub>2</sub> carrying D<sub>2</sub>O vapor exposure diluted by 400 ml/min N<sub>2</sub> at 189, 319, 380, 439, 496, 605 and 715°C. The IR spectra of H/Si(100) exposed to the same D<sub>2</sub>O vapor exposure at 319, 380, 439, 496 and 605°C substrate temperatures in the most left panel for comparison.

**Fig. 2-8** shows that upon exposure to D<sub>2</sub>O at 319°C, 3-4 Å thick silicon nitride film starts to lose Si-N mode  $\sim 840\text{ cm}^{-1}$  and give rise to N-rich non-stoichiometric silicon oxynitride modes at 921 and  $1093\text{ cm}^{-1}$ . Further D<sub>2</sub>O exposure at higher temperature forms more oxygen-rich non-stoichiometric silicon oxynitride ( $\sim 987\text{ cm}^{-1}$ ) which evolves into stoichiometric silicon oxide clusters at 605°C similar to the thermal D<sub>2</sub>O

grown silicon oxide as shown in the left panel of **Fig. 2-8**. Since the homogeneity of silicon nitride film is unknown, we cannot tell whether the silicon oxide cluster is only formed on the top of silicon nitride. The broad and intense band at  $\sim 2550\text{ cm}^{-1}$  is from the condensed  $\text{D}_2\text{O}$  on KBr window or the sample. Chemically bonded OD group (stretching mode  $\sim 2760\text{ cm}^{-1}$ ) doesn't appear until  $496^\circ\text{C}$   $\text{D}_2\text{O}$  exposure.

The “step difference” spectra show no significant change in the silicon nitride film at temperature lower than  $150^\circ\text{C}$ . At  $250^\circ\text{C} \sim 300^\circ\text{C}$  interstitial Si-O bond in N-rich silicon oxynitride ( $901\text{ cm}^{-1}$  and  $1093\text{ cm}^{-1}$ ) starts to grow. At temperature higher than  $350^\circ\text{C}$  the Si-N mode  $\sim 840\text{ cm}^{-1}$  decreases significantly during  $\text{D}_2\text{O}$  exposure, and  $987\text{ cm}^{-1}$  mode appears and evolves into stoichiometric silicon oxide  $1014\text{ cm}^{-1}$  TO and  $1193\text{ cm}^{-1}$  LO modes (“Ref. to H/Si(100) spectra”). It implies that in  $\text{D}_2\text{O}$ -abundant ambient at higher temperature silicon oxide is thermodynamically favored over silicon nitride or silicon oxynitride which is composed of interstitial Si-O in silicon nitride.

More experiments are carried out with different thermal ammonia nitridized samples; silicon nitride grown at  $500, 600, 700^\circ\text{C}$  for 30 seconds and  $700^\circ\text{C}$  for 7 minutes on H/Si(100) after pre-heated to  $200^\circ\text{C}$ ,  $300^\circ\text{C}$  and  $400^\circ\text{C}$  (1minute for each stage) in ammonia ambient (40 sccm  $\text{NH}_3$  is diluted by 1000sccm  $\text{N}_2$  at pressure 20-30 Torr).  $\text{D}_2\text{O}$  is diluted by 400 ml/min  $\text{N}_2$  and exposed to the nitridized silicon surfaces for 1 minute. **Fig. 2-9, 2-10, 2-11** and **2-12** show the similar growth of silicon oxide on these films.

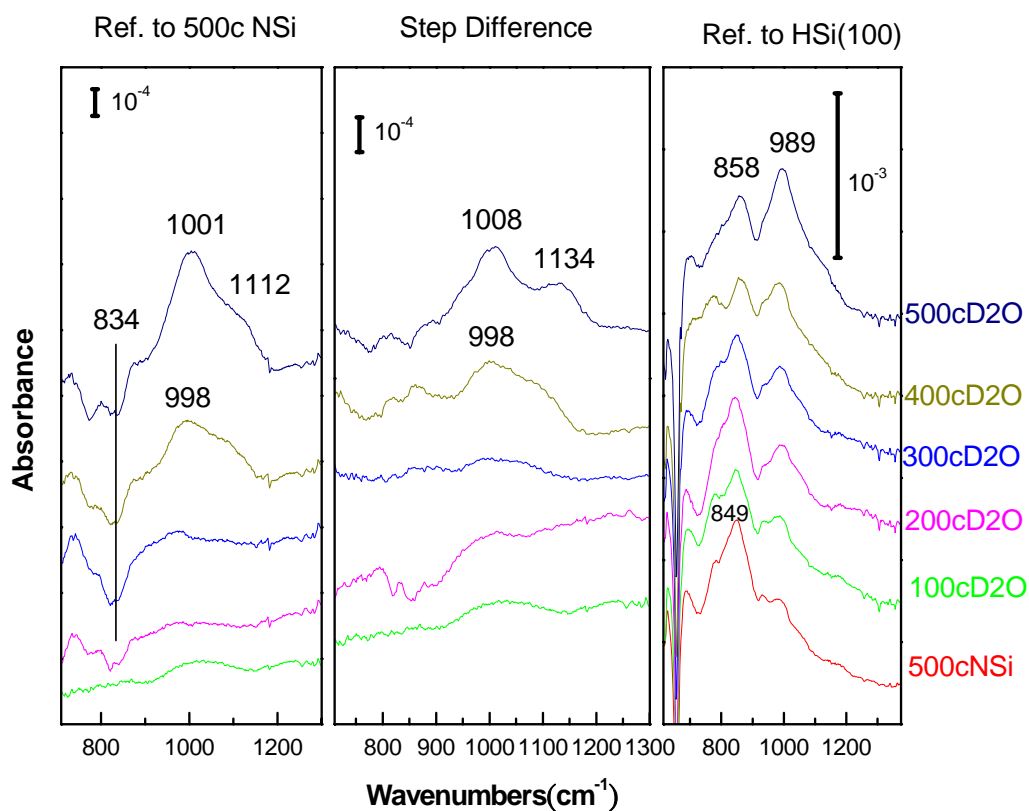


Fig. 2-9 The IR integrated area of 500°C (~30s ammonia exposure time) grown silicon nitride moiety shows estimated thickness of 1.5~2 Å which is impossible to fully cover substrate surface. Spectra referenced to starting H/Si(100) surface on right panel and nitridized surface on left panel show obvious Si-O/ silicon oxide species~ 900-1200cm<sup>-1</sup> starts to grow with D<sub>2</sub>O exposure at 300°C. The Step difference spectra of the middle panel show the silicon nitride species mode~830-900cm<sup>-1</sup> consumed at 200°C D<sub>2</sub>O exposure and obvious silicon oxide TO-LO mode splitting at 500°C D<sub>2</sub>O exposure.

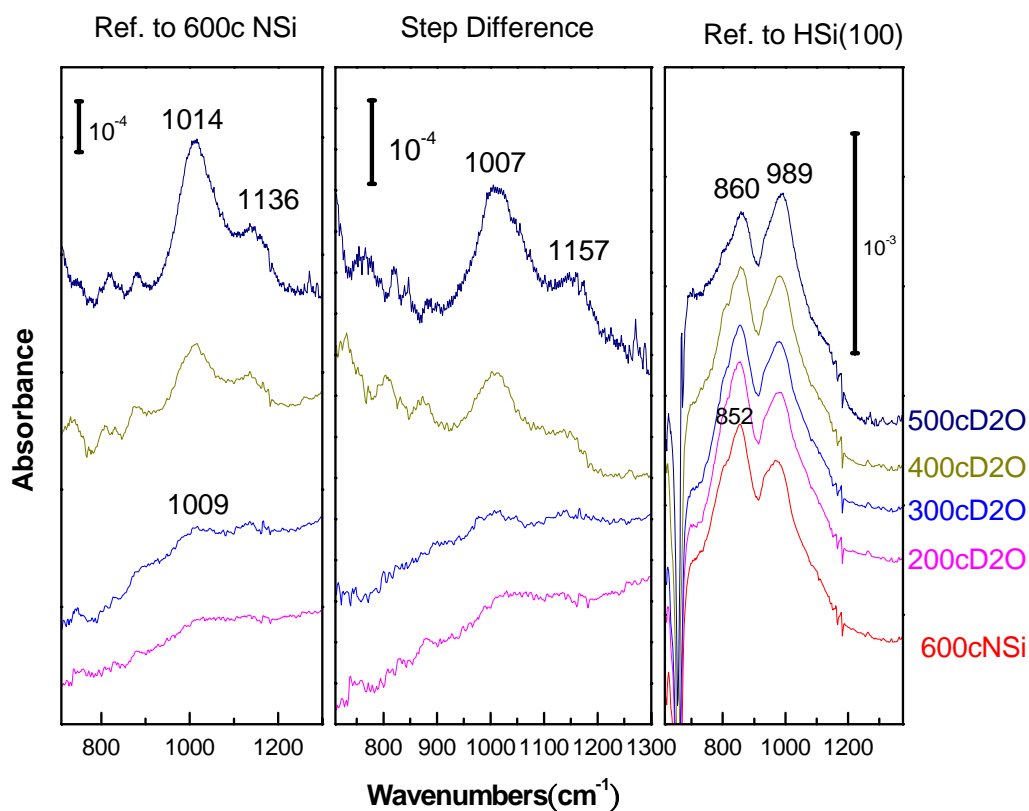


Fig. 2-10 The IR integrated area of 600°C (~30s ammonia exposure time) grown silicon nitride moiety shows estimated thickness of 3~4 Å which might barely cover substrate surface. The shapes of grown Si-O/silicon oxide moiety in spectra are similar to those of 500°C grown silicon nitride, while the loss of silicon nitride mode~830-900cm<sup>-1</sup> is not obvious.

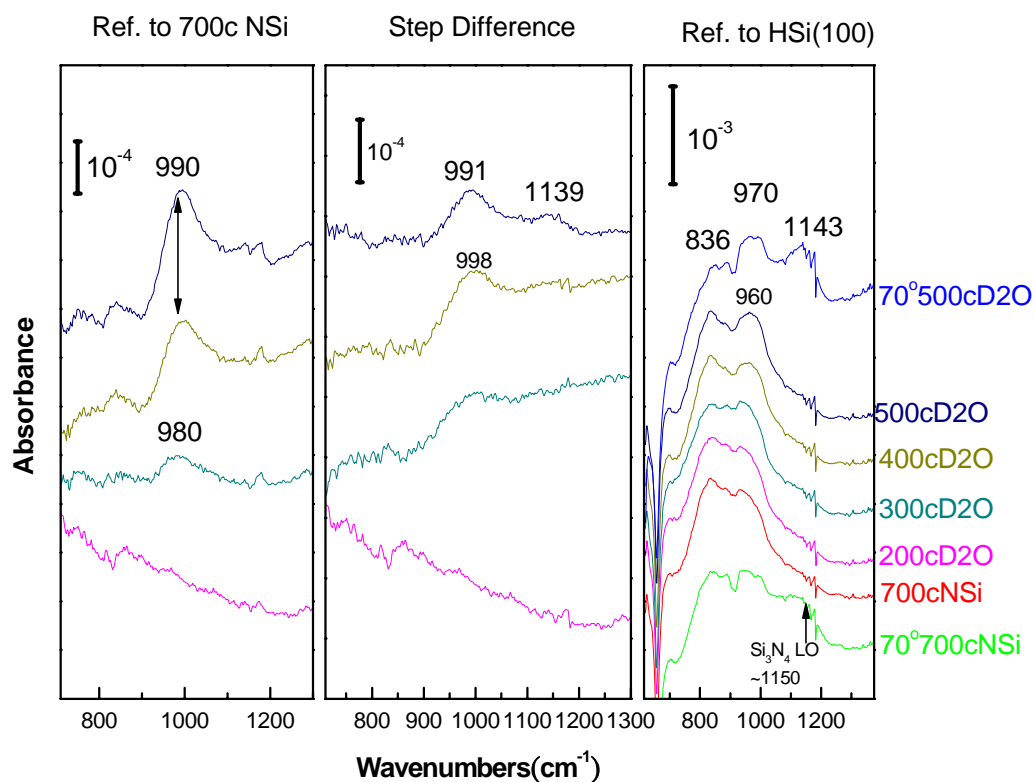


Fig. 2-11 The IR integrated area of 700°C grown (~30s ammonia exposure time) silicon nitride moiety shows estimated thickness of ~5 Å which might have fully covered substrate surface. The bottom nitride film spectrum taken at 70° incident angle in light green verifies 1150cm<sup>-1</sup> peak the silicon nitride LO mode. The structure of grown Si-O/ silicon oxide moiety modes is similar to that grown on other thermal ammonia nitridized silicon surfaces grown at 500 °C and 600°C.

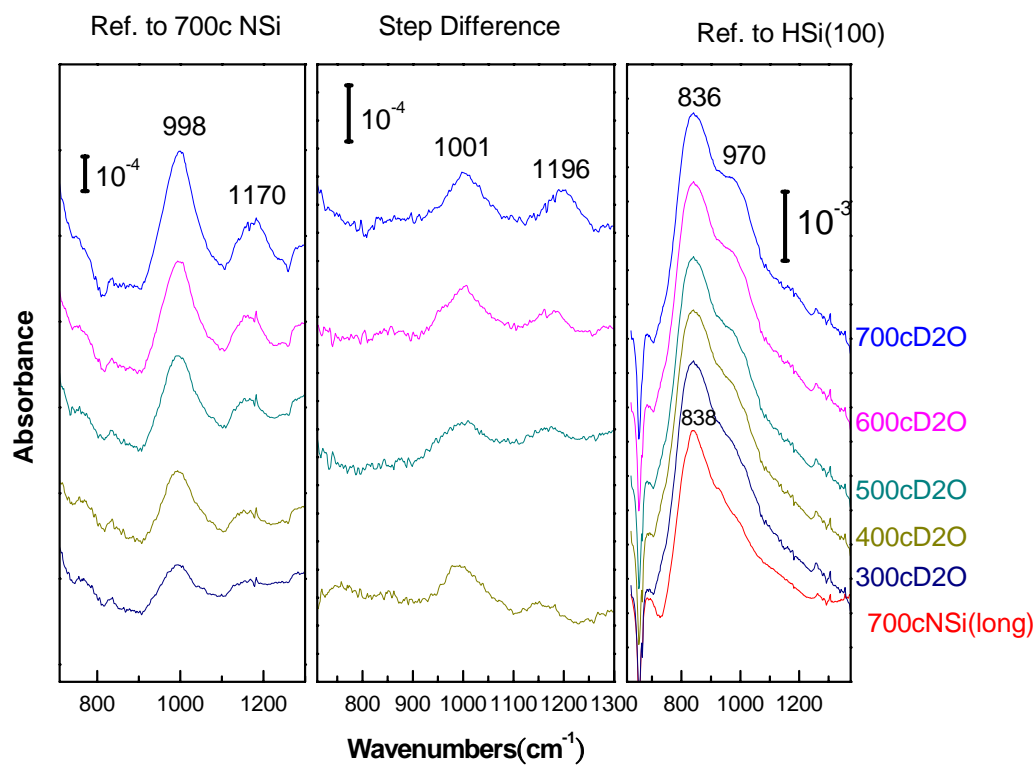


Fig. 2-12 The IR integrated area of 700°C grown saturated silicon nitride by extra long ammonia exposure time~7 minutes shows estimated thickness of 11~12 Å which surely cover substrate surface with a layer of stoichiometric silicon nitride. Again the structure of grown Si-O/ silicon oxide moiety modes is similar to that grown on nitridized surface with shorter (~30 seconds ) ammonia exposure.

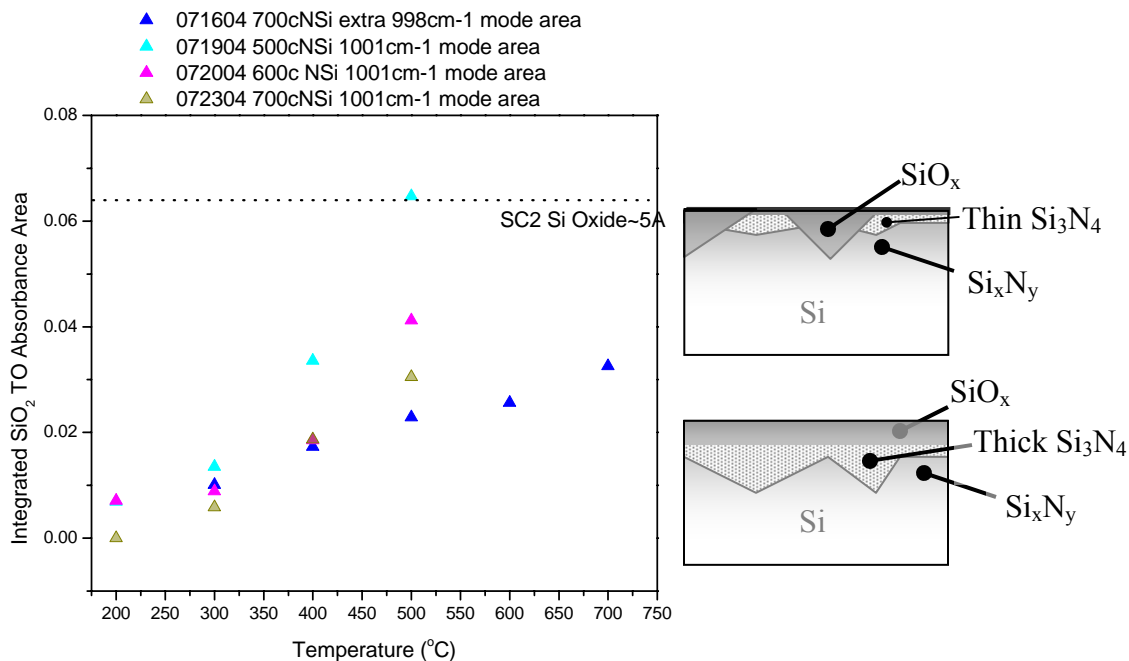


Fig. 2-13 Left plot: the integrated IR absorbance peak areas of silicon oxide moiety~1000cm<sup>-1</sup> grown by thermal D<sub>2</sub>O exposure on 500°C (light blue triangle), 600°C (pink triangle), 700°C (olive triangle) ammonia nitridized silicon surfaces and 700°C saturated silicon nitride (blue triangle) versus annealing temperatures. The dashed line indicating the absorbance peak area of SC2 wet chemistry silicon oxide TO mode (~1030cm<sup>-1</sup>). Right-top view graph: penetration growth of silicon-oxygen moiety; right-lower view graph: thick enough silicon nitride film sustaining oxidation.

With D<sub>2</sub>O exposure at 500°C, the thickness of silicon oxide grown on 500°C- (1.5~2Å thick) and 600°C-silicon nitride (3~4Å thick) is estimated to be about 5 Å and 3.2 Å respectively, while the IR spectra referenced to H/Si(100) still show the existence of silicon nitride TO mode ~ 840cm<sup>-1</sup>. **Fig. 2-13** shows the oxidation levels of 600 °C, 700 °C and saturated 700 °C nitride are comparable, but lower than that of 500 °C grown nitride during the D<sub>2</sub>O exposure at temperatures lower than 500°C, which suggests that the 600°C grown silicon nitride can barely cover most substrate surface to prevent the oxidation during D<sub>2</sub>O exposure. The contrast of the increasing oxidation level increments with 500 °C, 600 °C and 700 °C grown nitride to the constant oxidation level increment of 700 °C saturated nitride implies that the stoichiometric silicon nitride has higher oxidation

resistance than sub-stoichiometric silicon nitride.

### **2.3 TMA/D<sub>2</sub>O Aluminum Oxide ALD on Thermal Ammonia Nitridized Silicon Surfaces**

In this section *in-situ* IR spectra of Al<sub>2</sub>O<sub>3</sub> grown by ALD with TMA and D<sub>2</sub>O on different surfaces are presented: thinner, inhomogeneous silicon nitride and thicker, continuous nitride grown at 496°C and 605°C in ammonia ambient respectively, hydrogen terminated Si(100), and SC2 wet-silicon oxide surfaces. This study gives us better understanding of the functionality of different surfaces to TMA and some clues for fundamental surface reaction mechanisms.



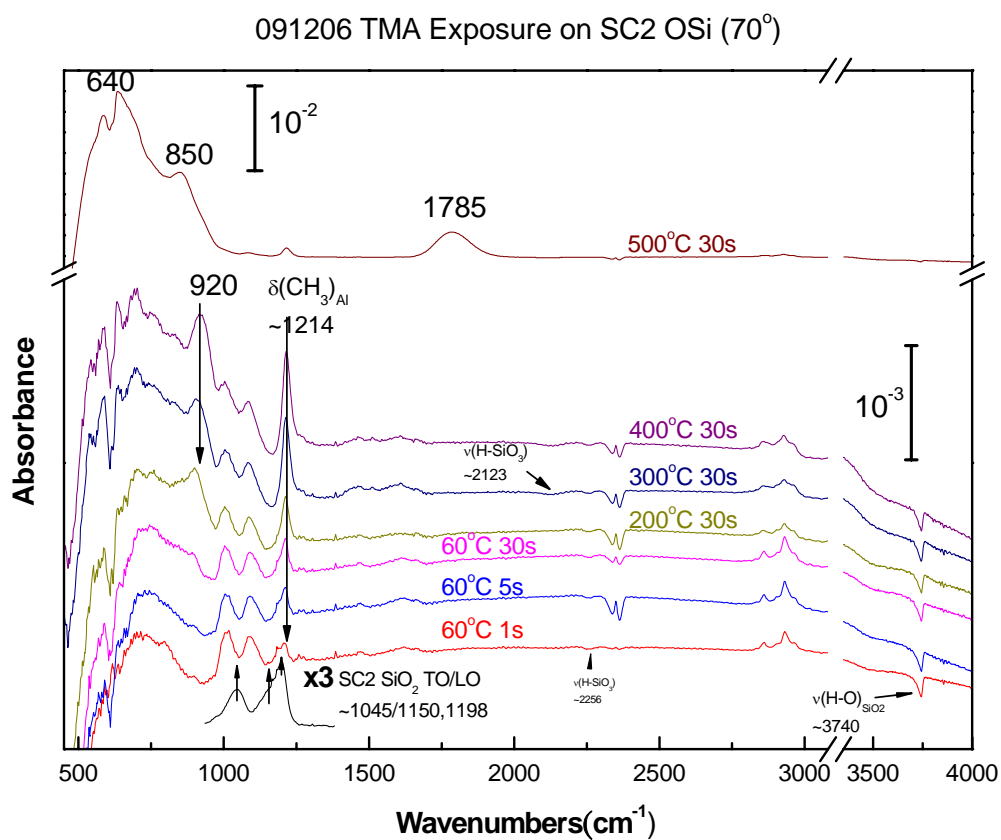


Fig. 2-14 Transmission IR absorption spectra referenced to the starting SC2 oxidized silicon surface and at incident angle 70° of sequential operations: 1, 5, 30 seconds 100 sccm N<sub>2</sub> carrying TMA exposure to 60°C silicon oxide surface followed by 30 seconds same flow exposure on substrate at 200, 300, 400 and 500°C in vacuum chamber.

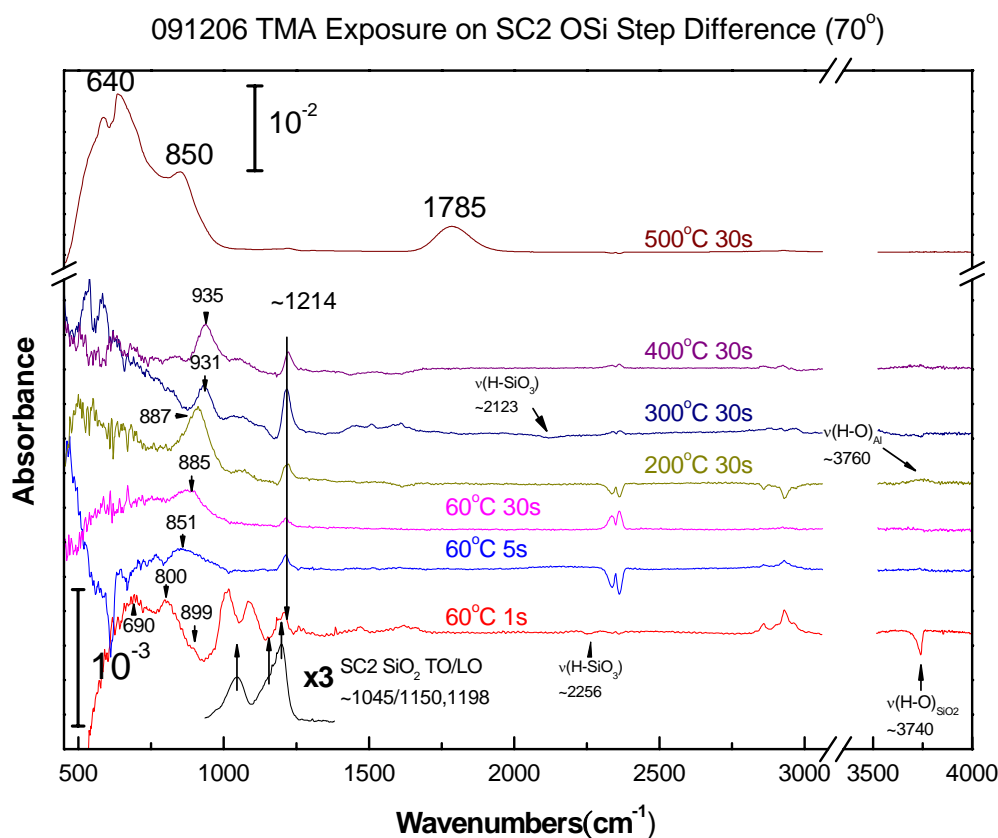


Fig. 2-15 Transmission IR absorption step difference spectra at incident angle  $70^\circ$  of sequential operations: 1, 5, 30 seconds 100 sccm  $\text{N}_2$  carrying TMA exposure to  $60^\circ\text{C}$  silicon oxide surface followed by 30 seconds same flow exposure on substrate at 200, 300, 400 and  $500^\circ\text{C}$  in vacuum chamber.

For ALD with self-limiting reaction and layer-by-layer growth, there is in general a narrow deposition temperature window which depends on the chemical properties of precursors and substrate surfaces. **Fig. 2-14** and **Fig. 2-15** show the spectra of SC2 oxidized silicon surface exposed to accumulative TMA dosing. The bottom three IR spectra of TMA exposure of different time lengths at  $60^\circ\text{C}$  show  $\text{CH}_x$  stretching  $\sim 2800$ - $3000 \text{ cm}^{-1}$  and metal oxide modes in the region of  $500$ - $1200 \text{ cm}^{-1}$ ;  $1005 \text{ cm}^{-1}$  for Al-O-Si and  $1089 \text{ cm}^{-1}$ ,  $899 \text{ cm}^{-1}$  and  $800 \text{ cm}^{-1}$  for  $\text{Al}_2\text{O}_3$  or Al-O. [34, 35] [36] [37] [2, 38] These

modes are accompanied by the loss of silicon oxide, surface hydroxyl group ( $\sim 3740\text{cm}^{-1}$ ) and trace residual  $\text{H-SiO}_3$  ( $\sim 2256\text{cm}^{-1}$ ). The mode at  $1214\text{ cm}^{-1}$  is an overlap of several components possibly for  $\delta(\text{CH}_3)$  of  $\text{CH}_3\text{-Al}$  ( $\sim 1217\text{ cm}^{-1}$ ) on surface,  $\delta(\text{CH}_3)$  and  $\nu(\text{C-C})$  of gaseous hydro-carbon in ambient and Si oxide LO mode. Except for surface Al-O-Al growth ( $800\text{-}851\text{cm}^{-1}$ ) [39], there is no significant change in the spectra with the different exposure times at  $60^\circ\text{C}$ . The top four IR spectra of 30s exposure with different temperatures ( $200\text{-}500^\circ\text{C}$ ) show a blue shift of the  $896\text{ cm}^{-1}$  mode up to  $920\text{ cm}^{-1}$ . The intensities of  $\delta(\text{CH}_3)$  and  $\nu(\text{CH}_x)$  increase with the substrate temperature from  $60^\circ\text{C}$  to  $400^\circ\text{C}$ . At  $200^\circ\text{C}$  the existence of  $\nu(\text{OH}) \sim 3760\text{ cm}^{-1}$  indicates residual interfacial hydroxyl group bonding to Al. A very weak mode at  $1511\text{cm}^{-1}$  from  $\text{C}=\text{C}$  at  $300^\circ\text{C}$  indicates a change in the termination of surface organic species. At  $500^\circ\text{C}$ , more silicon oxide LO/TO modes ( $1210$  and  $1083\text{cm}^{-1}$ ) grow, and the broad bands in  $500\text{-}1000\text{ cm}^{-1}$  (Al-O-Al ( $854\text{cm}^{-1}$ ), Al-C ( $760\text{cm}^{-1}$ ) [40] and Al-O ( $\sim 640\text{cm}^{-1}$ ) for bulk Al oxide [41] [1]) and the strong  $1785\text{ cm}^{-1}$  mode (related to either  $\nu_{\text{as}}(\text{H-Al})$  [42] or  $-(\text{CO})\text{-O-(CO)-}$  segment [43] [44]) imply CVD-type growth at this temperature. Thus it suggests the appropriate temperature for ALD using TMA is lower than  $500^\circ\text{C}$ . The reported ALD temperature window of  $350\text{-}550^\circ\text{C}$  for TMA/ $\text{NH}_3$  by Puurunen et al. [45-48] is in agreement with our data, though the surface alkyl and hydroxyl group replacement may not be possible to observe at temperature higher than  $300^\circ\text{C}$ .

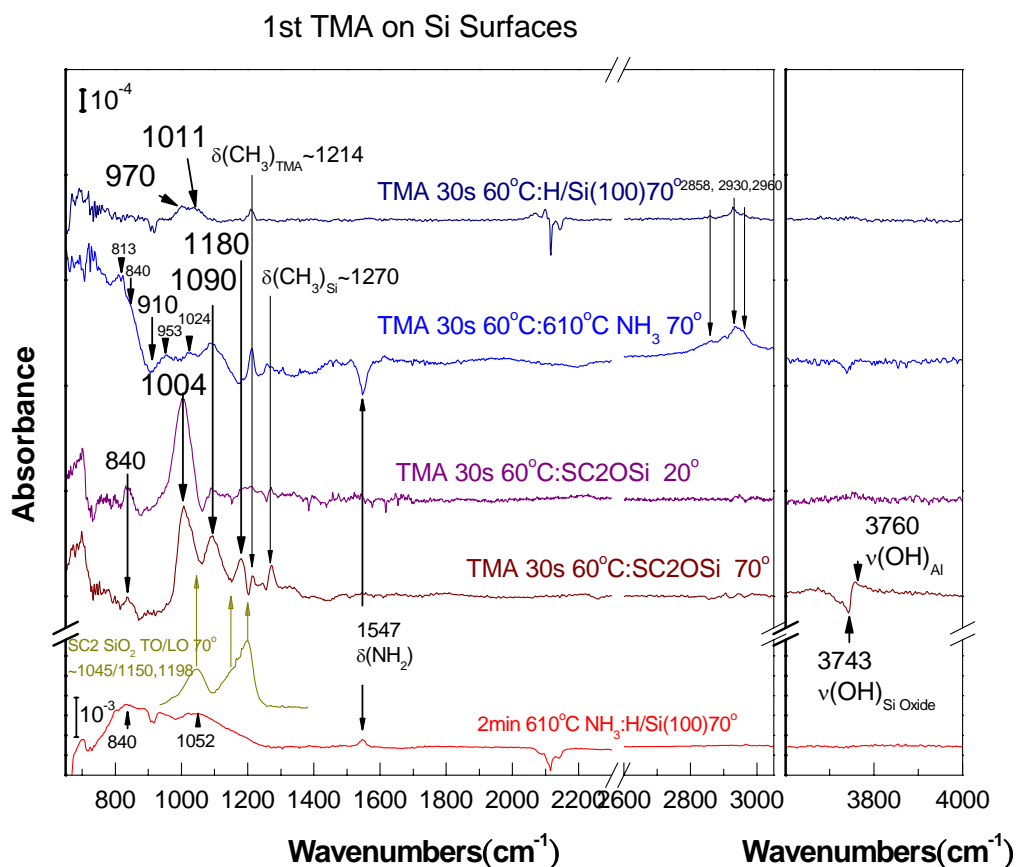


Fig. 2-16 Transmission IR absorption spectra of 30-second 100 sccm  $\text{N}_2$  carrying TMA exposure to  $60^\circ\text{C}$  H/Si(100) at  $70^\circ$  incident angle, thermal ammonia nitridized silicon surface (2-minute ammonia pretreated at  $610^\circ\text{C}$ ) at  $70^\circ$  incident angle and SC2 oxidized silicon surface at  $20^\circ$  and  $70^\circ$  incident angles. The bottom nitridized silicon surface referenced to H/Si(100) at  $70^\circ$  incident angle in red and local spectrum section of SC2 wet chemistry pre-treated H/Si(100) referenced to H/Si(100) at  $70^\circ$  incident angle in yellow-green are for comparison.

A single pulse of TMA is dosed onto three different silicon surfaces: H/Si(100), 2-minute ammonia pretreated H/Si(100) at  $610^\circ\text{C}$  ( $610^\circ\text{C}$  NSi) and SC2 oxidized silicon surface (OSi). The characterization of TMA adsorption on these silicon surfaces will benefit the followed analysis on IR absorption spectra of Al oxide ALD. By quantifying the relevant IR absorption peak area, the transmission IR absorption spectra (**Fig. 2-16**) show less than 2% H-Si stretching mode loss from fresh H/Si(100) (in agreement with reported result [2, 38] ), about 86% hydroxyl group stretching ( $\sim 3743\text{cm}^{-1}$ ) loss from OSi

and about 81-90%  $\text{NH}_2$  group scissoring mode ( $\sim 1547\text{cm}^{-1}$ ) loss from  $610^\circ\text{C}$  NSi. Additionally, new peaks of H-Si stretching red-shift mode  $\sim 2067\text{cm}^{-1}$  and very little ( $<0.6\%$  of full H-Si stretching mode absorbance peak area of H/Si(100)) blue-shifted H-Si stretching mode  $\sim 2253\text{cm}^{-1}$  for  $\text{H-SiO}_3$  surface groups on H/Si(100) and a blue-shifted H-O stretching mode  $\sim 3760\text{cm}^{-1}$  ( $\sim 20\%$  of full hydroxyl stretching absorbance peak area of OSi) for H-O-Al hydroxyl groups on OSi [36] appear after TMA pulse exposure. Therefore, the surface groups on freshly prepared silicon surfaces are only partially removed by the TMA exposure, and apparently H/Si(100) has a higher barrier against TMA adsorption.

The hydro-carbon intensity level of TMA pulse exposure on H/Si(100) is less than that on  $610^\circ\text{C}$  NSi. As shown by the spectra in **Fig. 2-16**, the absorption peak areas of as-grown  $\nu(\text{CH}_x) \sim 2800\text{-}3000\text{cm}^{-1}$  and symmetric  $\text{CH}_3$  bending mode of  $\text{CH}_3\text{-Al}$  groups ( $\delta(\text{CH}_3)_{\text{Al}} \sim 1214\text{cm}^{-1}$ ) of TMA exposure on H/Si(100) are respectively only  $\sim 25\%$  and  $40\%$  of those on  $610^\circ\text{C}$  NSi. The mode  $\sim 1270\text{cm}^{-1}$  found both in TMA pulse exposure on OSi and on  $610^\circ\text{C}$  NSi but not observed in TMA pulse exposure on H/Si(100) is associated with the symmetric  $\text{CH}_3$  bending mode of  $\text{CH}_3\text{-Si}$  groups ( $\delta(\text{CH}_3)_{\text{Si}}$ ) [1, 49]. They separately imply the consequences of higher TMA adsorption barrier with H/Si(100) and partial adsorbed-TMA decomposition on inhomogeneous OSi and NSi surfaces.

The band in frequency range of  $970\text{-}1011\text{ cm}^{-1}$  of TMA exposure on H/Si(100) is mainly for local surface moiety of  $\text{Al-O-Si}(\text{O}_x\text{Si}_{3-x})_{x \leq 2}$ . In TMA exposure on OSi, mode  $840\text{ cm}^{-1}$  (not found in the TEMAH exposure on OSi in next chapter) can be related to Al-O-Al moiety on surface[39], and the TO/LO modes of  $1004\text{ cm}^{-1}/1090, 1180\text{cm}^{-1}$  can be associated with Si-O stretching in the surface structure of Al-O-SiO<sub>3</sub>. While in TMA

exposure on 610°C NSi, 813, 953 and 1024 $\text{cm}^{-1}$  modes are likely related to relevant Al-O or Al-N stretching[50].

### A. TMA/D<sub>2</sub>O ALD on Annealed Nitridized Silicon Surface

In the reactor purged at atmospheric pressure, an annealed ammonia nitridized silicon substrate is exposed to alternative one-minute TMA and D<sub>2</sub>O pulses. 40 ml/min and 400 ml/min of N<sub>2</sub> are used to deliver TMA and D<sub>2</sub>O into the reactor, respectively which is purged by 1 liter/min of N<sub>2</sub>. The reactor is purged with 1.4 liter/min of N<sub>2</sub> flow for 20 minutes between each precursor dosing. The nitridized silicon surface was grown at 319°C for the first 2 minutes and 496°C for the last 2 minutes in 4 % NH<sub>3</sub>/N<sub>2</sub>, and then annealed at 605°C for 2 minutes with 1.4 liter/min of N<sub>2</sub> flow.

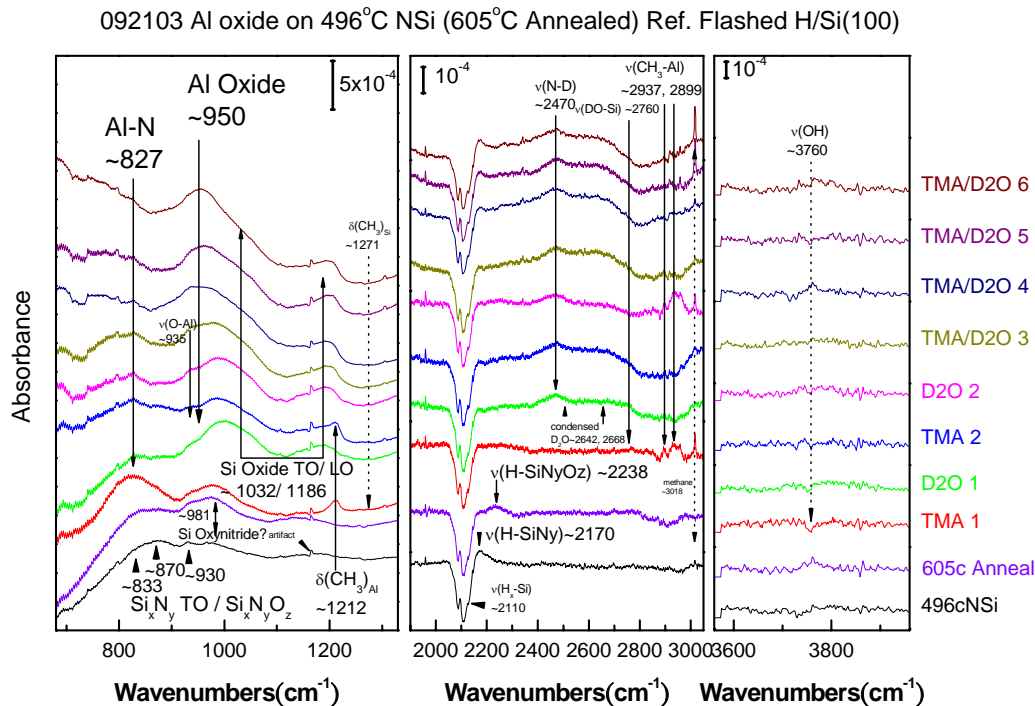


Fig. 2-17 The in-situ IR spectra referenced to H/Si(100) of 380°C aluminum oxide ALD on 605°C annealed 496°C ammonia treated H/Si(100) surface are taken at incident angle of 45°.

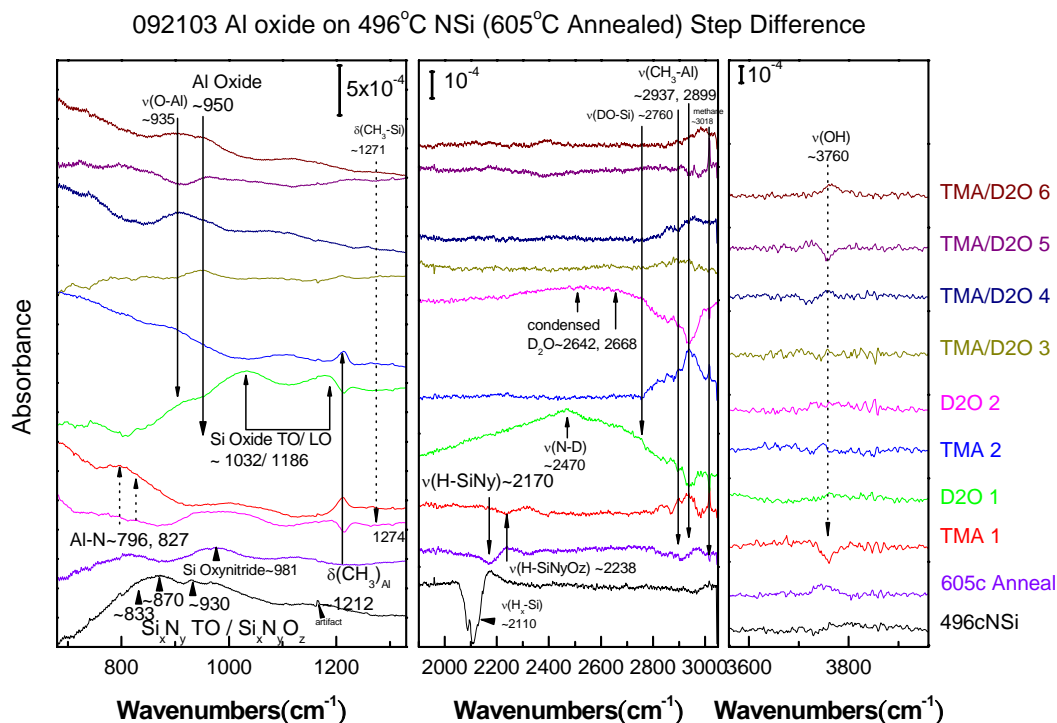


Fig. 2-18 The in-situ IR step difference spectra of 380°C aluminum oxide ALD on 605°C annealed 496°C ammonia treated H/Si(100) surface are taken at incident angle of 45°.

(**Fig. 2-17**) The IR spectra of 380°C aluminum oxide ALD on 605°C annealed 488°C NSi are taken at incident angle of 45°. Trace hydroxyl group~3760cm<sup>-1</sup> and silicon oxynitride~981 cm<sup>-1</sup> are grown during 605°C annealing. Thus the annealed 488°C NSi contains non-continuous silicon nitride, silicon oxide/oxynitride moiety and some surface hydrogen~2238cm<sup>-1</sup>. After TMA and D<sub>2</sub>O exposures, aluminum oxide mode~950cm<sup>-1</sup> grows with number of ALD cycles on annealed 488°C NSi. The very first TMA exposure removes the surface residual hydride~2238cm<sup>-1</sup> and grows 827cm<sup>-1</sup> Al-N surface mode. C-H bending mode  $\delta(\text{CH}_3)_{\text{Al}}$ ~1212cm<sup>-1</sup> and  $\nu(\text{CH}_x)_{\text{Al}}$ ~ 2899 and 2937cm<sup>-1</sup> shown in each TMA exposure indicate significant portion of TMA adsorbs on surface without methyl ligand decomposition. After the first D<sub>2</sub>O exposure, some silicon oxide, hydroxyl groups

$\nu(\text{DO})_{\text{Al}} \sim 2760 \text{ cm}^{-1}$  and amine groups (N-D)  $\sim 2470 \text{ cm}^{-1}$  grow. The broad lump structure  $\sim 2800\text{-}2400 \text{ cm}^{-1}$  (peaked at 2642 and  $2668 \text{ cm}^{-1}$ ) is assigned as multiple coordinated DO- $\text{Al}_x$  or condensed  $\text{D}_2\text{O}$  on the developing Al oxide network. (N-D stretching  $\sim 2470 \text{ cm}^{-1}$  produced by the first  $\text{D}_2\text{O}$  exposure doesn't change by latter ALD exposures, and is assumed the consequence of the deuterium-hydrogen interchange of N-H contamination in KBr window produced during nitridation. ) The weak loss of  $\sim 1140$  and  $820 \text{ cm}^{-1}$  peaks may be attributed to the loss of surface N-Si moiety change and the growth of disordered Al-O or Al-N stretching mode  $\sim 827 \text{ cm}^{-1}$ . (The reported surface Al-N mode grown by various growth methods fall in frequency range  $\sim 650\text{-}950 \text{ cm}^{-1}$ , which is overlapping with surface Al-O and Al-ON mode frequency ranges. [51-55] The broad mode  $\sim 750\text{-}850 \text{ cm}^{-1}$  appears upon the first TMA exposure on NSi but is never seen in the TMA exposure on H/Si and silicon oxide surfaces. Additionally the mode intensity at higher frequency  $\sim 827 \text{ cm}^{-1}$  is stronger with the TMA exposure on thicker silicon nitride covered surface (see **Section 2.3 B.**), so that concludes that the broad mode  $\sim 750\text{-}850 \text{ cm}^{-1}$  is more likely attributed to surface Al-N instead of Al-O. Upon the first  $\text{D}_2\text{O}$  exposure, the Si-O moiety indicated by  $1032 \text{ cm}^{-1}$  (TO) and  $1186 \text{ cm}^{-1}$  (LO) mode has been grown at the ALD growth temperature of  $380^\circ\text{C}$ .

The step difference spectra (**Fig. 2-18**) also show shallow  $870 \text{ cm}^{-1}$  Si-N mode loss,  $981$  and  $1126 \text{ cm}^{-1}$  silicon oxide/oxy-nitride peak modes, and manifest the hydride stretching mode  $\nu(\text{H-SiN}_y) \sim 2170 \text{ cm}^{-1}$  transmuting to  $\nu(\text{H-SiO}_x\text{N}_y) \sim 2238 \text{ cm}^{-1}$  due to oxygen insertion into silicon back bone during  $622^\circ\text{C}$  annealing. The first TMA exposure induces  $850\text{-}750 \text{ cm}^{-1}$  mode for surface Al-N formation and  $1006 \text{ cm}^{-1}$  mode for Al-O-Si to appear at the weak loss of  $922$  and  $1135 \text{ cm}^{-1}$  silicon oxynitride/ nitride modes. The



following D<sub>2</sub>O exposure (D<sub>2</sub>O 1) grows silicon oxide (TO~1032 cm<sup>-1</sup> and LO~1186cm<sup>-1</sup>) at some loss of silicon nitride and removes substantially the lump of 750-850cm<sup>-1</sup> for surface Al-N. As the argument in last paragraph, the peaks at 796 and 827cm<sup>-1</sup> in the frequency range of 750-850cm<sup>-1</sup> are directly related to Al-N formation, while the 835 and 950cm<sup>-1</sup> modes appear in latter 3<sup>rd</sup>-6<sup>th</sup> full ALD exposures are associated with the Al-O surface mode and Al oxide mode. The variation of  $\delta(\text{CH}_3)_{\text{Al}}$  CH<sub>3</sub>-Al~1212cm<sup>-1</sup> and correlated  $\nu(\text{CH}_x)$ ~2800-3000cm<sup>-1</sup> in the middle panel of **Fig. 2-18** during the first four half-cycles clearly shows the surface CH<sub>3</sub>-Al groups are grown and removed by TMA and D<sub>2</sub>O exposures. The interplay of Al-O stretching mode~935cm<sup>-1</sup> and Al oxide mode~950cm<sup>-1</sup> indicates the chemical environment variation of surface Al-O moiety and the growth of Al oxide cluster.

To sum up, the TMA/D<sub>2</sub>O exposures to substrate at 380°C can grow Al oxide on 496°C NSi (605°C annealed), but silicon oxide growth is still found in the first D<sub>2</sub>O exposure. After 5 full cycles of TMA/ D<sub>2</sub>O exposures, the grown silicon oxide mode intensity is about half of that of SC2 treated H/Si(100) by LO peak area, which is equivalent to ~2.5Å thick silicon oxide.

## **B. TMA/D<sub>2</sub>O ALD on Thicker Silicon Nitride**

In atmospheric pressure purge style reactor, TMA/ D<sub>2</sub>O aluminum oxide ALD (with the same exposure conditions as in **Section 2.3 A.**) is carried out on a thicker silicon nitride film grown by two-staged treatment of higher final ammonia exposure temperature of 605°C (2-minute at 319°C and 2-minute at 605°C in 4 % ammonia/N<sub>2</sub> flow).

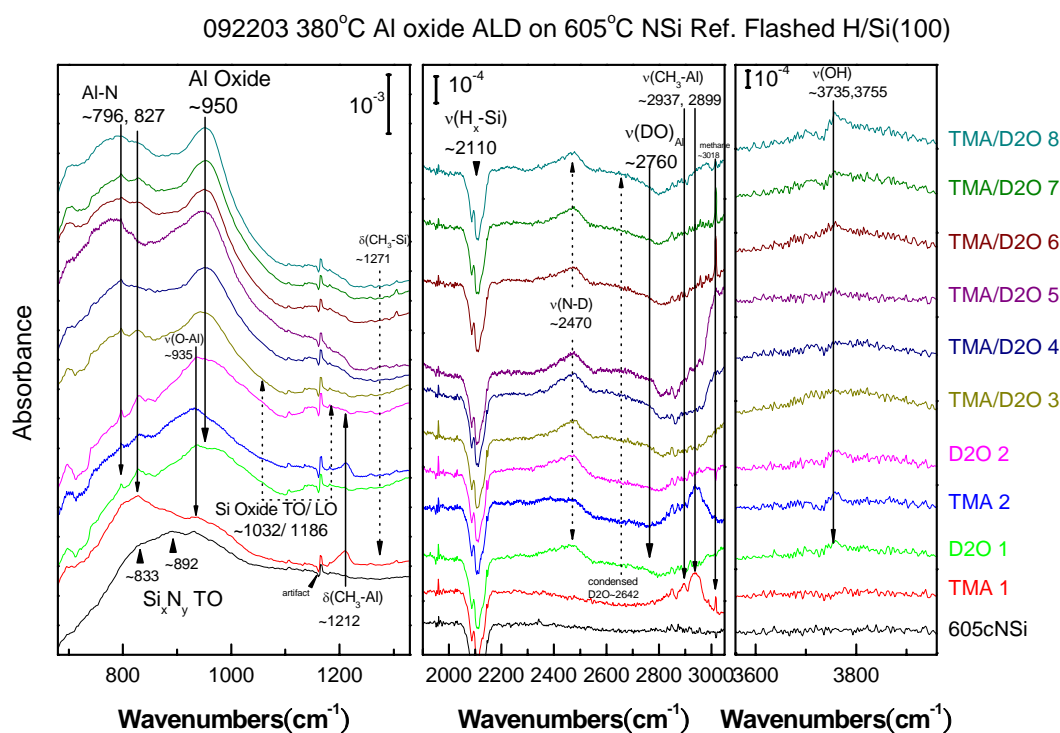


Fig. 2-19 The in-situ IR spectra referenced to H/Si(100) of 380°C aluminum oxide ALD on 605°C ammonia treated H/Si(100) surface are taken at incident angle of 45°.

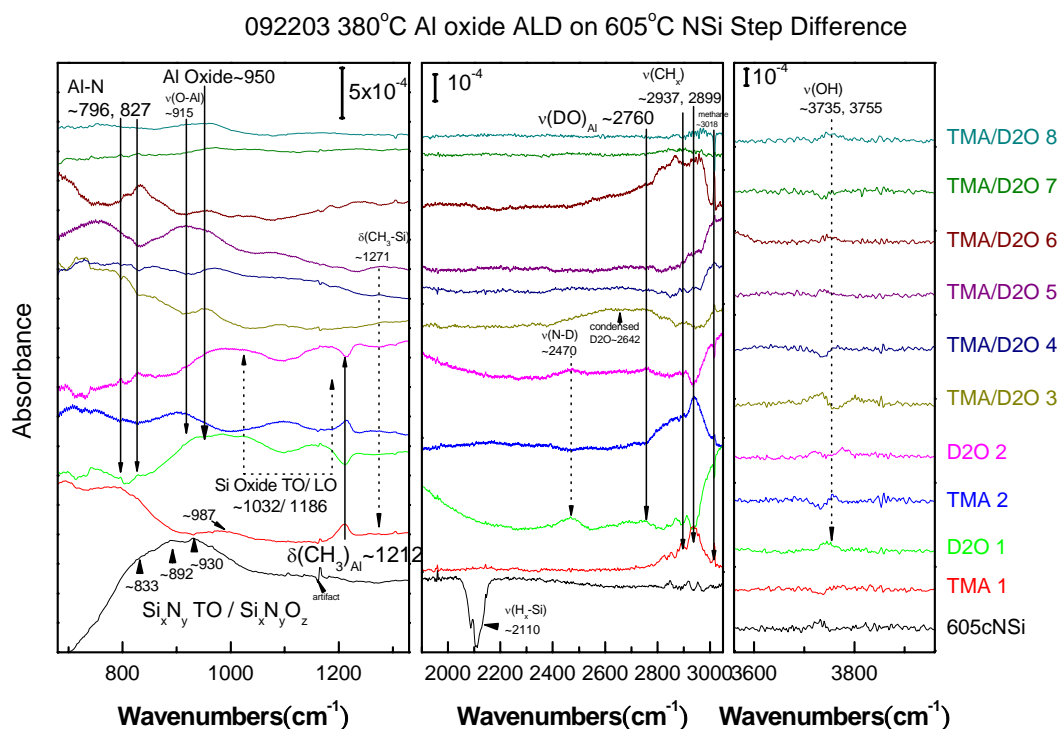


Fig. 2-20 The colored in-situ IR spectra referenced to 605°C ammonia treated surface of 380°C aluminum oxide ALD on 622°C ammonia treated H/Si(100) surface are taken at incident angle of 45°. The bottom 622cNSi spectrum in black is referenced to H/Si(100).

**Figure 2-19** shows better silicon nitride coverage on the initial surface and very similar evolution of the spectra during ALD with that of thinner silicon nitride in **Section 2.3 A**. The first TMA exposure produces 789  $\text{cm}^{-1}$  mode, and the 935  $\text{cm}^{-1}$  mode for Al-O moiety appears upon the first D<sub>2</sub>O exposure. Comparing with the ALD on thinner silicon nitride film, there is no distinct silicon oxide TO/LO modes observed up to 8 full TMA/D<sub>2</sub>O ALD cycles. It also shows stronger intensity of silicon nitride mode by the end of 6 full ALD cycles, although the silicon oxynitride mode at 1050-900  $\text{cm}^{-1}$  grown upon the first and second D<sub>2</sub>O exposure as shown in **Fig. 2-19** indicates partial surface oxidation. **Figure 2-20** shows the 1174  $\text{cm}^{-1}$  mode for the possible interstitial Si-O formation in silicon nitride through the oxidation by D<sub>2</sub>O exposure.

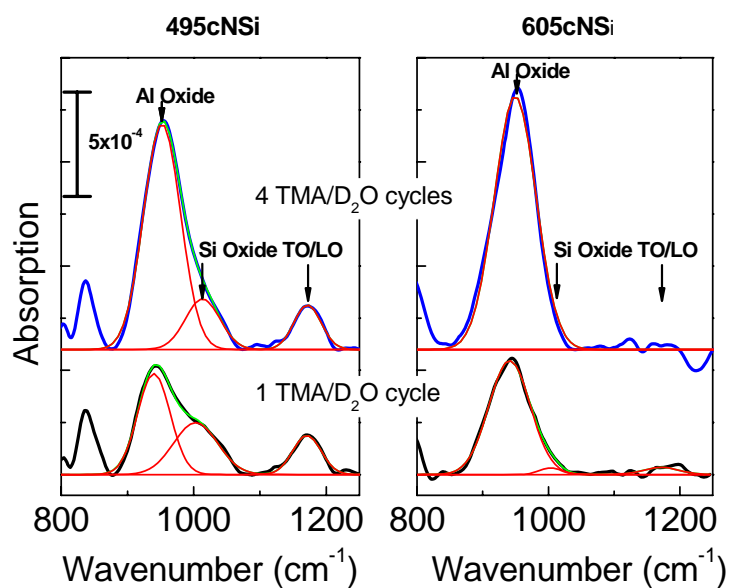


Fig. 2-21 Sections of base-lined and Gaussian curve fitted transmission IR spectra referenced to nitridized silicon surface in 800-1250 $\text{cm}^{-1}$  of 1 cycle and 4 cycles 380°C TMA/D<sub>2</sub>O ALD on 495°C (left panel) and 605°C (right panel) ammonia treated H/Si(100).

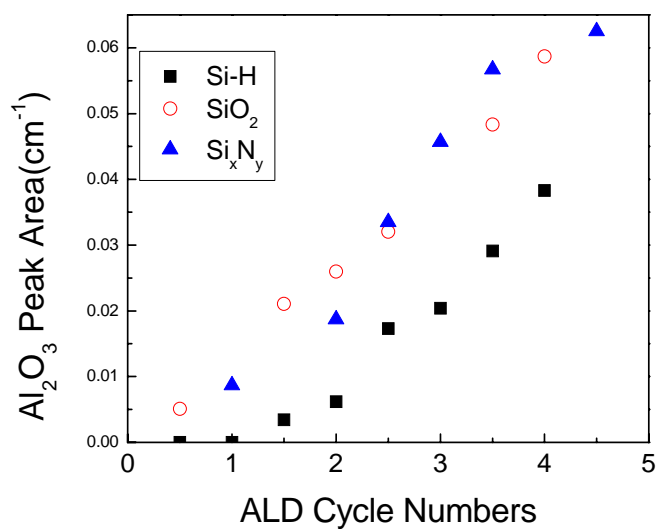


Fig. 2-22 Al oxide mode ( $\sim 950\text{cm}^{-1}$ ) absorbance peak area of 380°C TMA/D<sub>2</sub>O ALD grown on H/Si(100) (Si-H; black solid square), SC2 oxidized silicon surface (SiO<sub>2</sub>; red open circle) and 605°C-4% ammonia grown silicon nitride film (Si<sub>x</sub>N<sub>y</sub>; blue solid triangle) plot over ALD cycle numbers.

The quantitative comparison of grown ALD Al oxide mode~950cm<sup>-1</sup> peak area on different starting silicon surfaces (**Fig. 2-22**) (up to 5 full ALD cycle) shows the Al oxide growth of ammonia nitridized silicon surface to TMA/D<sub>2</sub>O ALD precursors is not only better than H/Si(100) but also comparable to the hydroxyl-group-containing SC2 oxidized silicon surface. Especially the ammonia nitridized silicon surface doesn't pose any incubation period and low nucleation rate as H/Si(100) does in the first three ALD cycles.

## Conclusion:

In thermal H/Si(100) nitridation by ammonia, di-hydrides and tri-hydrides on H/Si(100) are more reactive than mono-hydrides for nitrogen-contained radical adsorption. Extensive nitrogen insertion into silicon substrate won't take place until major removal of surface hydrides at temperature higher than 380°C for H/Si(100) nitridation and 496°C for H/Si(111) nitridation.

The appearance of  $\nu(\text{H-SiOx})$  mode in vacuum chamber ammonia thermal nitridation on H/Si shows oxygen is very easy to incorporate in the ammonia-silicon reaction, and surface Si-NH<sub>2</sub> is observed although the growth temperature for this species is not known because of the long cooling process in ammonia ambient. NH species is very little even though it might exist after ammonia nitridation. The ultra-thin silicon nitride/oxy-nitride film formation mechanism on H/Si by thermal ammonia exposure can be composed of an initial surface reactivity controlled reaction stage followed by a thermal limited diffusion transportation process of reactive nitrogen moiety into the depth of silicon substrate. When the substrate growth temperature goes up more than 600°C, the surface reactivity and diffusion transportation through the outmost and the next atomic

layer of silicon substrate become high enough for efficient nitride/ oxynitride formation. Grown silicon nitride/oxynitride of higher nitridation temperature and extra-long exposure have thicker average thickness and better structure against under-layer silicon oxidation by D<sub>2</sub>O.

The 605°C grown thermal silicon nitride film would form a continuous coverage on silicon substrate and under extreme D<sub>2</sub>O abundant ambient it grows nitrogen rich non-stoichiometric silicon oxynitride modes ~921 and 1093 cm<sup>-1</sup> and oxygen rich non-stoichiometric silicon oxynitride ~987 cm<sup>-1</sup> at further higher temperature D<sub>2</sub>O exposure temperature. The stoichiometric silicon oxide clusters won't be grown until 605°C D<sub>2</sub>O exposure. The higher nitridation temperature gives thicker silicon nitride film against under-layer silicon oxidation by D<sub>2</sub>O and the grown silicon nitride moiety of longer ammonia exposure has better resistance against D<sub>2</sub>O oxidation.

The transmission IR of single TMA pulse exposure experiments show TMA are more reactive to SC2 oxidized silicon surface and ammonia nitridized silicon surface than to H/Si. TMA/D<sub>2</sub>O ALD growth on silicon nitride/oxynitride surface does not have incubation period for aluminum oxide growth. Only minor silicon oxide formation is found in 380°C TMA/D<sub>2</sub>O ALD on 496°C NSi, and no evident silicon oxide interlayer formation can be found on 605°C NSi.

## References

1. Frank, Martin, Kai Wolter, Norbert Magg, Michael Heemeier, Ralf Kuhnemuth, Marcus Baumer, and Hans-Joachim Freund, *Phonons of clean and metal-modified oxide films: an infrared and HREELS study*. Surface Science, 2001. **492**(3): p. 270-284.
2. Frank, M. M., Y. J. Chabal, M. L. Green, A. Delabie, B. Brijs, G. D. Wilk, M. Y. Ho, E. B. O. da Rosa, I. J. R. Baumvol, and F. C. Stedile, *Enhanced initial growth*

- of atomic-layer-deposited metal oxides on hydrogen-terminated silicon*. Applied Physics Letters, 2003. **83**(4): p. 740-742.
3. Lanford, W.A. and M.J. Rand, *The hydrogen content of plasma-deposited silicon nitride*. Journal of Applied Physics, 1978. **49**(4): p. 2473-2477.
  4. Huang, Lin, K. W. Hipps, J. T. Dickinson, Ursula Mazur, and X. D. Wang, *Structure and composition studies for silicon nitride thin films deposited by single ion beam sputter deposition*. Thin Solid Films, 1997. **299**(1-2): p. 104-109.
  5. Shi, X., M. Shriver, Z. Zhang, T. Higman, and S. A. Campbell, *Properties of high-k/ultrahigh purity silicon nitride stacks*. Journal of Vacuum Science & Technology A: Vacuum, Surfaces, and Films, 2004. **22**(4): p. 1146-1151.
  6. Yokoyama, S., N. Ikeda, K. Kajikawa, and Y. Nakashima, *Atomic-layer selective deposition of silicon nitride on hydrogen-terminated Si surfaces*. Applied Surface Science, 1998. **132**: p. 352-356.
  7. Mahan, A. H., A. C. Dillon, L. M. Gedvilas, D. L. Williamson, and J. D. Perkins, *Properties of thin film silicon nitride deposited by hot wire chemical vapor deposition using silane, ammonia, and hydrogen gas mixtures*. Journal of Applied Physics, 2003. **94**(4): p. 2360-2367.
  8. Bandet, J., B. Despax, and M. Caumont, *Nitrogen bonding environments and local order in hydrogenated amorphous silicon nitride films studied by Raman spectroscopy*. Journal of Applied Physics, 1999. **85**(11): p. 7899-7904.
  9. Dupont, G., H. Caquineau, B. Despax, R. Berjoan, and A. Dollet, *Structural properties of N-rich a-Si-N:H films with a low electron-trapping rate*. Journal of Physics D-Applied Physics, 1997. **30**(7): p. 1064-1076.
  10. Ishidzuka, S., Y. Igari, T. Takaoka, and I. Kusunoki, *Nitridation of Si(100) surface with NH<sub>3</sub>*. Applied Surface Science, 1998. **130-132**: p. 107-111.
  11. de Almeida, R.M.C. and I.J.R. Baumvol, *Reaction-diffusion model for thermal growth of silicon nitride films on Si*. Physical Review B, 2000. **62**(24): p. R16255 LP - R16258.
  12. Watanabe, T., M. Sakuraba, T. Matsuura, and J. Murota. *Atomic-order thermal nitridation of Si(100) and subsequent growth of Si*. in *The 47th international symposium: Vacuum, thin films, surfaces/interfaces, and processing NAN06*. 2001. Boston, Massachusetts (USA): AVS.
  13. Zaibi, M.A., C.A. Sebenne, and J.P. Lacharme, *Temperature-activated reactions of H<sub>2</sub>O and NH<sub>3</sub> with H-passivated Si(111) surfaces*. Surface Review and Letters, 2001. **8**(1-2): p. 25-31.
  14. Choi, K.J., J.H. Kim, and S.G. Yoon, *Plasma nitration of HfO<sub>2</sub> gate dielectric in nitrogen ambient for improvement of TaN/HfO<sub>2</sub>/Si performance*. Electrochemical and Solid State Letters, 2004. **7**(10): p. F59-F61.
  15. Kim, J.W. and H.W. Yeom, *Thermal decomposition of NH<sub>3</sub> on the Si(1 0 0) surface*. Surface Science, 2003. **546**(2-3): p. L820-L828.
  16. Shih, An, Shin-Hung Yeh, Si-Chen Lee, and T. R. Yang, *Structural differences between deuterated and hydrogenated silicon nitride/oxy-nitride*. Journal of Applied Physics, 2001. **89**(10): p. 5355-5361.
  17. Tsu, D.V., G. Lucovsky, and M.J. Mantini, *Local atomic structure in thin films of silicon nitride and silicon diimide produced by remote plasma-enhanced chemical-vapor deposition*. Physical Review B, 1986. **33**(10): p. 7069 LP - 7076.

18. Firon, M., C. Bonnelle, and A. Mayeux, *Characterization of silicon oxynitride thin films by infrared reflection absorption spectroscopy*. Journal of Vacuum Science & Technology a-Vacuum Surfaces and Films, 1996. **14**(4): p. 2488-2492.
19. Fattal, E., M. R. Radeke, G. Reynolds, and E. A. Carter, *Ab initio structure and energetics for the molecular and dissociative adsorption of NH<sub>3</sub> on Si(100)-2 x 1*. Journal of Physical Chemistry B, 1997. **101**(43): p. 8658-8661.
20. Widjaja, Y. and C.B. Musgrave, *A density functional theory study of the nonlocal effects of NH<sub>3</sub> adsorption and dissociation on Si(100)-(2 x 1)*. Surface Science, 2000. **469**(1): p. 9-20.
21. Widjaja, Y., M.M. Mysinger, and C.B. Musgrave, *Ab initio study of adsorption and decomposition of NH<sub>3</sub> on Si(100)-(2x1)*. Journal of Physical Chemistry B, 2000. **104**(11): p. 2527-2533.
22. Queeney, K.T., Y.J. Chabal, and K. Raghavachari, *Role of interdimer interactions in NH<sub>3</sub> dissociation on Si(100)-(2 x 1)*. Physical Review Letters, 2001. **86**(6): p. 1046-1049.
23. Feijoo, D., Y.J. Chabal, and S.B. Christman, *Silicon wafer bonding studied by infrared absorption spectroscopy*. Applied Physics Letters, 1994. **65**(20): p. 2548-2550.
24. Weldon, M. K., Y. J. Chabal, D. R. Hamann, S. B. Christman, E. E. Chaban, and L. C. Feldman, *Physics and chemistry of silicon wafer bonding investigated by infrared absorption spectroscopy*. Journal of Vacuum Science & Technology B, 1996. **14**(4): p. 3095-3106.
25. Weldon, M. K., V. E. Marsico, Y. J. Chabal, D. R. Hamann, S. B. Christman, and E. E. Chaban, *Infrared spectroscopy as a probe of fundamental processes in microelectronics: Silicon wafer cleaning and bonding*. Surface Science, 1996. **368**: p. 163-178.
26. Chabal, Y.J., *Infrared study of the chemisorption of hydrogen and water on vicinal Si(100) 2 x 1 surfaces*. Journal of Vacuum Science & Technology A: Vacuum, Surfaces, and Films, 1985. **3**(3): p. 1448-1451.
27. Chabal, Y.J. and K. Raghavachari, *New Ordered Structure for the H-Saturated Si(100) Surface: The (3 x 1) Phase*. Physical Review Letters, 1985. **54**(10): p. 1055 LP - 1058.
28. Nakanishi, K., *Infrared absorption spectroscopy, practical*. 1962: San Francisco, Holden-Day, 1962. 233.
29. Kim, J. W., H. W. Yeom, K. J. Kong, B. D. Yu, D. Y. Ahn, Y. D. Chung, C. N. Whang, H. Yi, Y. H. Ha, and D. W. Moon, *Spontaneous N Incorporation onto a Si(100) Surface*. Physical Review Letters, 2003. **90**(10): p. 106101.
30. Ghoshtagore, R.N., *Diffusion of Nickel in Amorphous Silicon Dioxide and Silicon Nitride Films*. Journal of Applied Physics, 1969. **40**(11): p. 4374-4376.
31. Gupta, D., K. Vieregge, and K.V. Srikrishnan, *Copper diffusion in amorphous thin films of 4% phosphorus-silicate glass and hydrogenated silicon nitride*. Applied Physics Letters, 1992. **61**(18): p. 2178-2180.
32. D. Gupta, P.S.H., *Diffusion Phenomena in Thin Films and Microelectronic Materials*. 1988: Noyes, New Jersey, 1988.



33. Brewer, R. T., M. T. Ho, K. Z. Zhang, L. V. Goncharova, D. G. Starodub, T. Gustafsson, Y. J. Chabal, and N. Moumen, *Ammonia pretreatment for high-kappa dielectric growth on silicon*. Applied Physics Letters, 2004. **85**(17): p. 3830-3832.
34. Chowdhuri, A. R., C. G. Takoudis, R. F. Klie, and N. D. Browning, *Metalorganic chemical vapor deposition of aluminum oxide on Si: Evidence of interface SiO<sub>2</sub> formation*. Applied Physics Letters, 2002. **80**(22): p. 4241-4243.
35. Desai, S. R., H. B. Wu, C. M. Rohlffing, and L. S. Wang, *A study of the structure and bonding of small aluminum oxide clusters by photoelectron spectroscopy: Al<sub>x</sub>O<sub>y</sub>- (x=1-2, y=1-5)*. Journal of Chemical Physics, 1997. **106**(4): p. 1309-1317.
36. Davydov, A., *Molecular spectroscopy of oxide surfaces*, ed. N.T. Sheppard. 2003: Wiley, c2003. 668.
37. Dillon, A. C., A. W. Ott, J. D. Way, and S. M. George, *Surface-Chemistry of Al<sub>2</sub>O<sub>3</sub> Deposition Using Al(Ch<sub>3</sub>)<sub>3</sub> and H<sub>2</sub>O in a Binary Reaction Sequence*. Surface Science, 1995. **322**(1-3): p. 230-242.
38. Frank, M.M., Y.J. Chabal, and G.D. Wilk, *Nucleation and interface formation mechanisms in atomic layer deposition of gate oxides*. Applied Physics Letters, 2003. **82**(26): p. 4758-4760.
39. Bermudez, V.M., R.L. Rubinovitz, and J.E. Butler, *Study of the vibrational modes of subsurface oxygen on Al(111) using diode laser infrared reflection--absorption spectroscopy*. Journal of Vacuum Science & Technology A: Vacuum, Surfaces, and Films, 1988. **6**(3): p. 717-721.
40. Ning, Jiang, S. Xu, K. N. Ostrikov, Chai Jianwei, Li Yinan, Koh Mei Ling, and S. Lee, *Synthesis and structural properties of Al---C---N---O composite thin films*. Thin Solid Films, 2001. **385**(1-2): p. 55-60.
41. Misra, A., H. D. Bist, M. S. Navati, R. K. Thareja, and J. Narayan, *Thin film of aluminum oxide through pulsed laser deposition: a micro-Raman study*. Materials Science and Engineering B-Solid State Materials for Advanced Technology, 2001. **79**(1): p. 49-54.
42. Wadayama, T., K. Takeuchi, K. Mukai, T. Tanabe, and A. Hatta, *Infrared spectroscopic study of dimethylaluminum-hydride adsorption on oxidized, hydrogen-terminated, and reconstructed Si surfaces*. Journal of Vacuum Science & Technology a-Vacuum Surfaces and Films, 2002. **20**(2): p. 299-304.
43. Bellamy, L.J., *The infra-red spectra of complex molecules*. 3rd ed. 1975: London : Chapman and Hall ; New York : Wiley,. 433.
44. Koji Nakanishi, P.H.S., *Infrared absorption spectroscopy*. 2 ed. 1977: San Francisco, Holden-Day, 1977. 286.
45. Puurunen, R.L., A. Root, P. Sarv, M.M. Viitanen, H.H. Brongersma, M. Lindblad, and A.O.I. Krause, *Growth of Aluminum Nitride on Porous Alumina and Silica through Separate Saturated Gas-Solid Reactions of Trimethylaluminum and Ammonia*. Chem. Mater., 2002. **14**(2): p. 720-729.
46. Puurunen, R.L., M. Lindblad, A. Root, and A.O.I. Krause, *Successive reactions of gaseous trimethylaluminum and ammonia on porous alumina*. Physical Chemistry Chemical Physics, 2001. **3**(6): p. 1093-1102.
47. Puurunen, R.L., A. Root, S. Haukka, E.I. Iiskola, M. Lindblad, and A.O.I. Krause, *IR and NMR Study of the Chemisorption of Ammonia on Trimethylaluminum-Modified Silica*. J. Phys. Chem. B, 2000. **104**(28): p. 6599-6609.

48. Puurunen, R.L., A. Root, P. Sarv, S. Haukka, E.I. Iiskola, M. Lindblad, and A.O.I. Krause, *Growth of aluminum nitride on porous silica by atomic layer chemical vapour deposition*. Applied Surface Science, 2000. **165**(2): p. 193-202.
49. Alpert, N.L., W.E. Keiser, and H.A. Szymanski, *IR; theory and practice of infrared spectroscopy*. 2d ed. 1970, New York: Plenum Press. 380.
50. Bermudez, V.M., *Study of the chemistry of NH<sub>3</sub> on aluminum nitride and oxynitride under steady-state conditions using external-reflection infrared spectroscopy*. Thin Solid Films, 1999. **347**(1-2): p. 195-200.
51. McNeil, L.E.G., M.; French, R.H., *Vibrational spectroscopy of aluminum nitride*. Journal of the American Ceramic Society, 1993. **76**(5): p. 1132-1136.
52. Russell, J.N., V.M. Bermudez, and A. Leming, *Low temperature growth of AlN(0001) on Al(111) using hydrazoic acid (HN<sub>3</sub>)*. Journal of Vacuum Science & Technology a-Vacuum Surfaces and Films, 1996. **14**(3): p. 908-912.
53. Karch, K. and F. Bechstedt, *Ab initio lattice dynamics of BN and AlN: Covalent versus ionic forces*. Physical Review B, 1997. **56**(12): p. 7404 LP - 7415.
54. Davydov, V. Yu., Yu. E. Kitaev, I. N. Goncharuk, A. N. Smirnov, J. Graul, O. Semchinova, D. Uffmann, M. B. Smirnov, A. P. Mirgorodsky, and R. A. Evarestov, *Phonon dispersion and Raman scattering in hexagonal GaN and AlN*. Physical Review B, 1998. **58**(19): p. 12899 LP - 12907.
55. Odriozola, J.A., *Surface characterization of nitrides and oxynitrides of groups IIIA and IVA*. Journal of the European Ceramic Society, 1997. **17**(15-16): p. 1989-1999.

## **CHAPTER 3**

### **INFRARED ABSORPTION STUDY OF TEMAH**

TEMAH (trakis-ethyl-methyl-amido hafnium), a yellowish liquid compound at room temperature, will be used for the hafnium source in Hf oxide ALD growth. Fourier transform infrared (FTIR) absorption spectra of TEMAH vapor, and of its products resulting from exposures to O<sub>2</sub>, D<sub>2</sub>O, H<sub>2</sub>O and ozone have been examined, in conjunction with Density Functional Theory (DFT) based calculations and a simple wavenumber-linear scaling scheme. The suitable substrate temperature window for ALD deposition by using TEMAH is also determined by IR absorption spectra as a preliminary knowledge for Hf oxide ALD on silicon surfaces in the next chapter.

#### **3.1 TEMAH Gas Phase IR Spectrum**

Transmission Fourier transform infrared absorption (FTIR) is a convenient non-destructive technique to characterize gas phase molecules. In this section, the TEMAH gas phase transmission FTIR absorption spectrum is compared to the results of two types of Density Functional Theories (DFT), the DFT/B3LYP[1-4]/LANL2DZ[5] and the DFT/PBE/modified TZVP[6-9], using the Wavenumber-Linear-Scaling (WLS)[10-14] scheme to correct the systematic errors associated with the theory. In this manner, the atomic motions associated with the characteristic normal modes can be identified and related to the major IR absorption lines. For the C-H stretching modes ( $\nu(\text{C-H})$ ), it is necessary to consider the role of Fermi resonances between the stretch and the overtone of the bending vibrations.

Density functional theory (DFT)-based calculations were performed to determine the structure and vibrational properties of the precursors and possible reaction products. Two sets of calculations were carried out. The first uses a Gaussian 98[15] package with DFT/B3LYP exchange-correlation functionals [1-4], LANL2DZ basis sets and pseudo-potential for Hf [Kr], 4d10, 4f14 core electrons [5]. The other uses a Gaussian03 package[16] with gradient corrected PBE functionals [7], TZVP basis sets[8, 9] and Stuttgart pseudo-potential for Hf 60 core electrons [6]. The modes calculated with DFT are grouped in bands comprising modes that are both close in frequency (within a few wavenumbers) and have similar vibrational motion (i.e. atomic displacements). The resulting bands are broadened by the experimental resolution ( $4\text{cm}^{-1}$ ). These bands, labeled  $\nu_{\text{calculated}}$ , are then compared to those in the measured spectra, labeled  $\nu_{\text{observed}}$ . Since the calculations do not include anharmonicity, the calculated vibration peak mode frequencies deviate from observed frequencies by a scaling factor (a), defined to first order as  $\nu_{\text{observed}} = b \nu_{\text{calculated}} + a \nu_{\text{calculated}}^2$  in the WLS scheme [10-14]. With this two-parameter scaling scheme, the empirical anharmonicity coefficient is  $\chi = (1/2)[(1-b) - a \nu_{\text{calculated}}]$  up to first order of  $\nu_{\text{calculated}}$ . These parameters are obtained by matching the twelve strongest modes among the observed TEMAH IR absorption spectrum to the strongest DFT calculated IR active modes. The least squares fit yields:  $a = -1.89078 \times 10^{-5} \pm 2.28993 \times 10^{-6} \text{ cm}$ ,  $b = 1.00429 \pm 0.0049$  for B3LYP/LANL2DZ(5D,7F), and  $a = -2.1472 \times 10^{-5} \pm 1.63256 \times 10^{-6} \text{ cm}$ ,  $b = 1.03476 \pm 0.0035$  for PBE/modified TZVP through  $\nu_{\text{observed}}/\nu_{\text{calculated}}$  versus  $\nu_{\text{calculated}}$  plot (**Fig. 3-1(a)**).

In the following, the assignment of observed TEMAH vibrational bands is performed on the basis of comparison of observed EtMeNH and calculated TEMAH

bands. The scaled DFT calculated IR mode frequencies are in good agreement with observed TEMAH IR absorption frequencies (the maximum error is  $28\text{ cm}^{-1}$  for the observed  $1454\text{ cm}^{-1}$  mode matching with WLS scaled B3LYP calculated  $1501\text{ cm}^{-1}$  mode and  $25\text{ cm}^{-1}$  for the observed  $2969\text{ cm}^{-1}$  mode matching with WLS scaled PBE calculated  $2944\text{ cm}^{-1}$  mode) and the relative intensities of modes are in great similarity to the observed spectrum except for the C-H stretching region (**Fig. 3-1(b)**). In the low frequencies part ( $<2000\text{ cm}^{-1}$ ), we can notice that improving the basis set results in a narrower scattering of calculated frequencies *vs.* observed ones. However, in the C-H stretching region, the anharmonicity effects are larger and improving the basis set shows little effect. Most of the errors can be attributed to the difference in anharmonicity between modes, which is related to details of the generalized potential surface. Even an improved anharmonicity coefficient function derived by two-parameter fitting is not able to account for all the anharmonicity effects.

TEMAH has four ethyl-methyl-amino ( $-\text{N}(\text{CH}_3)(\text{C}_2\text{H}_5)$ ) ligands tetrahedrally bonded to a hafnium atom. (see **Fig. 0-1**) Comparing the spectrum of the TEMAH vapor with that of N-Ethylmethylaniline ( $\text{EtMeNH}$  (CAS # 624-78-2; ethyl group  $-\text{C}_2\text{H}_5$  denoted by “Et” and methyl group  $-\text{CH}_3$  denoted by “Me”) [17] (see **Table 3-1**), it is apparent that there is a great similarity between the modes of the alkyl-amino group ( $-\text{N}(\text{Et})(\text{Me})$ ) and those of  $\text{EtMeNH}$ , though the relative absorption intensities of modes are different. This is because the alkyl-amino groups are decoupled due to the heavy mass of the hafnium atom (atomic weight  $\sim 178.5$ ). This result suggests that the TEMAH vapor delivered by ultra-pure  $\text{N}_2$  in the chamber is not decomposed. Besides the obvious difference of  $\nu(\text{NH}) \sim 3330\text{ cm}^{-1}$  between TEMAH and  $\text{EtMeNH}$ , the main discrepancy between the two

molecules is the lack of a mode in EtMeNH corresponding to the TEMAH  $565\text{ cm}^{-1}$  mode. This suggests that the  $565\text{ cm}^{-1}$  mode should be related to vibrational modes involving the tetrahedral Hf-N<sub>4</sub> structure. The DFT calculations of the normal modes involving motions of this core structure confirm this point. The similarity between TEMAH and EtMeNH in the  $2850\text{-}2750\text{ cm}^{-1}$  spectral region (assigned to the C-H stretching of alkylamino groups) confirms the existence of alkylamino ligands. [17-20]

DFT calculations also provide quantitative information for mode assignment, which is particularly important because assignments cannot be reached by merely consulting published work on similar molecules. For example, one would assign the peak at  $2920\text{ cm}^{-1}$  to the CH<sub>2</sub> asymmetric stretching mode of the ethyl groups according to the stated CH<sub>3</sub> and CH<sub>2</sub> asymmetric stretching frequency ranges of  $\sim 2992\text{-}2952\text{ cm}^{-1}$  ( $\nu_a(\text{CH}_3)$ ) and  $\sim 2950\text{-}2916\text{ cm}^{-1}$  ( $\nu_a(\text{CH}_2)$ ) given in Ref. 36. However DFT calculations show this mode is related to CH<sub>3</sub> asymmetric stretch vibration of the methyl groups, not to the ethyl groups. Additionally, the two peaks of very strong intensities at  $1372$  and  $1349\text{ cm}^{-1}$  falling within the characteristic frequency ranges are either for general CH<sub>3</sub> symmetric bending  $\delta_s(\text{CH}_3)$  or for CH<sub>2</sub> scissoring in ethyl groups. DFT calculations can resolve that the mode at  $1372\text{ cm}^{-1}$  is associated to general CH<sub>3</sub> symmetric bending  $\delta_s(\text{CH}_3)$  accompanied with CH<sub>2</sub> scissoring in ethyl groups and the mode at  $1349\text{ cm}^{-1}$  is associated to CH<sub>3</sub> asymmetric bending  $\delta_a(\text{CH}_3)$  in ethyl groups accompanied with CH<sub>3</sub> symmetric bending  $\delta_s(\text{CH}_3)$  in methyl groups. The characteristic frequency overlap of varying characteristic frequency range for C-N stretching ( $\sim 1230\text{-}1130\text{ cm}^{-1}$ ) and C-C skeleton structure vibration range ( $\sim 1300\text{-}1100\text{ cm}^{-1}$ ) due to the comparable atomic masses and bonding strengths makes unambiguous mode assignment in  $1300\text{-}1100\text{ cm}^{-1}$

frequency range impossible. The DFT calculations have contributed to make the unambiguous mode assignment for TEMAH in this frequency range as listed in **Table 3-1**.

A group of weak peaks  $\sim 2730\text{-}2600\text{cm}^{-1}$  containing peaks 2727, 2699, 2680, 2649 and  $2606\text{cm}^{-1}$  and a very weak mode  $\sim 1595\text{cm}^{-1}$  are found without any corresponding WLS scaled calculation modes around the frequency ranges. They can be the overtones of observed  $\delta(\text{C-H})\sim 1371, 1348, 1310\text{cm}^{-1}$  (the frequency ranges of anharmonicity corrected overtone  $\sim 2764\text{-}2691\text{ cm}^{-1}$ ,  $2715\text{-}2659\text{cm}^{-1}$  and  $2635\text{-}2588\text{cm}^{-1}$  respectively) and ethyl group skeleton twisting  $\tau(\text{C}_2\text{H}_5)\sim 792\text{cm}^{-1}$ . [NOTE: as a reasonable guess, peak 2727, 2699/2680 and  $2606\text{cm}^{-1}$  can be the overtone of 1372, 1349 and  $1310\text{cm}^{-1}$  respectively.] The comparison of two DFT calculations in **Fig. 3-1(a)** shows PBE calculation has better WLS fitting than that of B3LYP. The most obvious deviation of B3LYP calculation from WLS fitting line is found in the calculated frequency range  $\sim 1550\text{-}1450\text{cm}^{-1}$ , which is equivalent to the scaled frequency  $\sim 1500\text{-}1400\text{cm}^{-1}$  associated with general characteristic C-H bending mode ( $\delta(\text{CH}_x)$ ). The data points in red solid squares for B3LYP calculation in calculated frequency range  $\sim 1550\text{-}1450\text{cm}^{-1}$  fall farther off the B3LYP linear fitting than the solid triangles for PBE calculation do. In addition, as shown in Table 3-1, the B3LYP scaled calculation frequencies ( $1501$  and  $1488\text{cm}^{-1}$ ) are higher than the PBE scaled calculation ( $1469\text{cm}^{-1}$ ) and observed frequency ( $1473\text{cm}^{-1}$ ) in this frequency range. Therefore the correct motion assignment for observed IR peaks for  $\text{CH}_3$  and  $\text{CH}_2$  C-H bending ( $\delta(\text{CH}_x)$ ) in  $1473\text{-}1300\text{cm}^{-1}$  region should be as following (and denoted as the PBE vibration motion in the fourth column of **Table 3-1**): peak  $1473\text{cm}^{-1}$  is mainly associated with  $\delta_a(\text{CH}_3)$  in the ethyl groups of ethyl-methyl-amino ligand, and peak  $1420\text{ cm}^{-1}$ ,  $1442\text{ cm}^{-1}$  and  $1454\text{cm}^{-1}$  are assigned respectively as  $\delta_s(\text{CH}_3)$

in the ethyl and methyl groups combining ethyl CH<sub>2</sub> wagging, ethyl and methyl  $\delta_s(\text{CH}_3)$  combining ethyl CH<sub>2</sub> scissoring, and ethyl and methyl CH<sub>3</sub>  $\delta_a(\text{C-H})$  combining ethyl CH<sub>2</sub> scissoring.

Comparing the scaled PBE DFT calculated mode frequencies with the observed FTIR peak frequencies, there finds an anomalous inconsistency of relative intensity at the lower frequency part of C-H stretching region  $\sim 3000\text{-}2750\text{ cm}^{-1}$ . Based on the anharmonicity consideration of simple molecule, the scaling form in terms of anharmonicity coefficient  $\chi$  is:  $\nu_{\text{observed}} = \nu_{\text{calculated}} - 2\chi\nu_{\text{calculated}}$ . The extraordinary high relative absorption of PBE DFT calculation at  $\sim 2799\text{ cm}^{-1}$  is not observed in experiment spectrum. (**Fig. 3-2**) Additionally the relative intensities of scaled calculated modes at  $2858$  and  $2828\text{ cm}^{-1}$  are too small to be consistent with experiment spectrum. Both above concerns motivate the consideration of Fermi Resonance mechanism [18, 21] to account the inconsistency. Our Fermi resonance mechanism scheme suggests the overtone of observed  $\delta_s(\text{C-H})_{\text{CH}_3\text{-N}}$   $1420\text{ cm}^{-1}$  (within the frequency range  $2858\text{-}2788\text{ cm}^{-1}$ , obtained by  $\nu_{\text{Overtone}} = 2\nu_{\text{calculated}} - 6\chi\nu_{\text{calculated}}$ ,  $\nu_{\text{calculated}} = 1438\sim 1409\text{ cm}^{-1}$  and  $\chi_{1420} = 0.017763\sim -0.00606$ ) couples with the predicted unperturbed extraordinary strong mode around  $2799\text{ cm}^{-1}$  via Fermi resonance mechanism to generate a mode nearby  $2850\text{-}2830\text{ cm}^{-1}$  ( $2858\text{ cm}^{-1}$ ) and the other unknown but weaker mode [NOTE: This weaker mode frequency needs to be lower than the extraordinary strong mode, and therefore  $2649\text{ cm}^{-1}$  can be a potential candidate.], and thus cause the intensity enhancement of mode  $2875\text{ cm}^{-1}$  and disappearance of the extraordinarily intense  $2799\text{ cm}^{-1}$   $\nu_s(\text{C-H})_{\text{CH}_3\text{-N}}$  mode predicted by DFT calculation.



Table 3-1 Comparison of major observed TEMAH, EtMeNH and scaled DFT calculated peak modes

| TEMAH                         | EtMeNH*   | Scaled<br>(B3LYP)<br>PBE | Vibration Motion by<br>(B3LYP)<br>PBE **  |
|-------------------------------|-----------|--------------------------|---|
|                               |           | 3330(m)                  |   |
| 2969                          | 2970(s)   | (2957)<br>2944           | (Et-CH <sub>3</sub> asym str.)<br>Et-CH <sub>3</sub> asym str.  |
| 2938                          | 2940sh(s) |                          |   |
| 2920<br>sh(m)                 |           | (2916)<br>2920           | (Me /Et-CH <sub>3</sub> and Et-CH <sub>2</sub> asym str.)<br>Me asym str.   |
| 2875                          | 2870(w)   | (2880)<br>2877           | (Et-CH <sub>3</sub> sym str./ Et-CH <sub>2</sub> and Me asym str.)<br>Et-CH <sub>3</sub> sym str./ Me asym str.   |
| 2858                          |           | (2858)<br>2857           | (Me asym str.)<br>Et-CH <sub>2</sub> asym str./Et-CH <sub>3</sub> asym str.   |
| 2828                          |           | (2830)<br>2837           | (Et-CH <sub>2</sub> asym str./ Et-CH <sub>3</sub> and Me asym str.)<br>Me asym str./Et-CH <sub>x</sub> sym str.   |
|                               |           | (2815)<br>2799           | (2-Me sym str.)<br>(4-Me sym str.)  |
| 2788                          | 2790(s)   | (2804(sh))<br>2787(sh)   | (Et-CH <sub>2</sub> sym str.)<br>Et-CH <sub>2</sub> and Me sym str.   |
|                               |           | 2740(m)                  |   |
| 2730-<br>2600(vw)<br>1595(vw) |           |                          | Overtones   |
|                               |           | (1501,<br>1488)          | (Me/Et-CH <sub>3</sub> asym bd./ Et-CH <sub>2</sub> sym bd.)  |
| 1473(m)                       | 1470sh(s) | (1475)<br>1469           | (Me/Et-CH <sub>3</sub> asym bd. / Et-CH <sub>2</sub> sym bd.)<br>Me/Et-CH <sub>3</sub> asym bd./ Et-CH <sub>2</sub> sym bd.   |
| 1454(m)                       | 1450(s)   | (1467)<br>1449           | (Me and Et-CH <sub>3</sub> asym bd./ Et-CH <sub>2</sub> sym bd.)<br>Me and Et-CH <sub>3</sub> asym bd./ Et-CH <sub>2</sub> sym bd.  |
| 1441(m)                       |           | (1438)<br>1434           | (Me sym. bd./Et-CH <sub>3</sub> asym. bd. and Et-CH <sub>2</sub> sym bd.)<br>Me and Et-CH <sub>3</sub> asym bd./ Et-CH <sub>2</sub> sym bd.                                     |
| 1420(m)                       | 1420sh(m) | 1423                     | Me sym bd./ Et-CH <sub>2</sub> sym bd. and Et-CH <sub>3</sub> asym bd.  |
| 1372                          |           | (1392)<br>1359           | (Et-CH <sub>3</sub> and CH <sub>2</sub> sym bd./ Me sym bd.)<br>Et-CH <sub>3</sub> sym bd. and CH <sub>2</sub> wag./Et-C-C str. and Me asym bd.                                 |
| 1349                          | 1350(w)   | (1358)<br>1340           | (Et-CH <sub>2</sub> wag. and Et-CH <sub>3</sub> asym bd./Me sym bd.)<br>Et-CH <sub>2</sub> wag./ Et-CH <sub>3</sub> and Me sym bd.  |
| 1310(m)                       |           | (1313)<br>1304           | (Et-CH <sub>2</sub> tw. CH <sub>3</sub> asym bd./ Me sym str./ C-N-C sym str. /<br>Hf-N str.)<br>Et-CH <sub>2</sub> tw. CH <sub>3</sub> asym bd. C-N-C asym str. / Hf-N str.    |
|                               |           | 1270(w)                  |   |
| 1213                          | 1220(w)   | (1218)<br>1208           | (Et-CH <sub>2</sub> tw. CH <sub>3</sub> asym bd. /Me asym str./C-N-C sym str. /<br>Hf-N str.)<br>CH <sub>3</sub> asym bd. C-N-C sym str. and Et-CH <sub>2</sub> tw. / Hf-N str. |
| 1157                          | 1150(w)   | (1150)<br>1161           | (CH <sub>x</sub> asym bd./ Et-Me-amino C-N-C-C asym str./ HfN4<br>bd.)<br>(CH <sub>x</sub> asym bd./ Et-Me-amino C-N-C-C asym str./ HfN4<br>bd.)                                |

|            |         |                   |   |
|------------|---------|-------------------|---|
| 1114(m)    | 1120(m) | (1108)<br>1104    | (CH <sub>x</sub> asym bd. /Et-Me-amino C-N-C-C asym str./Hf-N bd.)<br>CH <sub>x</sub> asym bd. /C-N-C wag./Hf-N bd.   |
| 1084(m)    | 1090(w) | (1088)<br>1080    | (Me and Et-CH <sub>3</sub> asym bd. /Et-CH <sub>2</sub> wag. / Et-Me-amino C-N-C-C skeleton bd.)<br>Me and Et-CH <sub>2</sub> asym bd. /Et-Me-amino skeleton tw.  |
| 1056(m)    | 1060(m) | (1061)<br>1055    | (Me and Et-CH <sub>3</sub> asym bd. /Et-CH <sub>2</sub> wag. / Et-Me-amino C-N-C-C skeleton str.)<br>Me and Et-CH <sub>3</sub> asym bd. /Et-CH <sub>2</sub> wag. / Et-Me-amino skeleton str./ Hf-N <sub>4</sub> bd. |
| 1045(m)    |         |                   |   |
| 1014 sh(w) |         | (1029)            | (Et-Me-amino skeleton str./ Hf-N bd.)   |
| 980        | 990(w)  | (986, 971)<br>984 | (Et-Me-amino skeleton str./ Hf-N str.)<br>CH <sub>x</sub> asym bd. /Et-Me-amino skeleton str./ Hf-N str.  |
| 877        | 880(m)  | (871)<br>877      | (Et-Me-amino skeleton (Et C-C) str./ Hf-N <sub>4</sub> str.)<br>CH <sub>x</sub> asym bd./ N-Hf-N asym str.  |
| 850(m)     |         |                   |   |
| 792(m)     |         | (802)<br>791      | (Et skeleton tw.)<br>Et skeleton tw.  |
| 565        |         | (564)<br>566      | (C-N-C sym bd./ CH <sub>x</sub> wag./ Hf-N <sub>4</sub> str.)<br>CH <sub>x</sub> wag./ C-N-C sym bd./ Hf-N <sub>4</sub> str.  |
| 460(s)     |         |                   |   |

\*Aldrich-Sigma FTIR Spectra (s: strong; sh: shoulder; vw: very weak; w: weak; m: medium)

\*\*asym= asymmetric; sym= symmetric; str.=stretching; bd.= bending; wag.=wagging; tw.=twisting; Me= methyl group; Et= ethyl group; CH<sub>x</sub>=All alkyl group

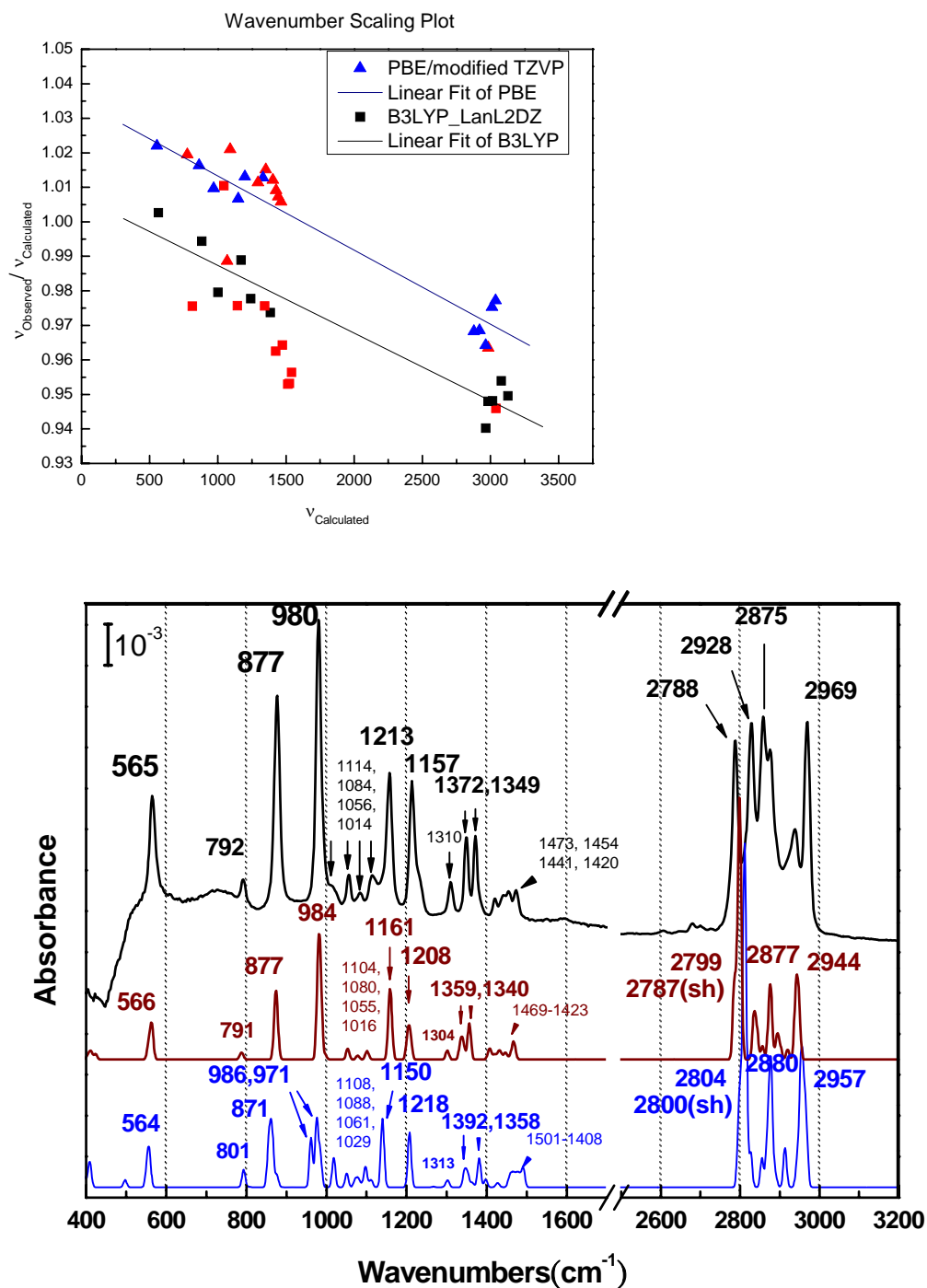


Fig. 3-1 (a)  $\nu_{\text{Observed}} / \nu_{\text{Calculated}}$  scaling fitting plots and fitting lines. (solid squares and triangles in red are minor peaks not included for linear fitting) (b) Top in black is the observed TEMAH FTIR absorption spectrum, the middle in brown is the WLS scaled DFT/PBE/modified TZVP calculation peak profile, and the bottom is the WLS scaled DFT/ B3LYP/LANL2DZ(5D,7F) calculation peak profile. DFT calculation peak profiles are made by superposing all 144  $4\text{cm}^{-1}$ -wide Gaussian shape functions parametrized by the DFT calculated intensities and WLS scaled frequencies. All the major peak frequencies are denoted therein.

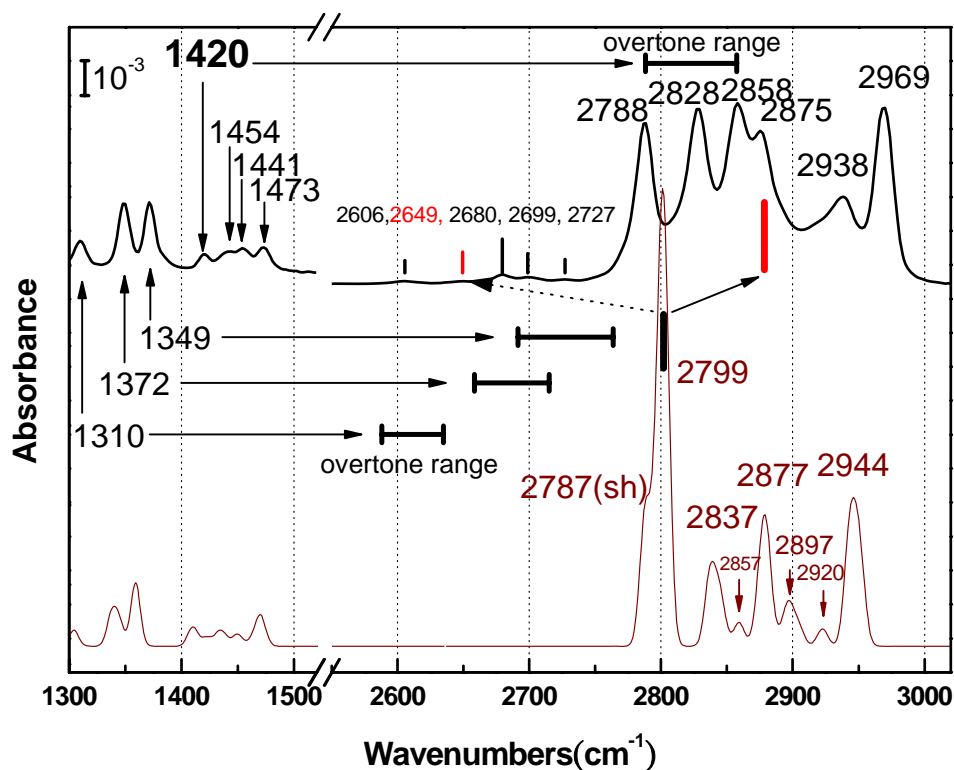


Fig. 3-2 Local  $\nu(\text{C-H})$  and  $\delta(\text{C-H})$  details of the observed TEMAH FTIR absorption spectrum (top in black) and the WLS scaled DFT/PBE/modified TZVP calculation peak profile (bottom in brown). The overtone of TEMAH  $1420\text{cm}^{-1}$  C-H bending mode couples with the DFT-suggested  $2799\text{cm}^{-1}$  C-H stretching mode through Fermi resonance mechanism to eliminate the extraordinary strong DFT-suggested band and enhance the absorption bands around  $2875\text{cm}^{-1}$  (and possibly  $2649\text{cm}^{-1}$ ).

### 3.2 TEMAH Gas Phase Reaction Products

The nature of the TEMAH gas is examined after introduction of  $\text{D}_2\text{O}$  vapor,  $\text{H}_2\text{O}$  vapor,  $\text{O}_2$  gas or ozone/ $\text{O}_2$  gas. The FTIR spectra of both reactants and products are thus obtained. By suitably subtracting the spectrum of pure TEMAH gas and of the other oxygen source reactant, the absorption lines of the major reactants can be removed from the measured spectrum of the original mixture. The spectrum of the reaction products can thus be obtained. In summary, these “processed” FTIR absorbance spectra of reaction

products only are analyzed and discussed.

The IR absorption spectra of mixtures of TEMAH vapor with different oxygen sources, such as D<sub>2</sub>O (H<sub>2</sub>O), O<sub>2</sub> and ozone/O<sub>2</sub>, can provide qualitative information to help identify their major reaction products and the relative TEMAH reactivity with these oxygen sources. To best detect the reaction products, the IR absorbance spectra of each gas phase reactant is subtracted from the spectrum of mixture, using a suitable subtraction coefficient  $\mu_{reactant}$  (i.e.  $Absorbance_{mixture} - \mu_{reactant} \times Absorbance_{reactant}$ ). This procedure essentially removes the component of the spectrum due to unreacted gases, yielding the features associated with the reaction products. For example, in **Fig. 3-3** the subtraction of D<sub>2</sub>O and H<sub>2</sub>O spectra from their mixture gives the IR absorption spectrum of their reaction product HOD. Thus, analysis of the mixture spectra obtained under controlled conditions makes it possible to determine the relative reactivity of TEMAH vapor with the various oxygen sources. The main results, summarized in **Fig. 3-4** indicate that oxygen gas (O<sub>2</sub>) is the least reactive oxidant to TEMAH vapor, as discussed below.

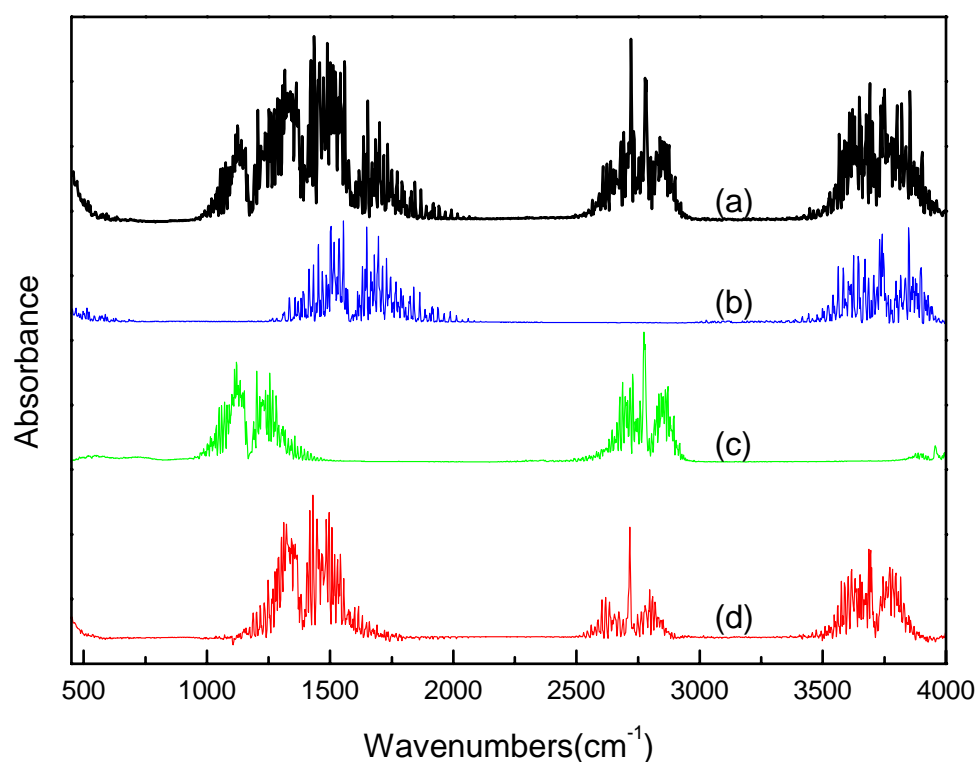


Fig. 3-3 Example of processing technique of absorbance spectrum subtraction: The subtraction result HOD absorbance spectrum (d) is obtained by subtracting the reactant, H<sub>2</sub>O (b) and D<sub>2</sub>O (c), absorbance spectra from the absorbance spectrum of D<sub>2</sub>O+H<sub>2</sub>O mixture (a).

### A. TEMAH Vapor Reaction with O<sub>2</sub>

**Fig. 3-4(a)** shows the spectrum of the TEMAH+O<sub>2</sub> mixture (enhanced atmospheric pressure) referenced to the pure TEMAH spectrum ( $\mu_{\text{TEMAH}}=1.1785$ ). The resulting spectrum does show modes that indicate reaction, but many are similar to what is observed for a TEMAH+H<sub>2</sub>O mixture (**Fig. 3-4(d)**). (However the IR absorption peak areas of the major bands in atmospheric pressure TEMAH+O<sub>2</sub> mixture are only about 1%-2% of those in atmospheric pressure TEMAH+D<sub>2</sub>O or TEMAH+H<sub>2</sub>O mixture) For instance, spectral features at 2969, 2805, 1460, 1380, 1130, 1040 and 725 cm<sup>-1</sup> are all

observed in spectrum **(d)** and will be discussed later. This observation suggests that the partial pressure of residual water molecules is high enough to react with TEMAH. In addition to these modes, there are peaks at  $\sim 1670$  and  $1694\text{cm}^{-1}$ . (They are not observed at lower pressure such as  $\sim 8.5$  Torr shown in spectrum **(c)**). These modes suggest that there are tertiary amide ( $\text{R}-(\text{C}=\text{O})-\text{N}(\text{R}_1\text{R}_2)$ ) or  $\text{R}-\text{O}-\text{N}=\text{O}$  compounds in the product mixture. Naively, one would expect reaction products containing a  $\text{HfO}_x$ , particularly when higher pressures of  $\text{O}_2$  are used. However, there are no detectable modes expected for bonding structures such as  $\text{Hf}-\text{O}$  or  $\text{Hf}=\text{O}$  stretching vibrations around  $700\text{ cm}^{-1}$  and  $900\text{ cm}^{-1}$ , [22] except for the peak  $725\text{cm}^{-1}$  associated with  $-(\text{CH}_2)_n$ - rocking.

The absence of  $\text{HfO}_x$ -related modes in the spectra indicates that either (1) there is no such chemical configuration in the products, or (2) the  $\text{HfO}_x$  absorption is below our detection sensitivity. In the first case, it would indicate that  $\text{O}_2$  molecules do not attack  $\text{Hf}-\text{N}$  bonds at  $\sim 65^\circ\text{C}$ . Since the subtraction coefficient  $\mu_{\text{TEMAH}} \sim 1.1785$  for  $\text{TEMAH}+\text{O}_2$  is much larger than the coefficients for the other mixtures, we conclude that  $\text{O}_2$  does not react with TEMAH. Instead, trace amount of water can explain the observed products. Under abundant oxygen source ambient condition and comparing the mixture spectra (before subtraction processing) of different oxygen sources,  $\text{TEMAH}+\text{O}_2$  mixture absorbance spectrum has dominant TEMAH vapor IR absorption features in the mixture spectrum while no TEMAH peak features found in the mixing with  $\text{H}_2\text{O}$ ,  $\text{D}_2\text{O}$  and ozone/ $\text{O}_2$  abundance ambient, it implies  $\text{O}_2$  is not so reactive to TEMAH as the other oxygen sources at the temperature  $\sim 65^\circ\text{C}$ , and by comparing the absorbance peak integration area of  $\nu(\text{CH}_x) \sim 3000\text{-}2800\text{cm}^{-1}$  in the raw and processed  $\text{TEMAH}+\text{O}_2$  mixture absorbance spectra about 60% of TEMAH survives in the mixture with  $\text{O}_2$  under

the previous stated exposure condition. The processed TEMAH+O<sub>2</sub> mixture absorbance spectrum shows exactly the same peak profile as that of TEMAH+H<sub>2</sub>O(**Fig. 3-4 (d)**). However, if the reaction pressure is increased by partially closing the throttle valve, stopping TEMAH supply and keeping purified N<sub>2</sub> and O<sub>2</sub> supply, the mixture absorbance spectrum (**Fig. 3-4 (a)**) starts to grow an extra peak structure~1670 and 1694cm<sup>-1</sup> suggesting the existence of tertiary amide (R-(C=O)-N(R<sub>1</sub>R<sub>2</sub>)) or R-O-N=O compound in mixture. In this long time TEMAH degrading mixture experiment, the typical IR active Hf-O or Hf=O stretching (lower than 700cm<sup>-1</sup> and 900 cm<sup>-1</sup>) [22] can be either too low and too weak in concentration and induced active dipole moment intensity, or too low in frequency for the frequency detection range of current spectrometer setup, although we still can not exclude the possibility of hafnium-oxygen moiety suppression due to the inaccessibility of radicals containing oxygen to Hf atom.

## B. TEMAH Vapor Reaction with D<sub>2</sub>O or H<sub>2</sub>O

Spectrum (**d**) in **Fig. 4** shows the absorbance of TEMAH+H<sub>2</sub>O (16-25 Torr) after removal of the H<sub>2</sub>O spectrum ( $\mu_{\text{H}_2\text{O}}=0.6221$   $\mu_{\text{TEMAH}}=0$  ). There is no significant spectral contribution in the 3500-3020 cm<sup>-1</sup> range, suggesting that the major reaction products do not contain NH<sub>x</sub> and OH groups. This observation rules out the formation of primary and secondary alkylamines (R-NH<sub>2</sub> and (R<sub>1</sub>R<sub>2</sub>)NH) and amides (-(C=O)-NH<sub>2</sub>, and -(C=O)-NH-R) and acids (-(CO)-OH) for the major reaction products. The relatively strong bands at 2969, 2805 cm<sup>-1</sup> and 1460, 1380 cm<sup>-1</sup> for  $\nu(\text{CH}_x)$  and  $\delta(\text{CH}_x)$  and the lack of features at ~3080-3000 cm<sup>-1</sup> for  $\nu(\text{C-H})$  in R=(CH)- are consistent with the presence of aliphatic saturated C<sub>N</sub>H<sub>2N+1</sub>-O or C<sub>N</sub>H<sub>2N+1</sub>-N and -CH<sub>2</sub>- groups in the products. From these observations, we conclude that the local bonding structure of nitrogen containing



compound in product mixture is dominated by tertiary alkylamino-type  $((R_1R_2R_3)N)$  structures. A peak at  $\sim 1130\text{ cm}^{-1}$  ( $\nu(C-O)$  or  $\nu(C-O-C)$ ) and another strong peak at  $\sim 725\text{ cm}^{-1}$  respectively point to the existence of C-O or C-O-C groups and  $-(CH_2)_n-$  in the final gas mixture [18-20].

Spectrum (b) in **Fig. 3-4** shows the absorbance of TEMAH+D<sub>2</sub>O (atmospheric pressure) after removal of the D<sub>2</sub>O (and also HDO) spectrum ( $\mu_{D_2O}=0.5898$   $\mu_{HDO}=0.4596$   $\mu_{TEMAH}=0$ ). There are some differences in spectral profile when compared to the TEMAH+H<sub>2</sub>O spectrum [**Fig. 3-4(d)**]: (1) modes at  $725\text{ cm}^{-1}$  and  $1460\text{ cm}^{-1}$  (and to a lesser extent at  $2940\text{--}2850\text{ cm}^{-1}$ ) are stronger for the TEMAH+H<sub>2</sub>O system than for the TEMAH+D<sub>2</sub>O system, while the mode at  $590\text{ cm}^{-1}$  is much stronger for the TEMAH+D<sub>2</sub>O system; (2) the mode at  $1160\text{ cm}^{-1}$  is substantially reduced for TEMAH+D<sub>2</sub>O, while the band at  $1130\text{ cm}^{-1}$  (in TEMAH+H<sub>2</sub>O) slightly shifts to lower frequency  $\sim 1126\text{ cm}^{-1}$ , and a mode at  $1236\text{ cm}^{-1}$  appears in TEMAH+D<sub>2</sub>O; and (3) very weak modes  $\sim 2210$  and  $2080\text{ cm}^{-1}$  for C-D stretching ( $\nu(CD_x)$ ) are found. All these differences can be the consequences of H-D substitution.  $\nu(CD_x)$  in (3) clearly indicates the existence of CD<sub>x</sub> produced by H-D substitution in products. In (1) the frequency ratio of  $725\text{ cm}^{-1}$  and  $590\text{ cm}^{-1}$  close to the squared root of deuterium-hydrogen mass ratio ( $725\text{ cm}^{-1}/590\text{ cm}^{-1}=1.23\sim\sqrt{2}$ ) implies mode  $590\text{ cm}^{-1}$  is associated with  $-(CD_2)_n-$  rocking. Thus the decrease of  $-(CH_2)_n-$  rocking  $\sim 725\text{ cm}^{-1}$  and the growth of  $-(CD_2)_n-$  rocking  $\sim 590\text{ cm}^{-1}$  in [**Fig. 3-4(b)**] compared to TEMAH+H<sub>2</sub>O spectrum [**Fig. 3-4(d)**] indicate an isotopic red-shift induced by H-D substitution. As the CH<sub>3</sub> rocking and C-O-C stretching frequencies of CH<sub>3</sub>-O-CD<sub>3</sub> perturbed by H-D substitution and shift from those of CH<sub>3</sub>-O-CH<sub>3</sub>[23], the frequency shifts of the modes at  $1160$  and  $1130\text{ cm}^{-1}$  in

TEMAH+H<sub>2</sub>O to 1236 and 1126 cm<sup>-1</sup> in TEMAH+D<sub>2</sub>O stated in (2) can be the similar CH<sub>3</sub> rocking and C-O-C stretching frequency shifts caused by H-D substitution. The prominent peaks for -(CH<sub>2</sub>)<sub>n</sub>- rocking, -(CD<sub>2</sub>)<sub>n</sub>- rocking,  $\nu(\text{CD}_x)$  and  $\nu(\text{CH}_x)$  imply the coexistence of CD<sub>x</sub> and CH<sub>x</sub> in final products.

Spectrum (c) (**Fig. 3-4**) ( $\mu_{\text{D}_2\text{O}}=0.8580$   $\mu_{\text{HDO}}=0$   $\mu_{\text{TEMAH}}=0$ ) shows the absorbance of lower pressure TEMAH+D<sub>2</sub>O (~8 Torr). By comparing this spectrum with **Fig. 3-4(b)** taken at atmospheric pressure, it shows no peak feature in the frequency range 2100-2300cm<sup>-1</sup> for  $\nu(\text{CD}_x)$ , a relatively stronger mode at ~590 cm<sup>-1</sup> for -(CD<sub>2</sub>)<sub>n</sub>- rocking and a weaker and broader -(CH<sub>2</sub>)<sub>n</sub>- rocking mode at ~725 cm<sup>-1</sup>. [The strong features of the coexistence of CD<sub>x</sub> and CH<sub>x</sub> in products shown in spectrum **Fig. 3-4(b)** should be the consequence of prevalent H-D interchange taking place in high pressure reaction ambient. Higher reaction pressure implies shorter mean free path and higher collision frequency for CH<sub>x</sub>-contained molecules to encounter D<sub>2</sub>O, the deuterium source, to form CD<sub>x</sub> through H-D interchange reaction. Much higher HDO subtraction coefficient  $\mu_{\text{HDO}}$  for atmospheric pressure TEMAH+D<sub>2</sub>O ( $\mu_{\text{HDO}}=0.4596$ ) than that for lower pressure TEMAH+D<sub>2</sub>O ( $\mu_{\text{HDO}}=0$ ) also supports the prevalent H-D interchange taking place in high pressure reaction ambient.]

The spectral profiles of TEMAH+D<sub>2</sub>O and TEMAH+H<sub>2</sub>O are very similar to that of TEMAH+O<sub>2</sub> indicates, suggesting that the reaction products are the same. In all cases, there is no evidence that ethyl-methyl-amino ligands are replaced by hydroxyl groups to form hafnium hydroxyl (-Hf-OH) species in gas phase reactions. However this by no means implies the ligand replacement reaction never takes place, since the formed -Hf-OH species may quickly react with TEMAH or the other products to produce reaction

products without hydroxyl groups. Also, the similarity of the modes suggests that there is residual water in the environment during the  $O_2$  exposures, with little direct reaction of TEMAH with  $O_2$ .

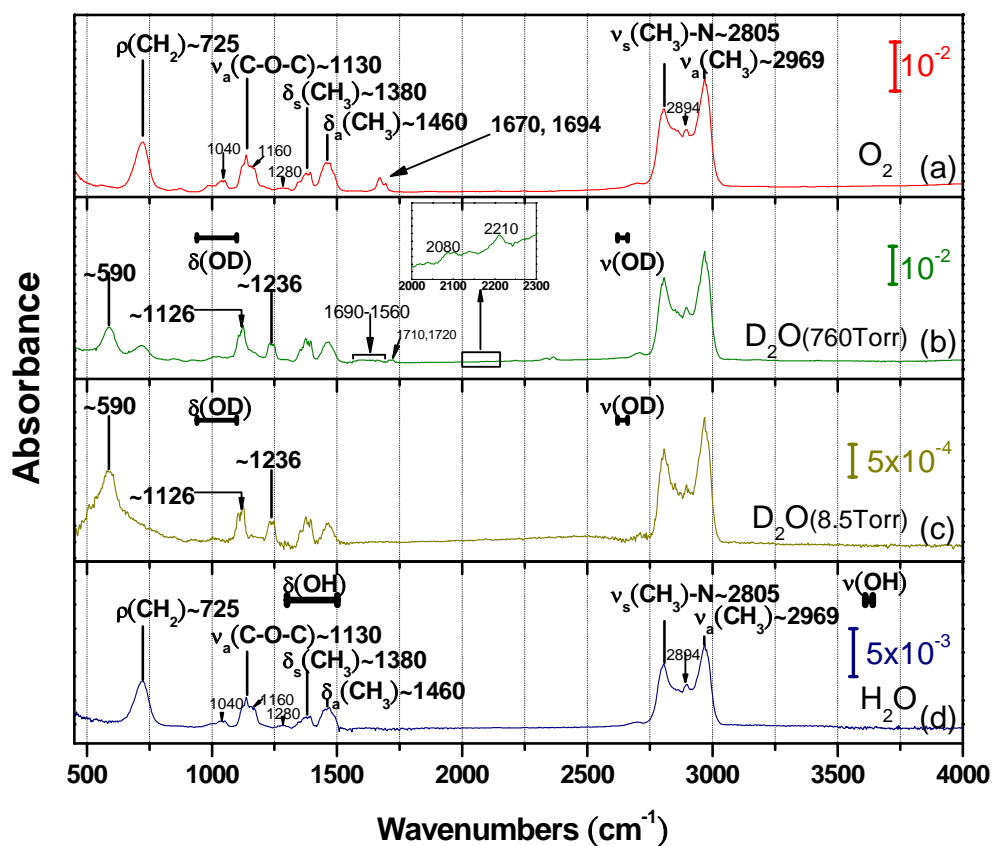


Fig. 3-4 Comparison of the processed mixture spectra referenced to empty reactor made by suitable spectrum subtractions and the relevant subtraction coefficients: (a) enhanced atmospheric pressure TEMAH in  $O_2$  ambient at  $\mu_{\text{TEMAH}}=1.1785$ , (b) atmospheric pressure TEMAH+ $D_2O$  mixture at  $\mu_{D_2O}=0.5898$ ,  $\mu_{HDO}=0.4596$  and  $\mu_{\text{TEMAH}}=0$  (c) low pressure ( $\sim 8.5$  Torr) TEMAH+ $D_2O$  mixture at  $\mu_{D_2O}=0.8580$ ,  $\mu_{HDO}=0$  and  $\mu_{\text{TEMAH}}=0$  and (d) high pressure ( $\sim 16$ - $25$  Torr) TEMAH+ $H_2O$  mixture at  $\mu_{H_2O}=0.6221$  and  $\mu_{\text{TEMAH}}=0$

### C. TEMAH Vapor Reaction with Ozone/ $O_2$

The formation of water vapor and  $CO_2$  gas are evident during experiments using TEMAH+ozone/ $O_2$  mixtures, as the concentration of both species increases with

TEMAH pressure in the presence of ozone. Thus, CO<sub>2</sub> and water vapor are reaction products. That implies ozone can rupture the hydro-carbon compounds during exposure. After removing the CO<sub>2</sub> and water vapor bands, the subtracted TEMAH+ozone/O<sub>2</sub> mixture spectrum (~8.5 Torr) (**Fig. 3-5**) shows fine structure at 2897, 2863, 2802, 1763, 1746 and 1722 cm<sup>-1</sup>, on top of the broader bands in the 2980-2700cm<sup>-1</sup> and 1820-1670cm<sup>-1</sup> regions. This fine structure suggests the presence of a molecule with large rotational structure, such as formaldehyde (CH<sub>2</sub>O) in the mixture. [17] The lack of absorption in the 3640-3200 cm<sup>-1</sup> region rules out the presence of major hydroxyl, primary or secondary alkylamine species in the reaction products. The strong  $\nu(\text{CH}_x)$  absorption band in the 2980-2800 cm<sup>-1</sup> region suggest the abundant presence of CH<sub>3</sub>-O- or C<sub>2</sub>H<sub>5</sub>-O- species in the product mixture, and the absorption tail extending over 2800-2650 cm<sup>-1</sup> points to the possible existence of tertiary-alkylamine (R<sub>1</sub>R<sub>2</sub>R<sub>3</sub>-N) or amine salts (NH<sub>3</sub><sup>+</sup> or NH<sub>2</sub><sup>+</sup>). The 2287 cm<sup>-1</sup> band in the subtracted spectrum is either due to nitrile ( $\nu(-\text{C}\equiv\text{N})$ ) bonding or isocyanates  $\nu(-\text{N}=\text{C}=\text{O})$  bonding[18-20]. However, comparison of relative intensities of CH<sub>3</sub>(NCO), CH<sub>3</sub>CN and C<sub>2</sub>H<sub>5</sub>CN[23] suggests that the nitrile species (also with a mode at 2287 cm<sup>-1</sup>) can be excluded due to the absence of 3200 and 2620 cm<sup>-1</sup> in the mixture spectrum. Thus, the 2287 cm<sup>-1</sup> mode should be assigned as the  $\nu_a(-\text{N}=\text{C}=\text{O})$  mode of CH<sub>3</sub>(NCO). The doublets at 1572, 1590 cm<sup>-1</sup> and at 1379, 1394 cm<sup>-1</sup> are assigned to nitromethane (CH<sub>3</sub>NO<sub>2</sub>) by comparison with a nitromethane gas spectrum[23]. The 1710 cm<sup>-1</sup> mode can be assigned to C=O bonding and the 1675 cm<sup>-1</sup> mode to imine (C=N-) species. The presence of abundant carbon-nitrogen-oxygen fragments in the TEMAH+ozone/O<sub>2</sub> mixture indicates that the ethyl-methyl-amino ligand of TEMAH is strongly attacked by the ozone radicals.

The lump~800-500  $\text{cm}^{-1}$  in subtracted TEMAH+ozone/ $\text{O}_2$  spectrum falls within the Hf-O or Hf=O stretching frequency range. A similar weak extended lump~800-400  $\text{cm}^{-1}$  can also be observed in subtracted TEMAH+ $\text{D}_2\text{O}$  spectrum (**Fig. 3-4(c)**) of low ambient pressure (and low pressure TEMAH+ $\text{H}_2\text{O}$  spectrum not shown). That may not be sufficient to associate the lump~800-500  $\text{cm}^{-1}$  to the existence of Hf-O or Hf=O bonding. We are still not able to identify the local bonding structure of Hf atom or to determine the chemical structure of the reaction products containing Hf atom.

Could there be any hafnium nitrate (Hf-O-N-) species in TEMAH+ozone/ $\text{O}_2$  products? The reported stretching frequencies of coordination metal (M) nitrate(M-O-N-) species vary in several correlation frequency range sections of 1650-1480 $\text{cm}^{-1}$ , 1300-1170  $\text{cm}^{-1}$ , 1520-970  $\text{cm}^{-1}$  and 1350-1180  $\text{cm}^{-1}$ [24]. Unfortunately they overlap with other reaction product characteristic group frequencies, and, therefore, the subtracted IR spectrum can not tell whether hafnium nitrate species ever exists as a reaction product of TEMAH+ozone/ $\text{O}_2$  or not.

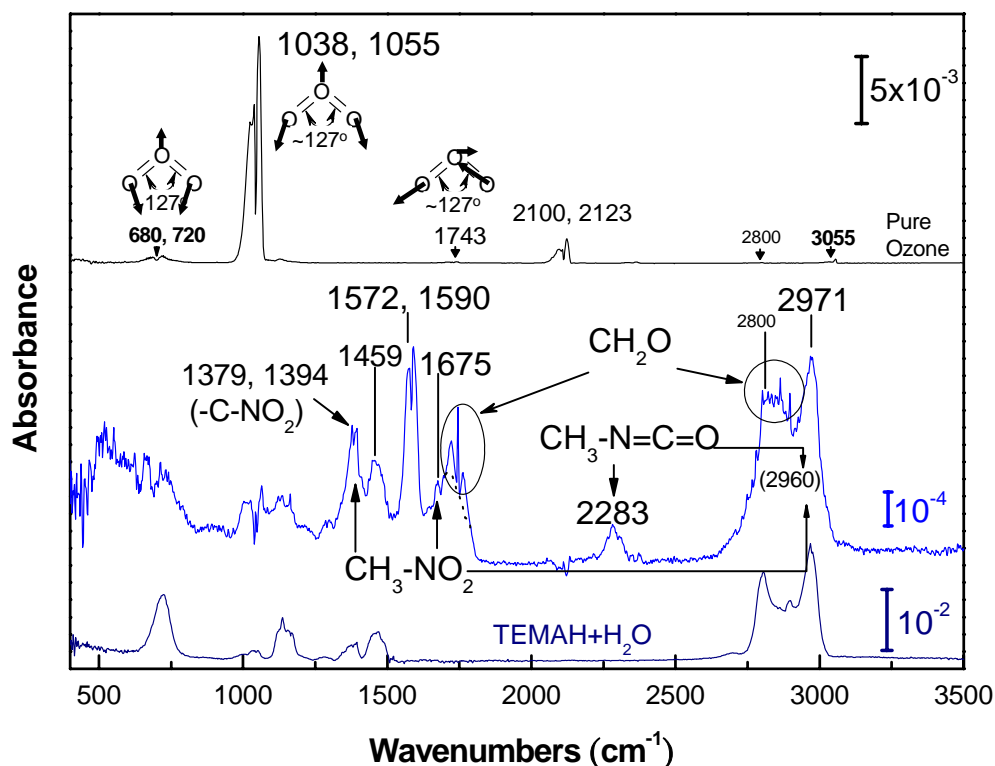


Fig. 3-5 Ozone (top) absorbance spectrum and its three primary fundamental vibrations  $\sim 680, 720\text{cm}^{-1}$  doublet ( $\nu_2$ ),  $1038, 1055\text{cm}^{-1}$  doublet ( $\nu_1$ ) and  $1743\text{cm}^{-1}$  ( $\nu_3$ ) and overtones  $\sim 2100, 2123\text{cm}^{-1}$  ( $3\nu_2$  or  $2\nu_1$ )  $3055\text{cm}^{-1}$  ( $3\nu_1$ ) as the cited assignment by Sutherland-Penney in Ref.30 ;  $2800\text{cm}^{-1}$  and  $1165, 1131\text{cm}^{-1}$  doublet are too weak to be manifested in current plot scale. The processed TEMAH+ozone/ $\text{O}_2$  ( $\sim 8.5$  Torr) IR absorption spectrum made by subtraction coefficients,  $\mu_{\text{ozone}}=0.9904$ ,  $\mu_{\text{CO}_2}=1.2062$ ,  $\mu_{\text{H}_2\text{O}}=0.2941$  and  $\mu_{\text{TEMAH}}=0$ , (middle) shows the existence of  $\text{CH}_2\text{O}$ ,  $\text{CH}_3\text{NO}_2$ ,  $\text{CH}_3\text{-N=C=O}$  and other  $\text{-C(=O)-}$  and  $\text{-C-O-}$  features  $\sim 1710\text{cm}^{-1}$  and  $1250\text{-}1000\text{cm}^{-1}$  respectively in gas phase reaction products. (the dips around  $710$ ,  $1043$  and  $2110\text{cm}^{-1}$  are due to imperfection of ozone spectrum subtraction and  $2060\text{cm}^{-1}$  indicated in parenthesis is  $\nu_s(\text{CH}_3)$  frequency for  $\text{CH}_3\text{NO}_2$  and  $\text{CH}_3\text{-N=C=O}$  ) The high pressure ( $\sim 16\text{-}25$  Torr) TEMAH+ $\text{H}_2\text{O}$  spectrum is shown in bottom for contrast.

### 3.3 TEMAH Reaction on Silicon Surfaces/ Accumulative TEMAH Exposure on Silicon Surfaces at Different Temperatures

The principles of ideal ALD assume the ALD surface self-termination reactions are dominated by ligand replacement and the ligands of adsorbed precursor molecules don't

dissociate[25-27]. Ligand replacement condition is stricter than self-termination reaction condition. In practical ALD, self-terminated surface reaction could be the least operational criterion for ALD. Both the dissociation of the ligands of adsorbed precursor molecules and CVD-like continuous growth may be avoided by suitable kinetic condition control during precursor exposure. Among the controllable kinetics parameters, substrate temperature is more critical a parameter than exposure pressure and exposure time for the control of the rate of precursor adsorption. Therefore the determination of the appropriate substrate temperature range to avoid severe continuous CVD growth turns out to be an important and preliminary task for all ALD studies. By dosing TEMA<sub>3</sub>H<sub>9</sub> accumulatively onto silicon surfaces at different temperatures, the IR spectra are beneficial to determine the suitable or applicable temperature range for ALD growth by using TEMA<sub>3</sub>H<sub>9</sub> precursor.

## A. TEMAH Exposure on H/Si(100) Surface

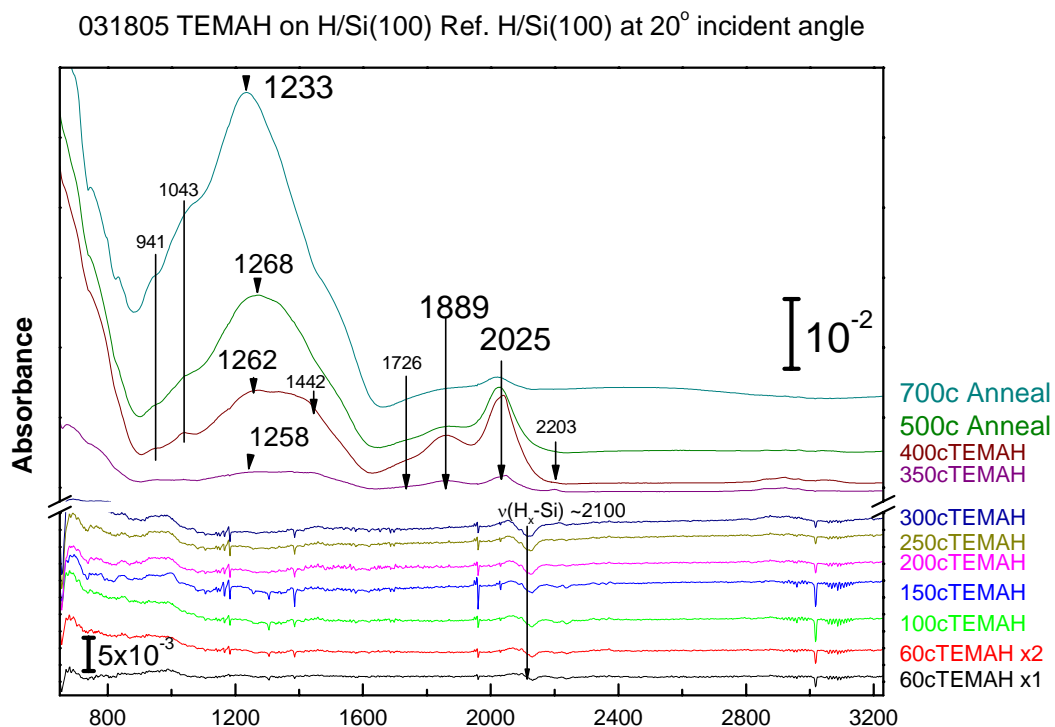


Fig. 3-6 The colored spectra at 20° incident angle referenced to initial surface of the accumulatively dosing TEMAH (10 seconds 50 s.c.c.m. carrying N<sub>2</sub>) to H/Si(100) in vacuum chamber with 100 s.c.c.m. N<sub>2</sub> flow at different temperatures of the first 60°C, the second 60°C, 100°C, 150°C, 200°C, 250°C, 300°C, 350°C and 400°C, then 2 minutes of annealing at 500°C and 700°C.



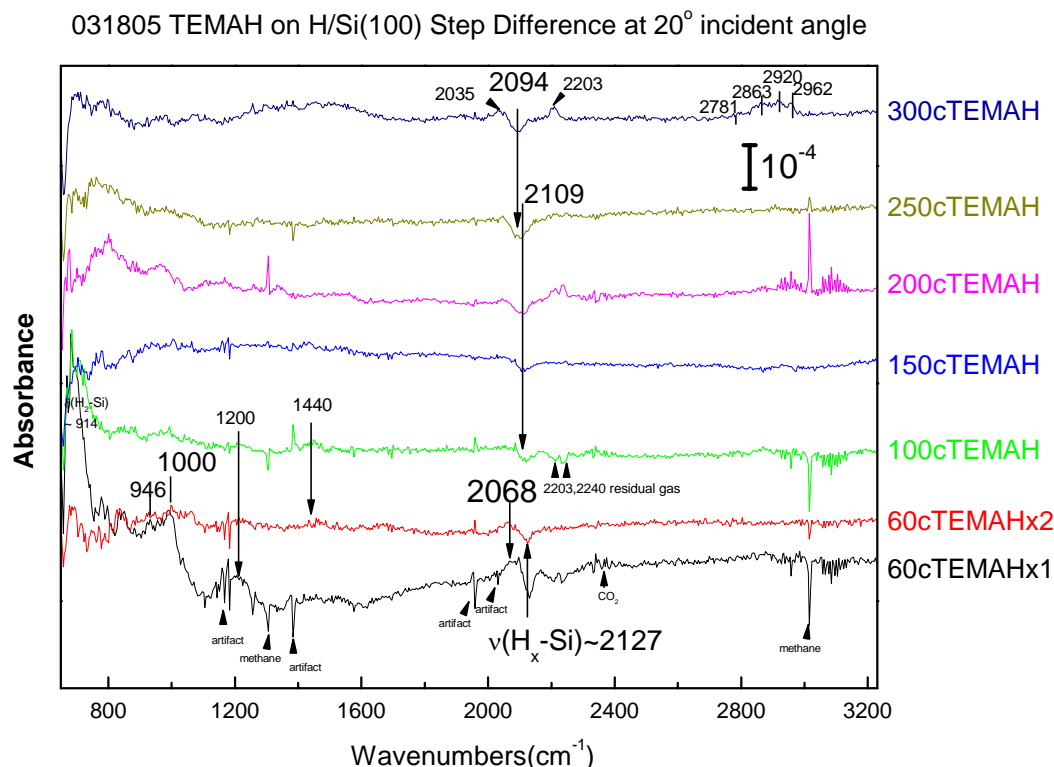


Fig. 3-7 Selected colored step difference spectra at 20° incident angle of the accumulatively dosing TEMAH (10 seconds 50 s.c.c.m. carrying  $\text{N}_2$ ) to H/Si(100) in vacuum chamber with 100 s.c.c.m.  $\text{N}_2$  flow at stepped temperatures from 60°C-300°C.

**Fig. 3-6** shows when substrate temperature is higher than 300°C, strong D-band at lower frequency( $\sim 1200\text{-}1500\text{cm}^{-1}$ ) [28-30] and G-band at higher frequency( $\sim 1500\text{-}1700\text{cm}^{-1}$ ) [28, 31-35] for carbon-nitrogen-oxygen alloy start to appear in spectra. D-band contains  $\nu(\text{C-N})\sim 1250\text{cm}^{-1}$  and  $\nu(\text{C-C})\sim 1442\text{cm}^{-1}$  [32, 36] and G-band contains  $\nu(\text{C=C})/\nu(\text{C=N})$  in  $1500\text{-}1700\text{cm}^{-1}$  as in the CVD carbon-nitride alloy[28, 31-35]. The broad and strong peaks at  $1889\text{cm}^{-1}$  and  $2035\text{cm}^{-1}$  are too high in frequency for  $\nu(\text{H-Hf})\sim 1600\text{-}1700\text{cm}^{-1}$  [37, 38]. These two peaks can be associated with the as-formed network of metallic carbonyl [19], which contain linkages of  $\text{M-C}\equiv\text{O}$  or  $\text{M=C=O}$ . The other weak peak at  $\sim 2203\text{cm}^{-1}$  is either for  $-\text{N=C=O}$  or for  $\nu(\text{C}\equiv\text{N})$  [22, 31, 34, 39]. (The

$\nu(\text{C-H}_x) \sim 2800\text{--}3100\text{cm}^{-1}$  intensity becomes extraordinarily stronger than those of substrate temperature less than or equal to  $300^\circ\text{C}$ . After the post-annealing at  $500^\circ\text{C}$  and  $700^\circ\text{C}$ , hydrogen is ripped from alkyl group in grown moiety and  $\nu(\text{C-H}_x) \sim 2800\text{--}3100\text{cm}^{-1}$  intensity is greatly reduced,  $\nu(\text{C-N}) \sim 1250\text{cm}^{-1}$  becomes sharper and stronger while  $\nu(\text{C=C})/\nu(\text{C=N})$  and  $\nu(\text{C}\equiv\text{N})$  modes decrease and disappear respectively. This indicates huge amount of amino ligand decomposes during surface reaction then forms thick alloy moiety composed of C, N and Hf atoms during exposure at substrate temperature higher than  $300^\circ\text{C}$  and the post-annealing spectra suggest C-N bonding structure is favored over C=N at higher temperature. Therefore the spectra in **Fig. 3-6** suggest the appropriate ALD temperature using TEMAH as precursor is below  $350^\circ\text{C}$ . Also during TEMAH exposure at substrate temperature lower than  $350^\circ\text{C}$ , a red-shifted  $\nu(\text{H-Si}) \sim 2055\text{cm}^{-1}$  appears and the  $\nu(\text{H-Si}) \sim 2130\text{cm}^{-1}$  loss increases with substrate temperature. Weak  $\delta_s(\text{CH}_3) \sim 1210\text{cm}^{-1}$ ,  $\delta(\text{CH}_x) \sim 1457\text{cm}^{-1}$  and  $\nu(\text{CH}_x) \sim 2700\text{--}3000\text{cm}^{-1}$  barely can be observed and they slightly increase with growth temperature up to  $300^\circ\text{C}$ . In low frequency region, modes at  $\sim 941\text{cm}^{-1}$  and  $\sim 990\text{cm}^{-1}$  appear upon the very first TEMAH exposure at as low substrate temperature as  $60^\circ\text{C}$ .

The step difference spectra (**Fig. 3-7**) show clearly the  $\nu(\text{H}_x\text{-Si})$  loss slightly increased with substrate temperature and the red-shifted  $\nu(\text{H}_x\text{-Si})$  appearance: more TEMAH exposure at  $60^\circ\text{C}$  ("60c TEMAH x2" in red) exposure increases the intensity of the red-shifted  $\nu(\text{H-Si})$  and  $\nu(\text{H}_x\text{-Si})$  loss, which indicate the exposure time is not long enough for TEMAH to saturate all the active sites on  $60^\circ\text{C}$  H/Si surface. The frequency of surface hydrogen loss  $\sim 2109\text{cm}^{-1}$  during  $100\text{--}250^\circ\text{C}$  exposures is different from that of  $60^\circ\text{C}$  ( $\sim 2127\text{cm}^{-1}$ ), which suggests higher substrate temperature energetically activates

some more surface mono-hydrides to desorb or to react with TEMA. When substrate temperature is raised up to 300°C for TEMA exposure, the loss of  $\nu(\text{H-Si}) \sim 2094 \text{ cm}^{-1}$  indicates some residual surface mono-hydride is removed, while some other portion of residual surface mono-hydride is turned into surface  $\text{H-SiO}_x$  due to oxygen insertion to silicon substrate as shown by the growth of  $\nu(\text{H-SiO}_x) \sim 2210 \text{ cm}^{-1}$  peak (this mode frequency is too high to be  $\nu(\text{H-SiN}_3) \sim 2165 \text{ cm}^{-1}$  [40-42]). The mode assignment of the low frequency band at  $\sim 941\text{-}1000 \text{ cm}^{-1}$  grown by the very first TEMA exposure will be shortly discussed in next paragraph and be detailed in length in Chapter 4.

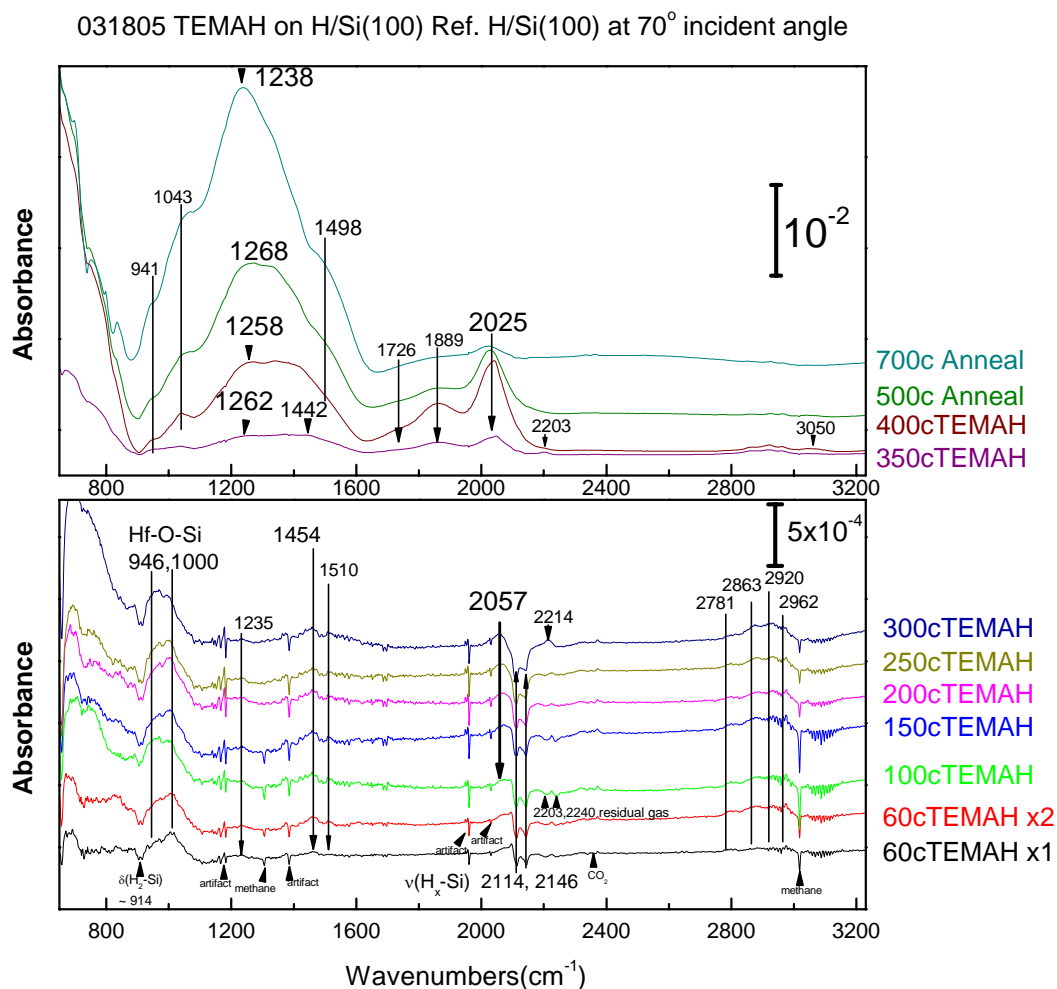


Fig. 3-8 The colored spectra at 70° incident angle referenced to initial surface of the accumulatively dosing TEMAH (10 seconds 50 s.c.c.m. carrying N<sub>2</sub>) to H/Si(100) in vacuum chamber with 100 s.c.c.m. N<sub>2</sub> flow at different temperatures of the first 60°C, the second 60°C, 100°C, 150°C, 200°C, 250°C, 300°C, 350°C, 400°C, then 2 minutes of annealing at 500°C and 700°C.

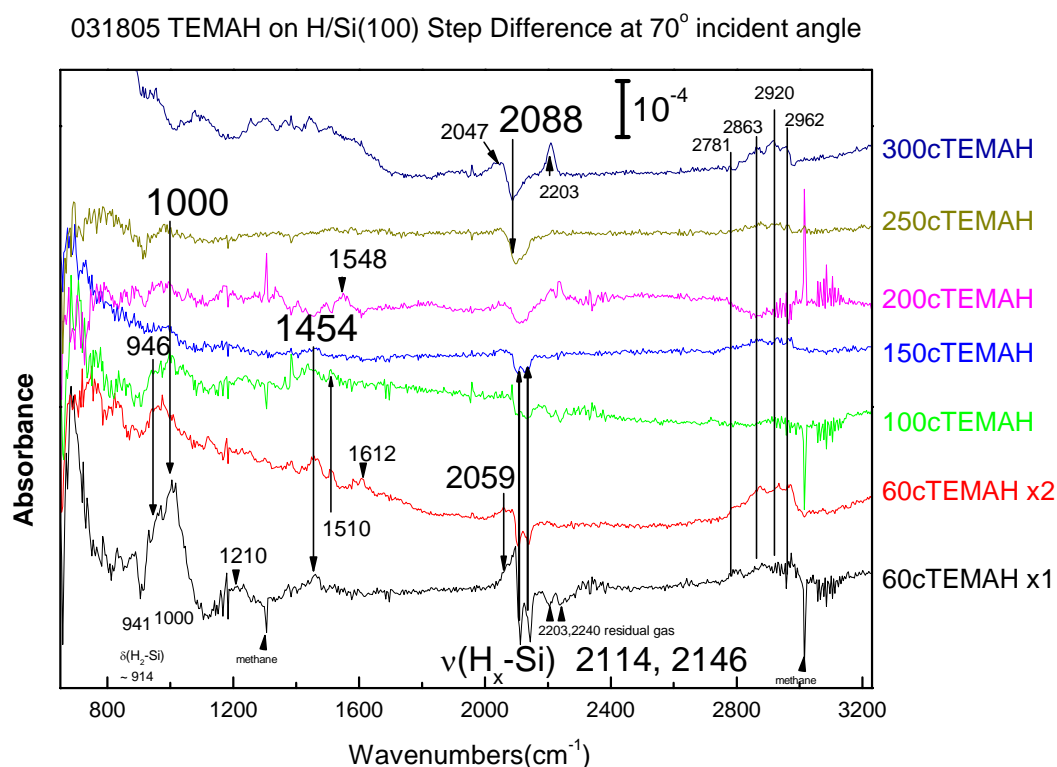


Fig. 3-9 Colored selected step difference spectra in of the accumulatively dosing TEMAH (10 seconds 50 s.c.c.m. carrying  $N_2$ ) to H/Si(100) in vacuum chamber with 100 s.c.c.m.  $N_2$  flow at lower temperatures of the first 60°C, the second 60°C, 100°C, 150°C, 200°C, 250°C and 300°C at 70° incident angle.

The IR spectra of more grazing angle (incident angle of 70°) of higher surface sensitivity will provide more information to help resolve the adsorbed species. By comparing **Fig. 3-9** with **Fig. 3-6**, the accumulatively dosing TEMAH to H/Si(100) surface at raising temperatures the spectra at incident angle of 70° shows almost the same peak structure and intensities for higher temperature exposure (>350°C) as the spectra at incident angle of 20°, and this implies the corresponding peak structure is due to IR absorption of thick bulk, which doesn't vary with IR transmission incident angles.

Compared to the spectra of 20° incident angle in **Fig. 3-7**, the spectra of 70° incident angle in **Fig. 3-9** clearly show the loss of  $\nu(H_x-Si) \sim 2114$  and  $2146\text{cm}^{-1}$  for surface di- and tri- hydrides, during TEMAH exposure at substrate temperature lower than 300°C, and a

red-shift H-Si stretching  $\sim 2059\text{cm}^{-1}$  grows upon the first TEMAH exposure at  $60^\circ\text{C}$ . The surface di- and tri- hydride loss indicates they are more reactive than H/Si mono-hydride species, while the growth of the red-shifted H-Si stretching  $\sim 2059\text{cm}^{-1}$  is either associated with the newly formed mono-hydrides reduced from the surface di- and tri-hydrides by reaction, or due to the chemical red-shift incurred by the interaction between the adsorbed and the existent surface mono-hydride. (In Chapter 2, the system of thermal ammonia nitridation of silicon surface also presents a similar red-shifted H-Si stretching mode, and we will come back to this red-shifted H-Si stretching mode in Chapter 4.) The adsorbed carbon-hydride bending mode  $\delta_s(\text{CH}_3)\sim 1210\text{cm}^{-1}$ ,  $\delta(\text{CH}_x)\sim 1457\text{cm}^{-1}$  and stretching mode  $\nu(\text{CH}_x)\sim 2700\text{-}3000\text{ cm}^{-1}$  have stronger intensities at grazing incident angle. Especially,  $\nu(\text{C-H})$  in  $\text{CH}_3\text{-N}\sim 2781\text{cm}^{-1}$  for surface alkyl-amino group is observed in the very first TEMAH exposure at  $60^\circ\text{C}$ , and survive as high substrate temperature as  $350^\circ\text{C}$ . In low frequency region, the band  $\sim 941\text{-}1000\text{cm}^{-1}$  appears to be stronger in intensity and a new mode at  $\sim 1510\text{ cm}^{-1}$  can be observed at grazing angle geometry. Apparently the formation of the mode at  $2055\text{cm}^{-1}$  and the band in  $941\text{-}1000\text{ cm}^{-1}$  related to Hf-O-Si species is due to TEMAH reaction with H/Si, and they will be discussed in length in Chapter 4.

## B. TEMAH Exposure on SC2 Wet Chemistry Silicon Oxide Surface

033004 TEMAH on SC2 OSi Ref. OSi at 45° incident angle

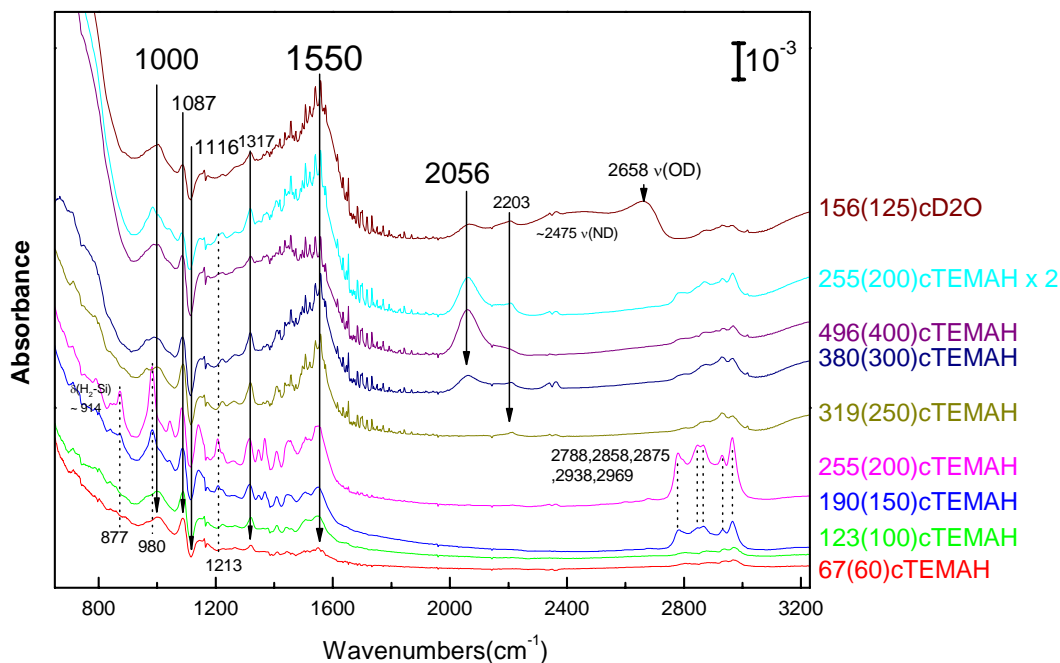


Fig. 3-10 The colored spectra at 45° incident angle referenced to the initial surface of the accumulatively dosing TEMAH (40 s.c.c.m. N<sub>2</sub> carrying) for 20 minutes to SC2 oxidized silicon surface in atmospheric pressure purge style chamber with 200 s.c.c.m. and 440 s.c.c.m. N<sub>2</sub> flow purge in KBr window and chamber through precursor delivery lines during TEMAH dosing and extra 600 s.c.c.m. N<sub>2</sub> flow purge in KBr window after dosing and IR spectrum taking at different calibrated temperatures (thermocouple temperatures in parenthesis) of 67°C, 123°C, 190°C, 255°C, 319°C, 380°C, 496°C, then 255°C again, and final 1 minute D<sub>2</sub>O exposure (400 s.c.c.m. N<sub>2</sub> carrying) at 156°C.

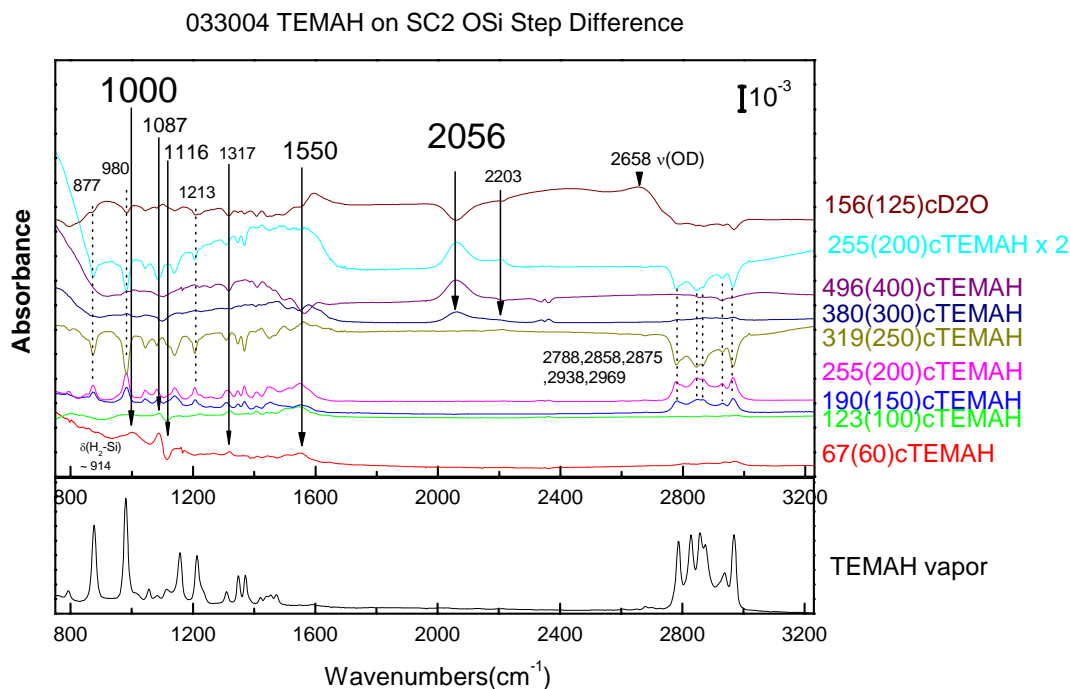


Fig. 3-11 The colored step difference spectra at  $45^\circ$  incident angle of the accumulatively dosing TEMAH (40 s.c.c.m.  $\text{N}_2$  carrying) for 20 minutes to SC2 oxidized silicon surface in atmospheric pressure purge style chamber with 200 s.c.c.m. and 440 s.c.c.m.  $\text{N}_2$  flow purge in KBr window and chamber through precursor delivery lines during TEMAH dosing and extra 600 s.c.c.m.  $\text{N}_2$  flow purge in KBr window after dosing and IR spectrum taking at different calibrated temperatures (thermocouple temperatures in parenthesis) of  $67^\circ\text{C}$ ,  $123^\circ\text{C}$ ,  $190^\circ\text{C}$ ,  $255^\circ\text{C}$ ,  $319^\circ\text{C}$ ,  $380^\circ\text{C}$ ,  $496^\circ\text{C}$ , then  $255^\circ\text{C}$ , and final 1 minute  $\text{D}_2\text{O}$  exposure (400 s.c.c.m.  $\text{N}_2$  carrying) at  $156^\circ\text{C}$ . Those peaks at 877, 980, 1213, 2788, 2858, 2875, 2938 and 2969 denoted by dashed lines in the top panel are due to TEMAH vapor residual in chamber and the spectrum in black in the bottom panel is the TEMAH gas phase spectrum for contrast.

**Fig. 3-10** shows the spectra of TEMAH exposure onto SC2 oxidized silicon surface at different temperatures. The modes at  $2056$  and  $2203\text{cm}^{-1}$  showing up at  $319^\circ\text{C}$  TEMAH exposure indicate severe precursor decomposition at this temperature. The strong and distinct C-H stretching modes  $\sim 2800\text{--}3000\text{ cm}^{-1}$  and their correlation peaks, such as  $877$ ,  $980$  and  $1213\text{ cm}^{-1}$ , in spectrum  $190\text{cTEMAH}$  and  $255\text{cTEMAH}$  are for residual TEMAH vapor in chamber due to incomplete evacuation.(Also see the bottom panel of **Fig. 3-11** for the TEMAH gas phase spectrum) The strong intensity of G-band or D-band keeps growing with substrate temperature higher than  $319^\circ\text{C}$  for TEMAH



exposure. Two new modes at  $1000\text{cm}^{-1}$   $1087\text{cm}^{-1}$  grow during the very first TEMAH exposure, while the loss of silicon oxide TO mode  $\sim 1057\text{cm}^{-1}$  and LO mode  $\sim 1116\text{cm}^{-1}$  is observed. The appearance of the mode at  $1000\text{cm}^{-1}$  of TEMAH exposure on OSi partially supports the mode assignment of Hf-O-Si as discussed in the end of **Section 3.3.B**.

Step difference spectra in **Fig. 3-11** show the silicon oxide TO  $\sim 1057\text{cm}^{-1}$  loss and  $1116\text{cm}^{-1}$  transmutation take place not only during the first TEMAH exposure on  $60^\circ\text{C}$  OSi (in red) but also during the second TEMAH exposure on  $123^\circ\text{C}$  OSi (in light green). Under such a purge style exposure conditions different from the vacuum style of the accumulative exposure on H/Si(100) in last sub-section, the G-band (higher frequency) is stronger than D-band (lower frequency) in purge style ambient while reverse for vacuum style ambient. That might imply high organic precursor (TEMAH) concentration ambient favors double-bond-contained CVD moiety growth.

The  $1591\text{cm}^{-1}$  (or  $1595\text{cm}^{-1}$  mode in TEMAH accumulative exposure on  $605^\circ\text{C}$  ammonia nitridized silicon surface) due to  $\text{D}_2\text{O}$  exposure is assigned as  $\nu(\text{C}=\text{O})$  or  $\nu(\text{N}=\text{O})$ . The broad but strong peaks  $\nu(\text{OD})\sim 2658\text{cm}^{-1}$  and  $\nu(\text{ND})\sim 2475\text{cm}^{-1}$  due to  $\text{D}_2\text{O}$  exposure in the spectrum are denoted therein for reference.

### C. TEMAH Exposure on 605°C Ammonia Nitridized Silicon Surface

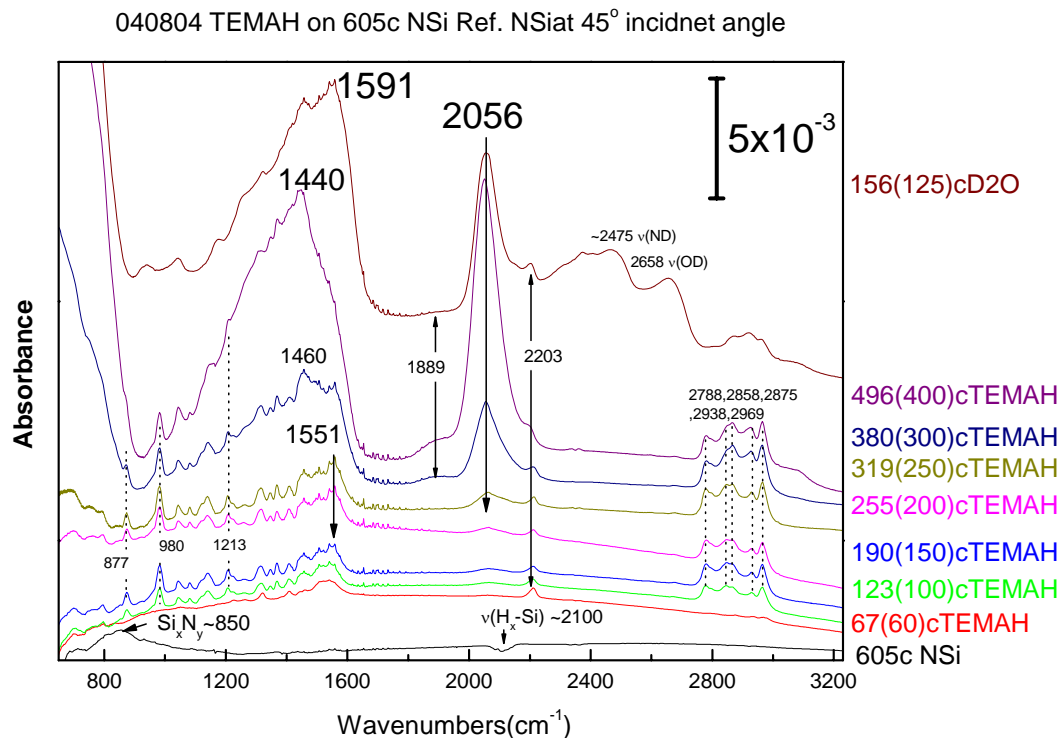


Fig. 3-12 The colored spectra at 45° incident angle referenced to the initial surface of the accumulatively dosing TEMAH (40 s.c.c.m. N<sub>2</sub> carrying) for 20 minutes to ammonia pretreated 605°C H/Si(100) surface in atmospheric pressure purge style chamber with 200 s.c.c.m. and 440 s.c.c.m. N<sub>2</sub> flow purge in KBr window and chamber through precursor delivery lines during TEMAH dosing and extra 600 s.c.c.m. N<sub>2</sub> flow purge in KBr window after dosing and IR spectrum taking at different calibrated temperatures (thermocouple temperatures in parenthesis) of 67°C, 123°C, 190°C, 255°C, 319°C, 380°C, 496°C and final 1 minute D<sub>2</sub>O exposure (400 s.c.c.m. N<sub>2</sub> carrying) at 156°C. Those peaks at 877, 980, 1213, 2788, 2858, 2875, 2938 and 2969 denoted by dashed lines in the top panel are due to TEMAH vapor residual in chamber.

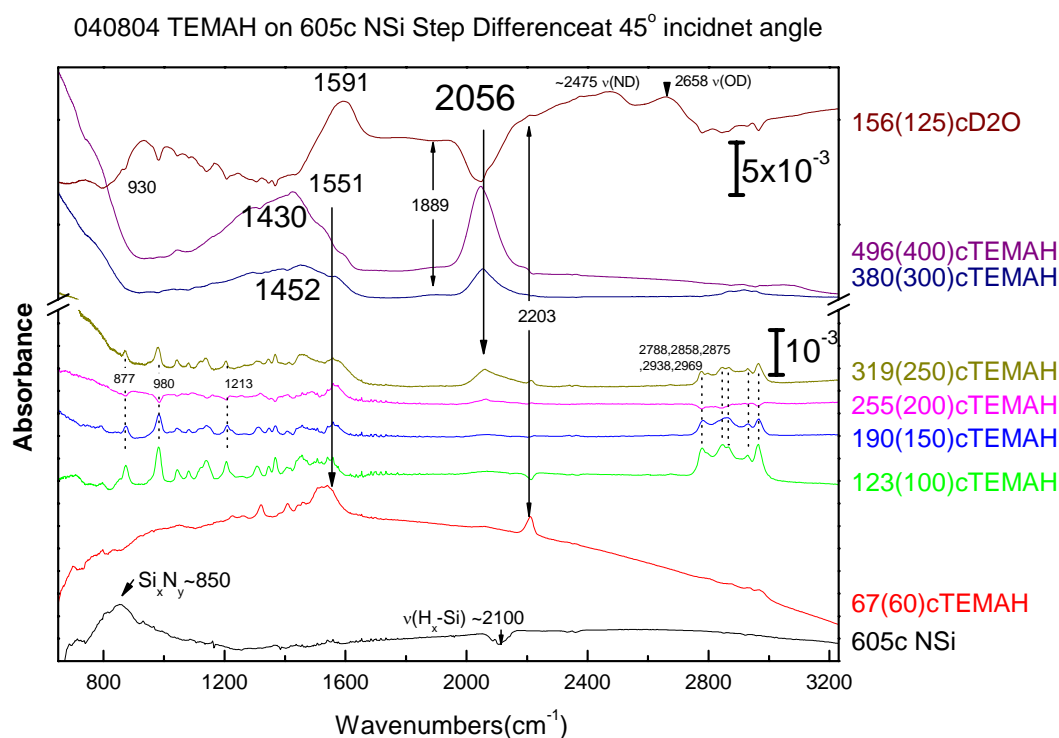


Fig. 3-13 The colored step difference spectra at 45° incident angle of the accumulatively dosing TEMAH (40 s.c.c.m.  $\text{N}_2$  carrying) for 20 minutes to ammonia pretreated 605°C H/Si(100) surface in atmospheric pressure purge style chamber with 200 s.c.c.m. and 440 s.c.c.m.  $\text{N}_2$  flow purge in KBr window and chamber through precursor delivery lines during TEMAH dosing and extra 600 s.c.c.m.  $\text{N}_2$  flow purge in KBr window after dosing and IR spectrum taking at different calibrated temperatures (thermocouple temperatures in parenthesis) of 67°C, 123°C, 190°C, 255°C, 319°C, 380°C, 496°C and final 1 minute  $\text{D}_2\text{O}$  exposure (400 s.c.c.m.  $\text{N}_2$  carrying) at 156°C. Those peaks at 877, 980, 1213, 2788, 2858, 2875, 2938 and 2969 denoted by dashed lines in the top panel are due to TEMAH vapor residual in chamber.

The spectra of TEMAH exposures on 605°C thermal ammonia nitridized silicon surface at different temperatures (**Fig. 3-12** and **Fig. 3-13**) show extraordinarily high intensities of D-band, which contains the mode at  $\sim 1452\text{cm}^{-1}$  for  $\nu(\text{C-C})$ , grows during TEMAH exposure on NSi at substrate temperatures higher than 319°C. That indicates a continuous alloy film growth on NSi starts at 319°C. Surface reactive nitrogen-contained radicals on NSi are responsible for the early appearance of the  $\nu(\text{C}\equiv\text{N})$  mode at  $\sim 2203\text{cm}^{-1}$  during the TEMAH exposure on NSi at 67°C. Again, the strong and distinct C-H stretching modes at  $\sim 2800\text{-}3000\text{ cm}^{-1}$  and their correlation peaks, such as 877, 980

and  $1213\text{ cm}^{-1}$  for TEMAH vapor due to incomplete evacuation shown in the spectra of 123-496°C TEMAH exposure are not related to any change on substrate (also see **Fig. 3-1 (b)** the TEMAH vapor spectrum). Different from TEMAH exposures on H/Si(100) and OSi, no prominent peak at  $1000\text{ cm}^{-1}$  is found in the very first TEMAH exposure on NSi at 67°C. The prevailing nitrogen-contained groups on NSi substrate would have reduced the growth of Hf-O-Si moiety, and this observation is consistent with the mode assignment of  $1000\text{ cm}^{-1}$  for Hf-O-Si.

As shown by the spectra in **Section 3.3 A-C**, the CVD growth features start to appear in IR absorption spectra during TEMAH exposure when silicon substrate temperatures are raised up to more than about 300°C. The CVD grown films contain carbon-nitrogen-oxygen alloy compounds and metallic carbonyl network. At substrate temperatures lower than 300°C before CVD continuous growth takes place, the appearance of the peak at  $\sim 1550\text{ cm}^{-1}$  indicates a portion of ethyl-methyl-amino groups of adsorbed TEMAH has been oxidized under the existent growth conditions.

## Conclusion

The vibrational spectra of pure TEMAH vapor can be well described by *ab initio* DFT vibrational calculations, using a two-parameter anharmonicity scaling. An inconsistency in mode frequencies and intensities of the lower C-H stretching frequency region  $\sim 2850\text{-}2750\text{ cm}^{-1}$  can be accounted for by Fermi resonances due mostly to the coupling of unperturbed (calculated)  $\nu_s(\text{CH}_3)_{\text{methylamino group}} \sim 2799\text{ cm}^{-1}$  and the overtone of  $\delta_s(\text{CH}_3)_{\text{methylamino group}} \sim 1420\text{ cm}^{-1}$ . TEMAH vapor was found to be much less reactive to  $\text{O}_2$  than to  $\text{H}_2\text{O}$  or  $\text{D}_2\text{O}$ . The major mixture products with  $\text{O}_2$ ,  $\text{D}_2\text{O}$  and  $\text{H}_2\text{O}$  are of ether-

like (-C-O-C-) and tertiary alkylamine-like (N(R<sub>1</sub>R<sub>2</sub>R<sub>3</sub>)) compounds. TEMAH also reacts with ozone to form CH<sub>2</sub>O, CH<sub>3</sub>NO<sub>2</sub>, CH<sub>3</sub>-N=C=O gaseous products and other carbonyl containing -(C=O)- and -C-O-C- (or -O-C-) compounds. There is no evidence for the formation of oxidized Hf-compounds.

The IR spectra of accumulative TEMAH exposures on different silicon surfaces at raising temperatures show the upper temperature limit for non-continuous CVD growth is about 300°C and is not sensitive to the starting surface reactivity. While raising the substrate temperature will activate reaction as shown in the case with H/Si, in which only its surface defects sites of di- and tri- hydrides are reactive to TEMAH at as low temperature as 67°C.

## References

1. Becke, A.D., *Density-functional exchange-energy approximation with correct asymptotic behavior*. Physical Review A, 1988. 38(6): p. 3098 LP - 3100.
2. Becke, A.D., *Density-functional thermochemistry. III. The role of exact exchange*. The Journal of Chemical Physics, 1993. 98(7): p. 5648-5652.
3. Lee, C., W. Yang, and R.G. Parr, *Development of the Colle-Salvetti correlation-energy formula into a functional of the electron density*. Physical Review B, 1988. 37(2): p. 785 LP - 789.
4. Stephens, P. J., F. J. Devlin, C. F. Chabalowski, and M. J. Frisch, *Ab-Initio Calculation of Vibrational Absorption and Circular-Dichroism Spectra Using Density-Functional Force-Fields*. Journal of Physical Chemistry, 1994. 98(45): p. 11623-11627.
5. Hay, P.J. and W.R. Wadt, *Ab initio effective core potentials for molecular calculations. Potentials for the transition metal atoms Sc to Hg*. The Journal of Chemical Physics, 1985. 82(1): p. 270-283.
6. Andrae, D., U. Huermann, M. Dolg, H. Stoll, and H. Preu, *Energy-adjusted ab initio pseudopotentials for the second and third row transition elements*. Theoretical Chemistry Accounts: Theory, Computation, and Modeling (Theoretica Chimica Acta), 1990. 77(2): p. 123-141.
7. Perdew, J.P., K. Burke, and M. Ernzerhof, *Generalized gradient approximation made simple*. Physical Review Letters, 1996. 77(18): p. 3865-3868.
8. Schafer, A., C. Huber, and R. Ahlrichs, *Fully optimized contracted Gaussian basis sets of triple zeta valence quality for atoms Li to Kr*. The Journal of Chemical Physics, 1994. 100(8): p. 5829-5835.

9. Weigend, F. and R. Ahlrichs, *Balanced basis sets of split valence, triple zeta valence and quadruple zeta valence quality for H to Rn: Design and assessment of accuracy*. Physical Chemistry Chemical Physics, 2005. 7(18): p. 3297-3305.
10. Yoshida, H., K. Takeda, J. Okamura, A. Ehara, and H. Matsaura, *A new approach to vibrational analysis of large molecules by density functional theory: Wavenumber-linear scaling method*. Journal of Physical Chemistry A, 2002. 106(14): p. 3580-3586.
11. Kudoh, S., M. Takayanagi, and M. Nakata, *Infrared spectra of Dewar 4-picoline in low-temperature argon matrices and vibrational analysis by DFT calculation*. Chemical Physics Letters, 2000. 322(5): p. 363-370.
12. Berezin, K.V., V.V. Nechaev, and T.V. Krivokhizhina, *Application of a method of linear scaling of frequencies in calculations of the normal vibrations of polyatomic molecules*. Optics and Spectroscopy, 2003. 94(3): p. 357-360.
13. Berezin, K.V., V.V. Nechaev, and P.M. El'kin, *Anharmonic analysis of the vibrational states of pyrimidine by the density functional method*. Optics and Spectroscopy, 2004. 97(2): p. 210-220.
14. Berezin, K.V. and V.V. Nechaev, *Comparison of theoretical methods and basis sets for ab initio and DFT calculations of the structure and frequencies of normal vibrations of polyatomic molecules*. Journal of Applied Spectroscopy, 2004. 71(2): p. 164-172.
15. M. J. Frisch, G. W. Trucks, H. B. Schlegel, G. E. Scuseria, , J. R. Cheeseman M. A. Robb, V. G. Zakrzewski, J. A. Montgomery, Jr., , J. C. Burant R. E. Stratmann, S. Dapprich, J. M. Millam, , K. N. Kudin A. D. Daniels, M. C. Strain, O. Farkas, J. Tomasi, , M. Cossi V. Barone, R. Cammi, B. Mennucci, C. Pomelli, C. Adamo, , J. Ochterski S. Clifford, G. A. Petersson, P. Y. Ayala, Q. Cui, , P. Salvador K. Morokuma, J. J. Dannenberg, D. K. Malick, , K. Raghavachari A. D. Rabuck, J. B. Foresman, J. Cioslowski, , A. G. Baboul J. V. Ortiz, B. B. Stefanov, G. Liu, A. Liashenko, , I. Komaromi P. Piskorz, R. Gomperts, R. L. Martin, D. J. Fox, , M. A. Al-Laham T. Keith, C. Y. Peng, A. Nanayakkara, M. Challacombe, , B. Johnson P. M. W. Gill, W. Chen, M. W. Wong, J. L. Andres, , and M. Head-Gordon C. Gonzalez, E. S. Replogle, and J. A. Pople, *Gaussian 98*. 2001, Gaussian, Inc.: Pittsburgh PA.
16. M. J. Frisch, G.W.T., H. B. Schlegel, G. E. Scuseria, M. A. Robb, J. R. Cheeseman, J. A. Montgomery, Jr., T. Vreven, K. N. Kudin, J. C. Burant, J. M. Millam, S. S. Iyengar, J. Tomasi, V. Barone, B. Mennucci, M. Cossi, G. Scalmani, N. Rega, G. A. Petersson, H. Nakatsuji, M. Hada, M. Ehara, K. Toyota, R. Fukuda, J. Hasegawa, M. Ishida, T. Nakajima, Y. Honda, O. Kitao, H. Nakai, M. Klene, X. Li, J. E. Knox, H. P. Hratchian, J. B. Cross, C. Adamo, J. Jaramillo, R. Gomperts, R. E. Stratmann, O. Yazyev, A. J. Austin, R. Cammi, C. Pomelli, J. W. Ochterski, P. Y. Ayala, K. Morokuma, G. A. Voth, P. Salvador, J. J. Dannenberg, V. G. Zakrzewski, S. Dapprich, A. D. Daniels, M. C. Strain, O. Farkas, D. K. Malick, A. D. Rabuck, K. Raghavachari, J. B. Foresman, J. V. Ortiz, Q. Cui, A. G. Baboul, S. Clifford, J. Cioslowski, B. B. Stefanov, G. Liu, A. Liashenko, P. Piskorz, I. Komaromi, R. L. Martin, D. J. Fox, T. Keith, M. A. Al-Laham, C. Y. Peng, A. Nanayakkara, M. Challacombe, P. M. W. Gill, B. Johnson, W. Chen, M.

- W. Wong, C. Gonzalez, and J. A. Pople, *Gaussian 03*. 2004, Gaussian, Inc.: Wallingford CT.
17. Pouchert, C.J. and A.C. Company, *The Aldrich library of FT-IR spectra*. Ed. 1 ed. 1985, Milwaukee, Wis: Aldrich Chemical Co.
  18. Alpert, N.L., W.E. Keiser, and H.A. Szymanski, *IR; theory and practice of infrared spectroscopy*. 2d ed. 1970, New York: Plenum Press. 380.
  19. Bellamy, L.J., *The infra-red spectra of complex molecules*. 3rd ed. 1975: London : Chapman and Hall ; New York : Wiley,. 433.
  20. Nakanishi, K., *Infrared absorption spectroscopy, practical*. 1962, San Francisco: Holden-Day. 233.
  21. Herzberg, G., *Infrared and Raman Spectra Of Polyatomic Molecules*. Molecular Spectra and Molecular Structure. Vol. II. 1945: Van Nostrand Reinhold Co.
  22. Andrews, G.V.C.a.L., *Reactions of Laser Ablated Titanium, Zirconium, and Hafnium Atoms with Oxygen Molecules in Condensing Argon*. J. Phys. Chem., 1995. 99(17): p. 6356-6366.
  23. Stein, S.E., "Infrared Spectra", in *NIST Chemistry WebBook, NIST Standard Reference Database Number 69*, P.J. Linstrom and W.G. Mallard, Editors. 2005.
  24. Davydov, A., *Molecular spectroscopy of oxide surfaces*, ed. N.T. Sheppard. 2003: Wiley, c2003. 668.
  25. Elliott, S.D., *Models for ALD and MOCVD growth of rare earth oxides*, in *Rare Earth Oxide Thin Films: Growth, Characterization , and Applications*. 2007, SPRINGER-VERLAG BERLIN: Berlin. p. 73-86.
  26. Jones, A. C., H. C. Aspinall, P. R. Chalker, R. J. Potter, T. D. Manning, Y. F. Loo, R. O'Kane, J. M. Gaskell, and L. M. Smith, *MOCVD and ALD of high-kappa dielectric oxides using alkoxide precursors*. Chemical Vapor Deposition, 2006. 12(2-3): p. 83-98.
  27. Puurunen, R.L., M. Lindblad, A. Rootc, and A.O.I. Krausea, *Successive reactions of gaseous trimethylaluminium and ammonia on porous alumina*. Physical Chemistry Chemical Physics, 2001. 3(6): p. 1093-1102.
  28. Lacerda, M.M., F.L. Freire, and G. Mariotto, *Raman spectroscopy of annealed carbon nitride films deposited by RF-magnetron sputtering*. Diamond and Related Materials, 1998. 7(2-5): p. 412-416.
  29. Shi, J.R., Y.J. Xu, and J. Zhang, *Study on amorphous carbon nitride film prepared by facing target sputtering*. Thin Solid Films, 2005. 483(1-2): p. 169-174.
  30. Widlow I., C.Y.-W., *Synthesis and characterisation of carbon nitride thin films*. International Materials Reviews, 2002. 47: p. 153-167.
  31. Ning, Jiang, S. Xu, K. N. Ostrikov, Chai Jianwei, Li Yinan, Koh Mei Ling, and S. Lee, *Synthesis and structural properties of Al---C---N---O composite thin films*. Thin Solid Films, 2001. 385(1-2): p. 55-60.
  32. Gao, Y., J. Wei, D. H. Zhang, Z. Q. Mo, P. Hing, and X. Shi, *Effects of nitrogen fraction on the structure of amorphous silicon-carbon-nitrogen alloys*. Thin Solid Films, 2000. 377-378: p. 562-566.
  33. Kouvetakakis, J., Michael Todd, Barry Wilkens, Anil Bandari, and Nigel Cave, *Novel Synthetic Routes to Carbon-Nitrogen Thin Films*. Chem. Mater., 1994. 6(6): p. 811-814.

34. M. Ricci, M.T., F. Auguste, R. Canet, P. Delhaes, C. Guimon, G. Pfister-Guillouzo, B. Nysten, J.P. Issi, *Relationship between the structural organization and the physical properties of PECVD nitrogenated carbons*. Journal of Materials Research, 1993. 8(3): p. 480-488.
35. Moalla, S. and H. Zarrouk, *Sol-gel processing of Zr(C,N,O) and Al(C,N,O) powders*. Journal of Materials Synthesis and Processing, 1999. 7(3): p. 137-143.
36. Szorenyi, T., C. Fuchs, E. Fogarassy, J. Hommet, and F. Le Normand, *Chemical analysis of pulsed laser deposited a-CN<sub>x</sub> films by comparative infrared and X-ray photoelectron spectroscopies*. Surface and Coatings Technology, 2000. 125(1-3): p. 308-312.
37. Chertihin, G.V. and L. Andrews, *Infrared-Spectra of Zrh<sub>4</sub> and Hfh<sub>4</sub> in Solid Argon*. Journal of the American Chemical Society, 1995. 117(23): p. 6402-6403.
38. Chertihin, G.V. and L. Andrews, *Reactions of Laser-Ablated Zr and Hf Atoms with Hydrogen - Matrix Infrared-Spectra of the Mh, Mh(2), Mh(3), and Mh(4) Molecules*. Journal of Physical Chemistry, 1995. 99(41): p. 15004-15010.
39. Mazur, U., *Infrared study of aluminum nitride films prepared by ion beam deposition. 1. Effects of film thickness, aging, and moisture*. Langmuir, 1990. 6(8): p. 1331-1337.
40. Tsu, D.V., G. Lucovsky, and M.J. Mantini, *Local atomic structure in thin films of silicon nitride and silicon diimide produced by remote plasma-enhanced chemical-vapor deposition*. Physical Review B, 1986. 33(10): p. 7069 LP - 7076.
41. Lin, K.-C. and S.-C. Lee, *The structural and optical properties of a-SiN<sub>[sub x]</sub>:H prepared by plasma-enhanced chemical-vapor deposition*. Journal of Applied Physics, 1992. 72(11): p. 5474-5482.
42. Shih, An, Shin-Hung Yeh, Si-Chen Lee, and T. R. Yang, *Structural differences between deuterated and hydrogenated silicon nitride/oxy-nitride*. Journal of Applied Physics, 2001. 89(10): p. 5355-5361.



## CHAPTER 4

# TEMAH/ D<sub>2</sub>O HAFNIUM OXIDE ALD ON SILICON SURFACES

ALD of hafnium oxide is carried out by alternate dosing of TEMA and an oxidizing precursor (D<sub>2</sub>O (H<sub>2</sub>O) and ozone/O<sub>2</sub>) separated by the evacuation of residual precursors and gas phase products [1-5]. The stationary growth stage at a higher number of cycles shows a linear growth rate [6-9], while at the initial and the transitional stages the growth rate and the film composition are strongly affected by the chemistry and the adsorbed species on the starting surfaces. These surface reactions are not so well understood and more investigations are needed to better understand the nucleation and the film growth mechanisms. In this chapter, *in situ* IR spectra are presented to look into the early stages of film growth by TEMA and D<sub>2</sub>O exposure of SC2 oxidized, H-terminated and nitridized silicon surfaces.

### 4.1 ALD of Hafnium Oxide on H/Si(111)

H/Si(111) is prepared according to the sample preparation procedures in Chapter 1 and immediately loaded in the ALD chamber. The heated substrate (100°C) is then exposed to 10-sec TEMA carried by ultra-pure nitrogen gas (200 sccm) and subsequent 10-sec D<sub>2</sub>O vapor (~ 3 Torr). IR spectra have been obtained at 60°C substrate temperature in the grazing incidence (70°) geometry.

#### A. Transmission IR Spectrum Overview

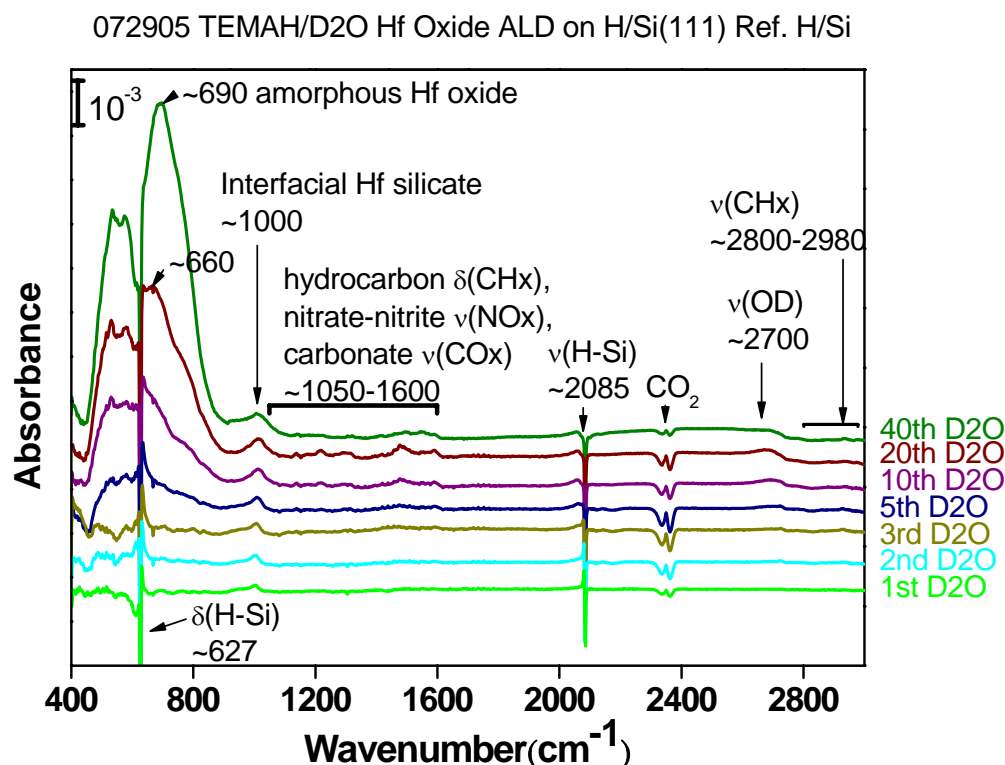


Fig. 4-1 Transmission IR absorption spectra of TEMAH/D<sub>2</sub>O hafnium oxide ALD on H/Si(111) up to 40 cycles referenced to the starting H/Si(111) surface.

**Figure 4-1** shows transmission absorption IR spectra of H/Si(111) during TEMAH/D<sub>2</sub>O ALD cycles. The CO<sub>2</sub> features in 2300–2400  $\text{cm}^{-1}$  are due to the purge variation in the IR optical setup, while the water vapor feature due to the same course has been subtracted from the presented spectra to show the profile of peaks in the 1050-1600  $\text{cm}^{-1}$  frequency range. Besides CO<sub>2</sub> and H<sub>2</sub>O artifacts due to the purge variation, the condensed water from the liquid nitrogen cooled MCT/B detector gives rise to a very intense and broad signal at 3020 – 3620  $\text{cm}^{-1}$ , thus obscuring OH, NH<sub>x</sub> and CH<sub>x</sub> stretching modes on the substrate surface. The intensities of H-Si bending (627  $\text{cm}^{-1}$ ) and stretching mode (2085  $\text{cm}^{-1}$ ) are decreased, but the modes at 690  $\text{cm}^{-1}$ , 1000  $\text{cm}^{-1}$ , 1050-1600  $\text{cm}^{-1}$ , 2700  $\text{cm}^{-1}$  and 2800-2980  $\text{cm}^{-1}$  are growing with the ALD cycles. The broad

band at  $690\text{cm}^{-1}$ , growing almost linearly with ALD cycles is assigned to hafnium oxide. The interfacial mode at  $1000\text{ cm}^{-1}$  can be assigned to either Si-O-Si as the result of oxygen insertion to Si backbonds [10-16] or Hf-O-Si stretching [17].

According to Davydov/ Nakamoto [18, 19], solid state metal-oxygen bond vibrational frequencies are  $800\text{-}900\text{ cm}^{-1}$  for M-O-M or  $900\text{-}1000\text{ cm}^{-1}$  for M=O. But M=O (Hf=O) is very unlikely to be responsible for the mode at  $\sim 1000\text{cm}^{-1}$  for the following three reasons. (1) M=O is not stable at high temperature, and no loss of the mode is observed during post-annealing up to  $> 300^{\circ}\text{C}$ . (2) There is no apparent reason why M=O should increase during the first 10 ALD cycles and stop growing after 10 ALD cycles. (3) Assuming the same force constant, the stretching frequency is inversely proportional to the reduced mass. Due to its heavy mass (hafnium atomic weight  $\sim 178$ ) Hf=O stretching frequency should shift to a lower frequency by  $\sim 100\text{cm}^{-1}$  compared to that of the period IV transition metals such as Cr, Mn, V, Fe and Cu (atomic weight  $48\sim 65$ ).

The Mode at  $2700\text{cm}^{-1}$ , right in the characteristic O-D stretching range, comes from the reaction product segment of  $\text{D}_2\text{O}$ . The modes in  $2800\text{-}2980\text{cm}^{-1}$  are the characteristic C-H stretching modes of hydrocarbon species. While there are many overlaps of characteristic modes related to TEMAH/ $\text{D}_2\text{O}$  reaction products in the  $1050\text{-}1600\text{cm}^{-1}$  frequency range, some modes in this range could be related to the C-H stretching modes. Therefore more elaborate systematic work and care will be needed for further mode assignments in  $1050\text{-}1600\text{cm}^{-1}$  to identify the surface species.

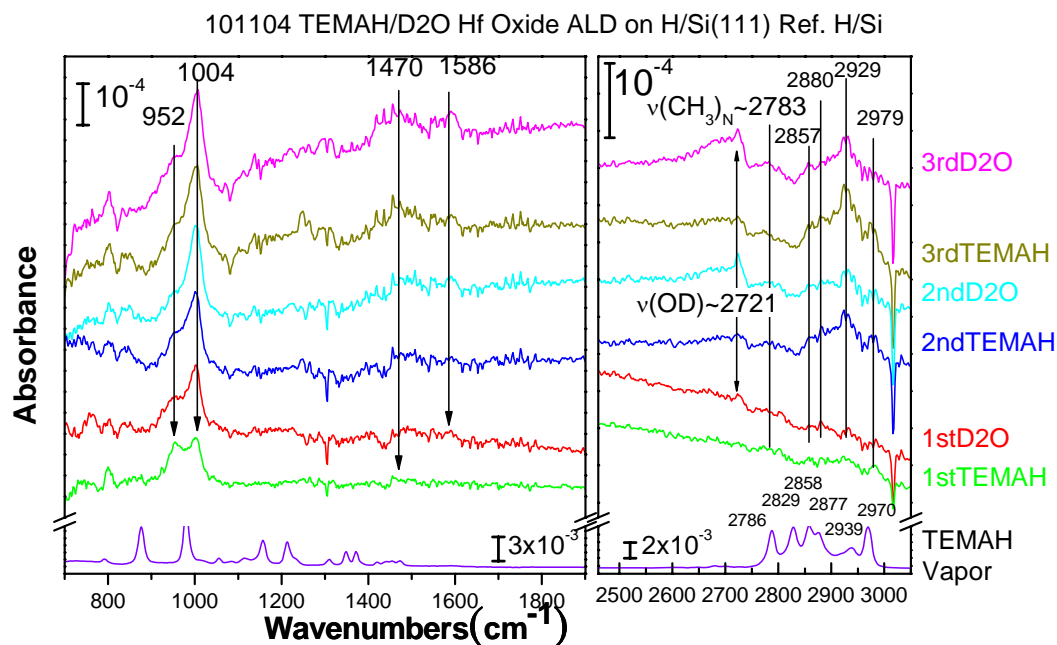


Fig. 4-2 Comparison of the half-cycle exposure transmission IR spectra of TEMAH/D<sub>2</sub>O hafnium oxide ALD growth and the TEMAH gas phase spectrum in the frequency range 700-1900  $\text{cm}^{-1}$  and 2550-3050  $\text{cm}^{-1}$ .

**Fig. 4-2** shows the IR absorption spectra of surface species after each ALD half cycle steps together with the TEMAH gas phase spectrum. The observed C-H stretching ( $2979, 2929, 2880, 2857, 2783 \text{ cm}^{-1}$ ), O-D stretching ( $2721, 2699 \text{ cm}^{-1}$ ), and modes at  $1470, 1586, 952$  and  $1004 \text{ cm}^{-1}$  are originated from the adsorbed species. Compared with the TEMAH gas phase spectrum, they show little resemblance in mode frequencies and relative intensities. The modes at  $1586 \text{ cm}^{-1}$  and  $1050\text{-}1400 \text{ cm}^{-1}$  range do not correspond to the alkylamino ligand, thus indicating some alkylamino ligand decomposition during the ALD process.

The weak and broad  $2783 \text{ cm}^{-1}$  mode, however, can be related to the C-H stretching of methylamino group and might imply some remaining alkylamino groups. The modes at  $2979, 2929, 2880$  and  $2857 \text{ cm}^{-1}$  respectively correspond to asymmetric and symmetric

C-H stretching vibrations of  $-\text{CH}_3$  and  $-\text{CH}_2-$  groups. They grow upon the TEMAH exposure but are only partially removed upon the  $\text{D}_2\text{O}$  exposure.

The sharp  $2721\text{cm}^{-1}$  O-D stretching mode can be assigned either to the isolated OD at the outmost layer of newly adsorbed clusters separated by  $>3\text{\AA}$  from each other or the isolated D-OSi formed by the reaction of  $\text{D}_2\text{O}$  with the Hf-Si sites formed in TEMAH exposure as suggested by Kelly et al. [20]. The broad and asymmetric  $2699\text{cm}^{-1}$  O-D stretching has a lower frequency [19, 21] due to either inter- and intra- molecular hydrogen bonding with another hydroxyl groups or other high electronegative radicals such as C=O, C=N-, -O- and -N-. The broad O-D stretching mode at a low frequency may indicate a portion of OD groups reside in the hafnium oxide moiety.

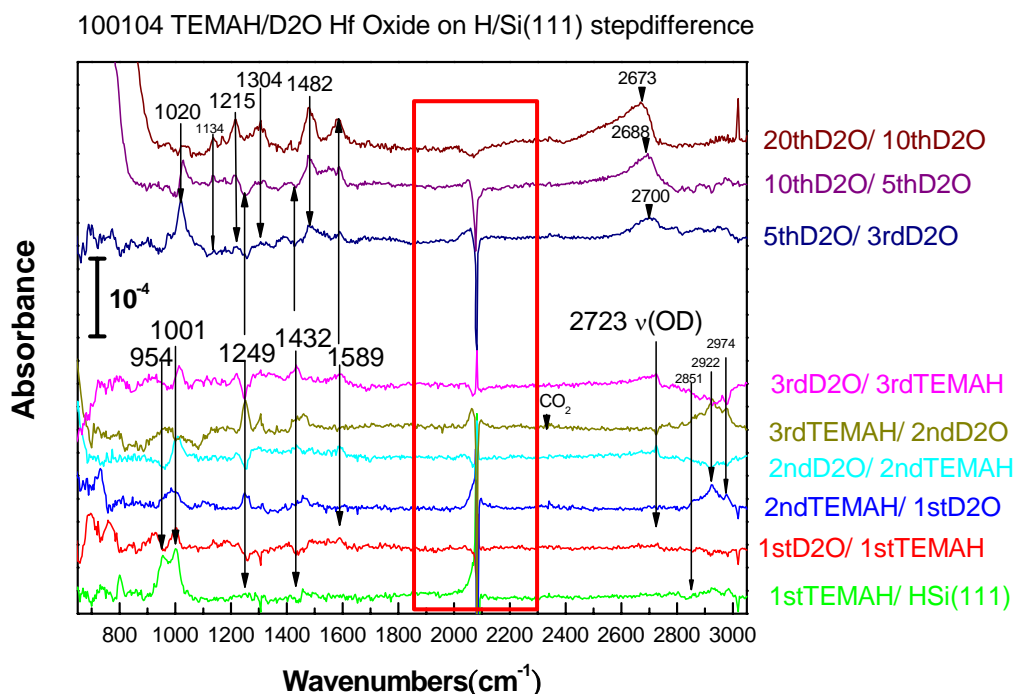


Fig. 4-3 Step difference transmission IR absorption spectra of TEMAH/ $\text{D}_2\text{O}$  hafnium oxide ALD on H/Si(111) in the frequency range of  $650\text{--}3050\text{ cm}^{-1}$ .

**Fig. 4-3** shows an incomplete ligand exchange in the C-H stretching ranges, which may imply the incorporation of trace amount of hydro-carbon residual into the ALD grown film. The absence of adsorbed C-D stretching mode excludes the possibility of the removal the C-H stretching mode by the deuterium replacement.

Step difference spectra of  $1800\text{-}2300\text{cm}^{-1}$  range (see the red blocked region in **Fig. 4-3**) show the continual loss of H-Si stretching mode even at the 20th ALD cycle accompanied by broadening and frequency shifting mostly induced by TEMAH exposure. Overall the H-Si stretching mode shifts to lower frequency with the number of ALD cycles; e.g.,  $\nu(\text{H-Si})$  at  $2076\text{cm}^{-1}$  during  $5^{\text{th}}\sim 10^{\text{th}}$  and  $2066\text{cm}^{-1}$  during  $10^{\text{th}}\sim 20^{\text{th}}$  ALD cycles. Other spectral features include an increase in the modes at  $1589\text{cm}^{-1}$  and  $1432\text{cm}^{-1}$  especially after  $\text{D}_2\text{O}$  exposure, changes in the Hf-O-Si region at  $1100\text{-}900\text{cm}^{-1}$ , ligand removal at  $1463$  and  $1249\text{cm}^{-1}$ , incomplete removal of C-H ( $2990\text{-}2800\text{cm}^{-1}$ ) and OD ( $2723\text{ cm}^{-1}$ ) during the first 3 ALD cycles. At higher number of ALD cycles, the OD stretching mode is red-shifted, and new modes appear at  $1482$ ,  $1304$ ,  $1215$ ,  $1134$  and  $1020\text{cm}^{-1}$ . Weak modes at  $2170$  and  $2120\text{cm}^{-1}$  are due to the variation of trace gaseous product containing  $\text{CD}_x$  groups in the reactor diminishing with time.

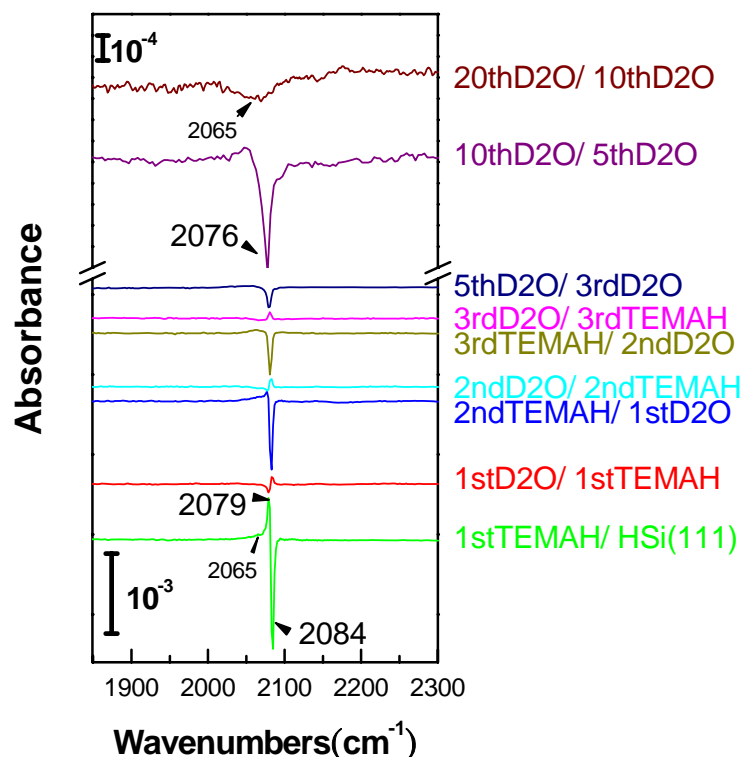
100104 TEMAH/D<sub>2</sub>O Hf Oxide on H/Si(111) stepdifference-H-Si stretching

Fig. 4-4 IR half-cycle step difference absorption spectra of TEMAH/D<sub>2</sub>O hafnium oxide ALD on H/Si(111) in the frequency range of 1850-2300 cm<sup>-1</sup> relevant to H-Si stretching mode.

**Fig. 4-4** shows that TEMAH exposures induce the surface hydrogen loss while the D<sub>2</sub>O exposures mostly change the H-Si nearby environment, giving rise to a blue-shift in the H-Si stretching mode. Even at the 20<sup>th</sup> cycle, trace surface hydrogen is observed. Compared with the loss after TEMAH exposures ( $45 \times 10^{-4} \text{ cm}^{-1}$ ,  $32 \times 10^{-4} \text{ cm}^{-1}$ , and  $24 \times 10^{-4} \text{ cm}^{-1}$  after the 1<sup>st</sup>, 2<sup>nd</sup> and 3<sup>rd</sup> TEMAH exposure), the intensity loss of  $\nu(\text{Si-H})$  after D<sub>2</sub>O exposures is small ( $\sim 4 \times 10^{-4} \text{ cm}^{-1}$ ). Together with the facts that there is only a small overall frequency shift ( $< 17 \text{ cm}^{-1}$ ), this indicates that D<sub>2</sub>O molecules do not have a prevailing reaction with H-Si and there is no significant oxygen insertion into the Si backbond, which would have made more than  $70 \text{ cm}^{-1}$  blue-shift. It may imply that D<sub>2</sub>O

only reacts with the existing ALD grown clusters and the weak blue shift is due to dipole coupling or hydrogen-bond coupling.

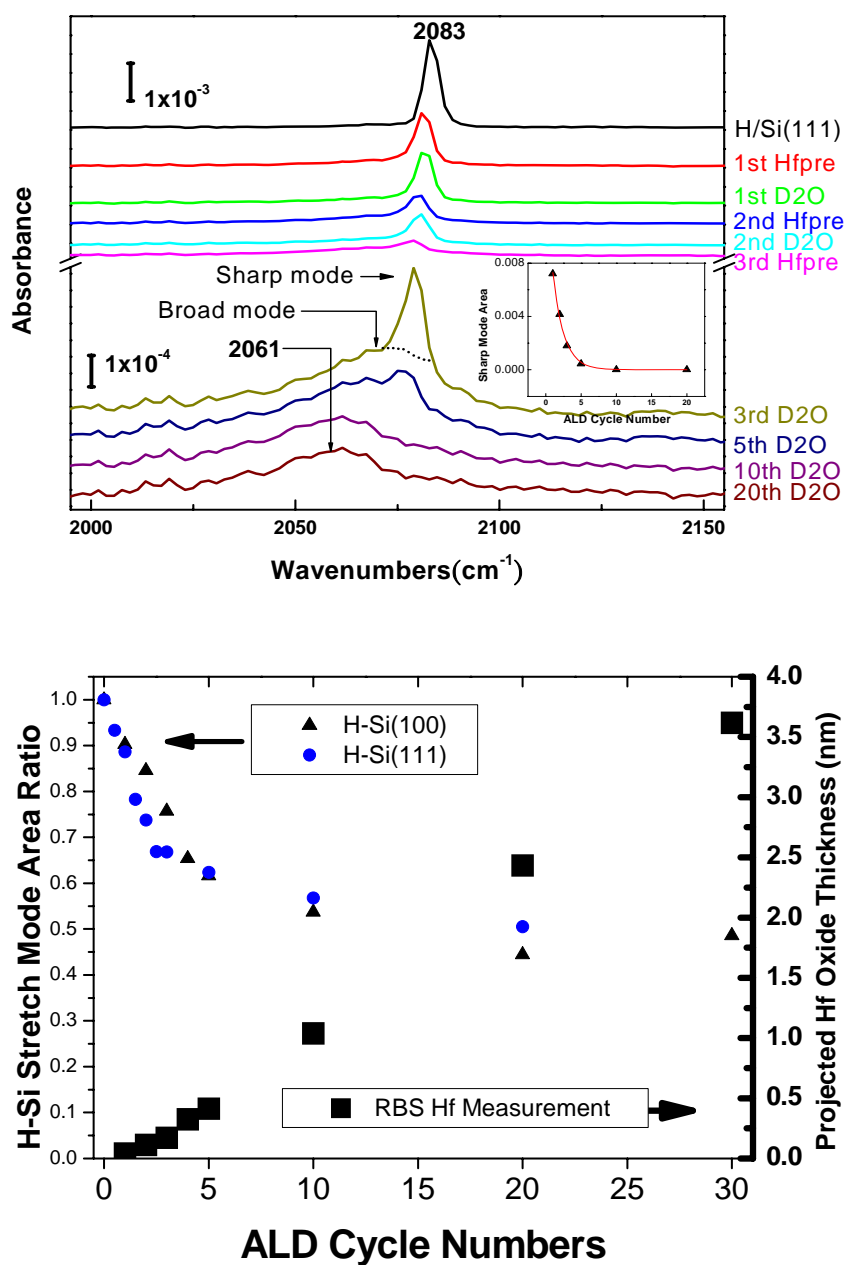


Fig. 4-5 (a) (Top) Transmission IR absorption spectra of H-terminated Si(111) after the specific number of TEMAH and water exposures in the H-Si stretch region. All spectra are referenced to an oxidized surface. Inset plot shows the sharp mode integrated absorbance area varying with ALD cycle numbers. (b) (Bottom) Surface hydrogen coverage after TEMAH and water exposures. The ratio is calculated from the integration of the Si-H stretch mode intensity after a specific number ALD cycles. The hafnium oxide thickness measured with RBS increases linearly with the number of ALD cycles with a slightly smaller growth rate in the first three cycles.



A closer examination of the H–Si stretching absorption band reveals that the initial sharp H–Si band centered at  $2083\text{ cm}^{-1}$  (full width at half-maximum (FWHM) limited by  $4\text{ cm}^{-1}$  resolution) separates into two components (see the 3<sup>rd</sup> D<sub>2</sub>O exposure spectrum of **Fig. 4-5(a)**): a sharp band that slightly red-shifts to  $2076\text{ cm}^{-1}$ , and a broader band (FWHM  $\sim 25\text{ cm}^{-1}$ ) centered at  $2070\text{ cm}^{-1}$  which slowly red-shifts to  $2060\text{ cm}^{-1}$  by the end of 20 cycles. The sharp component represents patches of un-reacted surface hydrogen, while the red-shifted, broader band is associated with Si–H surrounded by surface silicon atoms reacted either directly with Hf, oxygen or other constituents of ALD grown clusters. The presence of a sharp component in the first five cycles (also see the solid triangles in the inset of **Fig. 4-5(a)**) is consistent with a rather inhomogeneous attack of the surface, leaving patches of un-reacted H–Si area.

The summary of the Si–H stretch mode and RBS measurements of hafnium oxide thickness as a function of cycles are presented in the **Fig. 4-5(b)**. The RBS data show that the average number of hafnium atoms per unit area increases linearly ( $2.77 \times 10^{14}\text{ Hf/cm}^2$ , or growth rate  $0.1\text{ nm/cycle}$ ), suggesting that there is no significant incubation period, despite the evidence for nucleation and for an inhomogeneous interface up to five cycles. Although the deposition is slightly slower during the first three cycles, these results are in sharp contrast to the long incubation present for Al<sub>2</sub>O<sub>3</sub> growth at  $300\text{ }^{\circ}\text{C}$  using TMA and D<sub>2</sub>O. TMAH is therefore much more reactive with H-terminated silicon than TMA. Furthermore, about 50% hydrogen remains on the surface even after 30 cycles as shown as the solid circles in **Fig. 4-5(b)**. This hydrogen effectively prevents any oxygen incorporation into the silicon substrate, as evidenced by the lack of SiO<sub>x</sub> TO/LO mode in the range  $1020\text{--}1300\text{ cm}^{-1}$  (see **Fig. 4-2** or **Fig. 4-3**). This result differs from the growth

of  $\text{Al}_2\text{O}_3$  for which interfacial  $\text{SiO}_2$  is formed during the first a few ALD cycles. Hydrogen removal and subsequent oxidation in the latter case may be due to the higher growth temperature (300 °C for  $\text{Al}_2\text{O}_3$  versus 100°C for hafnium oxide), but the present results clearly show that hydrogen stabilizes the interface.

## **B. Initial Nucleation Stage**

The average number of hafnium atoms per unit area after 20 ALD cycles on H/Si(100) and H/Si(111) is similar ( $202 \times 10^{14} \text{ cm}^{-2}$  for H/Si(100) and  $205 \times 10^{14} \text{ cm}^{-2}$  for H/Si(111)) and the variation of the intensity loss of  $\nu(\text{H-Si})$  suggests TEMAH/ $\text{D}_2\text{O}$  reactivity is not sensitive to the surface morphology difference between H/Si(100) and H/Si(111) surfaces. But the initial nucleation seeding during the initial ALD (< 5cycles) shows some dependence on the details of their microscopic surface morphologies.

A typical surface hydrogen area density on H/Si(111) is about  $7.8 \times 10^{14} \text{ cm}^{-2}$  [22]. The corresponding defect density for ideal H/Si(111)  $\sim 0.5\%$  [23] to 3% (Jacob et al. 1991:  $5 \times 10^3$  H-Si unit per domain  $\sim 6 \times 10^4 \text{ \AA}^2$  per domain) [24], so the defect (step dihydride and tri-hydride) site area density reactive to TEMAH is estimated about  $0.23 \times 10^{14} \text{ cm}^{-2}$  for H/Si(111). After the 1<sup>st</sup> TEMAH exposure the number of hafnium atoms is about  $1.3 \times 10^{14} \text{ cm}^{-2}$ , and the loss of H-Si stretching area is about 4.2%-6%, i.e.  $0.33 \times 10^{14}$ - $0.47 \times 10^{14} \text{ cm}^{-2}$  H atoms. This implies that TEMAH may react not only with the dihydride and tri-hydride defect sites but also with some terrace mono-hydride sites, and  $\sim 3$ -4 TEMAH molecules form the initial nucleation clusters on H/Si(111) during the first ALD cycle. In the case of H/Si(100) (see Fig. ), a typical hydrogen area density is  $\sim 6.8 \times 10^{14} \text{ cm}^{-2}$ . After the 1<sup>st</sup> ALD cycle the number of hafnium atoms is about  $3.5 \times 10^{14} \text{ cm}^{-2}$ , and the loss of H-Si stretching area is about 11%-16%, i.e.  $0.76 \times 10^{14}$ - $1.1 \times 10^{14} \text{ cm}^{-2}$

H atoms, thus  $\sim 3$ -5 TEMAH molecules forming the initial nucleation clusters on H/Si(100) during the first ALD cycle. In the 2<sup>nd</sup>-5<sup>th</sup> ALD cycles, 5-10 TEMAH molecules form the nucleation clusters on H/Si surfaces, implying that the fresh starting H/Si surface has a higher reaction barrier against TEMAH adsorption. Although the areal number density of hafnium atoms on H/Si(100) is higher than that of H/Si(111), the average nucleation cluster size at the initial growth stage is similar on both H/Si surfaces.

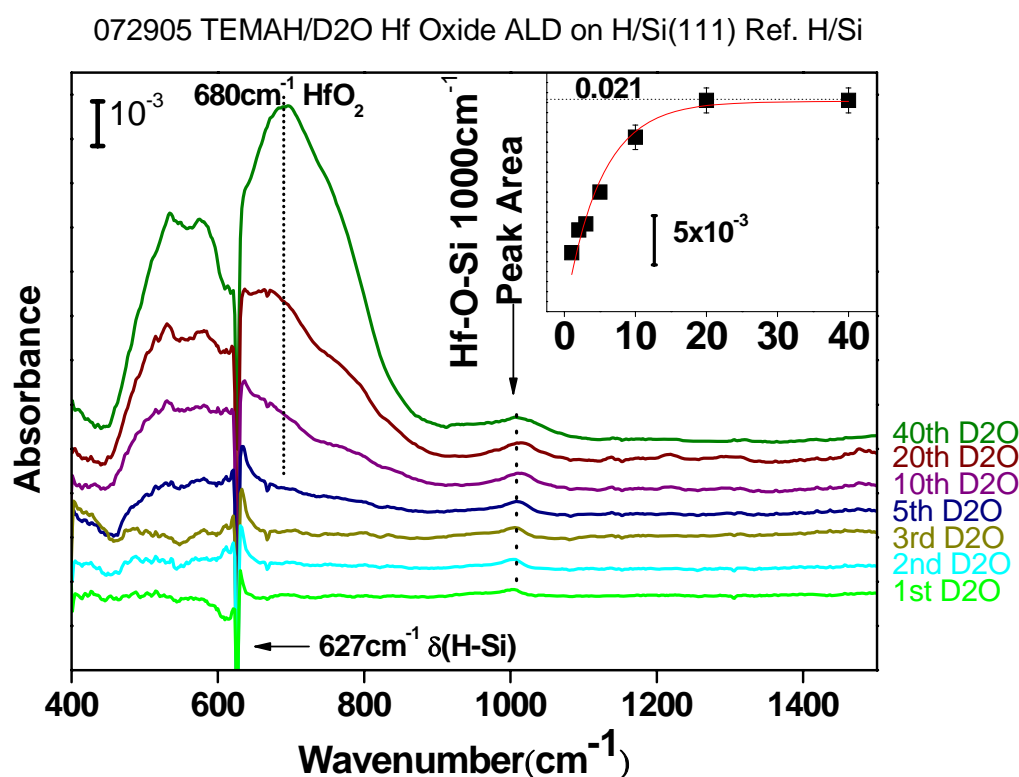


Fig. 4-6 Full-cycle transmission IR absorption spectra referenced to fully H-terminated Si of TEMAH/D<sub>2</sub>O hafnium oxide ALD on H/Si(111) in the frequency range of 400-1300 cm<sup>-1</sup> relevant to the interface and grown film phonon mode showing the development of peaks at  $\sim 510$ , 680 cm<sup>-1</sup>, 1000 cm<sup>-1</sup> during the ALD process (the anti-peak at 627 cm<sup>-1</sup> indicating the loss of surface hydrogen). The inset shows the absorbance integrated area of the 1000cm<sup>-1</sup> band, exhibiting saturation at  $\sim 0.021$  cm<sup>-1</sup> after about 5–10 cycles of hafnium oxide deposition.

**Fig. 4-6** shows the appearance of two bands with the growth of hafnium oxide film.

A broad and structured band centered about 510 and 680 cm<sup>-1</sup> steadily increases in

intensity with the number of ALD cycles, especially after ten cycles of precursor exposures. The amorphous hafnium oxide phonon mode at  $680\text{cm}^{-1}$  does not become manifest till a sufficient size of networked clusters are formed on the substrate.

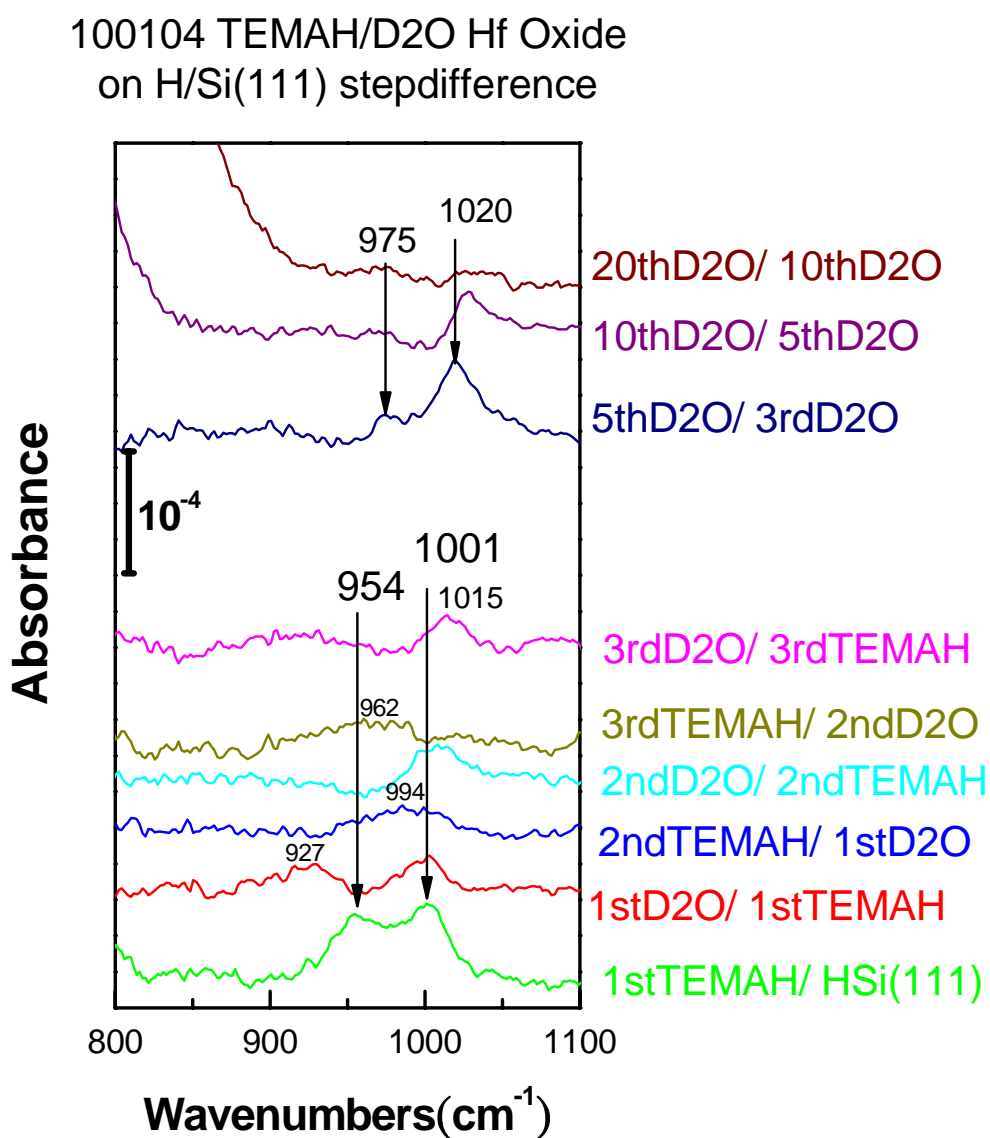


Fig. 4-7 Step difference transmission IR absorption spectra of TEMAH/D<sub>2</sub>O hafnium oxide ALD on H/Si(111) in the frequency range of 800-1100  $\text{cm}^{-1}$ .

The mode at  $1000\text{ cm}^{-1}$ , assigned to overall Hf-O-Si mode shows substructure

evolution during ALD processes (see **Fig. 4-7**). The first TEMAH exposure on H/Si(111) produces two Hf-O-Si modes at 954 and 1001 $\text{cm}^{-1}$ . After the 1<sup>st</sup> D<sub>2</sub>O exposure, the modes at 1001 and 927 $\text{cm}^{-1}$  grow and after the 2<sup>nd</sup> TEMAH exposure, a broad and weak mode at 995 $\text{cm}^{-1}$  appears. After the 2<sup>nd</sup> D<sub>2</sub>O exposure, the 1001 $\text{cm}^{-1}$  mode grows again with a little loss of 954 $\text{cm}^{-1}$  mode. After the 3<sup>rd</sup> TEMAH exposure, another broad and weak mode at 962 $\text{cm}^{-1}$  shows up and after the 3<sup>rd</sup> D<sub>2</sub>O exposure, the mode at 1015 $\text{cm}^{-1}$  grows. After 3 full ALD cycles, the growth rate of blue-shifted 1015 $\text{cm}^{-1}$  mode and the other weaker mode at 975 $\text{cm}^{-1}$  decreases with the ALD cycle. In general, the interfacial hafnium silicate mode gradually shifts to higher frequency when the interfacial network is completed.

The modes at 954 and 1001 $\text{cm}^{-1}$  after the first TEMAH exposure can be related either to the two different Si-O stretching frequencies in Hf-O-Si-O due to the oxygen insertion into the silicon backbond or to the coupled symmetric and anti-symmetric Si-O stretching modes in multiple-coordinated -Hf-(O-Si)<sub>2</sub> of bridging bonding on the surface. Our results concerning the initial nucleation analysis, i.e., ~ 3 hafnium atoms occupying a H-Si site, does not sufficiently disapprove the multiple-coordinated surface bonding, while the IR absorption spectrum comparison of the first TEMAH exposure on different silicon surfaces (**Fig. 4-33**) supports the oxygen insertion into the Si backbond.

### C. Surface Organic Complex

The surface adsorbates after each ALD haf cycle include chemical radical segments made of lighter atoms such as C, N, H (D) and O other than the heavy hafnium atom. These chemical segments, mostly on the surface or partially buried in the hafnium-oxygen aggregation, have infrared absorption bands at higher frequency than 800  $\text{cm}^{-1}$ .

We use a systematic way to analyze the frequency range of 800 - 4000  $\text{cm}^{-1}$  and attempt to identify the possible constituents and structure models for the surface after each ALD half cycle.

**Table 4-1 Principal Relevant Bond Stretching Frequencies[25-27] for TEMAH/D<sub>2</sub>O Hafnium Oxide Growth**

| Typical Bond Stretching Frequency ( $\text{cm}^{-1}$ ) | C  | N  | H (D)  | O   |
|--|--|--|--|---|
| C  | ** $\nu(-\text{C}-\text{C}-)$<br><br>* $\nu(-\text{C}=\text{C}-)$ ~1680-1580<br><br>$\nu(-\text{C}\equiv\text{C}-)$ ~2260-2100 | $\nu(-\text{C}-\text{N}-)$ ~1220-1020<br><br>$\nu(-\text{C}=\text{N}-)$ ~1690-1630<br><br>$\nu(-\text{C}\equiv\text{N}-)$ ~2260-2120 | $\nu(-\text{C}-\text{H}_x)$ ~3000<br><br>$\nu(-\text{C}-\text{D}_x)$ ~2150                         | $\nu(-\text{C}-\text{O}-)$ ~1300-1100<br><br>$\nu(-\text{C}=\text{O})$ ~1800-1650   |
| N  |  | ** $\nu(-\text{N}-\text{N}-)$<br><br>* $\nu(-\text{N}=\text{N}-)$ ~1630-1575   | $\nu(-\text{N}-\text{H}_x)$<br><br>~3500-3300<br><br>$\nu(-\text{N}-\text{D}_x)$<br><br>~2500-2350 | $\nu(-\text{N}-\text{O}-)$ ~1100<br><br>$\nu(-\text{N}=\text{O})$ ~1550;<br><br>$\nu(-\text{O}-\text{N}=\text{O})$ ~1681-1610<br><br>$\nu(-\text{C}-\text{N}=\text{O})$ ~1600-1500<br><br>$\nu(-\text{N}-\text{N}=\text{O})$ ~1500-1430<br><br>$\nu(-\text{C}-\text{NO}_2)$ ~1570-1500, 1370-1300<br><br>$\nu(-\text{O}-\text{NO}_2)$ ~1650-1600, 1300-1250<br><br>$\nu(-\text{N}-\text{NO}_2)$ ~1630-1550, 1300-1250 |
| H (D)  |  |  |  | $\nu(\text{H}-\text{O})$ ~3700<br><br>$\nu(\text{D}-\text{O})$ ~2630  |
| O  |  |  |  | ** $\nu(-\text{O}-\text{O}-)$   |

\*\* Due to the similarity of bonding strength to other single bonds between heterogeneous atoms and the suppressed local dynamic dipole of homogeneous constituents,  $\nu(-\text{C}-\text{C}-)$ ,  $\nu(-\text{N}-\text{N}-)$  and  $\nu(-\text{O}-\text{O}-)$  stretching frequency regions overlap and give weaker absorption intensity. Also the mode frequencies split and vary dramatically with structures and environments, so they are not good characteristic frequencies for the preliminary peak assignment.

\*Similar situation may apply to  $\nu(-\text{C}=\text{C}-)$  and  $\nu(-\text{N}=\text{N}-)$  as well, though to a lesser degree.

In **Fig. 4-3**, except for the H-Si stretching loss and trace  $\text{CD}_x$  gaseous product variation, no other peaks are found within the  $2100\text{-}2260\text{ cm}^{-1}$  region, which excludes the possibility of major surface  $\text{C}\equiv\text{C}$  and  $\text{C}\equiv\text{N}$  species. During the first three ALD cycles, the intensity gain of the C-H stretching ( $2990\text{-}2800\text{ cm}^{-1}$ ) and C-H bending ( $1249\text{-}1463\text{ cm}^{-1}$ ) modes upon TEMAH exposure is larger than the loss upon  $\text{D}_2\text{O}$  exposure, implying incomplete ligand exchange and the incorporation of  $\text{CH}_x$  into the film in this initial growth stage. After 3 full ALD cycles, the  $\text{CH}_x$  stretching modes do not vary as much and new modes at 1482, 1304, 1215 and 1134 (very weak)  $\text{ cm}^{-1}$  starts to increase with the number of ALD cycles. But they do not seem to be correlated with  $\nu(-\text{CH}_x)$ .

According to the characteristic band frequencies listed in Table 4-1, IR spectra in **Fig. 4-3** indicate:

(1) The gain/loss of the modes at 1249 and  $1463\text{ cm}^{-1}$  during TEMAH/ $\text{D}_2\text{O}$  exposures is concurrent with the gain/loss of the  $\text{CH}_x$  stretching at  $2800\text{-}3000\text{ cm}^{-1}$  in the adsorbed Hf-alkylaminno ligand.  $\text{CH}_3\text{-Si}$  ( $\sim 1250\text{ cm}^{-1}$ ) produced by decomposition of alkylaminno ligand may explain the mode at  $1249\text{ cm}^{-1}$ , while very low level of H-Si loss in this initial stage excludes the possibility of alkyl ligand bonding to the surface silicon atoms.

(2) The mode at  $1589\text{ cm}^{-1}$  is too low for the  $\text{C}=\text{O}$  stretching vibration. It is most probably related to  $\nu(-\text{C}=\text{N}-)$ ,  $\nu(-\text{N}=\text{O})$ ,  $\nu(-\text{N}=\text{N}-)$  or  $-\text{NO}_2$  bonding, and the mode at  $1482\text{ cm}^{-1}$  can be their structure-derived mode.

(3) The modes at 1304, 1215 and  $1134\text{ cm}^{-1}$  may be related to  $\nu(-\text{C}-\text{N}-)$ ,  $\nu(-\text{C}-\text{O}-)$ ,  $\nu(-\text{C}-\text{C}-)$ ,  $\nu(-\text{N}-\text{N}-)$ , or their related structure modes.

(4) The intensity increase of the mode at  $1001\text{ cm}^{-1}$  in the first a few ALD cycles and saturated growth of the mode at  $1020\text{ cm}^{-1}$  in 5-20 ALD cycles correlate with the intensity loss of  $\nu(\text{H-Si})$ , and thus are related to the interface formation, which is consistent with the Hf-O-Si assignment in the previous paragraph.

(5) The vibrational frequency of adsorbed species on metal or semiconductor surfaces may show a large shift from that of their molecular counterparts.  $-\text{C}=\text{O}$  on oxide surfaces, for example, has the characteristic frequency range of  $1700\text{-}1500\text{ cm}^{-1}$ , which is lower than that of molecules.

(6) The modes at  $1600\text{-}1100\text{ cm}^{-1}$  increase with  $\text{D}_2\text{O}$  exposures, which suggests that the oxygen-containing compounds (oxygen-nitrogen or oxygen-carbon) may be responsible for these modes.  $-\text{C}-\text{C}-$ ,  $-\text{C}=\text{C}-$ ,  $-\text{N}-\text{N}-$ ,  $-\text{C}-\text{N}-$ ,  $-\text{C}=\text{N}-$  and  $-\text{N}=\text{N}-$  species are covered extendedly in the review literature [19], and the oxygen complexes will be presented in this subsection. **Table 2** and **Table 3** show that  $(\text{Hf}-\text{O})_2\text{C}=\text{O}$ ,  $\text{Hf}-\text{NO}_2$  and  $\text{Hf}(-\text{O})_2\text{NO}$  can be ruled out as the possible surface structures.

The major residual species as a result of incomplete ligand exchange are  $\text{Hf}-\text{N}(-\text{O})(-\text{O}-\text{Hf})$ ,  $(\text{Hf}-\text{O})_2\text{NO}$ ,  $\text{Hf}-\text{O}-\text{N}=\text{O}$ ,  $(\text{Hf}-\text{O})_2\text{N}$ ,  $\text{Hf}-\text{O}-\text{NO}_2$ ,  $\text{Hf}(-\text{O})_2\text{C}=\text{O}$ , and  $\text{Hf}-\text{O}-(\text{CO}_2)$ . Among them,  $\text{Hf}-\text{N}(-\text{O})(-\text{O}-\text{Hf})$ ,  $(\text{Hf}-\text{O})_2\text{NO}$  and  $\text{Hf}-\text{O}-(\text{CO}_2)$  could be the dominant residual compound structures in the film. This observation is also supported by the post-annealing result in the next section. The absolute quantity of the residual compounds in the film, however, cannot be determined due to the lack of IR calibration. RBS does not have enough sensitivity for such light atoms as C, O and N. Moreover *ex situ* RBS measurements are susceptible to the C, O and N contamination during the transportation in atmosphere.



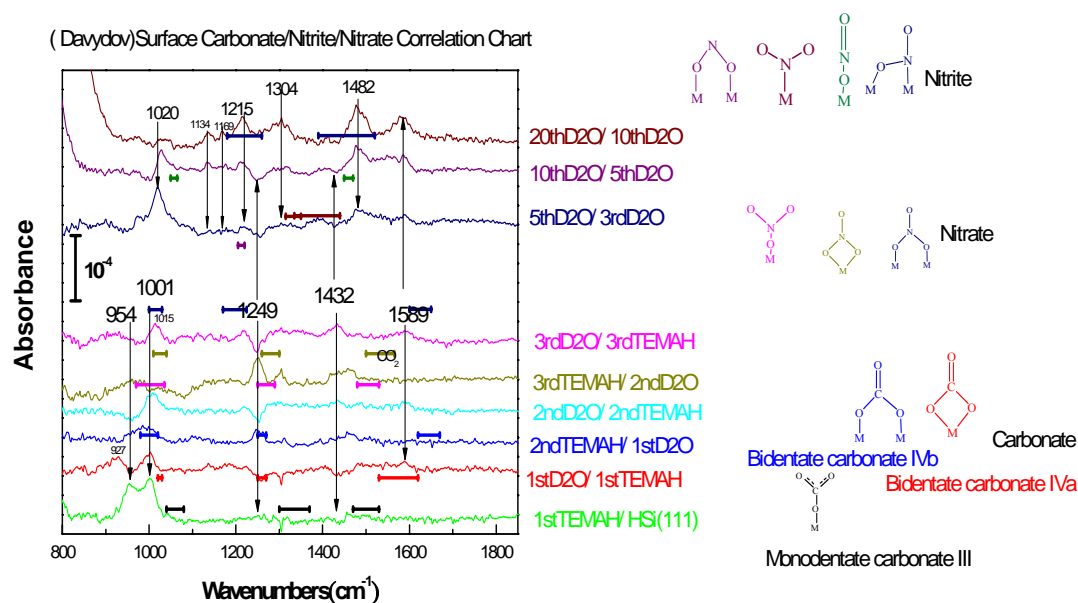
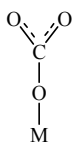
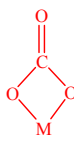
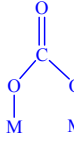
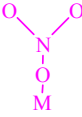
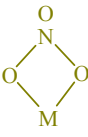




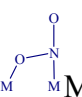


Fig. 4-8 Step difference transmission IR absorption spectra of TEMAH/D<sub>2</sub>O hafnium oxide ALD on H/Si(111) in the frequency range of 800-1850cm<sup>-1</sup> for surface organic complex species identification.

Table 4-2 Correlation Table of Surface Carbonate Compound[19]

| Type of compound   | Spectral range of CO bond stretching vibration (cm-1) |  |   |
|--|---|--|---|
| <br>Monodentate carbonate III | 1530-1470<br>$\nu_{\text{as}}\text{COO}^-$            | 1370-1300<br>$\nu_{\text{s}}\text{COO}^-$  | 1080-1040<br>$\nu\text{C-O}$              |
| M-O-(CO <sub>2</sub> )   |   |  |   |
| <br>Bidentate carbonate IVa   | 1620-1530<br>$\nu\text{C=O}$                          | 1270-1250<br>$\nu_{\text{as}}\text{COO}^-$ | 1030-1020<br>$\nu_{\text{s}}\text{COO}^-$ |
| M(-O-) <sub>2</sub> C=O  |   |  |   |
| <br>Bidentate carbonate IVb   | 1670-1620<br>$\nu\text{C=O}$                          | 1270-1250<br>$\nu_{\text{as}}\text{COO}^-$ | 1020-980<br>$\nu_{\text{s}}\text{COO}^-$  |
| (M-O-) <sub>2</sub> C=O  |   |  |   |

**Table 4-3 Stretching Vibration Frequencies of  $\text{NO}_3^-$  and  $\text{NO}_2^-$  in Inorganic Coordination Compounds[19]**

| Structure   | $\nu_3$ ( $\text{cm}^{-1}$ ) |           | $\nu_1$ ( $\text{cm}^{-1}$ )           |
|---|------------------------------|-----------|--|
| $\text{NO}_3^-$   | 1380                         |           | 1050                                   |
|  $\text{M-O-NO}_2$           | 1530-1480                    | 1290-1250 | 1035-970                               |
|  $\text{M(-O-)}_2\text{NO}$  | 1565-1500                    | 1300-1260 | 1040-1010                              |
|  $(\text{M-O-})_2\text{NO}$  | 1650-1600                    | 1225-1170 | 1030-1000                              |
| Structure   | $\nu_s$ ( $\text{cm}^{-1}$ ) |           | $\nu_{\text{as}}$ ( $\text{cm}^{-1}$ ) |
| $\text{NO}_2^-$   | 1260                         |           | 1330                                   |
|  $(\text{M-O-})_2\text{N}$ | 1220-1205                    |           |  |
|  $\text{M-NO}_2$           | 1440-1335                    |           | 1350-1315                              |
|  $\text{M-O-N=O}$          | 1470-1450                    |           | 1065-1050                              |
|  $\text{M-N(-O)(-O-M)}$    | 1520-1390                    |           | 1260-1180                              |

## D. Post Deposition Annealing

Hafnium oxide grown at 100°C by 20-cycle ALD is annealed at 300 - 700°C for 2 minutes in the vacuum chamber with 100 sccm ultra-pure  $\text{N}_2$  ( ~0.3 Torr). IR spectra were measured without  $\text{N}_2$  purge.

100104 20 cycle TEMAH/D2O Hf Oxide on H/Si(111) Annealing Ref. H/Si(111)

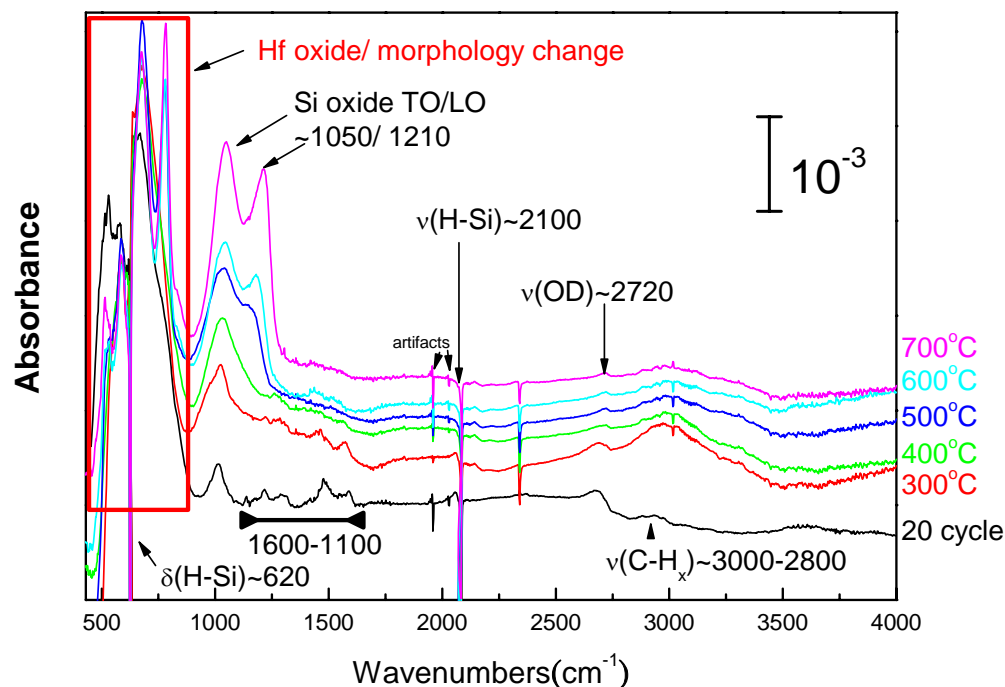


Fig. 4-9 The overall view of annealing spectra taken overnight referenced to H/Si(111) starting surface show baseline structure with a very broad lump in  $3500\text{--}2500\text{cm}^{-1}$  decreasing with spectrometer operation time. The grown OD,  $\text{CH}_x$  and modes in  $1600\text{--}1100\text{ cm}^{-1}$  during ALD are either partially removed or decreasing with the annealing temperatures, while silicon oxide and strong modes  $\sim 900\text{--}500\text{ cm}^{-1}$  appear during annealing.

The OD,  $\text{CH}_x$  and the species in  $1600\text{--}1100\text{ cm}^{-1}$  are partially removed with the annealing temperature, while silicon oxide LO/TO and strong modes at  $900\text{--}500\text{ cm}^{-1}$  appear after annealing.

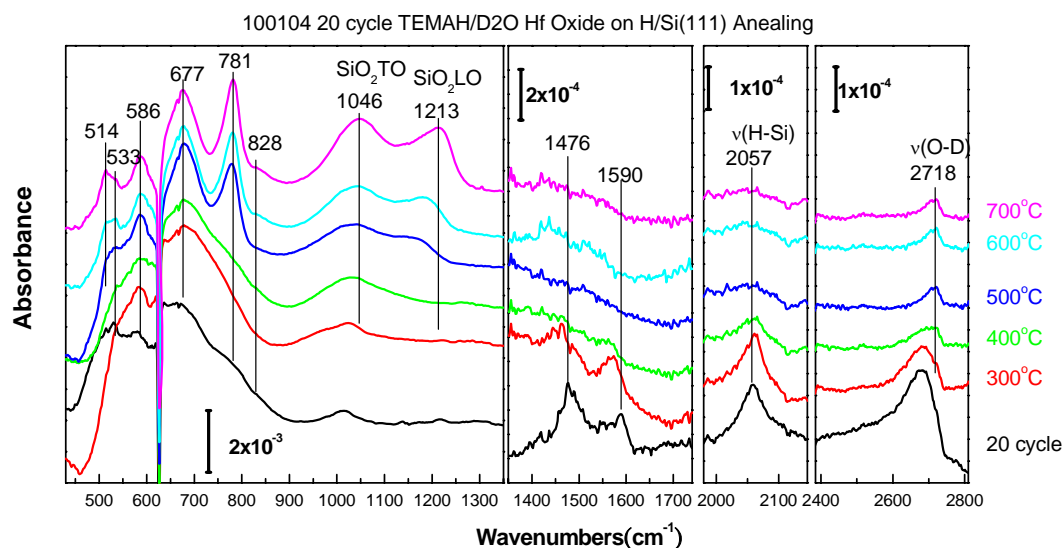


Fig. 4-10 Transmission IR spectra of 20 cycle TEMAH/D<sub>2</sub>O ALD grown hafnium oxide on H/Si(111) annealed up to 300, 400, 500, 600 and 700°C. (The spectra in the third panel from left are reference to the silicon oxide surface, and the spectra in the other panels are referenced to the initial H/Si(111) )

The spectra in **Fig. 4-10** show that the organic species ( $1590$  and  $1476\text{ cm}^{-1}$ ) start to decrease with  $300^{\circ}\text{C}$  annealing. At the same time the broad OD stretch mode peaked at  $2673\text{ cm}^{-1}$  decreases and shifts to a higher frequency  $\sim 2718\text{ cm}^{-1}$  with the annealing temperature. Interstitial non-stoichiometric Si-O ( $\sim 1046\text{ cm}^{-1}$ ) growth concurs with the loss of interfacial mono-hydride and the loss of the  $600\text{ cm}^{-1}$  mode at  $400^{\circ}\text{C}$ , which can be related to the oxygen insertion and the stoichiometry change of the hafnium oxide film which is followed by the interfacial silicon oxide formation at  $\geq 500^{\circ}\text{C}$ . The remaining surface hydrogen (interfacial mono-hydride  $\sim 2067\text{ cm}^{-1}$ ) is quite stable at  $300^{\circ}\text{C}$ , but starts to decrease at  $400^{\circ}\text{C}$  and mostly disappears at  $700^{\circ}\text{C}$ . The modes for crystallized hafnium oxide ( $\sim 514, 586, 677$  and  $781\text{ cm}^{-1}$ ) appear at the loss of the broad as-deposited hafnium oxide mode ( $500\text{--}800\text{ cm}^{-1}$ ) at  $500^{\circ}\text{C}$ . The silicon oxide TO and LO modes ( $\sim 1029$  and  $1166\text{ cm}^{-1}$ ) after  $500^{\circ}\text{C}$  annealing give  $\sim 3\text{--}4\text{ \AA}$  thickness according to the absorbance peak integrated area ( $0.095\text{ cm}^{-1}$ ) calibrated to SC2 chemical silicon oxide ( $5\text{ \AA}$ ).

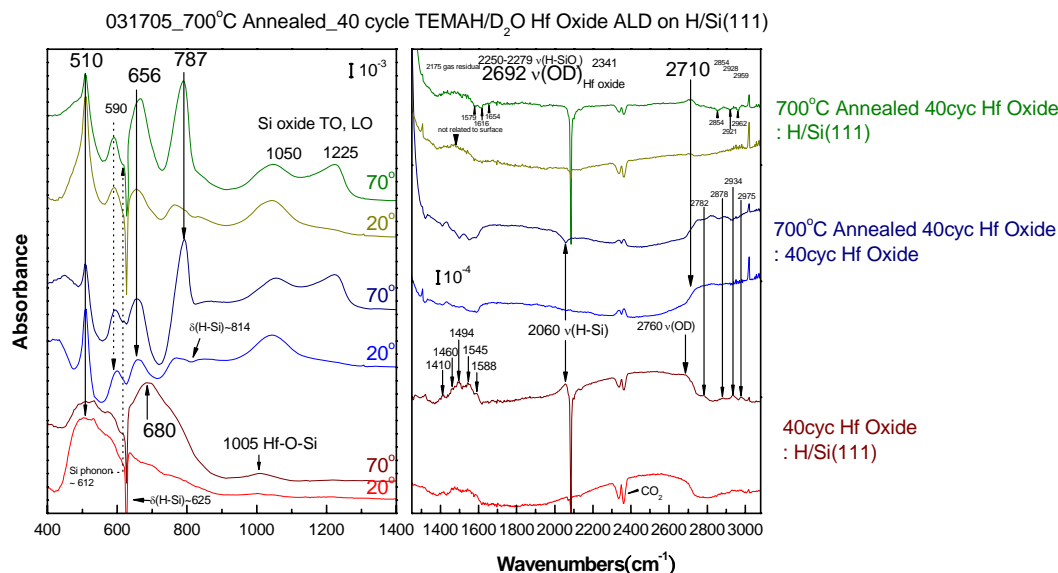


Fig. 4-11 Transmission spectra of 40 cycle TEMAH/D<sub>2</sub>O grown ALD hafnium oxide referenced to H/Si(111) and 700°C annealed spectra referenced to H/Si(111) and as-deposited 40 cycle grown film at incident angles of 20° and 70°.

The IR spectra of the as-deposited and 700°C annealed hafnium oxide film (40-ALD cycle) at 70° and 20° incident angles (**Fig. 4-11**) show the broader 680 cm<sup>-1</sup> mode of amorphous hafnium oxide and the sharper modes at 666 cm<sup>-1</sup> and 787 cm<sup>-1</sup> of crystalline. They are enhanced for polarization perpendicular to surface; i.e., LO modes. The broader 510 cm<sup>-1</sup> mode of amorphous hafnium oxide and the sharper 510 cm<sup>-1</sup> of monoclinic crystalline hafnium oxide [28, 29] are TO-like, which shows an enhancement for polarization parallel to the surface.

Between 20- and 40-cycle ALD hafnium oxide, the intensity of crystalline 40-cycle hafnium oxide modes (~512, 586, 677 and 780 cm<sup>-1</sup>) is ~ 2.5 times higher than that of 20-cycle hafnium oxide, thus supporting its correlation with hafnium oxide crystallization other than the interface variation or new interface formation due to the cross interface diffusion. However, the annealing induced silicon oxide with 20-cycle hafnium oxide is more than that with 40-cycle because of the deep oxidation by the reactor ambient

oxygen source.

## 4.2 Hafnium Oxide grown by ALD with TEMAH / D<sub>2</sub>O on H/Si(100)

Hafnium oxide is grown by ALD with TEMAH/D<sub>2</sub>O on H/Si(100) at the same growth condition as on H/Si(111) in section 4.1.

### A. IR Spectrum Overview

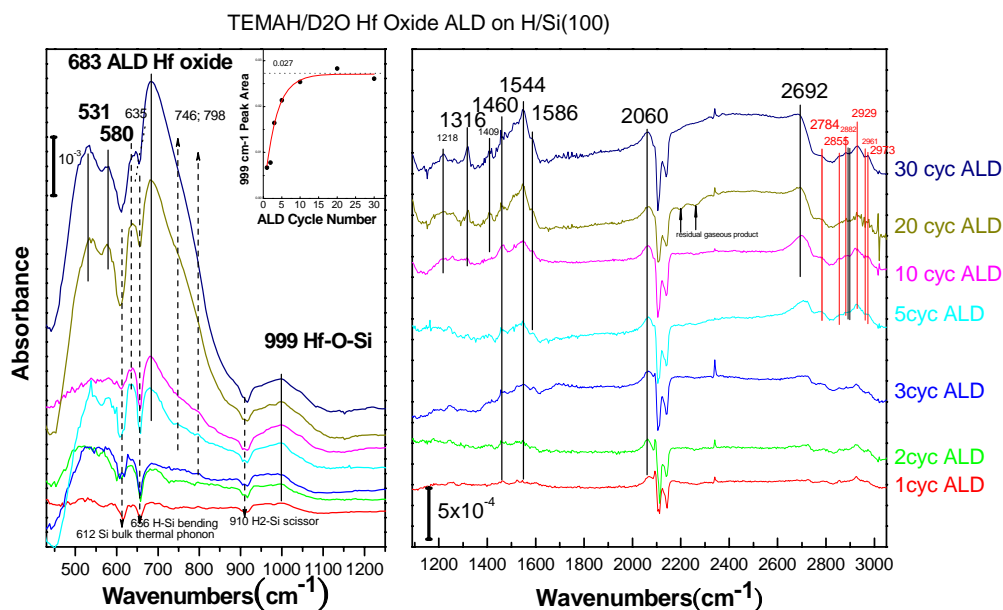


Fig. 4-12 Full cycle transmission spectra of 100°C grown TEMAH/D<sub>2</sub>O hafnium oxide ALD on H/Si(100) referenced to the starting surface

Similar to the hafnium oxide ALD on H/Si(111), IR absorption spectra in **Fig. 4-12** show the amorphous hafnium oxide mode ( $\sim 683\text{cm}^{-1}$ ), the interfacial Hf-O-Si mode ( $\sim 999\text{cm}^{-1}$ ), and the broad OD mode ( $\sim 2685\text{cm}^{-1}$ ) in the film increase with the number of ALD cycles. The bands in the  $1600\text{--}1200\text{cm}^{-1}$  region and the CH<sub>x</sub> stretching modes in  $3000\text{--}2700\text{cm}^{-1}$  are attributed to the organic complex contamination in the film. However,

the intensity of the Hf-O-Si mode eventually saturates at a higher band area of  $0.027\text{cm}^{-1}$  than that on H/Si(111), and the red-shifted H-Si stretching mode due to the environment change around H-Si caused by ALD surface reactions at  $2060\text{ cm}^{-1}$  is stronger in intensity than that on H/Si(111).

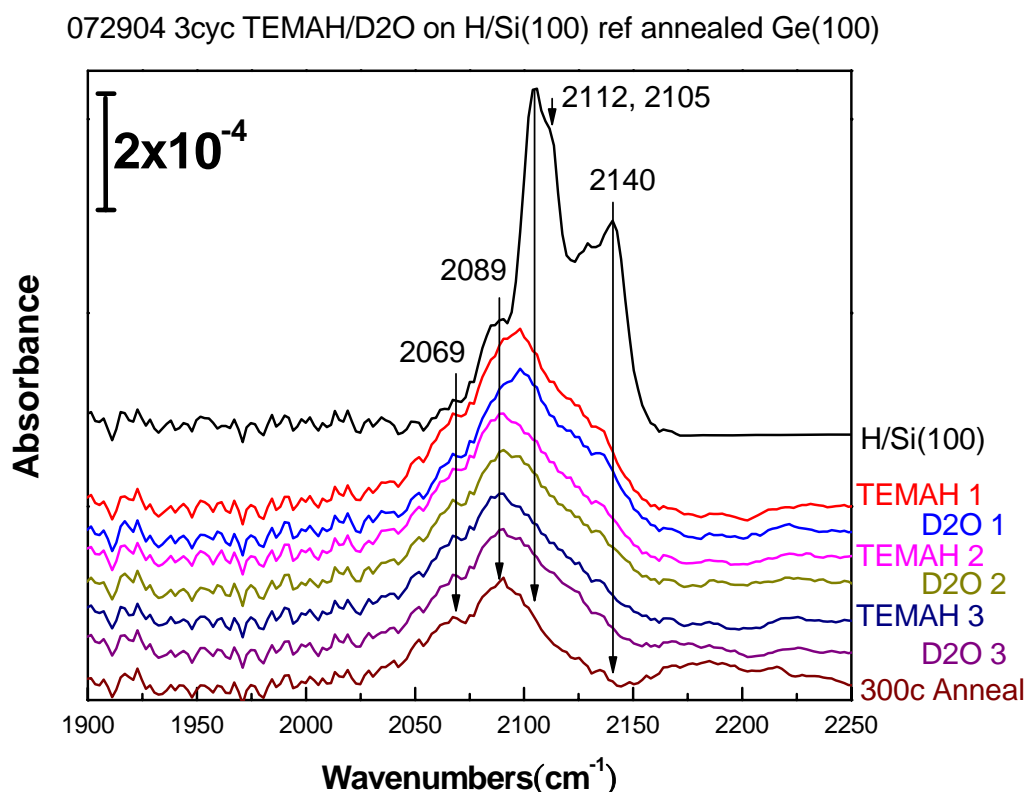


Fig. 4-13 Selected absorbance spectra of TEMAH/D2O exposures on H/Si(100) referenced to  $100^\circ\text{C}$  annealed Ge(100) surface.

**Figure 4-13** shows modes at 2140, 2105 and 2112, and 2089  $\text{cm}^{-1}$  related to the  $\text{H}_3\text{-Si}$ ,  $\text{H}_2\text{-Si}$ , and  $\text{H-Si}$  stretching on H/Si(100). Upon the first TEMAH exposure, the intensity of the  $\text{H}_3\text{-Si}$  and  $\text{H}_2\text{-Si}$  stretching modes decrease dramatically, but the mode at 2089  $\text{cm}^{-1}$  remains almost intact. The mode at 2069  $\text{cm}^{-1}$  grows with the ALD cycles, and the mode at 2100  $\text{cm}^{-1}$  partially survives the first ALD cycle, though this mode

diminishes with latter ALD exposures. There is no significant change in the H-Si stretching region after 2 ALD cycles. The annealing after 3 cycles at 300°C removes a part of 2140  $\text{cm}^{-1}$  shoulder and residual tri-hydride and produces a band at 2170  $\text{cm}^{-1}$  possibly from the oxygen insertion into the silicon backbond. Di-hydride and tri-hydride do not survive at this annealing temperature.

## B. Post Deposition Annealing

The hafnium oxide grown by 20 cycles of TEMAH/D<sub>2</sub>O ALD at 100°C on H/Si(100) is annealed at several different temperatures from 300°C ~ 600°C for 2 minutes in the vacuum chamber with 100 sccm ultra-pure nitrogen gas (~0.3 Torr). The N<sub>2</sub> purge is stopped when IR spectra are taken.

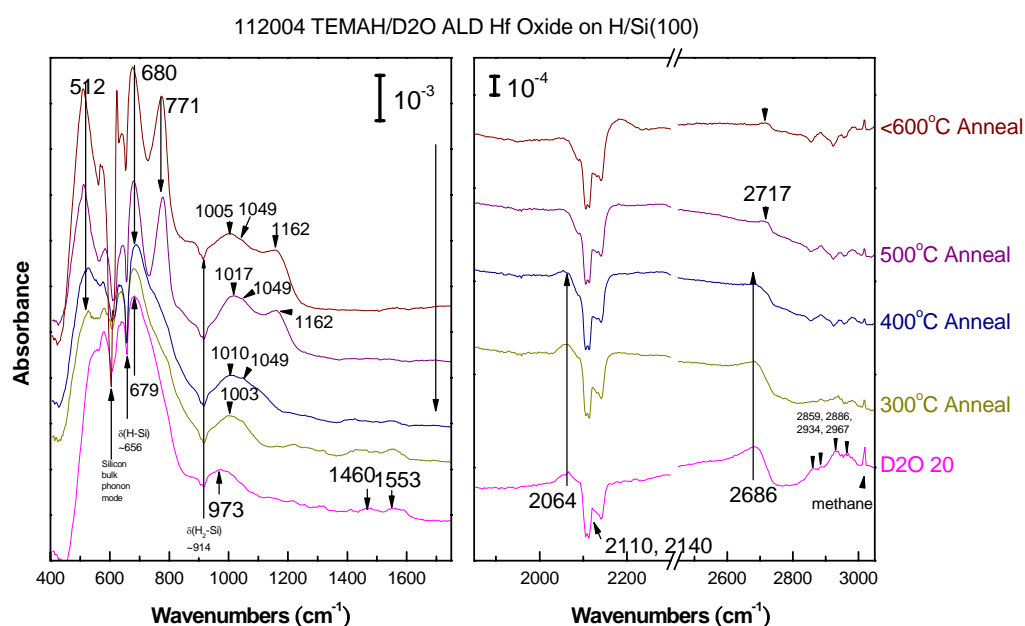


Fig. 4-14 Transmission absorbance spectra of 100°C grown 20 cycle TEMAH/D<sub>2</sub>O ALD hafnium oxide on H/Si(100) surface annealed to 300°C, 400°C, 500°C and some temperature higher than 500°C but lower than 600°C.



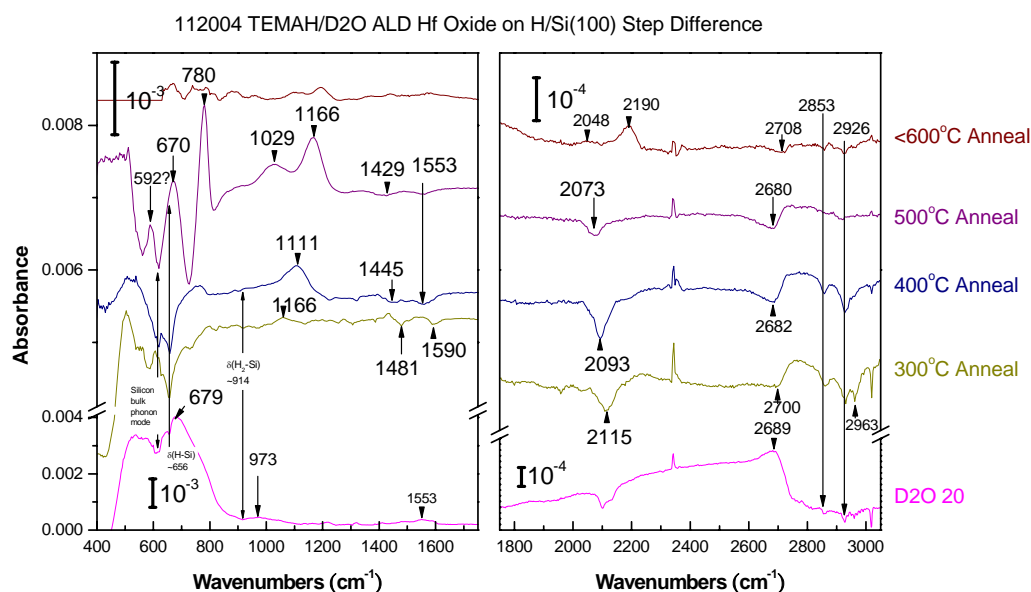


Fig. 4-15 Step difference absorbance spectra of 100°C grown 20 cycle TEMAH/D<sub>2</sub>O ALD hafnium oxide on H/Si(100) surface annealed to 300°C, 400°C, 500°C and some temperature higher than 500°C but lower than 600°C.

The spectra referenced to H/Si(100) starting surface in **Fig. 4-14** and step difference spectra in **Fig. 4-15** show similar changes with annealing in the organic species, hydroxyl groups, hydrides and broad amorphous hafnium oxide and similar growth of silicon oxide.

As shown in section 4.1 and 4.2, the hafnium oxide ALD on silicon oxide free hydrogen terminated silicon surface can grow amorphous hafnium oxide at moderate temperatures less than 300°C without interfacial silicon oxide formation, although the hydroxyl and organic species contamination in film due to incomplete ALD half-cycle reaction is inevitable in this temperature range.

### 4.3 H-Si Stretching Mode Red-shift

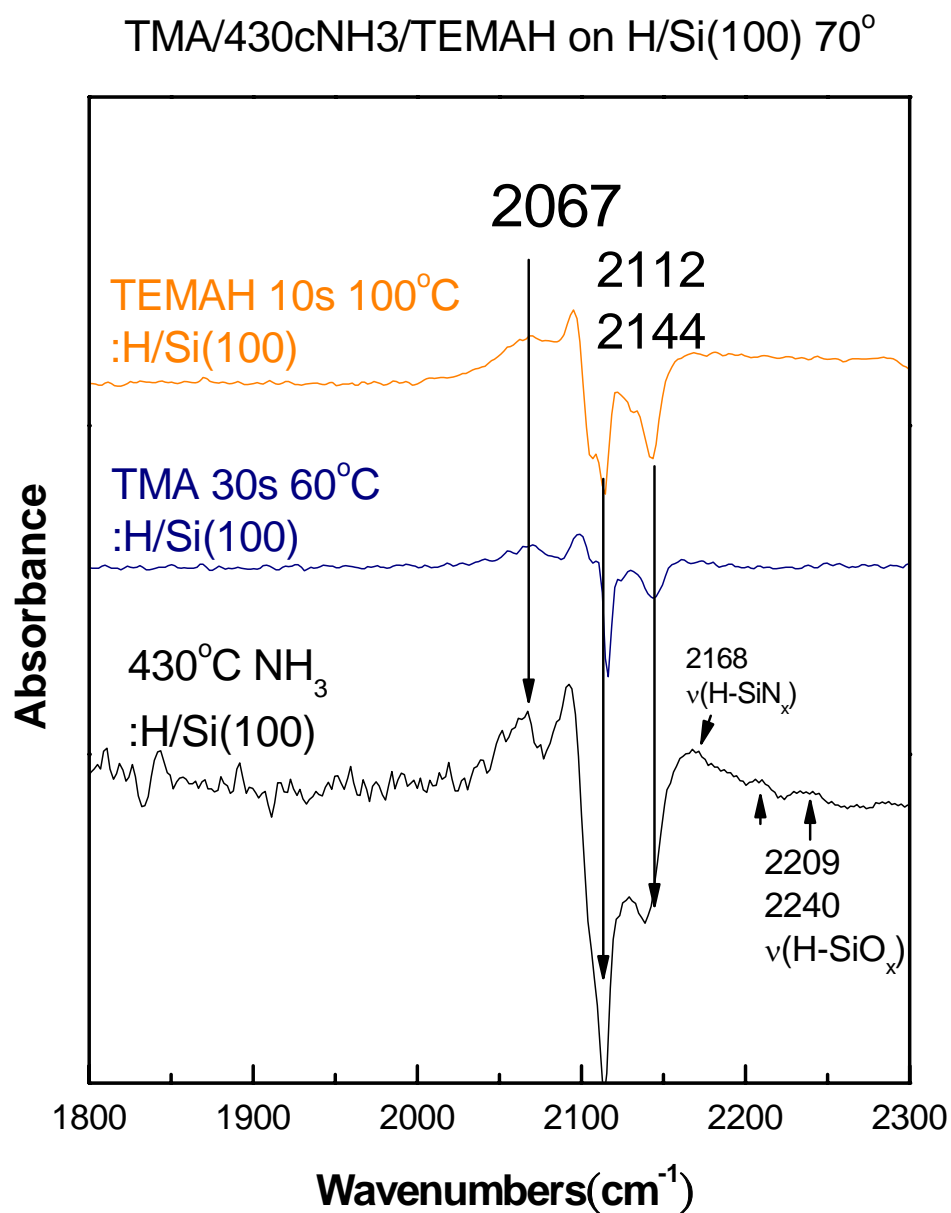
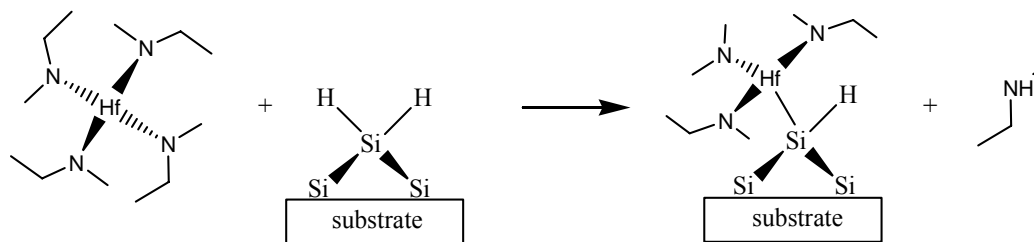


Fig. 4-16 Transmission spectra referenced to starting H/Si(100) of TEMAH, TMA and ammonia exposure respectively on 100°C, 60°C and 430°C H/Si(100).

The red-shift of H-Si stretching mode toward to  $\sim 2060\text{cm}^{-1}$  is observed when the H/Si surface is exposed to TEMAH, TMA and ammonia (see **Fig. 4-16**). In contrast to the

blue shift due to the insertion of high electronegative atoms (e.g., halide elements, oxygen and nitrogen) into the silicon backbond, the red-shift of H-Si stretching frequency can be the result of two possible causes: (1) the formation of Hf-bonded hydride such as  $\text{H-Si(Hf Si Si)}$  and  $\text{H-Si(Hf Hf Si)}$ , (2) the depolarization and local field effects on the  $\text{H}_x\text{-Si}$  dipole in the void of the interface of  $\text{Si-O-Hf-O-Si}$  network structure and silicon substrate.

The local  $\text{H-Si-(Hf Si Si)}$  moiety can be formed when TEMAH molecule reacts with surface di-hydride  $\text{H}_2\text{-Si(Si}_3\text{)}$  (see **Fig. 4-17** top) or breaks the surface mono-hydride dimer  $\text{HSi(Si}_2\text{)-Si(Si}_2\text{)H}$  bond.



Dependence of H-Si stretching frequency to All Neighbor Electronegativity/Stability Ratio

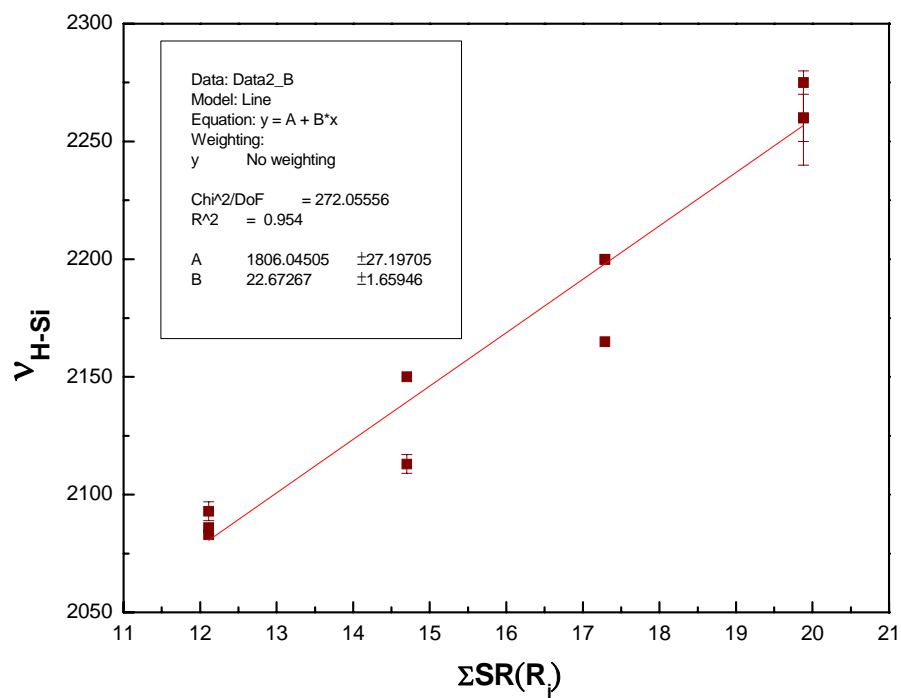


Fig. 4-17 Top: schematic drawing of TEMAH molecule reacting with surface silicon di-hydride. Bottom: the linear fitting plot of the dependence of H-Si stretching mode frequency on crystalline silicon surface to the stability-ratio electronegativity sum of its nearest bonding neighbor atoms.

An approach similar to Lucovsky's [30, 31] is adopted and the reported surface H-Si( $\text{Si}_x\text{O}_{3-x}$ ) stretching frequencies on crystalline silicon surfaces and the stability-ratio electronegativities (SR) [32, 33] of oxygen (5.21) and silicon (2.62) is used to derive the dependence of phenomenological linearity of  $\nu(\text{H-Si})$  frequency on the total SR sum of nearest bonding atoms. The hafnium atom SR (1.76) converted from its Pauling electronegativity via the empirical linearity relation

$\nu_{H-Si(R_1R_2R_3)}(cm^{-1}) = 1902.4 + 22.67 \times \sum_{j=1}^3 SR(R_j)$  is then used to extrapolate H-Si stretching frequency of H-Si-(Hf Si Si) to be  $2060\text{ cm}^{-1}$  with a fitting regression error of  $30\text{ cm}^{-1}$ , in good agreement with our observation. (**Fig. 4-17** bottom) (Also  $*SR(Al) \sim 1.94$  and the estimated H-Si stretching frequency of H-Si-(Al Si Si) is  $2065\text{ cm}^{-1}$  )

However Hf-O-Si is chemically more stable than Hf-Si and thus the oxygen from the ambient or the following D<sub>2</sub>O exposure tends to form the bond between H and Si(Hf Si Si), which decreases the red-shifted  $\nu(H-Si)$  intensity and produces blue-shifted  $\nu(H-Si)$  of H-Si(OSi Si) configuration. The decrease in intensity is never observed after D<sub>2</sub>O exposure nor is there any significant blue-shifted mode in the spectra. (see **Fig. 4-5(a)** and **Fig. 4-15**) Besides, it is kinetically unfavorable to replace the second layer Si atoms of H-Si(Si Si Si) by the hafnium atoms at  $100^\circ\text{C}$ . And the high level ( $\sim 40\text{-}50\%$  of full coverage) red-shifted H-Si stretching mode is observed on the H/Si(111), which has a very low defect level, after 10 ALD cycles (**Fig. 4-21**), indicating the red-shift is mostly from the terrace mono-hydride. All these imply the local chemical effect by Hf is not likely the mechanism to cause the H-Si stretching red-shift.

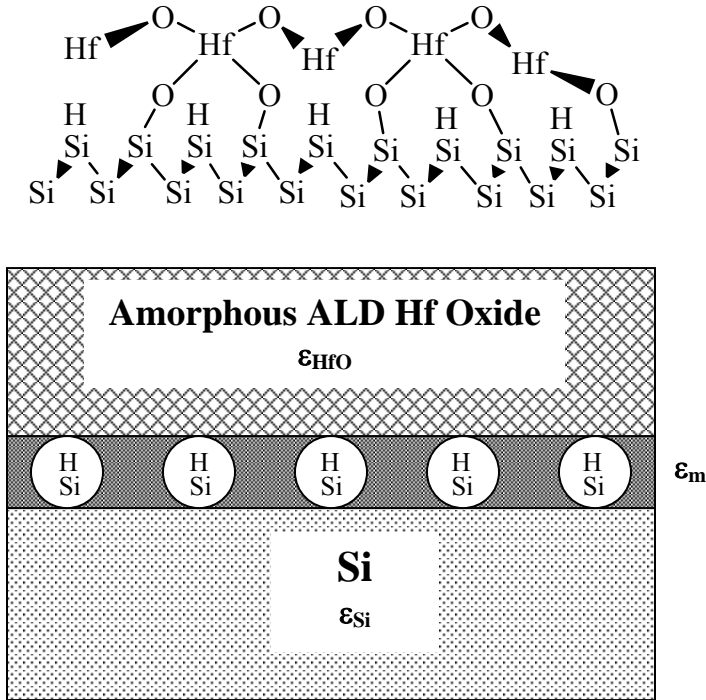


Fig. 4-18 Top: schematic drawing of hafnium oxide-silicon interface of hafnium oxide ALD on H/Si. Bottom: schematic drawing for simple dipole oscillator model.

Another possibility is the “solid state” effect [34, 35] as a result of the electrical depolarization of the H-Si dipole in a cavity or void in the dielectric medium. (see **Fig. 4-18**) Adopting E. Burstein’s model [36], the relative displacement  $u$  of a single dipole in a group of electric dipole harmonic oscillators in the presence of applied external electromagnetic field will follow the equation

$$\begin{aligned}\bar{m}\ddot{u}(t) + \bar{m}\gamma\dot{u}(t) + \bar{m}\omega_o^2 u(t) &= e_m^* E_{eff} \\ &= e_m^* (f_m E_{ext} + \eta_m \epsilon_0^{-1} P)\end{aligned}$$

$E_{eff}$  is the effective (local) electrical field on dipole oscillator

$e_m^*$  is the effective charge of dipole oscillator in the medium

$u$  is the relative displacement of dipole charges

$\omega_o$  is the intrinsic mode (angular) frequency of dipole oscillator without depolarization

$n$  is the number of dipole oscillator per unit volume in medium

$E_{ext}$  is the applied external electrical field

$\eta_m$  is the Lorentz field factor depends on the model and dielectric constant of medium

$f_m$  is a local field enhancement factor depends on the model and dielectric constant of medium

Polarization  $P = ne_m^*(x_+ - x_-) = ne_m^*u$

By taking  $u(t) \sim e^{-i\omega t}$  into the above equations, we obtain:

$$u(\omega) = \frac{f_m(e_m^*/\bar{m})E_{ext}}{\omega_o^2 - \Delta\omega^2 - \omega^2 - i\gamma\omega} \Rightarrow P(\omega) = \frac{f_m(ne_m^{*2}/\bar{m})E_{ext}}{\omega_o^2 - \Delta\omega^2 - \omega^2 - i\gamma\omega} = \varepsilon_0\chi(\omega)E_{ext}$$

and dielectric function  $\varepsilon(\omega) = \varepsilon_0(1 + \frac{(4\pi f_m ne_m^{*2}/\bar{m})}{\omega_o^2 - \Delta\omega^2 - \omega^2 - i\gamma\omega})$ , where  $\Delta\omega^2 = \eta_m \varepsilon_0^{-1} ne_m^{*2}/\bar{m}$

$\Rightarrow$  resultant resonance angular frequency

$$\tilde{\omega} = \sqrt{\omega_o^2 - \Delta\omega^2} \approx \omega_o(1 - \frac{1}{2} \frac{\Delta\omega^2}{\omega_o^2} - \frac{1}{8} (\frac{\Delta\omega^2}{\omega_o^2})^2)$$

$\Rightarrow$  resultant resonance frequency in  $\text{cm}^{-1}$

$$\tilde{\nu} \approx \nu_o(1 - \frac{1}{2} \frac{\Delta\omega^2}{\omega_o^2} - \frac{1}{8} (\frac{\Delta\omega^2}{\omega_o^2})^2)$$

and resonance frequency shift  $\approx -\frac{\nu_o}{2} \frac{\Delta\omega^2}{\omega_o^2} - \frac{\nu_o}{8} (\frac{\Delta\omega^2}{\omega_o^2})^2$

The electrical field enhancement factor  $f_m$  not only enhances the absorption strength to a factor of  $f_m^2$  with respect to that of gaseous silane molecule but also implicitly affects the resonance frequency via the enhancement in the effective dipole charge  $e_m^*$ [34].

Besides, we assume the effective charge will be enhanced by the proportion to the field enhancement factor.  $e_m^* = f_m e_o^*$

The conversion relation of angular frequency and wave number,  $\omega = 2\pi\nu c$ , gives:  
( $c$  is the light speed,  $e$  is the elementary charge and  $m_H$  is the hydrogen atom mass)

$$\begin{aligned} \frac{\Delta\omega^2}{\omega_o^2} &= \frac{\eta_m f_m^2 n e_o^{*2} / \bar{m}}{\varepsilon_0 \omega_o^2} = \frac{\eta_m f_m^2 [n / \overset{\circ}{\text{\AA}}^{-3}] [e_o^* / e]^2 / [\bar{m} / m_H]}{[\nu_o / \text{cm}^{-1}]^2} \left[ \frac{(e^2 / m_H) \overset{\circ}{\text{\AA}}^{-3}}{(2\pi c \times \text{cm}^{-1})^2 \varepsilon_0} \right] \\ &= \frac{\eta_m f_m^2 [n / \overset{\circ}{\text{\AA}}^{-3}] [e_o^* / e]^2 / [\bar{m} / m_H]}{[\nu_o / \text{cm}^{-1}]^2} \times [4.9 \times 10^7], \text{ which is a scaleless quantity} \end{aligned}$$

If  $n = (4\pi a^3 / 3)^{-1}$ ,

( $a$  is the radius of the average spherical volume, but not the cavity volume, occupied by an dipole oscillator)

$$\frac{\Delta\omega^2}{\omega_o^2} = \frac{\eta_m f_m^2 [e_o^* / e]^2 / [\bar{m} / m_H]}{[a / \overset{\circ}{\text{\AA}}]^3 [\nu_o / \text{cm}^{-1}]^2} \times [1.17 \times 10^7]$$

The simplified cavity model (**Fig. 4-18**) of H-Si dipole in spherical volume at the interface of Si and hafnium oxide is characterized by a macroscopic dielectric constant  $\kappa_m$  whose value is between the amorphous hafnium oxide dielectric constant  $\kappa_{HfO}$  and silicon dielectric constant  $\kappa_{Si} \sim 12$ .

By solving for the electrical field of a spherical cavity ( $\kappa_{cavity}=1$ ) with an extended dipole moment with the polarization  $P$  of dielectric medium ( $\kappa_m$ ) under an external applied electrical field  $E_{ext}$ , [37] the electrical field in cavity containing  $E_{ext}$  and depolarization fields for source  $E_{ext}$  and  $P$  is obtained. By subtracting the self-field  $E_s = -P/(3\varepsilon_0)$  of the extended dipole moment from the field inside the spherical cavity, the effective electrical field (or local field)  $E_{eff}$  and thus the corresponding electrical field enhancement factor  $f_m$  and the Lorentz field factor  $\eta_m$  can be obtained:



$$E_{eff} = E_{in\ cavity} - E_s = \left( \frac{3\kappa_m}{2\kappa_m + 1} E_{ext} + \frac{-\varepsilon_o^{-1} P}{2\kappa_m + 1} \right) - \left( \frac{-\varepsilon_o^{-1} P}{3} \right) = f_m E_{ext} + \eta_m \varepsilon_o^{-1} P$$

$$f_m = \frac{3\kappa_m}{2\kappa_m + 1}; \quad \eta_m = \frac{2}{3} \frac{\kappa_m - 1}{2\kappa_m + 1}; \quad \kappa_m = \varepsilon_m \varepsilon_o^{-1} \text{ is the static dielectric constant of medium}$$

Our Lorentz field factor  $\eta_m$  is different from Wieder's[35]  $((3/4)(\kappa_m-1)/(\kappa_m+3))$  in MKSA unit system), which was used with the silane molecule H-Si stretching frequency  $\sim 2158\text{cm}^{-1}$  as the intrinsic mode frequency for the caged H-Si(SiSiSi), H-Si(SiSiC) and H-Si(CCC) stretching frequency shift calculation in amorphous Si-C film. It is also larger than Cardona's[34] by a factor of 2, which was used with H-Si stretching mode  $\sim 2080\text{cm}^{-1}$  as the intrinsic mode frequency for H-Si in amorphous silicon film stretching frequency calculation. (Cardona could have made a typo/mistake in either the frequency shift formula or unit conversion although the calculated numerical result turned out to be the same as ours.) The pre-factor  $\eta_m f_m^2$  is an up-bounded ( $< 3/4$ ) and slowly increasing function for  $19 > \kappa_m > 6$  [5, 38] although the appropriate value applied to this case should be the dielectric constant for the IR frequency range, not the static dielectric constant. Usually the optical dielectric constant is less than static dielectric constant. Therefore the mode frequency shift is more susceptible to the variation of intrinsic effective charge  $e^*$ , dipole oscillator density  $n$ , thus  $a$ , and intrinsic oscillation frequency  $\nu_o$ , than dielectric constant  $\kappa_m$ . In other words, it means the mode frequency shift is sensitive to the local details of residual H-Si. By taking reasonable  $19 > \kappa_m > 6$  (for silicon),  $e_0 = e_{H/Si} \sim 0.155e$  [39, 40],  $\bar{m} \sim m_H$ ,  $\nu_o = \nu_{H/Si} \sim 2083\text{cm}^{-1}$ , the estimated cavity radius  $a$  is about 1.1-1.2 Å to match the shifted frequency  $\tilde{\nu}_{H/Si} \sim 2060\text{cm}^{-1}$  in our case.

10cyc TEMAH/D<sub>2</sub>O ALD Hf Oxide on H/Si ref. Si Oxide surface

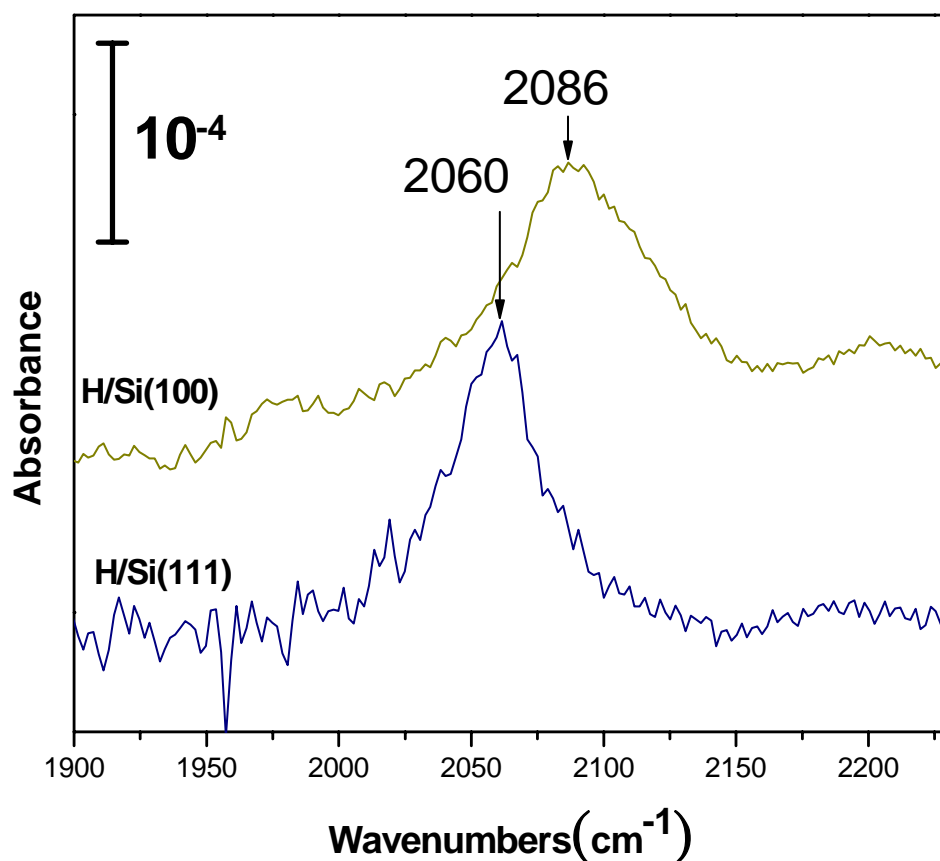


Fig. 4-19 Transmission IR absorption spectra of the H-Si stretching mode of 10 full cycle of TEMAH/D<sub>2</sub>O ALD growth on H/S(100)(top) and H/Si(111)(bottom).

In the case of 10-cycle ALD on H/Si(100), the red-shifted 2060 cm<sup>-1</sup> H-Si stretching (shoulder) mode is weaker in intensity and starts to develop after the second ALD cycle (see **Fig. 4-19**). The major H-Si stretching peak is at ~2086 cm<sup>-1</sup>, which is the same frequency of mono-hydride of H/Si(100). In contrast to the case of H/Si(111) the intensity of the red-shifted 2060 cm<sup>-1</sup> mode is stronger and keeps growing with the number of ALD cycles till ~ 5 cycles. This suggests that the micro-roughness difference of H/Si(100) [41] and H/Si(111) [23] might account for the difference in observation. The

microscopically rough H/Si(100) surface provides the topographical advantage for the formation of bigger cavities containing the major intact mono-hydrides, causing less frequency shift in mono-hydride stretching and weaker red-shifted mode intensity than H/Si(111). In the case of the atomically flat H/Si(111) surface, the residual mono-hydride is in smaller cavities, giving rise to prevailing and greater mode red-shift.

The interaction of mono-hydride with another surface silicon hydride (i.e. Si-H...H-Si) as in the H/Si(111) wafer bonding system[42, 43] and the interaction with adsorbed metal atoms (for example Si-H...Hf and Si-H...Al) could account for the red-shift of mono-hydride stretching mode. However the low kinetic energy condition of 100°C ALD on the flat H/Si(111) is impossible to cause large-scale surface topography changes to make closely packed mono-hydrides heading on one another. So the former mechanism (i.e. Si-H...H-Si) is not likely to be responsible for the redshift of the H-Si stretching mode. The latter is not only consistent with the IR observation but also can be combined with the phenomenological screening model scheme. The electronic level *ab initio* quantum mechanical calculation might be useful to resolve whether the interaction with adsorbed metal atoms contributes to the red-shift on a case-by-case basis, even though it might not be able to resolve how this interaction and the dielectric screening mechanism are associated to each other.

#### **4.4 TEMAH/D<sub>2</sub>O Hafnium Oxide ALD on SC2 Oxidized and Thermal Ammonia Nitridized Silicon Surfaces**

The half-cycle spectra of TEMAH/D<sub>2</sub>O ALD on SC2 oxidized and thermal ammonia nitridized silicon surfaces at the initial growth stage are studied, and the interactions of precursor exposures and starting surface functional groups are discussed in this section.

## A. Hafnium Oxide ALD on SC2 Oxidized Silicon Surface

080904 TEMAH/D<sub>2</sub>O Hf Oxide ALD On SC2 Silicon Oxide Ref. OSi(100)

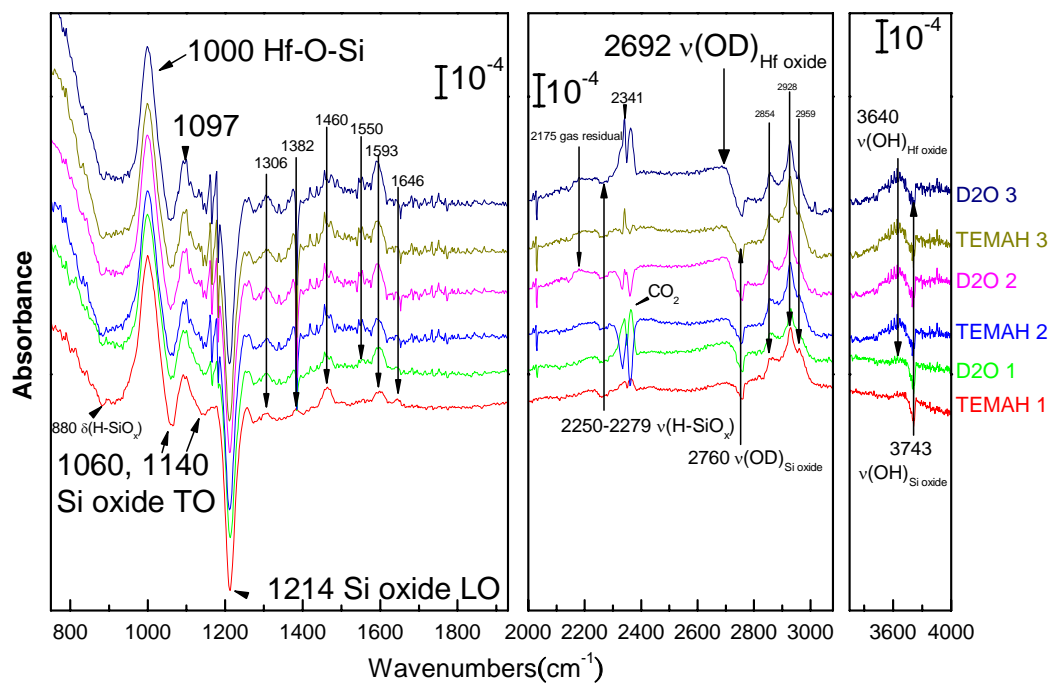


Fig. 4-20 Half-cycle transmission IR spectra of TEMAH/D<sub>2</sub>O hafnium oxide ALD exposures on SC2 treated H/Si(100) surface

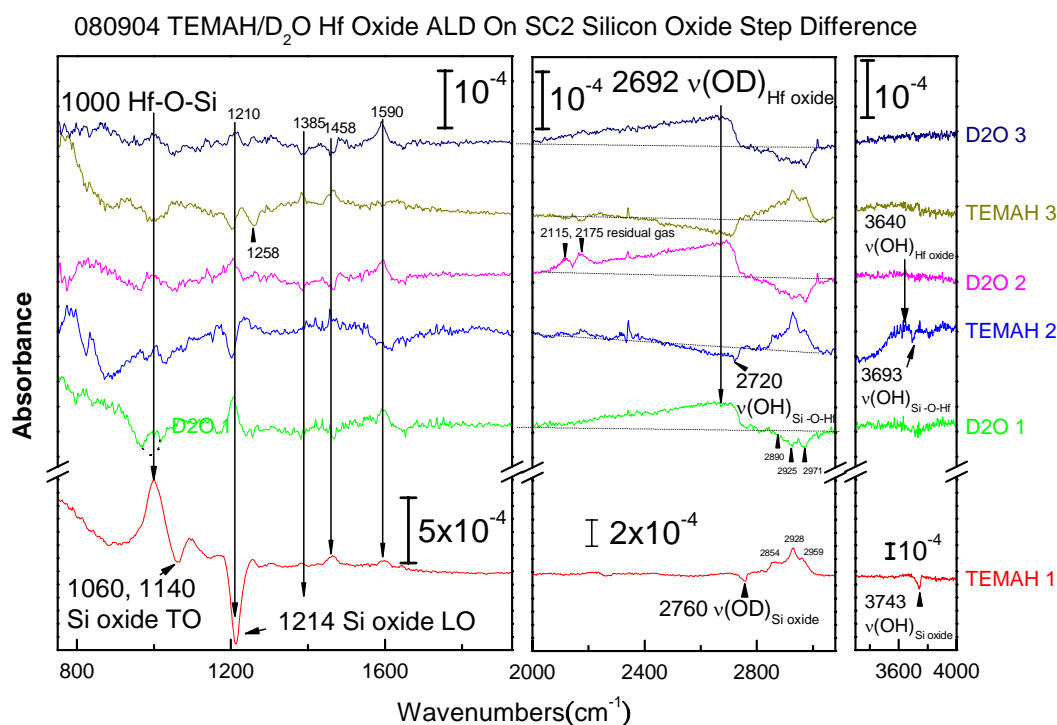


Fig. 4-21 Step difference spectra of TEMAH/D<sub>2</sub>O hafnium oxide ALD exposures on SC2 wet chemistry pre-treated H/Si(100).

The IR spectra of TEMAH/D<sub>2</sub>O hafnium oxide ALD referenced to the starting SC2 silicon oxide surface in **Fig. 4-20** show the growth of interfacial Hf-O-Si mode ( $\sim 1000\text{cm}^{-1}$  and  $1097\text{cm}^{-1}$ ), OD stretching ( $\sim 2692\text{cm}^{-1}$ , also OH stretching at  $\sim 3640\text{cm}^{-1}$  due to H-D substitution during the 2nd TEMAH exposure) and surface organic species featured by the peaks in  $1300\text{--}1650\text{cm}^{-1}$  and  $3000\text{--}2800\text{cm}^{-1}$ . At the same time the intensities of silicon oxide TO/LO modes ( $\sim 1060\text{ cm}^{-1}$  /  $1143, 1214\text{cm}^{-1}$ ), trace H-Si stretching of silicon oxide ( $\nu(\text{H-Si}(\text{O}_3))\sim 2270\text{--}2250\text{cm}^{-1}$ ), surface OH ( $3743\text{cm}^{-1}$ ) and OD ( $2760\text{cm}^{-1}$ ) stretching are all reduced. These decreased bands essentially characterize the surface groups as a result of reactions between SC2 oxidized silicon surface with TEMAH. The half-cycle step difference spectra in **Fig. 4-21** clearly show the partial surface group

replacement features of surface  $\text{CH}_x$  groups gain/loss (at 1385, 1458 and  $3000\text{-}2800\text{cm}^{-1}$ ) and Si-OD groups loss/gain (at  $\nu(\text{D-O})\sim 2720\text{cm}^{-1}$ ) during TEMAH/ $\text{D}_2\text{O}$  alternating exposures. The mode at  $1590\text{cm}^{-1}$  for surface carbonyl groups indicates some surface alkyl groups ( $\text{CH}_x$ ) are not removed but are oxidized by  $\text{D}_2\text{O}$  exposure.

Since more than 95% of the starting surface hydroxyl (OH/OD) groups are removed and the growth of interfacial Hf-O-Si is completed during the first TEMAH exposure, it is clear that SC2 oxidized silicon surface is very reactive to TEMAH. The grown absorbance peak area of Hf-O-Si mode ( $\sim 0.03\text{ cm}^{-1}$ ) by the 1<sup>st</sup> TEMAH exposure is higher than the saturation peak area of the growth on H/Si ( $0.021$  and  $0.027\text{ cm}^{-1}$  for the saturation growth on H/Si(111) and H/Si(100) respectively). Based on the IR absorption peak area estimation, the SC2 chemical Si oxide modes is decreased by less than 1/7 in the 1<sup>st</sup> TEMAH exposure, which suggests that TEMAH does not etch the silicon oxide substrate.

## **B. Hafnium Oxide ALD on Thermal Ammonia Nitridized Silicon Surface**

The same TEMAH/ $\text{D}_2\text{O}$  ALD exposures used in the previous sub-section were carried out on  $600^\circ\text{C}$  thermal ammonia nitridized silicon surface (100 s.c.c.m. ammonia flow diluted by 100s.c.c.m.  $\text{N}_2$ , total pressure $\sim 13\text{-}20$  Torr. for 30 seconds). The half-cycle spectra are presented as follows:

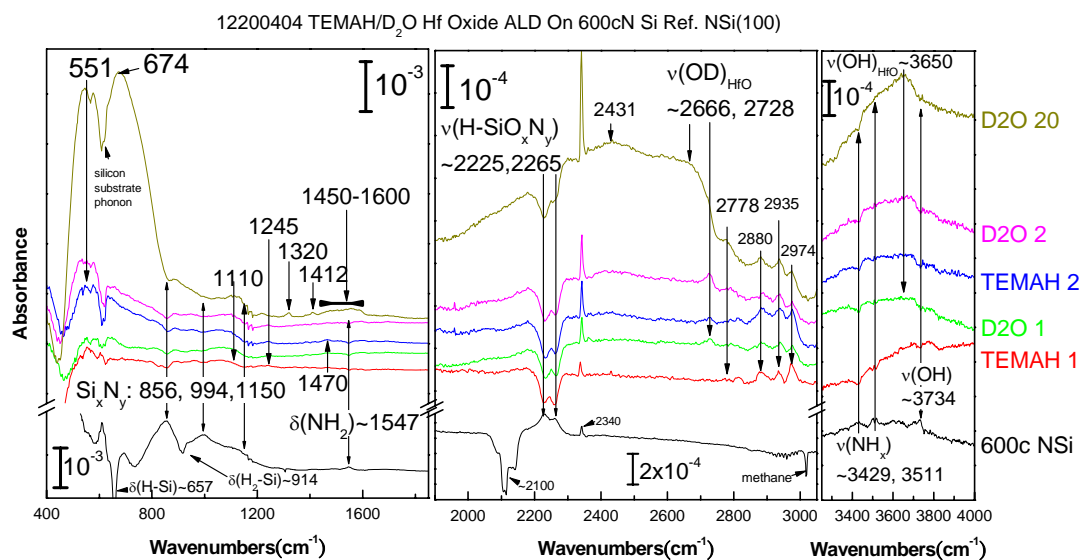


Fig. 4-22 Bottom black spectrum is the prepared ammonia treated 600°C H/Si(100) surface referenced to H/Si(100), the other colored are transmission IR spectra of TEMAH/D<sub>2</sub>O hafnium oxide ALD for the first four half cycles and the 20th full cycle referenced to the ammonia nitridized surface (the starting surface for ALD exposures).

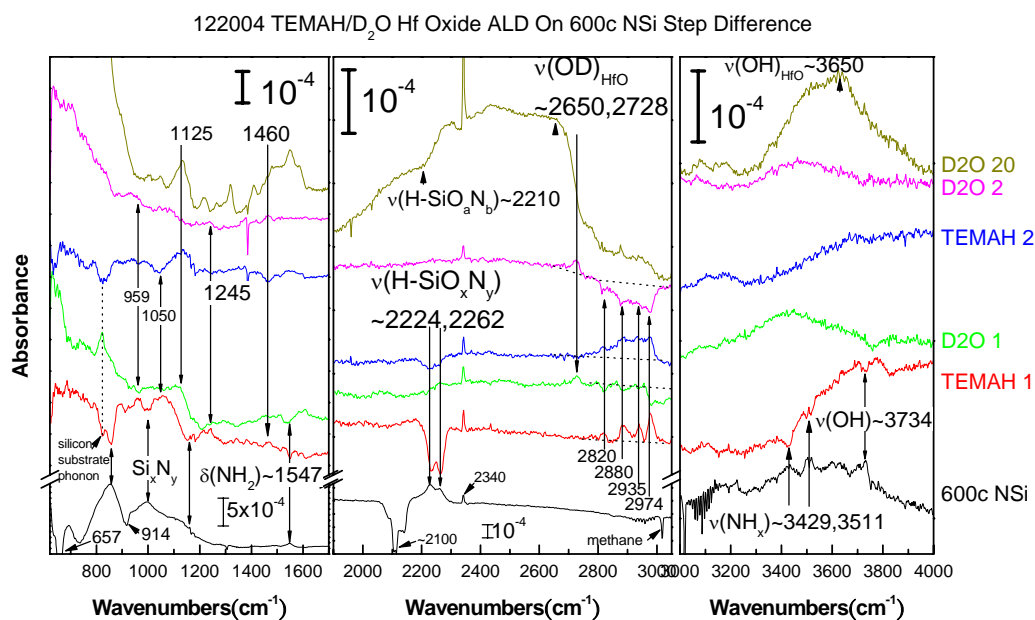


Fig. 4-23 Bottom black spectrum is the prepared ammonia treated 600°C H/Si(100) surface referenced to H/Si(100), the other colored are step difference spectra of TEMAH/D<sub>2</sub>O hafnium oxide ALD for the first four half cycles and the 20th full cycle.

In **Fig. 4-23**, the bottom black spectrum referenced to H/Si(100) shows the thermal ammonia nitridized surface contains average 2.5-5Å thick silicon (oxy-)nitride ( $\sim 856$ ,  $994$  and  $1158\text{cm}^{-1}$ ), surface  $\text{H}_x\text{-N}$  groups ( $\nu(\text{H-N})\sim 3439\text{cm}^{-1}$ ,  $\nu(\text{H}_2\text{-N})\sim 3511\text{cm}^{-1}$  and  $\delta(\text{H}_2\text{-N})\sim 1547\text{cm}^{-1}$ ), residual surface  $\text{H-SiO}_x\text{N}_y$  ( $\nu(\text{H-SiN}_2\text{O})\sim 2224\text{cm}^{-1}$  and  $\nu(\text{H-SiO}_3)\sim 2262\text{cm}^{-1}$ ) and trace hydroxyl groups ( $\nu(\text{OH})\sim 3734\text{cm}^{-1}$ ). Similar to the hafnium oxide ALD on SC2 oxidized silicon surface, the rest of spectra in colors show amorphous hafnium oxide ( $\sim 551$  and  $674\text{cm}^{-1}$ ), organic species in the film ( $2770\text{-}2975\text{cm}^{-1}$  and  $1240\text{-}1600\text{cm}^{-1}$ ) and deuterium hydroxyl groups ( $\nu(\text{OD})\sim 2666\text{cm}^{-1}$ ) on the surface and in the film ( $2728$  and  $2666\text{cm}^{-1}$ ) grow with the number of ALD cycles at a trace loss of silicon (oxy-)nitride and the removal of other surface groups in the thermal ammonia nitridized silicon surface. The peaks in  $950\text{-}1200$  for interface modes are different from those of ALD on SC2 silicon oxide surface. The step difference spectra in colors for ALD half-cycles in **Fig. 4-24** show surface OD and  $\text{CH}_x$  groups are partially removed and replaced in half-cycle ALD exposures, which is similar to the ALD on SC2 silicon oxide surface, while the  $\text{H-SiO}_x\text{N}_y$  groups on starting surface can not be completely removed by the first TEMA exposure.

The surface hydride coverage of the (oxy-)nitride surface is about 32%-39% of the HF etched H/Si(100) by IR absorbance peak integration area. Because of the absence of reliable transmission IR data of full amine-terminated surface, the quantitative characterization of this nitridized surface morphology cannot be determined explicitly. According to Ref.[44], the hydrogen and  $\text{NH}_2$  saturation of the Si(100) surface by ammonia exposure under UHV environment gives  $\sim 4\text{-}5 \times 10^{-3}\text{cm}^{-1}$  integrated area for 1/2 monolayer with  $60^\circ$ -incident transmission IR. On the assumption that (1) the



absorbance peak area is proportion to both the number of the species and the intensity of the IR beam polarized parallel to the nominal excitation direction of the mode, (2) the dynamical dipole polarization for  $\text{NH}_2$  stretching is perpendicular to the surface, and (3) the IR beam polarization gives incident angle ( $\theta$ )-dependent absorbance peak area of  $I_A \sim (\cos \theta)^{-1} (\sin \theta)^2$  by considering the IR beam spot size on the substrate and the associated electrical field polarization component perpendicular to surface [45], a full monolayer of  $\text{NH}_2$  at  $70^\circ$  incidence will give  $6.9\text{-}8.6 \times 10^{-3} \text{ cm}^{-1}$  absorbance peak area. Thus the  $\text{NH}_2$  coverage of the present nitridized sample is about 47-58%, leaving 3-20% of a monolayer for other moieties such as hydroxyl, epoxide[11, 16], dangling bonds or even hydro-carbon contamination on the nitridized surface. If we ignore this 3-20% of a monolayer, a rough estimate gives a lower bound of 36.6-44.8% of a monolayer of the thermal ammonia nitridized surface sites reacting with the 1<sup>st</sup> TEMAH exposure.

The detailed profile of IR spectrum in the phonon region around  $950\text{-}1200 \text{ cm}^{-1}$  (also see **Fig. 4-34** in later section) shows a broad structure associated with the non-homogenous Hf-O-Si and Hf-N-Si moiety formation. Among them, the mode at  $1064 \text{ cm}^{-1}$  of Hf-N-Si (assignment supported by simple mass effect on mode frequency consideration  $1000 \text{ cm}^{-1} \times (16/14)^{1/2} \sim 1069 \text{ cm}^{-1}$ ) is a little bit higher than the lower frequency Hf-O-Si mode intensity by the peak integration area ( $\sim 7:6$ ). The other mode at  $\sim 1028 \text{ cm}^{-1}$  can be associated with Hf-O-Si( $\text{O}_y\text{N}_z$ ) by a similar mass effect argument.

## **4.5 Post Deposition Annealing of ALD Grown Hafnium Oxide on SC2 Oxidized and Thermal Ammonia Nitridized Silicon Surfaces**

Similar to the annealing of hafnium oxide ALD film grown on H/Si in **Section 4.1 B.**, hafnium oxide films are grown with 20 cycles of TEMAH/D<sub>2</sub>O ALD on 100°C SC2 oxidized silicon and thermal ammonia nitridized silicon surfaces before they are annealed at several different temperatures from 300°C to 700°C for 2 minutes in vacuum chamber passed with 100 s.c.c.m. ultra-pure nitrogen gas (giving ~0.3 Torr. base pressure).

#### **A. Post Deposition Annealing of ALD Hafnium Oxide on SC2 Oxidized Silicon Surface**

After the 20-cycle TEMAH/D<sub>2</sub>O ALD hafnium oxide film is grown on 100°C SC2 oxidized silicon, the IR spectra are taken by flowing 200 s.c.c.m. ultra-pure nitrogen gas through the chamber. The post deposition annealing spectra referenced to the 20-cycle ALD grown hafnium oxide film, and the ALD starting surface, and the step difference spectra are respectively shown in **Fig. 4-24**, **Fig. 4-25**, and **Fig. 4-26**.

122706 20 cycle TEMAH/D<sub>2</sub>O Hf Oxide ALD On Hf Oxide SC2 Silicon Oxide Ref. 20cyc Hf Oxide

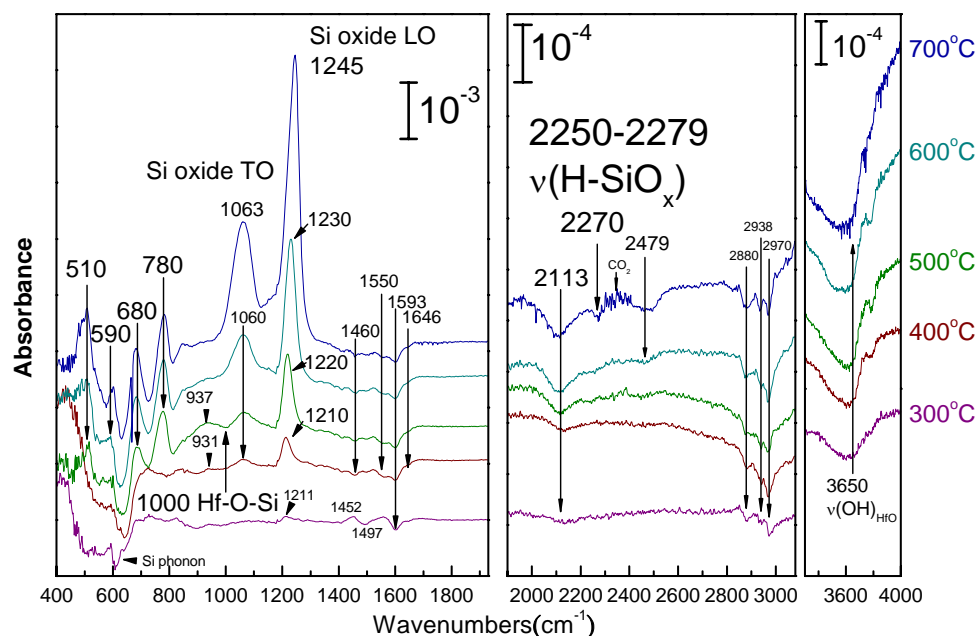


Fig. 4-24 Transmission IR absorbance spectra, referenced to the as-deposited hafnium oxide surface, of 100°C grown 20 cycle TEMAH/D<sub>2</sub>O ALD hafnium oxide on SC2 wet chemistry pre-treated H/Si(100) surface annealed to 300°C, 400°C, 500°C, 600°C and 700°C .

122706 20 cycle TEMAH/D<sub>2</sub>O Hf Oxide ALD On Hf Oxide SC2 Silicon Oxide Ref. OSi(100)

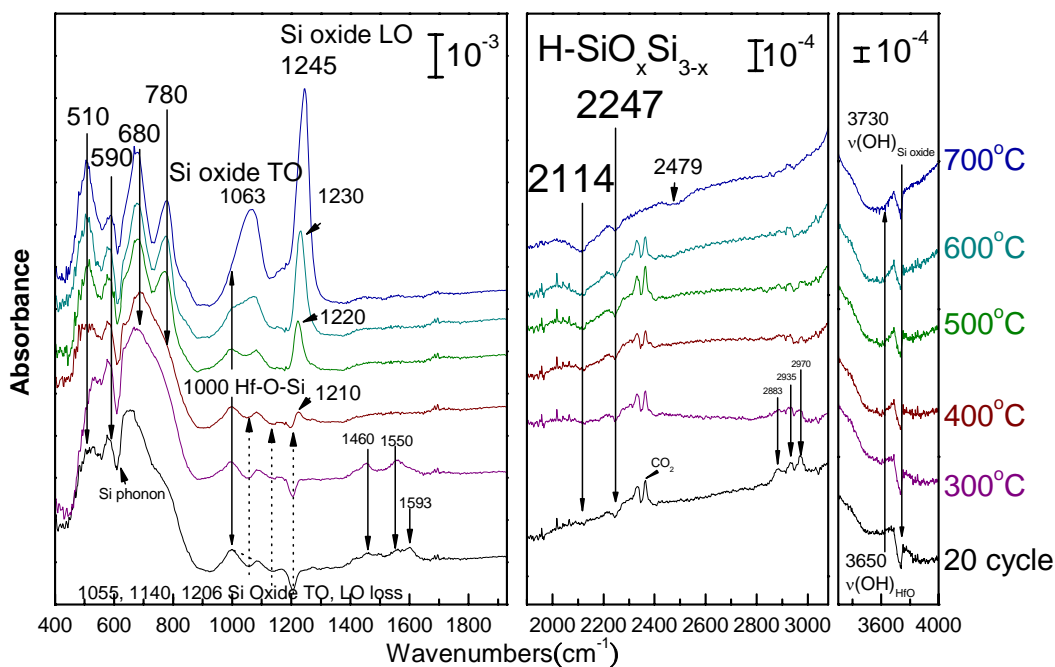


Fig. 4-25 Absorbance spectra, referenced to starting surface before ALD, of 100°C grown 20 cycle TEMAH/D<sub>2</sub>O ALD hafnium oxide on SC2 wet chemistry pre-treated H/Si(100) surface annealed to 300°C, 400°C, 500°C, 600°C and 700°C .

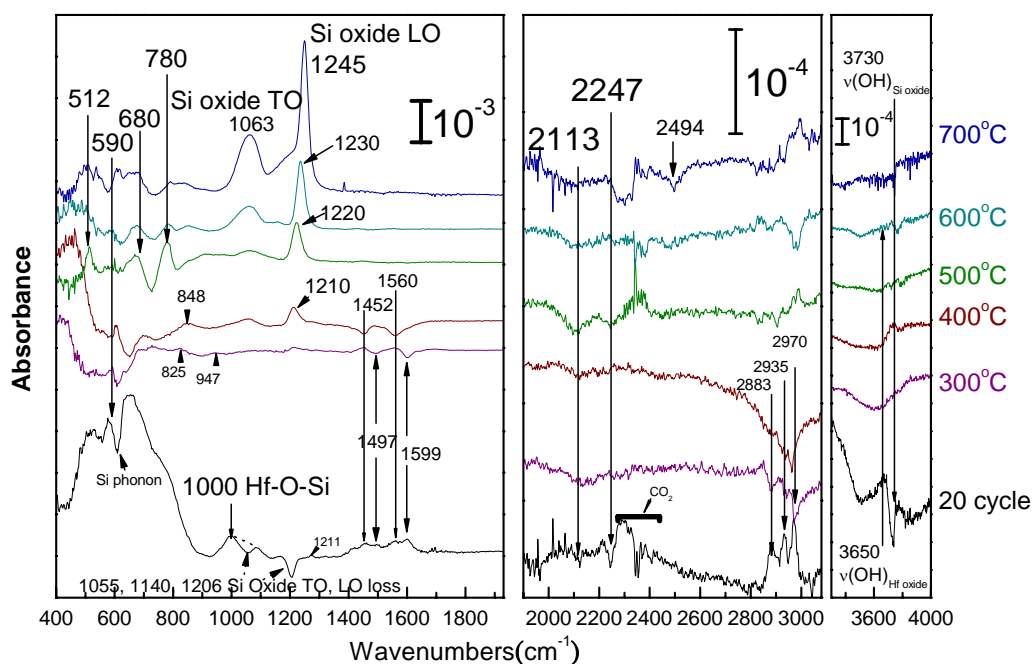
122706 20 cycle TEMAH/D<sub>2</sub>O Hf Oxide ALD On Hf Oxide SC2 Silicon Oxide Stepdiff

Fig. 4-26 Step differential absorbance spectra of 100°C grown 20 cycle TEMAH/D<sub>2</sub>O ALD hafnium oxide on SC2 wet chemistry pre-treated H/Si(100) surface annealed to 300°C, 400°C, 500°C, 600°C and 700°C .

Similar to the post deposition annealing of hafnium oxide ALD films grown on H/Si surfaces (**Section 4.1 B**), the spectra in **Fig. 4-24** and **Fig. 4-25** show organic groups in the film desorb during 300°C-500°C annealing, the interfacial silicon oxide starts to grow at 300°C annealing, and the crystallization modes (510, 590, 680 and 780 cm<sup>-1</sup>) appear at 500°C annealing. The increasing intensities of silicon oxide LO mode (~1220cm<sup>-1</sup>) and TO mode(~1060cm<sup>-1</sup>) are respectively shifting to higher and lower frequencies with increasing annealing temperature, which indicates the growth of interfacial silicon oxide.

The loss of the weak modes at 2114 and 2247 cm<sup>-1</sup> during 500°C annealing are due to desorption of the residual hydride (H-SiO<sub>x</sub>Si<sub>3-x</sub>) trapped in the interface of the native silicon oxide and ALD hafnium oxide. (This high temperature annealing rules out the

assignment of  $\nu(\text{CD}_x)$  due to deuterium substituted organic groups in film or on surface for the weak modes.).

The nitrogen purge flow during the spectrum taking processes reduces the deuterium source ( $\text{D}_2\text{O}$ ) degassed from the chamber wall, and, consequently, the OD groups in hafnium oxide film interact with the organic groups in the film and are turned into OH groups through hydrogen-deuterium exchange. This deuterium substitution accounts for the missing of the broad  $\nu(\text{OD})$  band at  $\sim 2660\text{cm}^{-1}$  and the appearance of the broad  $\nu(\text{OH})$  band at  $\sim 3650\text{cm}^{-1}$  in the as-grown 20 cycle ALD hafnium oxide film prior annealing, as well as the extensive loss of  $\nu(\text{OH})\sim 3650\text{cm}^{-1}$  after annealing.

The ALD grown hafnium oxide sectors of spectra in **Fig. 4-24** and **Fig. 4-25** show the loss of broad amorphous hafnium oxide mode during annealing is less than the full intensity of the band of as-grown hafnium oxide, which indicates the coexistence of the crystalline hafnium oxide and ALD amorphous hafnium oxide in film after annealing.

## **B. Post Deposition Annealing of ALD Hafnium Oxide on Nitridized Silicon Surface**

Similar 20-cycle ALD hafnium oxide film has been grown on  $600^\circ\text{C}$  thermal ammonia nitridized silicon surface and was annealed at the same temperatures and ambient conditions as being used in **Section 4.5 A**, but the chamber purge was stopped during spectrum taking. **Fig. 4-27** and **Fig. 4-28** respectively contain the post deposition annealing spectra referenced to 20-cycle ALD grown hafnium oxide film and the  $600^\circ\text{C}$  thermal ammonia nitridized silicon surface. The step difference spectra for different post deposition annealing temperatures are shown in **Fig. 4-29**.

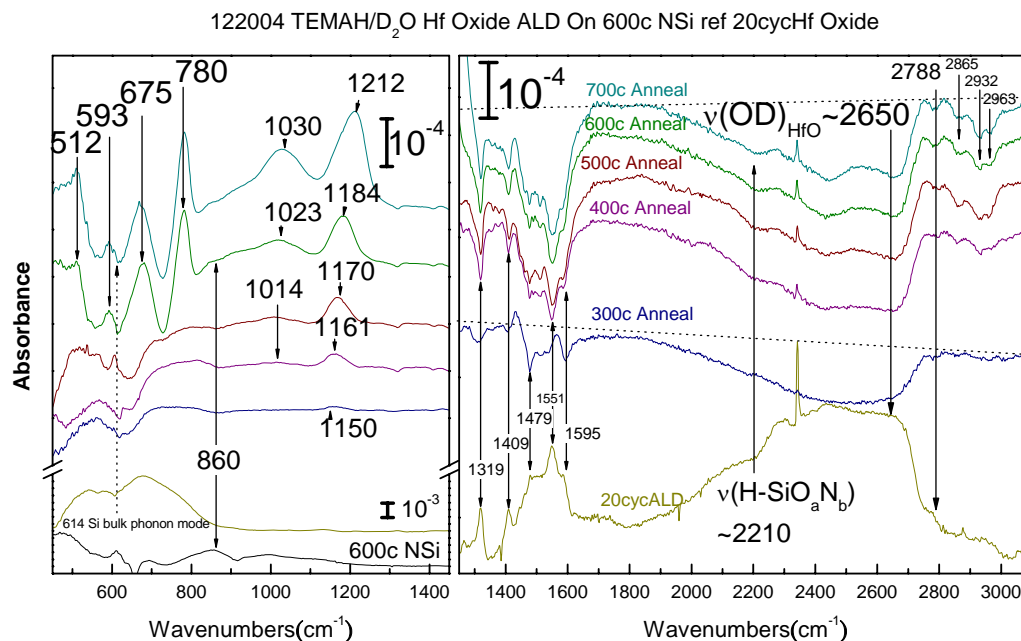


Fig. 4-27 The post-annealing absorbance spectra referenced to as-deposited 20-cycle 100°C TEMAH/D<sub>2</sub>O grown ALD hafnium oxide on ammonia treated 600°C H/Si(100); the spectrum (bottom in left panel) denoted “600c NSi” in black is the ammonia treated 600°C H/Si(100) referenced to H/Si(100).

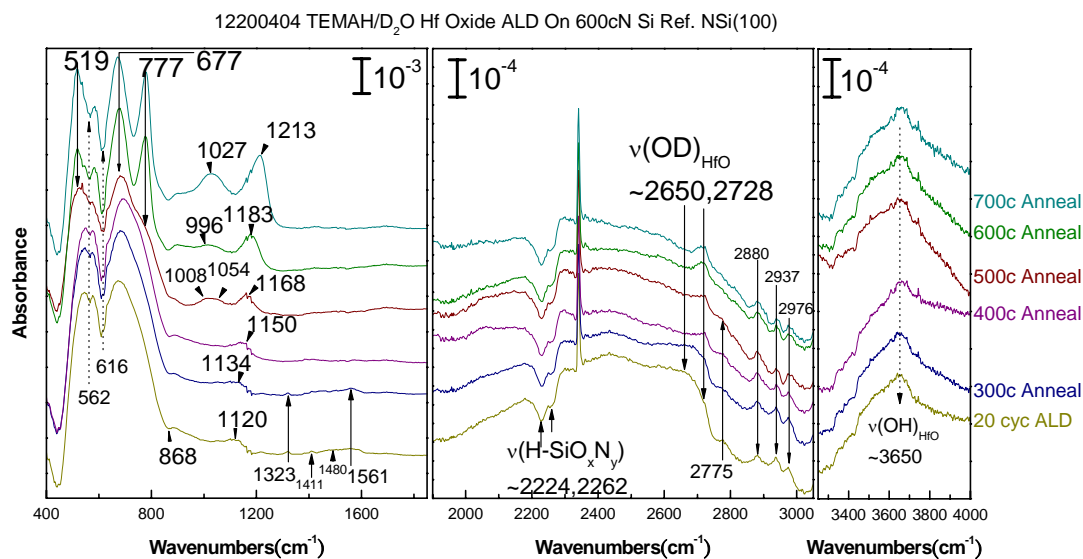


Fig. 4-28 Transmission IR spectra of 300c-700c post-deposition annealing of 20-cycle 100c TEMAH/D<sub>2</sub>O grown ALD Hf oxide on ammonia treated 600c H/Si(100) referenced to the ammonia treated H/Si(100) surface

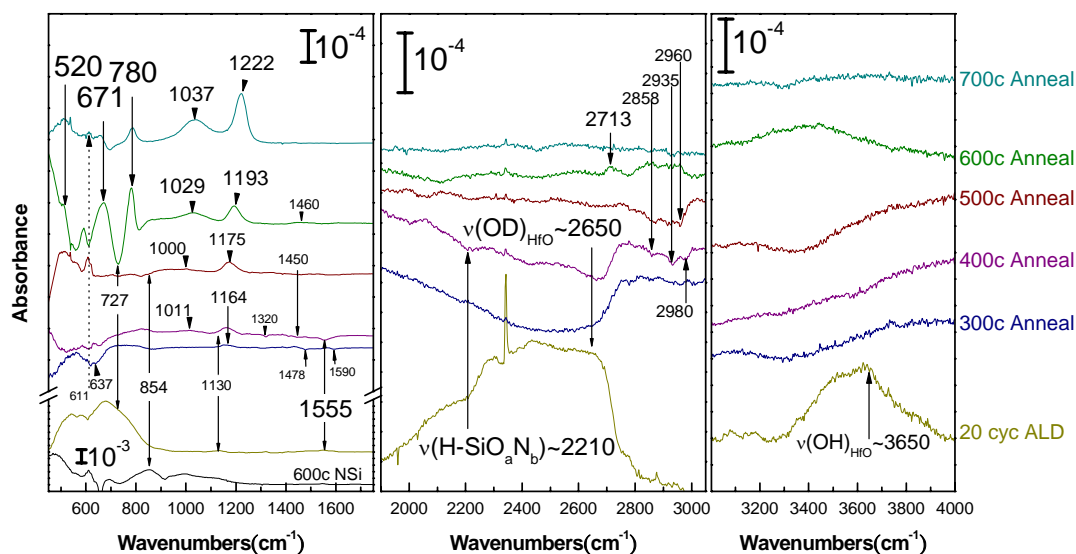


Fig. 4-29 Step difference IR spectra of 300°C-700°C post-deposition annealing of 20-cycle 100°C TEMAH/D<sub>2</sub>O grown ALD hafnium oxide on ammonia treated 600°C H/Si(100); the spectrum (bottom in left panel) denoted “600c NSi” in black is the ammonia treated 600°C H/Si(100) referenced to H/Si(100) referenced to the ammonia treated H/Si(100) surface.

All the IR spectra in **Fig. 4-27~Fig. 4-29** show very similar evolution of organic species ( $2770\text{--}2975\text{cm}^{-1}$  and  $1240\text{--}1600\text{cm}^{-1}$ ) and hydroxyl ( $\nu(\text{OD})\sim 2666\text{cm}^{-1}$  and  $\nu(\text{OH})\sim 3734\text{cm}^{-1}$ ) as well as the interfacial silicon oxide formation during  $300^{\circ}\text{C}\text{--}500^{\circ}\text{C}$  annealings. However the crystalline modes do not show up until  $600^{\circ}\text{C}$  annealing. At  $600^{\circ}\text{C}$ , besides the further oxidation evidenced by the modes at  $1023$  and  $1184\text{ cm}^{-1}$ , the strong peaks at  $512$ ,  $593$ ,  $675$  and  $780\text{ cm}^{-1}$  show the crystallization of the hafnium oxide film. At  $700^{\circ}\text{C}$ , thicker stoichiometric silicon oxide ( $1030$  and  $1212\text{ cm}^{-1}$ ) is formed.

The 600°C crystallization temperature of the ALD hafnium oxide on thermal ammonia nitridized silicon surface is higher than that (500°C) on H/Si or on SC2 oxidized silicon surface. The rise of crystallization temperature of nitrogen incorporated dielectric films has been widely observed [38, 46-54], so the straight forward account for the higher crystallization temperature in the grown ultra-thin hafnium oxide film on the

ammonia treated silicon surface is due to as low as a few percents of nitrogen incorporation. Also a comparison of the silicon oxide modes for the 700°C post-deposition annealed ALD grown hafnium oxide films on different silicon surfaces (**Fig. 4-30**) shows that the interfacial silicon oxide growth on nitridized silicon surface ( $\sim 3\text{Å}$ ) is less than on SC2 silicon oxide surface ( $\sim 8\text{Å}$ ) and H/Si(111) ( $\sim 15\text{Å}$ ).

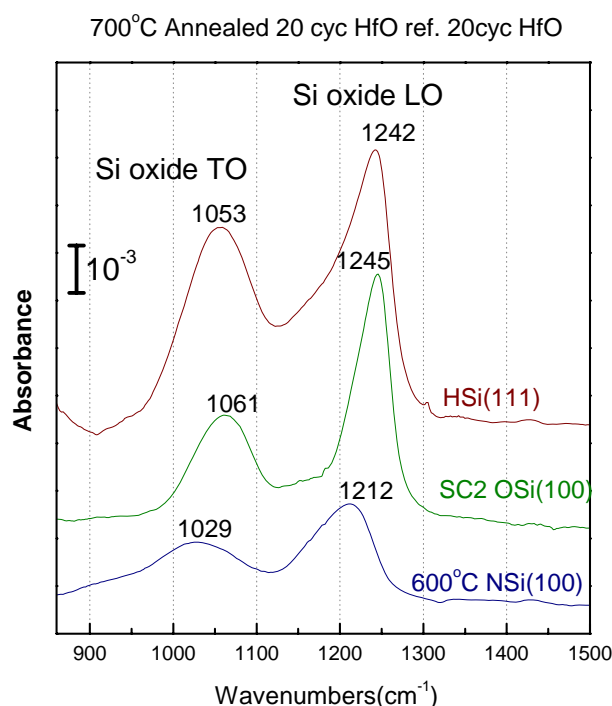


Fig. 4-30 Transmission IR spectrum sectors for 700°C annealed 20-cycle TEMAH/D<sub>2</sub>O ALD hafnium oxide grown at 100°C on H/Si(111), SC2 oxidized silicon surface and ammonia treated 600°C H/Si(100). All spectra are referenced to as-deposited 20-cycle ALD hafnium oxide surface.

## 4.6 Interfacial Bands of Single TMA and TEMAH Exposed Silicon Surfaces

This section is devoted to the detailed analysis of the interfacial band (850-1100cm<sup>-1</sup>) grown by TMA or TEMAH adsorption on different silicon surfaces. The local bonding models are summarized in **Fig. 4-35** denoted with the major mode frequency assignment.



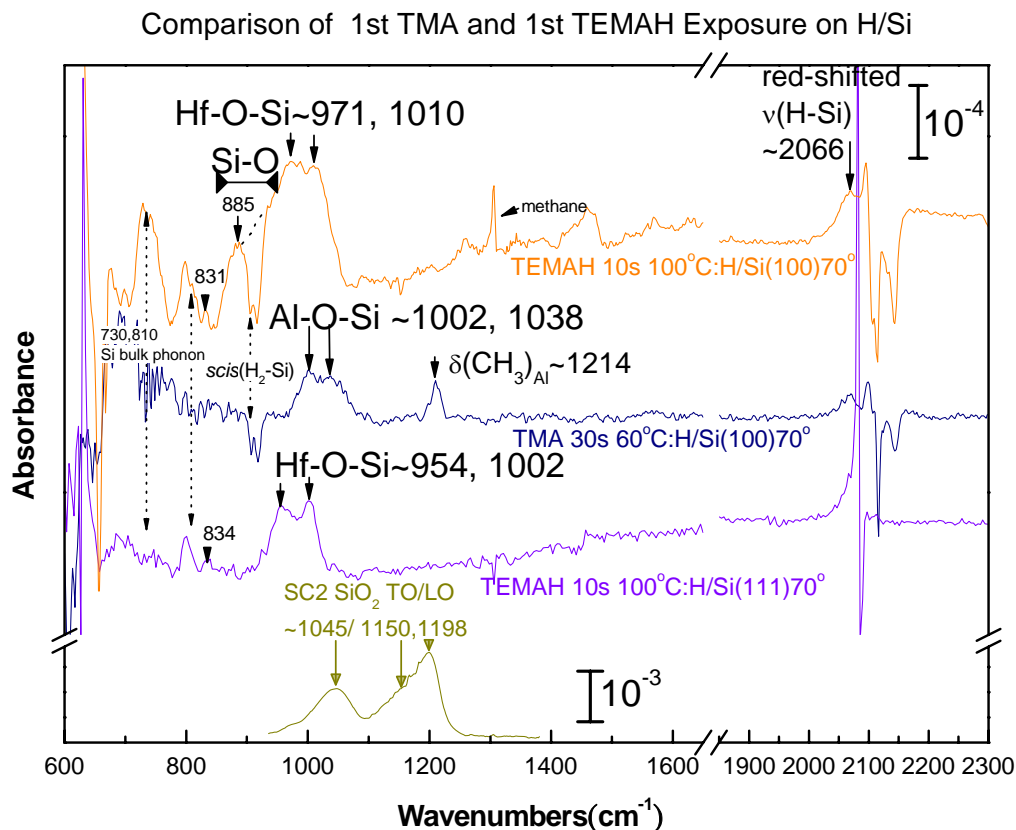


Fig. 4-31 70° incident angle transmission spectra referenced to starting H/Si surfaces of 10s TEMAH pulse exposure on 100°C H/Si(100) (the 1<sup>st</sup> from top) and H/Si(111) (the 3<sup>rd</sup> from top), and 30s TMA pulse exposure on 70°C H/Si(100) (the 2<sup>nd</sup> from top). The spectrum segment of SC2 wet chemistry silicon oxide TO/LO modes in different scale at bottom.

The IR spectrum of H/Si exposed to TMA in **Fig. 4-31** shows the mode frequencies of 1002 and 1038 $\text{cm}^{-1}$  are a little bit higher than those of 954 and 1002 $\text{cm}^{-1}$  for TEMAH. Also the losses of  $\nu(\text{H-Si})$  integrated area after the TMA exposure on 60°C H/Si(100), TEMAH exposure on 100°C H/Si(100) and on 100°C H/Si(111) are respectively 2%, 11%~16% and 4.2%~6%. The integrated areas of their interfacial band after the first TMA or TEMAH exposure are 0.005  $\text{cm}^{-1}$  for TMA on H/Si(100), 0.021 $\text{cm}^{-1}$  for TEMAH on H/Si(100), and 0.007  $\text{cm}^{-1}$  for TEMAH on H/Si(111). The proportion of the interfacial-band-increase to H-Si-loss ratio between TEMAH exposed H/Si(100) and TEMAH exposed H/Si(111) is 1~2.4. This means for each unit H-Si loss the increase in

the interfacial band from TEMAH exposed H/Si(100) is 1~2.4 times of that TEMAH exposed H/Si(111). It implies that besides the Hf-O-Si component of the interfacial band in TEMAH exposed H/Si(100) it may also contain other components such as the Si-O stretching from oxygen insertion into silicon back bonds. The broader interfacial band of TEMAH exposed H/Si(100) than TEMAH exposed H/Si(111) also support this scheme. Therefore, the components at  $850\text{-}950\text{cm}^{-1}$  in the interfacial band of TEMAH exposed H/Si(100) is associated with the additional Si-O stretching mode in such local structure of  $\text{Hf-O-Si}(\text{Si}_{3-x}\text{O}_x)$ [16] due to the oxygen insertion into silicon back bonds during TEMAH exposure. Unlike H/Si(111), the complexity of H/Si(100) surface morphology could have provided more reaction pathways for oxygen insertion into the Si backbond and thus give rise to the appearance of the extended band at  $850\text{-}950\text{ cm}^{-1}$ .

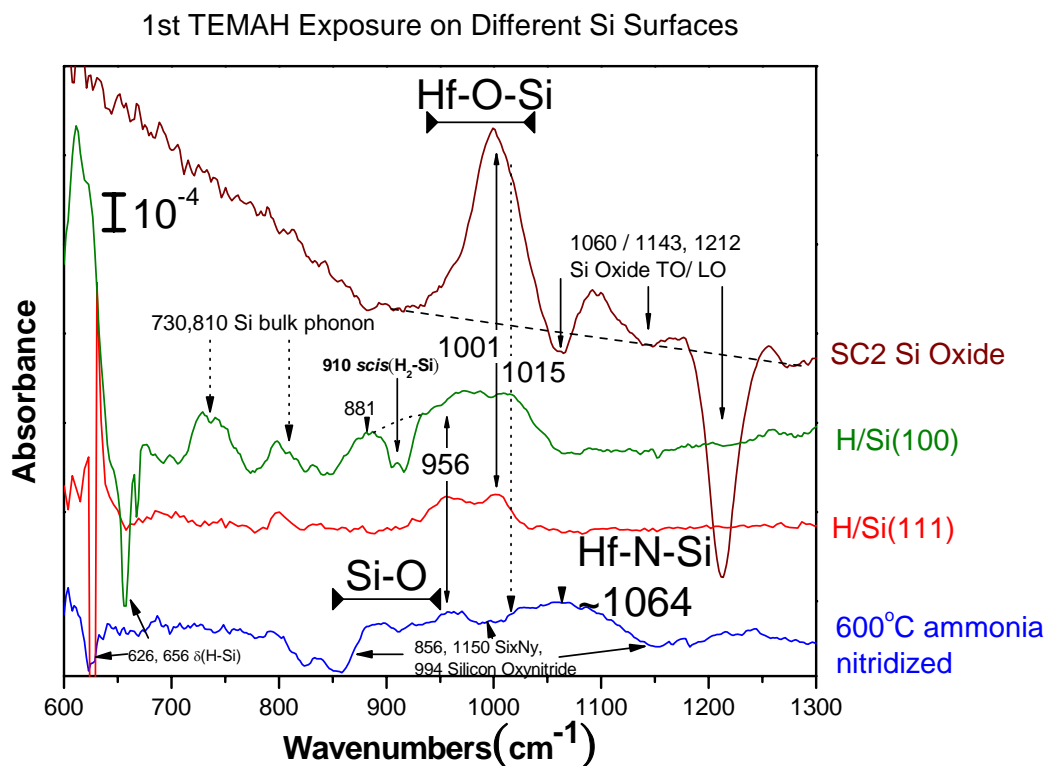


Fig. 4-32 Transmission IR spectra referenced to the starting surface of the 1<sup>st</sup> TEMAH in SC2 wet chemistry pre-treated H/Si(100), H/Si(100), H/Si(111) and ammonia treated 600°C H/Si(100).

The comparison of the 1<sup>st</sup> TEMAH exposure on different silicon surfaces is presented in **Fig. 4-32**. The comparative ratio of integrated interfacial band areas of single TEMAH exposure on SC2 oxidized silicon surface ( $0.029\text{cm}^{-1}$ ), H/Si(100) ( $0.021\text{cm}^{-1}$ ) and thermal ammonia nitridized surface ( $0.015\text{cm}^{-1}$ ) is about 1.9 : 1.4 : 1, which is comparable to the comparative ratio of hafnium atom counts per unit area by RBS measurements (2.2 : 1.1 : 1). This confirms the correlation of TEMAH adsorption and the overall assignment of interfacial band in  $850\text{-}1100\text{cm}^{-1}$ .

The extended interfacial band ranged from  $950$  to  $1150\text{cm}^{-1}$  in TEMAH exposed  $600^{\circ}\text{C}$  ammonia nitridized silicon surface contains three major components mainly associated with Hf-N-Si, Hf-O-Si segments on the surface and Si-O segment in substrate. [Note: the thermal ammonia nitridized surface also contains some oxy-nitride and hydroxyl moieties.] Based on the simple argument of oxygen-nitrogen substitution in **Section 4.5 A.**, the high frequency component at  $1064\text{cm}^{-1}$  has been assigned to Hf-N-Si mode. According to the The other band sector at  $956/1015\text{cm}^{-1}$  and the lower frequency component at  $880\text{cm}^{-1}$  are respectively assigned to Hf-O-Si stretching and Si-O stretching.

The H-Si stretching modes of TEMAH exposed H/Si(111) and H/Si(100) do not have blue-shifted bands at frequencies higher than  $2100\text{ cm}^{-1}$  (**Fig. 4-3** and **Fig. 4-5(a)**), which implies no evidence of oxygen insertion into the H-Si site back-bond..

The modes at  $730$  and  $810\text{cm}^{-1}$  are silicon bulk phonon modes due to instability of substrate temperature during IR data acquisitions. They are not associated with the TEMAH adsorption on silicon surfaces.

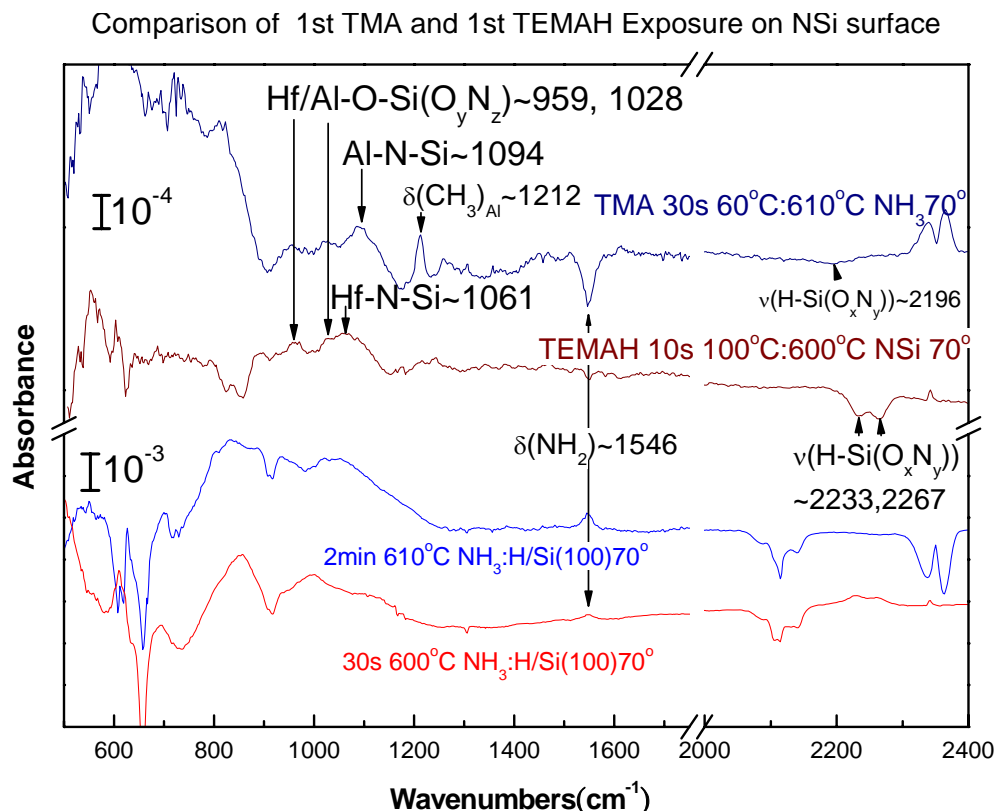


Fig. 4-33 70° incident angle transmission spectra of 30s TMA pulse exposure on 2-minute ammonia pretreated 610°C H/Si(100) at 60°C referenced to nitridized surface (the first from top), 2-minute ammonia pretreated 610°C H/Si(100) referenced to starting H/Si surfaces (the third from top), 10s TEMAH pulse exposure on 30s ammonia pretreated 600°C H/Si(100) at 100°C referenced to nitridized surface (the second from top), and 30s ammonia pretreated 600°C H/Si(100) referenced to starting H/Si(100)(the bottom).

Based on the similar argument of oxygen-nitrogen substitution as being used in **Section 4.5 A.**, [ (1)  $959\text{cm}^{-1}(\text{Hf-O-Si}(\text{O}_y\text{N}_z)) \times (16/14)^{1/2} \sim 1025\text{cm}^{-1}$  for observed  $1028\text{cm}^{-1}(\text{Hf-N-Si}(\text{O}_y\text{N}_z))$ , and (2)  $1038\text{cm}^{-1}(\text{Al-O-Si}) \times (16/14)^{1/2} \sim 1110\text{cm}^{-1}$  for observed  $1094\text{cm}^{-1}(\text{Al-N-Si})$ ] the modes at 1028 and  $1094\text{cm}^{-1}$  in **Fig. 4-33** of the single TMA or TEMAH exposure on thermal ammonia nitridized silicon surface are legitimately associated with the surface moieties of  $\text{Hf-O-Si}(\text{O}_y\text{N}_z)$  and  $\text{Al-N-Si}$ . The common weak peak  $\sim 959\text{cm}^{-1}$  of both TEMAH and TMA exposed thermal ammonia nitridized silicon surface is not sensitive to the metallic atomic masses of adsorbed species. That suggests that the existing oxy-nitride ( $\text{Si}(\text{O}_y\text{N}_z)$ ) modes of ammonia nitridized surface are shifted

by TMAH or TMA adsorption and the newly formed common mode at  $\sim 959\text{cm}^{-1}$  is associated with the local structure  $-\text{Hf-O-Si}(\text{O}_y\text{N}_z)$  or  $-\text{Al-O-Si}(\text{O}_y\text{N}_z)$ .

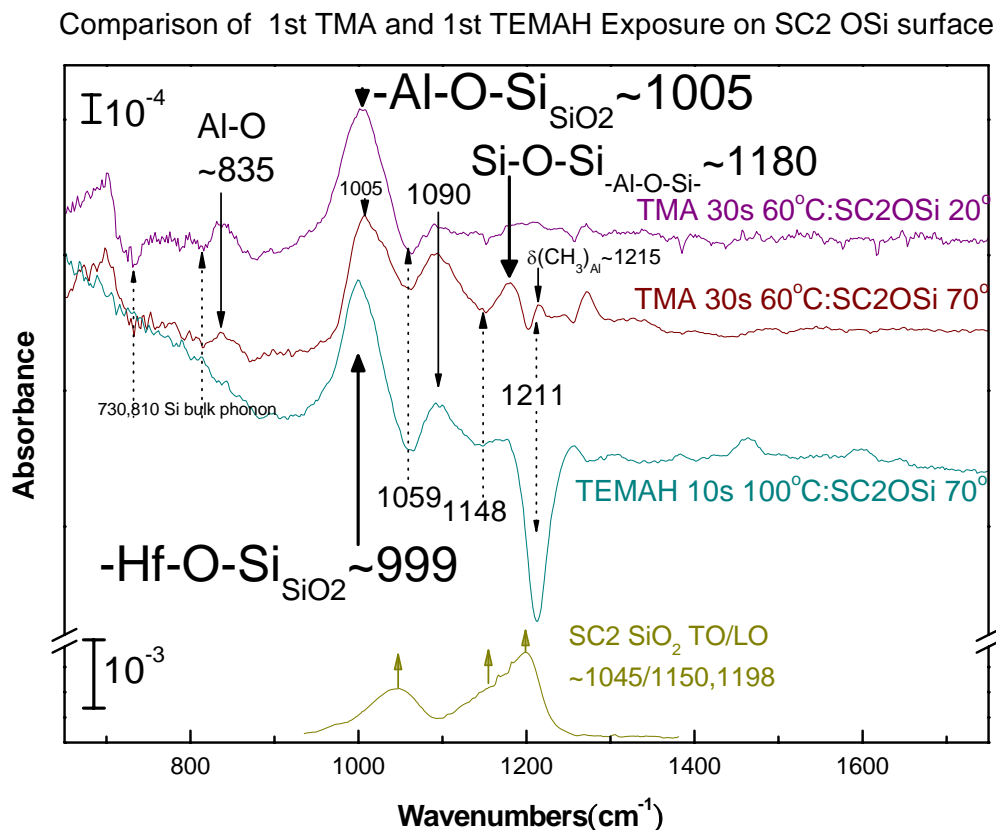


Fig. 4-34 Transmission spectra referenced to starting H/Si surfaces of (top two) 30s TMA pulse exposure on  $60^\circ\text{C}$  SC2 oxidized silicon surface at  $20^\circ$  and  $70^\circ$  incident angles, (the 3<sup>rd</sup> from top) 10s TMAH pulse exposure on  $100^\circ\text{C}$  SC2 oxidized silicon surface at  $70^\circ$  incident angle, and SC2 wet chemistry silicon oxide TO/LO modes in different scale at bottom.

In **Fig. 4-34**, the major Hf-O-Si mode in the interfacial band for TMA exposed SC2 oxidized silicon surface at  $1005\text{cm}^{-1}$  has slightly higher peak frequency than that for TMAH exposure. The overlap of the silicon oxide TO/LO mode (at  $1059$ ,  $1148$  and  $1211\text{cm}^{-1}$ ) with the as-grown interfacial band makes it difficult to resolve the other substructures in interfacial band, e.g., the debious peak at  $1090\text{cm}^{-1}$ . At  $70^\circ$  incident angle, the intensity of the silicon oxide LO mode is enhanced, while the intensity of the silicon oxide LO mode of the TMA exposed SC2 oxidized surface is much suppressed. That

implies the peak at  $\sim 1180\text{cm}^{-1}$  is a real LO-like surface mode associated with the TMA adsorption. The  $70^\circ$  incident angle spectrum of TMAH exposure does not have the similar peak in the frequency range for the interfacial band. That suggests the mode at  $1180\text{cm}^{-1}$  is a new surface LO mode due to the strong coupling of surface  $-\text{Al}-\text{O}-\text{Si}-$  species with the surface  $\text{Si}-\text{O}-\text{Si}$  network. Contrary to the heavy atomic mass of hafnium (178), which tends to decouple some local vibrations from the adsorbed+surface cluster normal modes, aluminum atomic mass (26) is comparable to silicon mass (28) and the vibrational modes associated with aluminum atoms can be more de-localized and higher in frequency by nature. On the other hand, such a high mode frequency suggests this surface mode is originated from the  $\text{Si}-\text{O}-\text{Si}$  network stretching. Therefore, the mode at  $1180\text{cm}^{-1}$  is associated with the surface  $\text{Si}-\text{O}-\text{Si}$  mode shifted by the coupling with  $-\text{Al}-\text{O}-\text{Si}-$ .

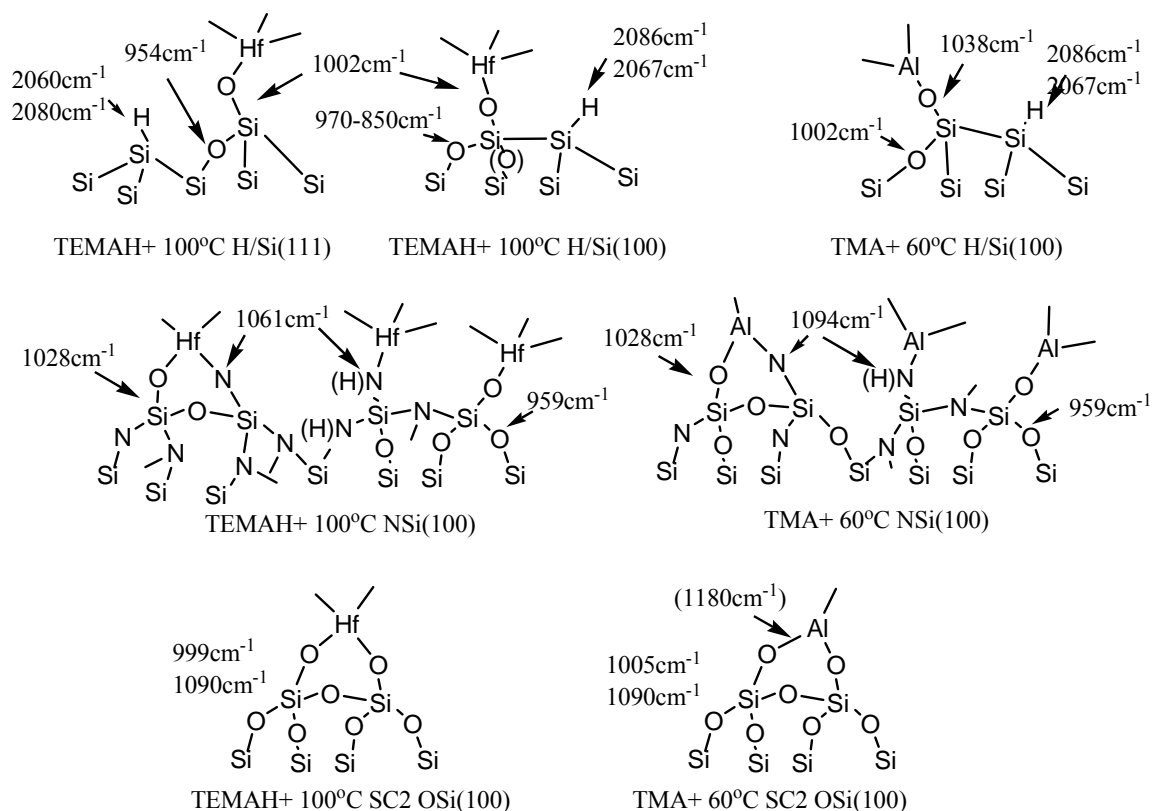


Fig. 4-35 Schematic local bonding models for TEMAH and TMA exposure on silicon surfaces and the associated major observed peak frequencies.

## Conclusion

Under high vacuum conditions TEMAH/D<sub>2</sub>O ALD grows amorphous hafnium oxide on the H/Si surfaces at 100°C at an average rate of 0.1 nm/ cycle without interfacial silicon oxide growth. TEMAH initiates the ALD growth on H/Si at coverages less than 10% in each exposure. The variation of the residual surface hydride coverages indicates the full coverage of hafnium oxide moiety is not achieved until more than 10 ALD cycles. About 40-50% of the hydride groups remains after > 30 ALD cycles. The analysis based on the IR H-Si mode and RBS hafnium coverage measurements suggests that the growth is not defect-site limited. The growth mechanism involves 3 hafnium atoms per adsorption site, followed by island expansions combined with the steric hindrance effect which is responsible for the residual hydride and deuterium-oxygen groups in the film. Besides the ligand substitution manifested by the appearance and partial removal of the 2721cm<sup>-1</sup> O-D stretching and 2783cm<sup>-1</sup> C-H stretching modes for methylamino groups in half-cycle exposures, the spectrum feature in 1100-1800cm<sup>-1</sup> suggests  $\text{Hf-N(-O)(-O-Hf)}$ ,  $(\text{Hf-O})_2\text{NO}$  and  $\text{Hf-O-(CO}_2\text{)}$  as the major residual metal-organic moiety in the film.

Upon 400°C annealing in nitrogen ambient, the ultra-thin amorphous hafnium oxide modes at 690cm<sup>-1</sup>(LO) and 510cm<sup>-1</sup>(TO), interfacial Hf-O-Si ~1000cm<sup>-1</sup>, interfacial silicon oxide mode ~1046cm<sup>-1</sup> increases while the residual silicon mono-hydride H-Si stretching mode at 2057cm<sup>-1</sup> starts to decrease. Distinct monoclinic structure crystallization modes at 787, 656cm<sup>-1</sup> (LO) and 510cm<sup>-1</sup> (TO) are observed with 500°C annealing. The unusual red-shift of the residual silicon mono-hydride stretching frequency common to both TEMAH and TMA exposure on H/Si can be caused either by the interaction of mono-hydride with adsorbed metal atoms (Si-H....Hf and Si-H....Al) or

by the dielectric screening effect by as-grown dielectric metal oxide (Hf-O and Al-O) moieties as shown in the simple cavity model.

A linear hafnium oxide growth rate without an incubation period on SC2 silicon oxide is observed. A higher hafnium coverage on SC2 silicon oxide than on nitridized silicon surfaces or on H/Si in the initial ALD stages (**Fig. 4-36**) indicates that the SC2 silicon oxide surface is more reactive than nitridized silicon surface or H/Si. The crystallization temperature ( $\sim 600^{\circ}\text{C}$ ) of ALD hafnium oxide on the nitridized silicon surface is higher than that of the other two silicon surfaces ( $\sim 500^{\circ}\text{C}$ ).

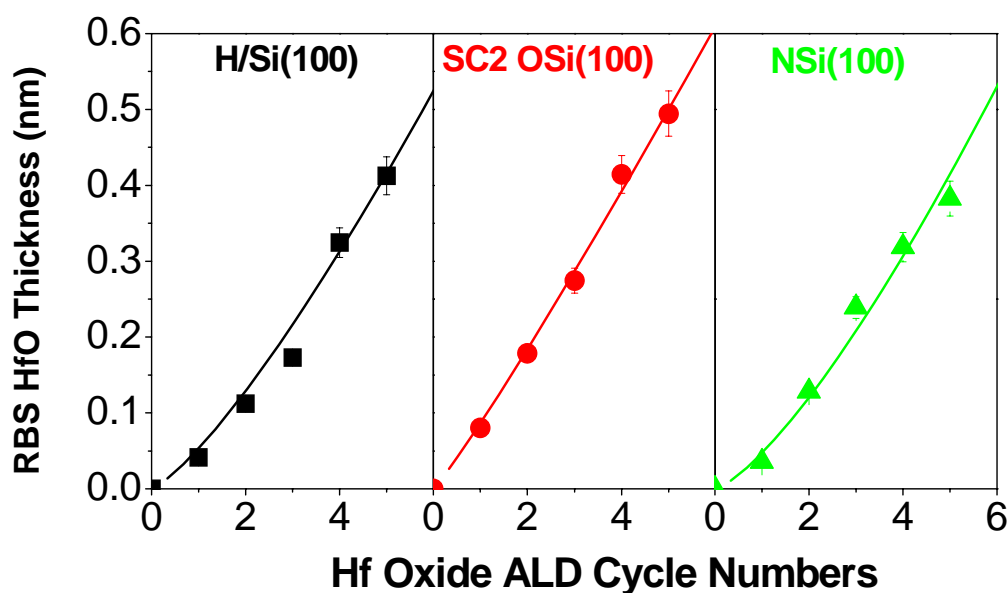


Fig. 4-36 Areal hafnium atom counts converted into bulk hafnium oxide thickness on different silicon surfaces as functions of ALD cycle numbers.

Based on the assumption of the oxygen-nitrogen substitution and no significant change in relevant force constants, details of sub-peak assignments in  $850\text{--}1100\text{cm}^{-1}$  region associated with interfacial formation by cross comparisons of TEMAH and TMA exposures on various silicon surfaces have been presented and summarized in the last



section.

## References

1. Kukli, K., M. Ritala, T. Sajavaara, J. Keinonen, and M. Leskela, Atomic layer deposition of hafnium dioxide films from hafnium tetrakis(ethylmethanamide) and water. *Advanced Materials*, 2002. **14**(17): p. A199-+.
2. Kukli, K., M. Ritala, T. Sajavaara, J. Keinonen, and M. Leskela, Atomic layer deposition of hafnium dioxide films from hafnium tetrakis(ethylmethanamide) and water. *Chemical Vapor Deposition*, 2002. **8**(5): p. 199-204.
3. Kukli, K., M. Ritala, J. Sundqvist, J. Aarik, J. Lu, T. Sajavaara, M. Leskela, and A. Harsta, Properties of hafnium oxide films grown by atomic layer deposition from hafnium tetraiodide and oxygen. *Journal of Applied Physics*, 2002. **92**(10): p. 5698-5703.
4. Kukli, K., M. Ritala, M. Leskela, T. Sajavaara, J. Keinonen, D. C. Gilmer, and P. J. Tobin, Hafnium silicon oxide films prepared by atomic layer deposition. *Materials Science and Engineering B-Solid State Materials for Advanced Technology*, 2004. **109**(1-3): p. 2-5.
5. Kukli, K., M. Ritala, J. Lu, A. Harsta, and M. Leskela, Properties of HfO<sub>2</sub> thin films grown by ALD from hafnium tetrakis(ethylmethanamide) and water. *Journal of the Electrochemical Society*, 2004. **151**(8): p. F189-F193.
6. Lim, J.W., H.S. Park, and S.W. Kang, Analysis of a transient region during the initial stage of atomic layer deposition. *Journal of Applied Physics*, 2000. **88**(11): p. 6327-6331.
7. Park, H. S., J. S. Min, J. W. Lim, and S. W. Kang, Theoretical evaluation of film growth rate during atomic layer epitaxy. *Applied Surface Science*, 2000. **158**(1-2): p. 81-91.
8. Puurunen, R.L. and W. Vandervorst, Island growth as a growth mode in atomic layer deposition: A phenomenological model. *Journal of Applied Physics*, 2004. **96**(12): p. 7686-7695.
9. Alam, M.A. and M.L. Green, Mathematical description of atomic layer deposition and its application to the nucleation and growth of HfO<sub>2</sub> gate dielectric layers. *Journal of Applied Physics*, 2003. **94**(5): p. 3403-3413.
10. Gurevich, Alejandra B., Boris B. Stefanov, Marcus K. Weldon, Yves J. Chabal, and Krishnan Raghavachari, Heterogeneous nucleation of oxygen on silicon: Hydroxyl-mediated interdimer coupling on Si(100)-(2 x 1). *Physical Review B*, 1998. **58**(20): p. R13434 LP - R13437.
11. Queeney, K. T., M. K. Weldon, Y. J. Chabal, and K. Raghavachari, The microscopic origin of optical phonon evolution during water oxidation of Si(100). *Journal of Chemical Physics*, 2003. **119**(4): p. 2307-2313.
12. Stefanov, B.B. and K. Raghavachari, Oxidation of Si(100)2 x 1: thermodynamics of oxygen insertion and migration. *Surface Science*, 1997. **389**(1-3): p. L1159-L1164.
13. Stefanov, B.B. and K. Raghavachari, Pathways for initial water-induced oxidation of Si(100). *Applied Physics Letters*, 1998. **73**(6): p. 824-826.

14. Weldon, M. K., B. B. Stefanov, K. Raghavachari, and Y. J. Chabal, Initial H<sub>2</sub>O-induced oxidation of Si(100)-(2x1). *Physical Review Letters*, 1997. **79**(15): p. 2851-2854.
15. Queeney, K. T., Y. J. Chabal, M. K. Weldon, and K. Raghavachari, Silicon oxidation and ultra-thin oxide formation on silicon studied by infrared absorption spectroscopy. *Physica Status Solidi a-Applied Research*, 1999. **175**(1): p. 77-88.
16. Weldon, M. K., K. T. Queeney, A. B. Gurevich, B. B. Stefanov, Y. J. Chabal, and Krishnan Raghavachari, Si-H bending modes as a probe of local chemical structure: Thermal and chemical routes to decomposition of H[<sub>sub</sub> 2]O on Si(100)-(2x1). *Journal of Chemical Physics*, 2000. **113**(6): p. 2440.
17. Cosnier, V., M. Olivier, G. Theret, and B. Andre, HfO<sub>2</sub>-SiO<sub>2</sub> interface in PVD coatings. *Journal of Vacuum Science & Technology a-Vacuum Surfaces and Films*, 2001. **19**(5): p. 2267-2271.
18. Nakamoto, K., *Infrared and Raman spectra of inorganic and coordination compounds*. 5th ed. **1997: New York : Wiley, c1997**.
19. Davydov, A., *Molecular spectroscopy of oxide surfaces*, ed. N.T. Sheppard. 2003: Wiley, c2003. 668.
20. Kelly, M. J., J. H. Han, C. B. Musgrave, and G. N. Parsons, In-situ infrared spectroscopy and density functional theory modeling of hafnium alkylamine adsorption on Si-OH and Si-H surfaces. *Chemistry of Materials*, 2005. **17**(21): p. 5305-5314.
21. A. V. Kiselev, V.I.L., *Infrared spectra of surface compounds / A. V. Kiselev, V. I. Lygin*. 1975: New York : Wiley ; distributed by Halsted Press, 1975. 384.
22. Marra, D. C., W. M. M. Kessels, M. C. M. van de Sanden, K. Kashefzadeh, and E. S. Aydil, Surface hydride composition of plasma deposited hydrogenated amorphous silicon: in situ infrared study of ion flux and temperature dependence. *Surface Science*, 2003. **530**(1-2): p. 1-16.
23. G.S. Higashi, Y.J.C., G.W. Trucks, Krishnan Raghavachari, Ideal hydrogen termination of the Si(111) surface. *Appl. Phys. Lett.*, 1990. **56**((7)): p. 656.
24. Jakob, P., Y.L. Chabal, and K. Raghavachari, Lineshape analysis of the Si---H stretching mode of the ideally H-terminated Si(111) surface: the role of dynamical dipole coupling. *Chemical Physics Letters*, 1991. **187**(3): p. 325-333.
25. Koji Nakanishi, P.H.S., *Infrared absorption spectroscopy*. 2 ed. 1977: San Francisco, Holden-Day, 1977. 286.
26. Nelson L. Alpert, W.E.K., Herman A. Szymanski, *IR; theory and practice of infrared spectroscopy*. 2d ed ed. 1970: New York, Plenum Press [1970]. 380.
27. Randall, H.M., *Infrared determination of organic structures*. 1949, New York: Van Nostrand Co. 239.
28. D.A. Neumayer, E.C., Materials characterization of ZrO<sub>2</sub>-SiO<sub>2</sub> and HfO<sub>2</sub>-SiO<sub>2</sub> binary oxides deposited by chemical solution deposition. *J. Appl. Phys.*, 2001. **90**(4): p. 1801.
29. Kazuyuki Tomida, K.K., Kentaro Kyuno and Akira Toriumi, Far Infrared Study of Structural Distortion and Transformation of HfO<sub>2</sub> by Introducing a Slight Amount of Si. *Extended Abstracts of the 2004 International Conference on Solid State Devices and Materials*, 2004: p. 790-791.

30. Lucovsky, G., Chemical effects on the frequencies of Si-H vibrations in amorphous solids. *Solid State Communications*, 1979. **29**(8): p. 571-576.
31. Lucovsky, G., R.J. Nemanich, and J.C. Knights, Structural interpretation of the vibrational spectra of a-Si: H alloys. *Physical Review B*, 1979. **19**(4): p. 2064 LP - 2073.
32. Sanderson, R.T., *Chemical periodicity*. 1960, New York: Reinhold Pub. Corp. 330.
33. Sen, K.D., C.K. Jorgensen, and J.A. Alonso, *Electronegativity. Structure and bonding* ; 66. 1987, Berlin; New York: Springer-Verlag. 198.
34. M. Cardona, *Vibrational Spectra of Hydrogen in Silicon and Germanium*. *physica status solidi (b)*, 1983. **118**(2): p. 463-481.
35. H. Wieder, M.C., C. R. Guarnieri,, *Vibrational spectrum of hydrogenated amorphous Si-C films*. *Physica Status Solidi (b)*, 1979. **92**(1): p. 99-112.
36. E. Burstein, S.I.a.Y.S., *The Effect of Geometry of a Medium on Its Optical Response*, in *The optical properties of solids*, J. Tauc, Editor. 1966, New York, Academic Press, 1966.: New York. p. 421.
37. Frohlich, H.H., *Theory of dielectrics. Monographs on the physics and chemistry of materials*. 1949: Oxford, Clarendon Press, 1949. 180.
38. Kang, C. S., H. J. Cho, R. Choi, Y. H. Kim, C. Y. Kang, S. J. Rhee, C. W. Choi, M. S. Akbar, and J. C. Lee, *The electrical and material characterization of hafnium oxynitride gate dielectrics with TaN-Gate electrode*. *Ieee Transactions on Electron Devices*, 2004. **51**(2): p. 220-227.
39. Chabal, Y.J., *Infrared spectroscopy of hydrogen on silicon surfaces*. *Physica B: Condensed Matter*, 1991. **170**(1-4): p. 447-456.
40. Ouwers, J.D., R.E.I. Schropp, and W.F. Vanderweg, *Interpretation of the Silicon-Hydrogen Stretching Doublet in a-Si:H Hydrogenated Amorphous-Silicon*. *Applied Physics Letters*, 1994. **65**(2): p. 204-206.
41. Y.J. Chabal, G.S.H., K. Raghavachari, *Infrared spectroscopy of Si(111) and Si(100) surfaces after HF treatment: Hydrogen termination and surface morphology*. *J. Vac. Sci. Technol. A*, 1989. **7**((3)): p. 2104.
42. Feijoo, D., Y.J. Chabal, and S.B. Christman, *Silicon wafer bonding studied by infrared absorption spectroscopy*. *Applied Physics Letters*, 1994. **65**(20): p. 2548-2550.
43. Weldon, M. K., Y. J. Chabal, D. R. Hamann, S. B. Christman, E. E. Chaban, and L. C. Feldman, *Physics and chemistry of silicon wafer bonding investigated by infrared absorption spectroscopy*. *Journal of Vacuum Science & Technology B*, 1996. **14**(4): p. 3095-3106.
44. Queeney, K.T., Y.J. Chabal, and K. Raghavachari, *Role of interdimer interactions in NH<sub>3</sub> dissociation on Si(100)-(2 x 1)*. *Physical Review Letters*, 2001. **86**(6): p. 1046-1049.
45. Valeri P. Tolstoy, I.V.C., Valeri A. Skryshevsky., *Handbook of infrared spectroscopy of ultrathin films*. 2003: Hoboken, N.J. : Wiley-Interscience, c2003. 710.
46. Pant, G., A. Gnade, M. J. Kim, R. M. Wallace, B. E. Gnade, M. A. Quevedo-Lopez, P. D. Kirsch, and S. Krishnan, *Comparison of electrical and chemical*

- characteristics of ultrathin HfON versus HfSiON dielectrics. *Applied Physics Letters*, 2006. **89**(3).
47. Lysaght, P., B. Foran, S. Stemmer, G. Bersuker, J. Bennett, R. Tichy, L. Larson, and H. R. Huff, Thermal response of MOCVD hafnium silicate. *Microelectronic Engineering*, 2003. **69**(2-4): p. 182-189.
  48. Liu, M., Q. Fang, G. He, L. Q. Zhu, and L. D. Zhang, Characterization of HfO<sub>x</sub>N<sub>y</sub> gate dielectrics using a hafnium oxide as target. *Applied Surface Science*, 2006. **252**(24): p. 8673-8676.
  49. Kang, Chang Seok, H.-J. Cho, K. Onishi, R. Choi, R. Nieh, S. Goplan, S. Krishnan, and J.C. Lee Improved thermal stability and device performance of ultra-thin (EOT<10 Å) gate dielectric MOSFETs by using hafnium oxynitride (HfO<sub>x</sub>N<sub>y</sub>). in *VLSI Technology, 2002. Digest of Technical Papers. 2002 Symposium on*. 2002.
  50. Nieh, R. E., C. S. Kang, H. J. Cho, K. Onishi, R. Choi, S. Krishnan, J. H. Han, Y. H. Kim, M. S. Akbar, and J. C. Lee, Electrical characterization and material evaluation of zirconium oxynitride gate dielectric in TaN-gated NMOSFETs with high temperature forming gas annealing. *Ieee Transactions on Electron Devices*, 2003. **50**(2): p. 333-340.
  51. Choi, Rino, Chang Seok Kang, Byoung Hun Lee, K. Onishi, R. Nieh, S. Gopalan, E. Dharmarajan, and J.C. Lee. High-quality ultra-thin HfO<sub>2</sub> gate dielectric MOSFETs with TaN electrode and nitridation surface preparation. in *VLSI Technology, 2001. Digest of Technical Papers. 2001 Symposium on*. 2001.
  52. Choi, K.J., J.H. Kim, and S.G. Yoon, Plasma nitration of HfO<sub>2</sub> gate dielectric in nitrogen ambient for improvement of TaN/HfO<sub>2</sub>/Si performance. *Electrochemical and Solid State Letters*, 2004. **7**(10): p. F59-F61.
  53. Cho, H.-J., C.S. Kang, K. Onishi, S. Gopalan, R. Nieh, R. Choi, E. Dharmarajan, and J.C. Lee Novel nitrogen profile engineering for improved TaN/HfO<sub>2</sub>/Si MOSFET performance. in *Electron Devices Meeting, 2001. IEDM Technical Digest. International*. 2001.
  54. Koyama, M., K. Suguro, M. Yoshiki, Y. Kamimuta, M. Koike, M. Ohse, C. Hongo, and A. Nishiyama Thermally stable ultra-thin nitrogen incorporated ZrO<sub>2</sub> gate dielectric prepared by low temperature oxidation of ZrN. in *Electron Devices Meeting, 2001. IEDM Technical Digest. International*. 2001.

## CURRICULUM VITA

Ming-Tsung Ho

- 1993 B.S. in physics National Cheng Kung University, Tainan, Taiwan
- 1995 M.S. in physics National Cheng Kung University, Tainan, Taiwan.  
(Thesis title: Differential renormalization and background field method study in quantum field theory)
- 2008 Ph.D. in physics Rutgers University, New Jersey, US  
(Thesis title: *In situ* transmission infrared spectroscopy of ultra-thin high- $\kappa$  oxide atomic layer deposition onto silicon surfaces)

## Publications:

1. Y. Wang, M. Dai, M. T. Ho, L. S. Wielunski and Y. J. Chabal, *Infrared characterization of hafnium oxide grown by atomic layer deposition using ozone as the oxygen precursor*. Applied Physics Letters, **90**(2), 022906 (2007).
2. M. M. Frank, Y. Wang, M. T. Ho, R. T. Brewer, N. Moumen and Y. J. Chabal, *Hydrogen barrier layer against silicon oxidation during atomic layer deposition of  $Al_2O_3$  and  $HfO_2$* . Journal of the Electrochemical Society, **154**(2), G44-G48 (2007).
3. L. S. Wielunski, Y. Chabal, M. Paunescu, M. T. Ho, R. Brewer and J. E. Reyes, *Ion backscattering study of ultra-thin oxides:  $Al_2O_3$  and  $AlHfO_x$  films on Si*. Nuclear Instruments & Methods in Physics Research Section B-Beam Interactions with Materials and Atoms, **241**(1-4), 377-381 (2005).
4. M. T. Ho, Y. Wang, R. T. Brewer, L. S. Wielunski, Y. J. Chabal, N. Moumen and M. Boleslawski, *In situ infrared spectroscopy of hafnium oxide growth on hydrogen-terminated silicon surfaces by atomic layer deposition*. Applied Physics Letters, **87**(13), 133103 (2005).
5. R. T. Brewer, M. T. Ho, K. Z. Zhang, L. V. Goncharova, D. G. Starodub, T. Gustafsson, Y. J. Chabal and N. Moumen, *Ammonia pretreatment for high-kappa dielectric growth on silicon*. Applied Physics Letters, **85**(17), 3830-3832 (2004).
6. Yaw-Hwang Chen, Min-Tsung He and Su-Lung Nyeo, *Differential renormalization of scalar field theory in the background-field method*. Chinese Journal of Physics, **34**, 1129-1135 (1996).